Structural Integrity Assessment of Metallic Components Based on Representative Specimens

Vom Fachbereich 13 – Bau- und Umweltingenieurwissenschaften
der Technischen Universität Darmstadt

zur

Erlangung des akademischen Grades eines

Doktor-Ingenieurs

genehmigte
DISSERTATION

vorgelegt von

M. Sc. Jiangchao Zhu

aus Shaanxi, China

Referent:	Prof. Dr.-Ing. Michael Vormwald
Korreferent:	Prof. Dr.-Ing. Uwe Zerbst
Tag der Einreichung:	24. Mai 2023
Tag der mündlichen Prüfung:	17. Juli 2023

Darmstadt 2023
D 17

Jiangchao Zhu
Structural Integrity Assessment of Metallic Components Based on Representative Specimens

Technische Universität Darmstadt
Jahr der Veröffentlichung der Dissertation auf TUprints: 2023
Tag der mündlichen Prüfung: 17.07.2023

URN: urn:nbn:de:tuda-tuprints-245119
URI: https://tuprints.ulb.tu-darmstadt.de/id/eprint/24511

Diese Arbeit erscheint gleichzeitig als vom Fachbereich 13 Bau- und Umweltingenieur-wissenschaften der Technischen Universität Darmstadt zur Erlangung des akademischen Grades eines Doktor-Ingenieurs eingereichte Dissertation (D 17).

Acknowledgements

I would firstly like to express my deepest appreciation to my supervisor, Dr. Mauro Madia, at Bundesanstalt für Materialforschung und -prüfung (BAM), who has always been my guiding light through the difficulties that I came across during the last four years. He has been consistently providing me with the freedom needed to allow this Ph.D. thesis to be my own work, while giving me valuable tips whenever I needed them.

I would also like to thank Dr. Michael Schurig and Dr. Hartmut Schlums from Rolls-Royce Deutschland for their great effort to make this joint research project possible. They have been providing me with opportunities to get in touch with the industry-leading engineering expertise since my Master-degree studies.

I would also like to thank my professors, Professor Michael Vormwald and Professor Uwe Zerbst, for their valuable advices and help on everything I ever needed to develop my research.

My special thanks also go to my colleagues Julius Kruse and Tiago Werner at BAM as well as Fabian Conrad at Materialprüfungsanstalt (MPA) Darmstadt for their extensive help on conducting experiments.

Eventually I must express my profound gratitude to my parents for providing me with unfailing support and continuous encouragement throughout my years of study and research in Germany.

Author

Jiangchao Zhu

Abstract

Safety relevant components, for which a failure in service could have catastrophic consequences, are usually designed for extremely low probability of failure and they are subjected to stringent part qualification procedures according to guidelines set by regulatory agencies. Manufacturers are often pushed to perform tests on full scale or scaled components to ensure the structural integrity under defined loading conditions, which are usually more severe than those expected in-service. This is usually related to a huge experimental and financial effort. Therefore, companies try to develop new strategies such as digital twins, which allow to reduce costs massively, without compromising safety. This work aims at introducing a new structural integrity assessment procedure, the main idea of which is to replace, or at least reduce, the experimental testing on components by designing specimens representative of the component, having the major benefit to be tested on conventional lab testing machines under quasi-static conditions. The effectiveness of the methodology is demonstrated on an industrial case study, namely the structural integrity of a Ni base superalloy disk used in gas turbine aero-engines at overspeed conditions. Firstly, the most stressed sites in the component under combined thermo-mechanical loads have been identified by numerical analyses. The maximum permissible defect defined by regulatory agencies has been introduced at the critical locations to calculate the crack-tip parameters to be used for the representative specimen design. Fracture mechanics specimens have been designed iteratively by numerical simulations to match the stress state including the constraint conditions and the crack-tip loading parameters determined on the component. An extensive experimental campaign has been conducted on representative specimens to determine the failure modes (ductile tearing or plastic collapse). The information about the stable crack extension have been determined post-mortem by fractographic analyses and used in conjunction with dedicated numerical analyses to determine the crack growth resistance curves (R-curves). These have been used in the frame of an analytical flaw assessment procedure based on the CDF philosophy according to the European SINTAP procedure, in order to predict the failure modes and the corresponding critical loads. The results are in good agreement with the experimental tests and show the potential of the presented methodology to predict failures in metallic components.

Kurzfassung

Sicherheitsrelevante Bauteile, bei denen ein Versagen im Betrieb katastrophale Folgen haben könnte, sind in der Regel auf eine extrem niedrige Versagenswahrscheinlichkeit ausgelegt und werden strengen Bauteilqualifizierungsverfahren gemäß von den Aufsichtsbehörden festgelegter Richtlinien unterzogen. Die Hersteller sind oft gezwungen, Tests an Komponenten in originaler bzw. skalierter Größe durchzuführen, um die Strukturintegrität unter definierten Belastungsbedingungen sicherzustellen. Diese sind in der Regel strenger, als die im Betrieb zu erwartenden. Dies ist in der Regel mit einem enormen experimentellen und finanziellen Aufwand verbunden. Daher versuchen die Hersteller, neue Strategien wie digitale Zwillinge zu entwickeln, mit denen die Kosten massiv gesenkt werden können, ohne die Sicherheit zu beeinträchtigen. Die vorliegende Arbeit zielt darauf ab, ein neues Verfahren zur Bewertung der Strukturintegrität einzuführen, dessen Hauptidee darin besteht, die experimentelle Prüfung von Bauteilen zu ersetzen oder zumindest zu reduzieren, indem für das Bauteil repräsentative Proben entworfen werden, die den großen Vorteil haben, dass sie auf herkömmlichen Laborprüfmaschinen unter quasi-statischen Bedingungen geprüft werden können. Die Wirksamkeit der Methodik wird anhand einer industriellen Fallstudie demonstriert, nämlich der Strukturintegrität einer Turbinenscheibe aus einer Ni-basierten Superlegierung, wie sie in Gasturbinen-Flugzeugtriebwerken eingesetzt wird, bei Überdrehzahl. Zunächst wurden die am stärksten belasteten Stellen im Bauteil unter kombinierten thermomechanischen Belastungen durch numerische Analysen bestimmt. An den kritischen Stellen wurden von den Aufsichtsbehörden vorgegebene, maximal zulässige Defekte angenommen. Für diese wurden die Rissspitzenparameter berechnet. Die später zu prüfenden Bruchmechanikproben wurden iterativ durch numerische Simulationen so entworfen, dass sie den Spannungszustand einschließlich der Constraintbedingungen und die am Bauteil ermittelten Rissspitzenbeanspruchungen reproduzierten. Mit ihnen wurde eine umfangreiche Versuchskampagne durchgeführt, bei denen das Versagen (*Ductile Tearing* oder plastischer Kollaps) experimentell untersucht wurde. Die Informationen über das stabile Risswachstum wurden post-mortem durch fraktographische Analysen ermittelt und in Verbindung mit speziellen numerischen Analysen zur Bestimmung der Risswiderstandskurven (R-Kurven) verwendet. Diese wurden im Rahmen eines analytischen Bauteilbewertungsverfahrens, das auf der CDF-Philosophie nach der europäischen SINTAP-Prozedur basiert, zur Vorhersage der Versagensarten und der entsprechenden kritischen Lasten verwendet. Die Ergebnisse stimmen gut mit den experimentellen Tests überein und zeigen das Potenzial der vorgestellten Methodik zur Vorhersage des Bauteilversagens.

Contents

ACKNOWLEDGEMENTS I

ABSTRACT II

KURZFASSUNG III

CONTENTS I

INTRODUCTION 1

1. STATE OF THE ART 3

1.1. Introduction 3

1.2. Standard component evaluation procedures 4

1.2.1. British Standard BS7910 4

1.2.2. Structural Integrity Assessment Procedure (SINTAP) 7

1.3. Failure assessment concepts 8

1.3.1. Failure Assessment Diagram 8

1.3.2. Crack Driving Force (CDF) analysis 11

1.4. Current improvements on failure assessment methods 12

1.4.1. Correction of fracture toughness values based on constraint parameters 12

1.4.2. Modification of failure assessment lines in Failure Assessment Diagram 15

1.4.3. Usage of reference yield load for ligament yielding parameter calculation 17

1.5. Burst speed assessment of turbine disk 19

1.5.1. Background and regulations 19

1.5.2. Failure modes and industrial analysis methods 19

2. METHODOLOGY AND MATERIAL 23

2.1. Introduction 23

2.2. Methodologies 24
2.2.1. Two-criteria failure assessment method 24
2.2.2. Determination of constraint parameters 26
2.2.3. Global stability criterion 29

2.3. Material properties 32

3. NUMERICAL SIMULATION 34

3.1. Introduction 34

3.2. Material models 34

3.3. FE simulations for the turbine disk 35
3.3.1. Reference overspeed calculation 35
3.3.2. Determination of critical locations on the turbine disk 39
3.3.3. Determination of fracture mechanics parameters for cracked turbine disk – crack at diaphragm. 40
3.3.4. Determination of fracture mechanics parameters for cracked turbine disk – crack at bore 45

3.4. Fracture mechanics specimen design 48
3.4.1. Biaxial fracture mechanics specimen for diaphragm crack 48
3.4.2. Uniaxial fracture mechanics specimen for bore crack 56

4. EXPERIMENTS AND ANALYSES 62

4.1. Introduction 62

4.2. Specimen extraction and finishing 62

4.3. Biaxial fracture mechanics experiments 64
4.3.1. Biaxial experiments with through-crack variant 64
4.3.2. Biaxial experiments with surface crack variant 75
4.3.3. Digital Image Correlation (DIC) analysis 79

4.4. Uniaxial fracture mechanics experiments 82
4.4.1. Test of uniaxial specimen A1 84
4.4.2. Determination of R-curve for uniaxial specimen 90

4.5. Spin-tests of turbine disk 92
4.5.1. Rim peel test 92

4.5.2. Hoop burst test 94

5. ANALYSIS OF THE REPRESENTATIVE SPECIMENS 98

5.1. Introduction 98

5.2. Analytical failure assessment for the biaxial specimens with through-crack 98
5.2.1. Determination of limit load for failure mode plastic collapse 99
5.2.2. Determination of load versus stable crack extension curve 102
5.2.3. Two-criteria failure assessment 104

5.3. Analytical failure assessment for biaxial specimen with surface crack 108
5.3.1. Determination of limit load for failure mode plastic collapse 109
5.3.2. Determination of load versus stable crack extension curve 111
5.3.3. Two-criteria failure assessment 113

5.4. Analytical failure assessment for uniaxial specimen 114
5.4.1. Determination of limit load for failure mode plastic collapse 115
5.4.2. Determination of load versus stable crack extension curve 118
5.4.3. Two-criteria failure assessment 119

6. IMPLEMENTATION OF THE METHODOLOGY FOR STRUCTURAL INTEGRITY ASSESSMENT OF METALLIC COMPONENT 122

6.1. Introduction 122

6.2. Determination of critical load for the turbine disk 122
6.2.1. Critical load for diaphragm (rim peel) 122
6.2.2. Critical load for bore (hoop burst) 125

6.3. Methodology validation with spin-test results 127

6.4. Critical load assessment based on global stability criterion 128

6.5. Formulation of structural integrity assessment procedure 131

CONCLUDING REMARKS 132

LIST OF FIGURES 134

LIST OF TABLES 145

LIST OF SYMBOLS 146

LIST OF ABBREVIATIONS **148**

REFERENCES **149**

APPENDIX **154**

Introduction

The present work aims to introduce a novel structural integrity assessment procedure for metallic components which makes use of representative specimens. The assessment procedure has been applied on the Ni base superalloy component used in the gas turbine aero-engine. In contrast to the failure assessment based on elaborate component test, the representative specimen-based assessment greatly reduced cost and time, while yielding comparable results.

Historically, for the safety-relevant components which operate under aggressive mechanical and thermal loading conditions, the failure load, or in engineering point of view, the safety load, has been acquired by conducting component test. While these tests provide, on the one hand, a reliable definition of the critical conditions for real components, on the other hand they represent an immense cost item. Beside the assessment using component test, there have been other approaches for component structural integrity assessment, e.g., making use of the standard component evaluation procedures such as BS7910. However, it has been proven in many cases that the assessment based on these standard procedures sometimes reveals over-conservative results. To address such issue, there are currently improvements suggested in the literature to help optimise the standard procedures with respect of a more precise fracture toughness value, modified assessment lines (boundary to failure) considering loading conditions and constraints and usage of less conservative reference loads. However, these approaches have been either component based but make use of standard or analytically corrected material properties, or test specimen based that cannot or only partially correlate to the real component loading conditions. Moreover, for the metallic components that fail due to overload, the effect of huge plastic deformation on the failure load has only been analytically considered based on material properties in the current approaches. The assessment procedure introduced in this work makes use of specially designed specimen tests to recreate the loading conditions of the critical locations in the flawed component with their corresponding failure mechanisms. Based on the test results of these specimens, fracture toughness values of the specific considered crack at different critical locations in the component under different loading conditions have been acquired. Besides, the failure loads of the representative specimens recorded in the tests can be converted to the failure loads of the component by means of a combine failure assessment method proposed in this work, in which the failure mode between ductile tearing and plastic collapse under consideration of stable crack extension and load increase is determined.

The present work has been developed as follows:

Chapter 1: State of the Art. Extensive literature review has been conducted regarding the structural integrity assessment procedures and recent developments. The standard component evaluation procedures such as BS7910 and SINTAP as well as the failure assessment concepts have been introduced. Current improvements on failure assessment methods were discussed, followed by the current industrial engineering assessment method for the turbine disk structural integrity analysis.

Chapter 2: Methodology and material. The methodologies proposed in this work and their benefits against the current approaches have been discussed. Also, the material properties of the Ni base superalloy Udimet 720 Li used in the investigated turbine disk component were discussed.

Chapter 3: Numerical simulation. The material models used in the FE simulation has been given. The FE simulations of the investigated turbine disk were carried out in order to determine the critical locations on the component. The next step has been creating the FE model with the considered surface crack at the determined critical locations (diaphragm and bore) on the component. Based on the simulation results of these models, the fracture mechanics parameters have been determined for these critical locations on the component and were used to design the representative specimens. The design criterion and results were presented.

Chapter 4: Experiments and analyses. The designed representative fracture mechanics specimens have been extracted and finished from a production turbine disk provided by the engine manufacturer. The biaxial specimens, designed for the turbine disk critical location diaphragm, as well as the uniaxial specimens for the critical location bore have been tested. The failure loads and modes of these specimens have been recorded and analysed. In addition, two spin-tests of production-similar turbine disks have been conducted by the engine manufacturer that were used for methodology validation.

Chapter 5: Structural integrity assessment. Based on the failure assessment methodologies proposed in this work, the biaxial and uniaxial test results were analysed. The plastic collapse load in relation with crack size and the load versus stable crack extension curve have been determined. Based on the two-criteria failure assessment method, the failure loads, failure modes and the critical ligament yielding parameters of both types of specimens have been determined.

Chapter 6: Implementation of the methodology on component. The failure assessment methodologies have been implemented on the turbine disk. Based on the two-criteria failure assessment method and the critical ligament yielding parameters acquired from representative specimens, the critical loads in terms of rotational speeds have been determined for both locations on the turbine disk. Methodology validation with spin-test results has been discussed. In addition, the burst speed of the turbine disk based on the global stability criterion has been determined and compared to the fracture mechanics-based results. Eventually, a formulation of the proposed structural integrity assessment procedure has been given.

1. State of the Art

1.1. Introduction

The structural integrity assessment has been an important process to evaluate and predict the performance and behaviours of structural components under different loading conditions. Analyses are to be conducted to examine the structure, material properties and the effects of defects or damage on the components' strength and mechanical behaviours.

The goal of the structural integrity assessment has been to ensure that the component can operate safely within its designed operation envelope and life limit by determining and preventing potential failure mechanisms. Traditionally, making use of analytical, numerical and experimental approaches, the loading conditions and their response could be determined for the analysed component and comparisons have been made between these values and the material limits, e.g., yield strength. Current structural integrity assessment involved the assessment using the standard component evaluation procedures. In this chapter, the standard evaluation procedures for components containing cracks or flaws such as BS7910 and SINTAP have been introduced. While on the one hand these standard evaluation procedures provide a convenient and conservative way for the structural integrity assessment, on the other hand however, over conservatism has been determined in many cases which led to weight increase and non-efficiency of the structure. To address this problem, many improvements have been proposed in the literature in recent years to optimise the standard procedures, which focused on correction of the fracture toughness of the material based on constraint parameters, modification of the failure assessment lines which defined the boundary between "safe" and "potential failure" of the component and the usage of reference yield load to replace the limit load.

Further, with respect to the investigated component in this work, the turbine disk used in the aero-engine, the structural integrity assessment in form of burst speed determination has been introduced. Firstly, background and regulations for turbine disk burst speed assessment were presented. Based on these requirements, the current industrial methodology to assess the failure modes as well as their corresponding failure loads have been discussed.

1.2. Standard component evaluation procedures

1.2.1. British Standard BS7910

The British Standard BS7910 [1.1] was a flaw assessment concept based on the principle of fitness-for-service. By this principle a structure is considered to be adequate for its purpose, provided the conditions to cause failure are not reached. The engineering critical assessment (ECA) is provided by the BS7910 for flaws that are more severe than the quality control levels. The sequence of the ECA is given as following [1.1]:

a) Identify the flaw type, i.e., planar, non-planar or shape.

b) Establish the cause of the flaw.

c) Establish the essential data, relevant to the particular structure.

d) Determine the size of the flaw.

e) Assess possible material damage mechanisms and damage rates.

f) Determine the limiting size for the final modes of failure.

g) Based on the damage rate, assess whether the flaw would grow to this final size within the remaining life of the structure or the in-service inspection interval, by sub-critical crack growth.

h) Assess the consequences of failure.

i) Carry out sensitivity analysis.

j) If the flaw would not grow to the limiting size, including appropriate factors of safety, it is acceptable. The safety factors should take account both of the confidence in the assessment and of the consequences of failure.

Like the R6 routine [1.2], the concept of the so-called two-criteria approach and the Failure Assessment Diagram (FAD) was introduced in the BS7910, in which failure was assumed either when the stress intensity factor in the component exceeds the fracture toughness or when the applied load exceeds the plastic collapse load of the net section of the component containing the crack (cf. Figure 1.1). The fracture of a specimen or a component can occur by different mechanisms such as cleavage fracture, micro-ductile fracture or plastic collapse, which are covered by the boundary curves in a FAD so that there is no need to determine whether a cracked component operates in small-scale yielding, net-section yielding or in the plastic-collapse region [1.3].

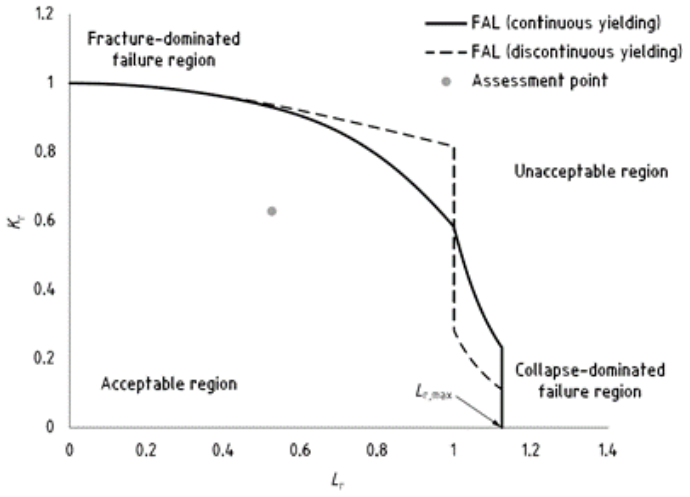

Figure 1.1 Example of a Failure Assessment Diagram according to BS7910 [1.1].

As shown in Figure 1.1, the ECA consists of evaluating parameters: fracture ratio K_{r} and load ratio L_{r}, dependent on the applied loads, material properties, as well as component and crack geometry. These evaluating parameters are defined as following:

$$K_{\mathrm{r}} = \frac{K}{K_{\mathrm{mat}}} \tag{1.1}$$

$$L_{\mathrm{r}} = \frac{P}{P_{\mathrm{L}}(\mathrm{a}, \sigma_{\mathrm{Y}})} = \frac{\sigma_{\mathrm{ref}}}{\sigma_{\mathrm{Y}}} \tag{1.2}$$

where K is the stress intensity factor at load P, P_{L} is the elastic perfectly plastic limit load for flaw size a and material's yield stress σ_{Y} and K_{mat} is the fracture toughness. The assessment point (L_{r} ,K_{mat}) is plotted in the FAD and compared with a Failure Assessment Line (FAL) defined as $K_{\mathrm{r}} = f(L_{\mathrm{r}})$ and an additional limit cut-off line given by $L_{\mathrm{r}}^{\max}$ to prevent plastic collapse failure, which is defined as

$$L_{\mathrm{r}}^{\max} = \frac{1}{2} \cdot \frac{\sigma_{\mathrm{Y}} + R_{\mathrm{m}}}{\sigma_{\mathrm{Y}}} \tag{1.3}$$

When the assessment point is located within the FAL and limit cut-off line, the flaw is acceptable and the component is judged as "safe", whereas in case of the assessment point lying outside of the limit curves, the component is considered to have potential failure.

There are several levels of treatment of flaws depending on the application and materials data available [1.1]:

- Option 1 is a conservative procedure that is relatively simple to employ and does not require detailed stress/strain data for the materials being analysed.
- Option 2 is based on the use of a material-specific stress-strain curve.
- Option 3 uses numerical analysis to generate a failure assessment diagram (FAD).

The FAL $K_{\mathrm{r}} = f(L_{\mathrm{r}})$ is analytically determined according to these three options with increasing accuracy.

An annex is provided in the BS7910 to discuss the conservatism in the procedure due to the influence of constraint on the fracture toughness K_{mat}. The K_{mat} used in the procedure is normally derived from deeply cracked bend specimen using recommended testing standards and validity criteria, which are designed to ensure plane strain conditions and high hydrostatic stresses near the crack-tip to provide a materials property independent of specimen size and geometry [1.1]. However, the fracture toughness is increased when specimens with shallow flaws are tested, which leads to lower hydrostatic stresses at the crack-tip and less restrained plastic flow fields referred to as lower constraint [1.1]. The annex is limited to T-stress and Q parameter, which are known as constraint parameter describing the constraint effect. Guidance is given in the annex on the inclusion of constraint-dependent toughness in a FAD-based assessment using two inputs: the magnitude of load-dependent constraint defined by the T-stress or Q parameter, and the constraint sensitivity of the material toughness defined by the parameters α and k [1.1]. Note that the T-stress is calculated elastically, whereas the Q parameter is expected to provide more accurate assessment, particularly with higher plasticity. The definitions of these constraint parameters are as following:

$$\sigma_{ij}(r,\theta) = \frac{K_I}{\sqrt{2\pi r}} f_{ij}(\theta) + T\delta_{1i}\delta_{1j} \tag{1.4}$$

$$\sigma_{ij} = \left(\sigma_{ij}\right)_{Ref} + Q\sigma_0\delta_{ij} \tag{1.5}$$

With σ_0 usually taken as the yield strength of the material and $\left(\sigma_{ij}\right)_{Ref}$ is a reference stress field which can be defined in different ways but usually represents the HRR field [1.4]. More detailed discussion of these constraint parameters can be found in [1.5]. As introduced, the fracture toughness K_{mat} is corrected for lower constraint based on the constraint parameters:

$$K_{\mathrm{mat}}^{\mathrm{c}} = K_{\mathrm{mat}}[1 + \alpha(-\beta L_{\mathrm{r}})^k] \text{ when } \beta L_{\mathrm{r}} \leq 0 \tag{1.6}$$

where a special structural constraint parameter β is calculated analytically from T-stress or Q parameter according to different crack-tip loading scenarios. The parameters α and k (material and temperature dependent constants) can be obtained by different ways, e.g., look-up table values, or curve-fitting [1.1]. With the corrected fracture toughness $K_{\mathrm{mat}}^{\mathrm{c}}$, the FAD is modified in which the FAL now becomes

$$K_{\mathrm{r}} = f(L_{\mathrm{r}})[1 + \alpha(-\beta L_{\mathrm{r}})^k] \text{ when } L_{\mathrm{r}} \leq L_{\mathrm{r}}^{\max} \tag{1.7}$$

Note that all three option FAL curves modified by Eq. (1.7) are now dependent on geometry (through β), on material toughness properties (through α, k) and also on material tensile properties if β is defined in terms of the Q parameter.

1.2.2. Structural Integrity Assessment Procedure (SINTAP)

The Structural Integrity Assessment Procedure (SINTAP) provides a fitness-for-service procedure, with the aim of devising a unified procedure for the assessment of fracture behaviour [1.3]. One of the main tasks in SINTAP is focused on failure of cracked components with the aim to extend the understanding of the behaviour of cracked components in the specific areas of constraint, influence of yield strength to tensile strength ratio, prior overload, leak-before-break, and stress intensity factor and yield load solutions [1.3]. Several improvements and novel features of the SINTAP procedure compared to other approaches (such as the R6 routine) are listed in [1.6], in which the most important changes are:

- Extension and more detailed outline of the principle of stepwise graded conservatism
- Redefined $f(L_r)$ functions for materials with and without yield plateau
- Guidance on statistical aspects, among others with respect to the fracture toughness
- A modified approach for treating combined primary and secondary stresses.

Similar to the BS7910, the SINTAP flaw assessment procedure also permits analyses at multiple levels of complexity and accuracy, in which higher options are much more complex than a lower one and need improved input information but provide less conservative results [1.3]. An overview of the SINTAP assessment options is given in Table 1.1.

Table 1.1 Overview of the SINTAP assessment options

option	SINTAP designation	Data needed	Application range remarks
		Basic option	
0	Default Level	Yield strength, Charpy data	When no other tensile data available
		Standard Options	
1	Basic Level	Yield strength, Tensile strength, Fracture toughness	When no complete stress-strain curve available
2	Mismatch Level	Yield strength, Charpy data	For yield strength mismatch > 10%
3	Stress-Strain Level	Complete stress-strain curve, Fracture toughness	Assessment modules for homogenous & yield strength mismatched components
		Advanced Options	
4	J-Integral Level	Complete stress-strain curve, Fracture toughness	Numerical determination of crack-tip parameters, e.g., J
5	Constraint Level	Geometry dependent fracture toughness	Based on two-parameter concepts

Like in the BS7910, the failure assessment diagram is used in the SINTAP for flaw assessment. Except for the advanced options, the failure assessment lines $f(L_r)$ are analytically determined according to different options, whereas in the advanced options the numerical simulations are used.

The effect of constraint is considered in Option 5 of the SINTAP procedure, where a constraint corrected fracture toughness K_{mat}^{c}, like in the BS7910, is applied. Since the constraint decreases with increasing ligament yielding, the constraint corrected fracture toughness will increase with increasing L_r [1.3]. There are three constraint parameters introduced in the SINTAP, namely the stress triaxiality factor h, T-stress and Q parameter. Note that although the h parameter can characterise the actual three-dimensional stress state without any limiting assumption, however, it is not recommended within SINTAP because it is not a constant but is dependent on the distance, r, to the crack-tip for strain hardening materials. Additionally, it requires a full three-dimensional finite element calculation for its determination [1.3]. The determination of constraint parameters T and Q as well as the structural constraint parameter β is similar to that in the BS7910. An example of a SINTAP assessment based on FAD approach including constraint effects is given in Figure 1.2.

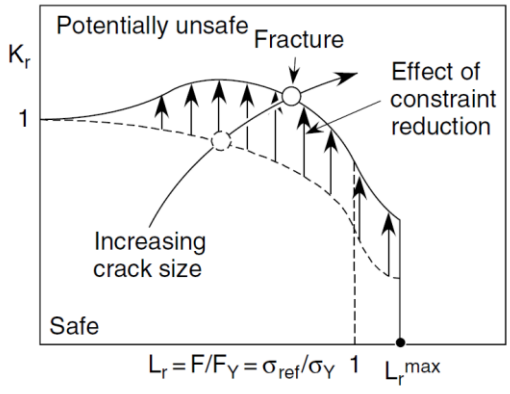

Figure 1.2 Example of a SINTAP assessment based on FAD approach including constraint effects [1.3].

1.3. Failure assessment concepts

1.3.1. Failure Assessment Diagram

In the FAD approach, a component geometry-dependent limit curve, or Failure Assessment Line (FAL) $K_r = f(L_r)$, is constructed by referring the crack driving force to the fracture resistance of the material (cf. Eq. (1.1)).

The assessment of the component is then based on the relative location of an assessment point (K_r, L_r), or path, with respect to this limit curve as illustrated in Figure 1.3 [1.3]. The assessment point (path) is a function of the component geometry, the applied loads, crack size and shape. According to [1.3], the information necessary for determining the assessment point includes:

1) The load either in terms of forces, moments, pressure etc. or stress distributions.

2) The stress intensity factor K for the given crack size.
3) The net section yield load F_{Y} or its equivalents in terms of the net section stress σ_{ref} or the ligament yielding parameter L_{r} for the given crack size.
4) The toughness of the material in terms of K_{mat}, a general term that can have different meanings:
   i) It can be identical to the plane strain fracture toughness K_{Ic}.
   ii) It can be identical to the resistance against stable ductile crack initiation, J_{i}, δ_{i}, $J_{0.2/\mathrm{BL}}$, $\delta_{0.2/\mathrm{BL}}$etc. but expressed in terms of the K-factor.

If the toughness is originally available in terms of J-integral, K_{J} value can be formally determined by

$$K_{\mathrm{J}} = \left[J \cdot \frac{E}{1-\nu^2} \right]^{\frac{1}{2}} \tag{1.8}$$

with the assumption of plane-strain conditions.

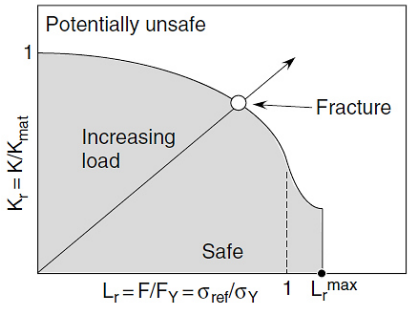

Figure 1.3 Failure Assessment Diagram (FAD) for a constant crack size under increasing load [1.3].

As introduced in section 1.3, The advantage of the FAD approach is that different failure modes including plastic collapse and unstable ductile tearing can be evaluated (Figure 1.4) using the same set of equations. The FAL, which can also be interpreted as a plastic correction function $f(L_{\mathrm{r}})$, can be calculated analytically or numerically according to different options, e.g., in BS7910 or SINTAP. In the following part of this section, the $f(L_{\mathrm{r}})$ function according to the different analysis levels will be discussed. Note that the turbine disk material investigated here does not display a yield plateau. As a result, the options for the material expected to display a yield plateau are not included in this work.

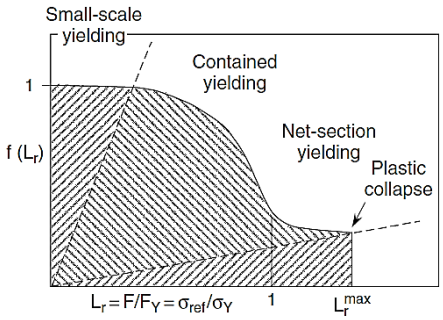

Figure 1.4 Ligament yielding ranges and corresponding failure mechanisms in a FAD [1.1].

In the Option 0 proposed by SINTAP, applicable if only the yield strength of the material is available, the plastic correction function $f(L_r)$ is expressed as

$$f(L_r) = [1 + 0.5 \cdot L_r^2]^{-\frac{1}{2}} \cdot [0.3 + 0.7 \cdot \exp(-0.6 \cdot L_r^6)] \tag{1.9}$$

with

$$L_r^{max} = 1 + \left(\frac{150}{R_{p0.2}}\right)^{2.5}. \tag{1.10}$$

In the Option 1 proposed by BS7910 (Option 1B in SINTAP), both the yield strength and the ultimate tensile strength of the material must be available. The plastic correction function $f(L_r)$ is given by

$$f(L_r) = [1 + 0.5 \cdot L_r^2]^{-\frac{1}{2}} \cdot [0.3 + 0.7 \cdot \exp(-\mu \cdot L_r^6)] \text{ for } 0 \le L_r \le 1 \tag{1.11}$$

$$f(L_r) = f(L_r = 1) \cdot L_r^{\frac{N-1}{2N}} \text{ for } 1 \le L_r \le L_r^{max} \tag{1.12}$$

with

$$\mu = \min\begin{cases} 0.001 \cdot \left(\frac{E}{R_{p0.2}}\right) \\ 0.6 \end{cases} \tag{1.13}$$

$$N = 0.3 \cdot \left[1 - \left(\frac{R_{p0.2}}{R_m}\right)\right] \tag{1.14}$$

$$L_r^{max} = 0.5 \cdot \left[\frac{R_{p0.2} + R_m}{R_{eL}}\right]. \tag{1.15}$$

The term μ in Eq. (1.13) is introduced in order to provide a conservative estimate of $f(L_r)$ in the strain range between $(R_{p0.2}/E)$ and $\left(\frac{R_{p0.2}}{E}\right) + 0.02$. This becomes necessary since the proof strength $R_{p0.2}$ refers to a significantly larger strain than R_{eL}. It belongs to the lower tail of the strain hardening branch of the stress–strain curve rather than assigning a transition between elastic and plastic deformation. The task of μ is to avoid any effect of strain hardening at and below $L_r = 1$ [1.3].

For the Option 2 of the BS7910 (Option 3 in SINTAP), the complete stress-strain curve of the material must be available. The plastic correction function $f(L_r)$ is

$$f(L_r) = \left[\frac{E \cdot \varepsilon_{ref}}{\sigma_{ref}} + \frac{1}{2} \cdot \frac{\sigma_{ref}}{E \cdot \varepsilon_{ref}} \cdot L_r^2\right]^{-\frac{1}{2}} \tag{1.16}$$

with

$$L_r^{max} = \frac{1}{2} \cdot \frac{\sigma_Y + R_m}{\sigma_Y}. \tag{1.17}$$

The highest analysis Option 3 (BS7910) is based on FE simulations for determining the crack driving force. Consequently, the plastic correction function $f(L_r)$ is determined based on numerically obtained values of J and J_e along the crack-front.

$$f(L_r) = \sqrt{\frac{J_e}{J}} \tag{1.18}$$

A failure assessment curve specific to a particular material, geometry and loading type can be determined using both elastic and elastic-plastic analyses of the flawed structure as a function of the loads giving rise to primary stresses, i.e., those which contribute to the evaluation of L_r [1.1].

1.3.2. Crack Driving Force (CDF) analysis

The CDF functions are given by

$$J = J_e \cdot [f(L_r)]^{-2} \tag{1.19}$$

in terms of the J-integral. The $f(L_r)$ function in Eq. (1.19) has been identical to those given in 1.3.1. However, in contrast to the FAD line, which is fully defined by $f(L_r)$ and the component geometry and loading conditions were only considered in K_r or L_r, the CDF functions are defined for specific component and loading geometries [1.3]. The fracture toughness is given as J_{mat} in terms of a specific value against stable crack extension or in terms of R-curve, which is not included in the CDF functions but is compared with the CDF separately. If the fracture toughness is given as a single value, the critical condition of the component is determined when the CDF curve exceeds this value or the plastic collapse limit given by L_r^{max}. An example is given in Figure 1.5 when the CDF curve exceeds the fracture toughness J_{mat}.

If the fracture toughness is given in terms of R-curve, the critical condition of the component with the failure mode ductile tearing is then determined as illustrated in Figure 1.6a. The CDF curves are determined for several different constant loads (marked with Load 1, Load 2 and Load 3 in Figure 1.6a) and are compared with the R-curve of the material. The load whose CDF curve remains tangent to the R-curve of the material is characterised as the critical load for the failure mode ductile tearing.

A second way to determine the instability load for failure mode ductile tearing is provided in Figure 1.6b with the analysis steps illustrated in Figure 1.7 with the complete load versus stable crack extension characteristics of the component predicted [1.3].

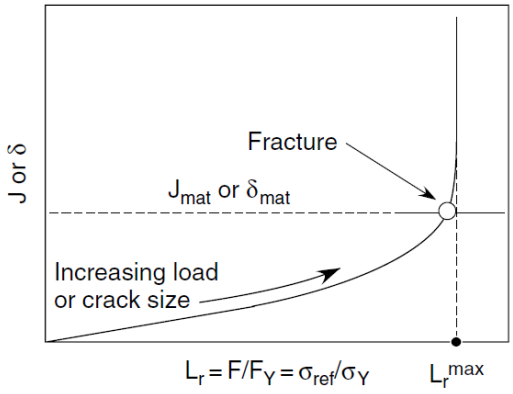

Figure 1.5 Determination of the critical condition of a component following the CDF philosophy when the fracture toughness is given by a single value. The L_r^{max} limit assigns the plastic collapse limit [1.3].

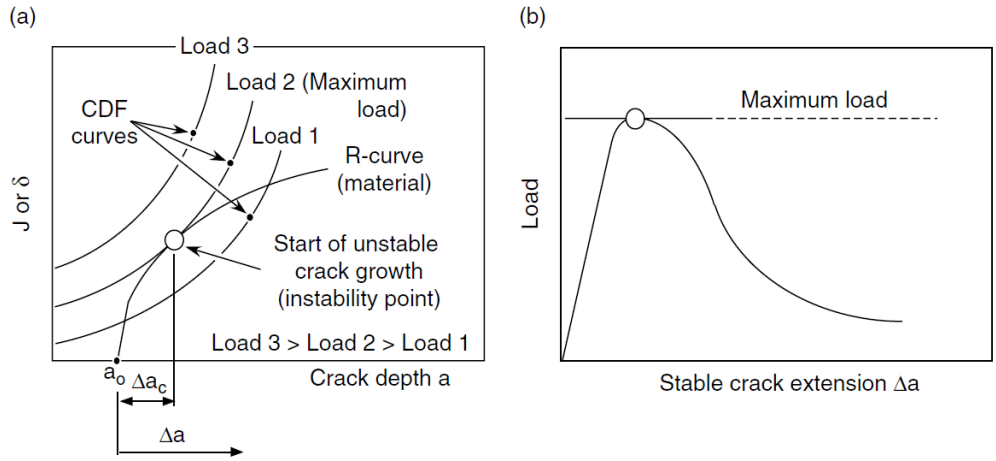

Figure 1.6 Types of CDF analysis for determining the instability load of a component for failure mode ductile tearing: (a) CDF curves are determined for constant applied loads and compared with the R-curve of the material (a_0 marks the original crack size in the component); (b) The load versus stable crack extension curve determined following the route in Figure 1.7 [1.3].

1.4. Current improvements on failure assessment methods

Currently, there have been several improvements made for failure assessment as well as failure prediction methods in the literature. Advantages over the standard component evaluation procedures have been focused on the following aspects:

- Correction of fracture toughness values based on constraint parameters
- Modification of failure assessment lines in Failure Assessment Diagram
- Usage of reference yield stress for ligament yielding parameter calculation

1.4.1. Correction of fracture toughness values based on constraint parameters

As introduced before, in the conventional failure assessment procedure, the failure criterion against fracture has been given by the fracture toughness or the ligament yielding correction function $f(L_r)$ as failure assessment line in a FAD. In the conventional testing standards such as ASTM E399 [1.7] to

measure fracture toughness for metallic component, three-point bend SE(B) and compact tension C(T) specimens with deep through-cracks have been used. The main reason for using these deeply cracked specimens has been to ensure a highly constrained crack ligament which resulted in limited plasticity on the ligament. Under such conditions, fracture toughness values characterize essentially the cleavage fracture failures. This has been considered conservative in component design, however, in the failure assessment of component, such crack-tip conditions have been rarely met since the flaw or defect sizes were often small in comparison to the component and the component loading conditions could also deviate from standard test. In order to correct the fracture toughness measured by the standard tests, constraint parameters have been used as correction factors. It has been discussed in Annex N of the BS7910 to use constraint parameters T or Q for fracture toughness K_{mat} or $f(L_{\mathrm{r}})$ correction (cf. section 1.2.1).

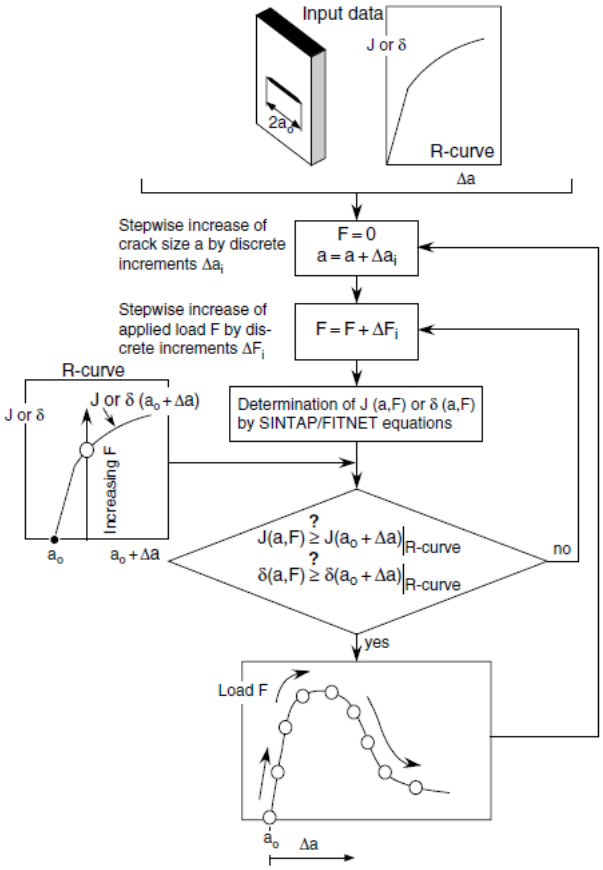

Figure 1.7 Flow chart for determining the applied load versus stable crack extension characteristics in Figure 1.6b [1.3].

Constraint effect on fracture toughness testing has been researched in [1.8] by using non-standard bend specimen geometries. A fracture toughness test methodology was described to evaluate J-integral and CTOD values with consideration of potential influence of specimen geometry and loading on fracture behaviour in terms of $J - Q$ descriptions to quantify constraint effects. In [1.9], the test methodology developed in [1.8] was utilised to evaluate the measured values of J-integral at cleavage instability, J_{c}, for fracture testing of non-standard bend specimens. In [1.10] and [1.11], computational

studies have been carried out to explore the applicability of single edge notch tension (SE(T)) specimens to characterize fracture behaviour of axially cracked pipes under plane-strain as well as 3-D conditions by using the $J-Q$ methodology. Comparisons of the $J-Q$ trajectories on the crack ligament were made between the cracked specimens and a pressurised cracked pipe based on the numerical simulations (Figure 1.8).

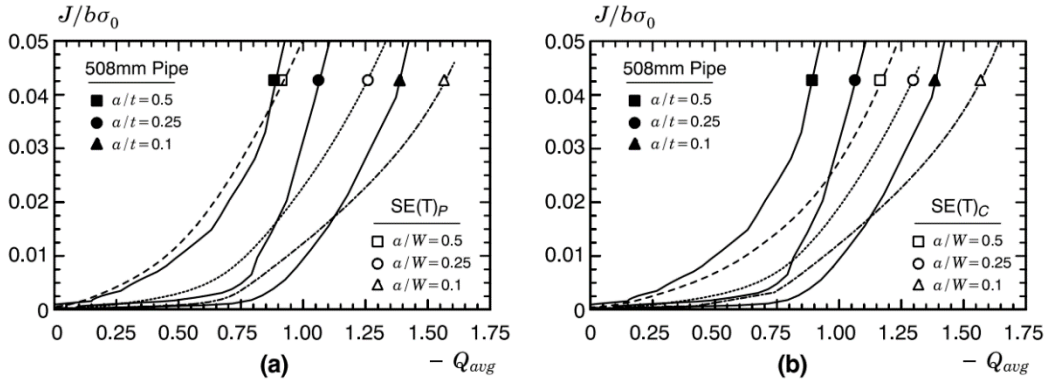

Figure 1.8 Comparison of $J-Q_{avg}$ trajectories for SE(T) specimens and cracked pipes: (a) pin-loaded SE(T); (b) clamped SE(T) [1.11].

In [1.12], two constraint parameters have been proposed to correct the fracture toughness of A508 steel and to assess the ductile fracture behaviour of the cracked pipes of this material. The crack driving force (CDF) approach for predicting ductile fracture based on two-parameter $J-A_p$ and $J-A_d$ has been investigated and developed, where A_p and A_d were the unified constraint parameters based on crack-tip equivalent plastic strain and crack-tip opening displacement (CTOD), respectively.

$$A_p=\frac{A_{PEEQ}}{A_{ref}} \qquad (1.20)\ [1.12]$$

$$A_d=\frac{\delta}{\delta_{ref}} \qquad (1.21)\ [1.12]$$

Where A_{PEEQ} was the area surrounded by the equivalent plastic strain isoline at the crack tip in a specimen or component, A_{ref} a reference area surrounded by the isoline in a standard plane strain specimen with high constraint at fracture, δ the CTOD of a cracked specimen or structure and δ_{ref} the CTOD of a standard plane strain reference specimen with high constraint at fracture. Analytical solutions for the corrected fracture toughness J_c were fitted with respect to A_p and A_d values, being J_{ref} the fracture toughness measure in a standard test at fracture. The ductile fracture toughness predicted by the $J-A_p$ and $J-A_d$ approaches compared with the reference values have been shown in Figure 1.9 [1.12].

$$\frac{J_c}{J_{ref}}=0.567A_p^{\frac{1}{2}}+0.428 \qquad (1.22)\ [1.12]$$

$$\frac{J_c}{J_{ref}} = 0.546A_d + 0.45 \qquad (1.23)\ [1.12]$$

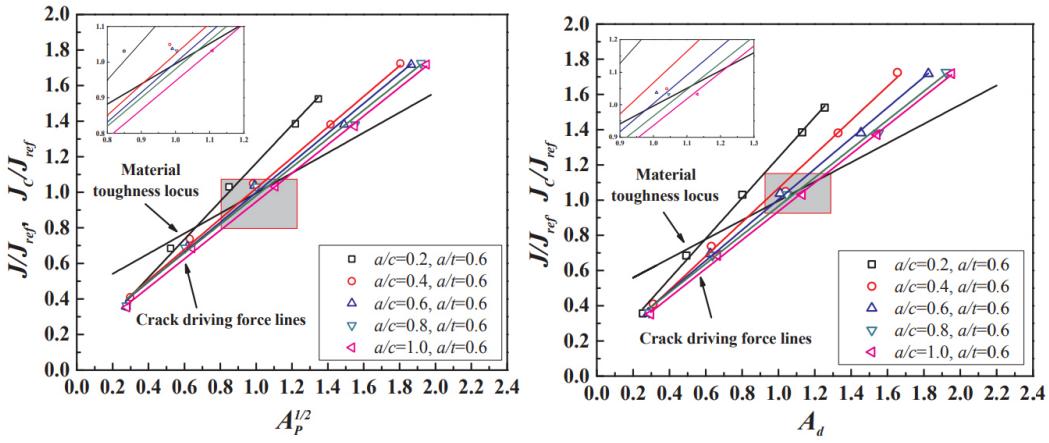

Figure 1.9 Intersection of crack driving force lines with material toughness locus for cracked pipes with different crack sizes based on $J - A_p$ and $J - A_d$ approaches [1.12].

In [1.13], a method has been presented that could be used to predict the influence of constraint on the cleavage and ductile fracture toughness of a range of ferritic steels, and hence the associated benefit to the onset upper shelf temperature by using area contour toughness scaling. The fracture toughness for a standard high constraint specimen J_{mat} could be correlated with an equivalent $J^{\mathrm{c}}_{\mathrm{mat}}$ for a low constraint structure by

$$\frac{J^{\mathrm{c}}_{\mathrm{mat}}}{J_{\mathrm{mat}}} = \sqrt{\frac{A^{SSY}}{A^{C}}} \qquad (1.24)\ [1.13]$$

where A^{SSY} is the area enclosed by an iso-stress contour for a high constraint, small scale yielding model, and A^{C} is the area enclosed by the same iso-stress contour for the low constraint model [1.13].

1.4.2. Modification of failure assessment lines in Failure Assessment Diagram

Another improvement aspect over the current component evaluation procedures has been the modification of the failure assessment lines (FAL) or the $f(L_{\mathrm{r}})$ in the Failure Assessment Diagram (FAD). As discussed in section 1.3.1, the FAL has been component geometry-dependent and thus constraint-dependent. Also, it has been reported in [1.14-1.17] that the FAL was also influenced by loading conditions. As a result, the FAL could be modified based on the loading conditions as well as constraint parameters to achieve less conservative assessment results for the component or structures.

In [1.14], biaxially and uniaxially loaded cruciform test results have been analysed in accordance with the current BS 7910 and R6 fracture assessment procedures as well as with the use of tailor-made FEA analyses. A constraint corrected FAL has been generated according to BS7910 (Eq.(1.7)). The structural constraint parameter β has been determined for different biaxiality ratios based on FE simulations.

The constraint corrected FALs for the cruciform specimen have been compared against the FALs based on BS7910 Option 3 in Figure 1.10.

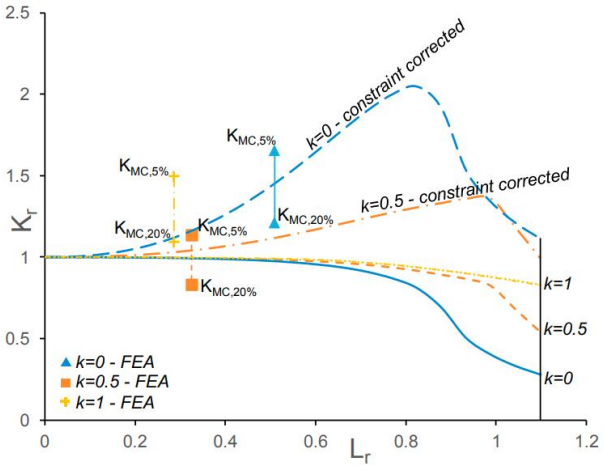

Figure 1.10 Constraint modified Option 3 FALs, k is the biaxiality ratio with k=0 being uniaxial [1.14].

In order to quantify elastic-plastic J under combined primary and secondary stresses within the FAD approach to fracture assessment, a simple approximation for the V-factor, which was a multiplication factor to quantify the interaction effects between mechanical and thermal loads, was proposed in [1.3, 1.17]. It has been researched in [1.15] to explore the applicability of this V-factor to biaxial stress states in case of circumferentially cracked pipes. The elastic-plastic J under combined primary and secondary stress can then be estimated from

$$J^{p+s} = \frac{(K^p + V \cdot K^s)^2}{E'} \left(\frac{E\sigma_{ref}}{\sigma_{ref}} + \frac{1}{2} L_r^2 \frac{\sigma_{ref}}{E\sigma_{ref}} \right) \qquad (1.25)\ [1.15]$$

being K^s the stress intensity factor due to secondary stress.

The interaction between coplanar circumferential cracks in pipes under combined internal pressure and axial tension has been examined in [1.16]. Different configurations of the coplanar cracks have been numerically analysed. An equivalent J value based on the constraint-based crack interaction factor Ψ was proposed. Based on this equivalent J-value, the option 3 FAL for circumferential coplanar cracks in pipes was modified and compared with the FALs with the existing approach for coplanar cracks in BS7910 (Figure 1.11). The modified FAL was given as

$$f(L_r) = \begin{cases} \dfrac{1}{\sqrt{\left(\dfrac{\Psi}{\Psi_e}\right)^{n+1}}} \sqrt{\dfrac{J_e}{J}} & \text{for } L_r < L_{r,max} \\ 0 & \text{for } L_r \geq L_{r,max} \end{cases} . \qquad (1.26)\ [1.16]$$

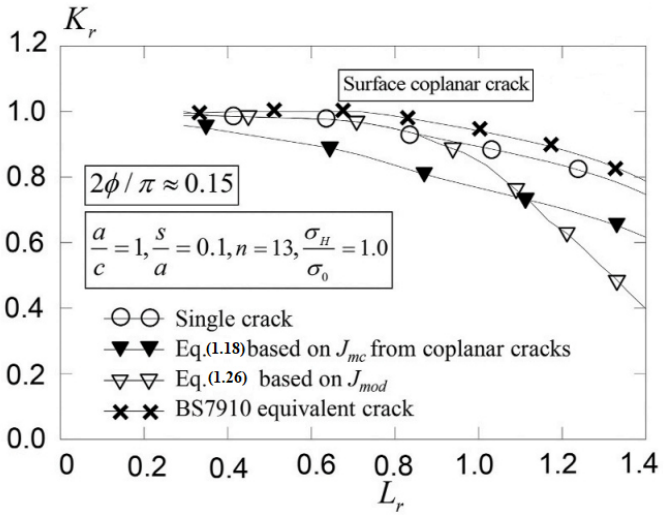

Figure 1.11 Failure Assessment diagram for a pipe with coplanar surface cracks under combined internal pressure and axial tension (modified from [1.16]).

1.4.3. Usage of reference yield load for ligament yielding parameter calculation

The net section limit load necessary for assessment at static loading is a key input for the accuracy of any elastic–plastic flaw assessment procedure of the R6 type. Unfortunately, available limit load solutions are of variable quality since they have been obtained over decades by different methods. As a consequence, the results of the fracture analyses such as the critical load or crack size are limited in their accuracy and are often significantly conservative. Further, common limit load solutions based on ligament yielding are inadequate in a number of cases even for through crack configurations and should be replaced by some kind of local yielding solutions [1.18]. In [1.18-1.20], methods have been proposed by which the limit or yield load in R6 type flaw assessment methods has been replaced by a reference load, which not only provided more exact fracture mechanics predictions, but showed also a wider and more general application range than the conventional parameter. This reference load is based on the condition that when the ligament yielding parameter L_{r} is equal to unity, J obtained by finite element analysis is equal to a value determined by the $f(L_{\mathrm{r}})$ function of the FAD or applied crack driving force curve [1.18].

It has been discussed in [1.18, 1.11] about the limit load and ligament yielding and the corresponding failure modes. A distinction must be made between two limiting conditions [1.18]:

- The load at which the whole ligament becomes plastic. This limit load is sometimes, e.g., in [1.3], designated as the net section yield load.
- The load at which the component finally fails due to plastic collapse. This limit load is higher than the yield load and is sometimes designated as the plastic collapse load.

For the structures containing a crack in a large ligament, the local limit or yield load has been defined which referred to bounded yielding within a certain area ahead of the crack-tip and not to the whole

ligament. Particularly, with respect to the important application field of semi-elliptical surface cracks the conventional methods of limit load determination reach their limit and have to be replaced by alternative solutions in that it is distinguished between ‘‘global” and ‘‘local” limit loads. The point is the definition of an adequate ligament when a comparatively small crack is embedded in a large structure such as the turbine disk. The rather general definition of a ‘‘local” limit load is that it causes local ligament yielding along the crack-front [1.4]. Note that the reference yield load is not a limit load, but a local parameter. Therefore, different σ_0 (reference yield load in terms of stress) values have to be obtained for various locations along the crack-front, using analytical solutions or FE simulations. As a result, the σ_0 values are influenced by the local plastic zones ahead of the crack and therefore depend on the constraint parameters, beside crack dimensions, component geometry and the loading scenario.

In [1.21], the analytical solutions of reference yield stress for different locations along the crack-front of a surface crack in plates under biaxial tensile loading conditions have been proposed. These reference yield stress values were then compared with the values acquired by numerical methods as well as literature solutions. A 10% higher reference yield stress was concluded over the equivalent stress, which represented a potential improvement in many applications.

A fail-safe design criterion for a steering knuckle of a commercial vehicle has been proposed in [1.22] to examine the effect of stiffness/constraint on the crack driving force in the component. When applying the standard failure assessment procedures such as R6, BS 7910 or SINTAP/FITNET in conjunction with substitute geometries for determining the model parameters K-factor and limit load, the conservatism was so pronounced that these procedures were in fact unusable. FE simulations were conducted to determine the reference yield stress as limit load for different locations along the crack-front.

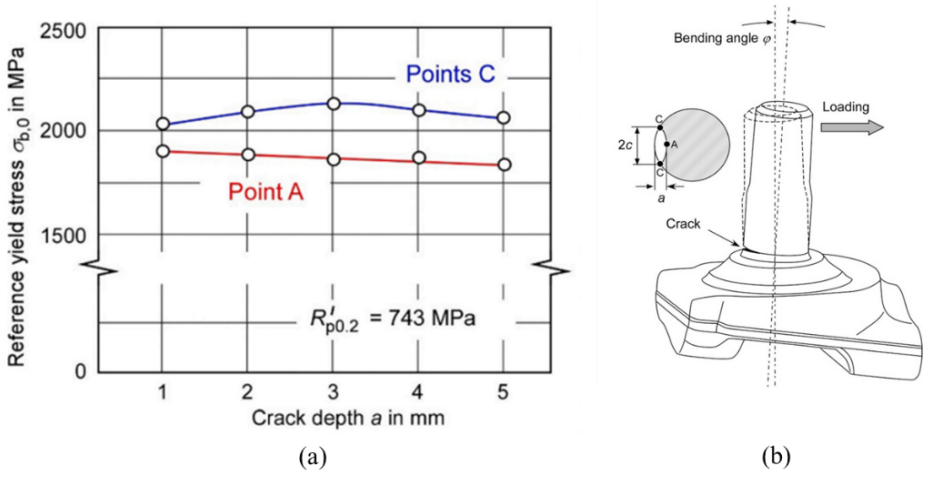

Figure 1.12 Reference yield stress as function of crack size determined for the steering knuckle by finite element analysis: (a) reference yield stress versus crack depth curves; (b) Schematic view of the investigated component (modified from [1.22]).

1.5. Burst speed assessment of turbine disk

1.5.1. Background and regulations

Aero-engine turbine disks are safety-relevant components which are operated under high thermal and mechanical stress conditions. The rotor integrity of an aero-engine turbine disk has to be established for the overspeed condition beyond the normal engine operation envelope. The turbine disk can experience an increased rotational speed during engine control system failure [1.23] or when mechanical failure occurs at other locations, e.g., failure of the shaft between compressor and turbine [1.24]. During such an event, the burst of the turbine disk must be avoided to prevent any catastrophic consequences [1.25], for the engine casing is not designed for such failures.

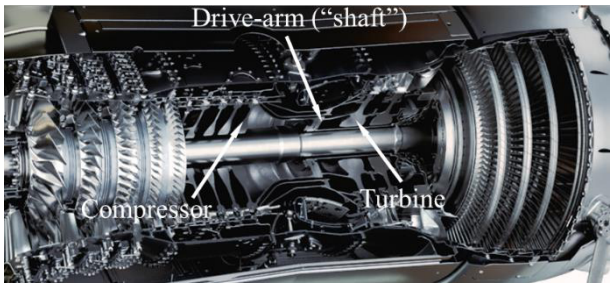

Figure 1.13 Cutaway of an aircraft engine (modified from [1.26]).

The corresponding regulations for rotor integrity compliance dictates that for the turbine rotor, it must be established by test, analysis, or combination thereof, that a rotor which has the most adverse combination of material properties and dimensional tolerances allowed by its type design will not burst when it is operated in the Engine for 5 minutes at the most critical speed and temperature conditions [1.27]. Conventionally, this requirement is ensured by performing finite element (FE) analyses for disk geometry by type design and conducting the so-called overspeed spin-test by the engine manufacturer [1.28]. During the overspeed spin-test, a specially designed production-similar disk is tested at the most limiting conditions for 5 minutes. Test disks that do not have the most adverse combination of material properties and dimensional tolerances must be tested at conditions which have been adjusted to ensure the minimum specification rotor possesses the required overspeed capability. This can be accomplished by increasing the test speed, temperature, and/or loads as accepted by the Acceptable Means of Compliance [1.27]. The mechanical and thermal stresses of the spin-test disk are then analysed for different failure modes by FE simulations which correlate to the production disk.

1.5.2. Failure modes and industrial analysis methods

Under overspeed conditions, discs are subjected to increased centrifugal loads and high stresses are generated with their peaks usually located in bore, diaphragm and stress concentration features (see Figure 1.14).

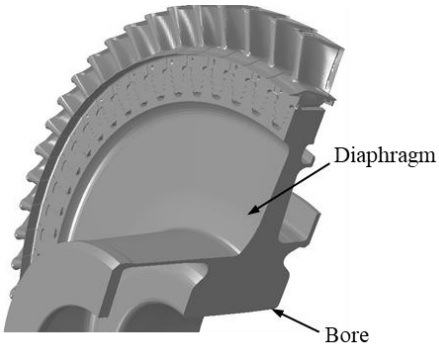

Figure 1.14 Cross section of a typical bladed turbine disk.

As the stresses in these features increase and exceed the yield stress of the disc material, some stress redistribution takes place depending on the strain hardening characteristics of the material until the component eventually fails. In general, there are two main failure modes: a) hoop burst and b) rim peel, as shown in Figure 1.15. In a hoop burst mode, the crack initiates at the bore area and grows along the radial direction and the disk disintegrates in several parts, whereas in rim peel mode, the crack initiates at diaphragm area and initially grows in circumferential direction before reaching a critical size and a peripheral part is released while the main section remains intact. Both failure modes could potentially lead to hazardous consequences and must therefore be avoided.

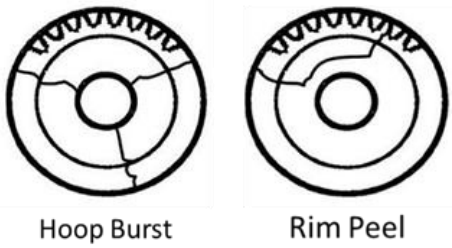

Figure 1.15 Rotor integrity failure modes.

The current industrial approaches to analyse these failure modes by means of data correlation are as following:

- Hoop burst

Hoop burst is driven by the hoop stress within the hoop carrying section of the turbine disk (cf. Figure 1.16). The corresponding criterion is based on the elastic Area-Weighted Mean Hoop Stress (AWMHS), the yield stress σ_{Y} and the ultimate tensile strength (UTS) R_{m} of the material:

$$\mathrm{AWMHS}_{\mathrm{limit}} = C_1 \cdot (C_2 + C_3 \cdot \frac{R_{\mathrm{m}}}{\sigma_{\mathrm{Y}}}) \cdot R_{\mathrm{m}} \tag{1.27}$$

where C_1, C_2 and C_3 refer to the correction factors. The burst limit is analytically calculated as in Eq. (1.27). The material property values in Eq. (1.27) are determined at the Area-Weighted Mean Temperature (AWMT) of the component at the worst overspeed condition due to the presence of the temperature gradient. The elastic AWMHS is then calculated by means of FE simulation for the hoop

carrying section of the turbine disk at growing rotational speeds until it matches the burst limit $\mathrm{AWMHS}_{\mathrm{limit}}$. The critical rotational speed for hoop burst is determined at which the elastic AWMHS equals $\mathrm{AWMHS}_{\mathrm{limit}}$.

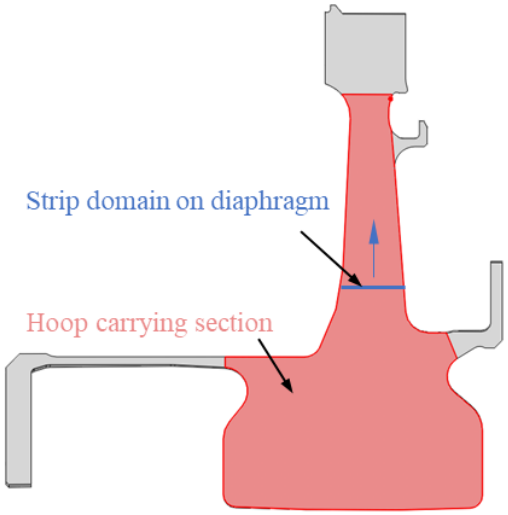

Figure 1.16 Hoop carrying section and strip domain on diaphragm of a typical turbine disk.

- Rim peel

Rim peel failure occurs in the diaphragm where the radial stresses are dominant. The radial stress is the result of centrifugal stress plus additional thermal stress induced by the temperature gradient between the hot disc rim and cooler bore. Rim peel becomes a threat to disc integrity at overspeed conditions where the radial stresses exceed the hoop stresses, usually in the diaphragm area of the disc. The current criterion for rim peel is based on the elastic Mean Radial Stress (MRS), the yield stress and the UTS of the material:

$$\mathrm{MRS}_{\mathrm{limit}} = C_1 \cdot (C_2 + C_3 \cdot \frac{R_{\mathrm{m}}}{\sigma_{\mathrm{Y}}}) \cdot R_{\mathrm{m}} \tag{1.28}$$

similar to Eq. (1.27), C_1, C_2 and C_3 are the correction factors for rim peel criterion. The rim peel limit $\mathrm{MRS}_{\mathrm{limit}}$ is analytically calculated as in Eq. (1.28). The material property values in Eq. (1.28) are determined at the Mean Section Temperature (MST) of the diaphragm area at the worst overspeed condition. The elastic MRS is calculated for each strip domain with a small thickness on diaphragm using FE simulations with growing rotational speeds as shown in Figure 1.16. Then, the elastic MRS values of all strip domains on diaphragm are compared to determine the critical position and value. Finally, the critical rotational speed for rim peel is determined when the critical elastic MRS value reaches rim peel limit.

While these elastic FE simulations and analytical methods provide a quick analysis, the influence of hardening during plastic deformation is not fully considered by the current industrial approach, resulting in conservatism which has to be compensated by some extra weight of the disk. Additionally, potential defects that can grow into cracks are not considered in such an approach or in the overspeed

spin-tests. However, the presence of defects cannot be excluded due to the limited sensitivity of non-destructive inspection in quality control [1.7, 1.8]. It is therefore important to investigate the worst-case-scenario referring to the end-of-life component with potential cracks. Where the conservatism is not acceptable for the component, direct testing of the components similar to the real ones is required. This imposes high cost and long execution time for the engine project.

2. Methodology and material

2.1. Introduction

For the failure assessment of a flawed component, the standard failure assessment procedures such as BS7910 have provided a conservative analysis approach. Besides, current improvements suggested in the literature also help optimise the assessment procedures with respect of a more precise fracture toughness value, modified assessment lines (boundary to failure) considering loading conditions and constraints and usage of less conservative reference loads. However, these approaches were either component based but made use of standard or analytically corrected material properties, or test specimen based that cannot or only partially correlate to the real component loading conditions. As a consequence, the assessment results were prone to over-conservatism and even inadequate if the real operation conditions of the component were not fully considered. Moreover, the effect of huge plastic deformation on the failure load has only been analytically considered based on material properties in the current approaches. The plastic collapse load has been defined as the flow stress (or equivalent in the assessment diagrams), which has been determined from yield strength and ultimate tensile strength of the material. While in recent years an increasing number of metallic components or structures, the most of which have been aero-space applications, failed with the failure mode plastic collapse, possible improvement has been considered for the current analytical definition of the plastic collapse load, since some of these failure loads have deviated apparently from the analytical solution.

A novel structural integrity assessment procedure for metallic components based on representative specimens has been proposed in this work with the application in case of a turbine disk used in the aero-engine. In contrast to the standard failure assessment procedures with improvements currently suggested in the literature, the assessment procedure introduced in this work makes use of specially designed specimen tests to recreate the loading conditions of the critical locations in the component with their corresponding failure mechanisms. The loading conditions recreated in the representative specimens account for the mechanical as well as thermal loadings. Based on the damage tolerance concept, the worst-case-scenario flaw for an end-of-life component has been considered at the critical locations in the component. In the representative specimens, the crack-tip loading parameter as well as the constraint parameters have been kept comparable to the component values. Based on the test results of these specimens, fracture toughness values of the specific considered crack at different critical locations in the component under different loading conditions have been acquired. Besides,

considering stable crack extension, a two-criteria failure assessment method has been proposed in this work, in which the failure mode between ductile tearing and plastic collapse could be determined with their corresponding failure load. The plastic collapse load has been formulated based on the critical ligament yielding parameter L_{r}, which have been determined by the test of the representative specimens. The failure mode and load of the component has been eventually determined using both fracture toughness values and critical ligament yielding parameter L_{r} determined from the representative specimen tests by means of the two-criteria failure assessment method.

2.2. Methodologies

The methodologies introduced or used in this work have been discussed in this section. A novel failure assessment method designated Two-criteria failure Assessment Method has been introduced, which considered stable crack extension under monotonically increasing load. In the extent of this method, the plastic collapse load has been determined with respect to the crack size. Subsequently, failure mode between ductile tearing and plastic collapse could be determined with their corresponding failure loads. Then, the constraint parameters used to characterise the 3-D crack-front constraint conditions against plastic deformation have been discussed. These constraint parameters have been utilised as one of the design criteria of the representative specimen. Lastly, as a supplemental independent burst speed assessment method for the turbine disk, the Hill's global stability criterion has been discussed. The criterion has been formulated for the bladed turbine disk with complex geometry and implemented into the FE software ABAQUS. The critical load for the investigated turbine disk in terms of rotational speed has been determined based on this criterion.

2.2.1. Two-criteria failure assessment method

A two-criteria failure assessment method has been established in this work, in order to take into consideration of the stable crack extension, failure mode of ductile tearing and failure mode of plastic collapse under increasing applied load at the same time.

In both FAD analysis and CDF analysis, the failure mode of ductile tearing is defined by the $f(L_{\mathrm{r}})$ functions, while the limit load for failure mode of plastic collapse given by $L_{\mathrm{r}}^{\max}$. However, the applied load and the crack size cannot vary at the same time in one analysis process. Both FAD analysis and CDF analysis are able to determine the failure mode and load for the component with constant crack size under increasing load or for the component under constant load with increasing crack size. In the load versus stable crack extension diagram (Figure 1.6b) based on CDF philosophy, the stable crack extension has been considered under increasing applied load. However, only the instability load for failure mode ductile tearing can be determined.

Since the limit load for failure mode plastic collapse is given by $L_{\mathrm{r}}^{\max}$, it can then be calculated based on the reference yield stress σ_0 (Eq. (2.1)) of the critical location along the crack-front for a given crack size on the component. The reference yield stress σ_0 has been chosen to replace the yield stress σ_{Y} in calculation of the ligament yielding parameter $\mathrm{L_r}$ (Eq. (1.19)), with σ_{app} denoting the applied stress. Both were calculated for the uncracked body at the crack coordinates.

$$L_r = \frac{\sigma_{ref}}{\sigma_Y} = \frac{\sigma_{app}}{\sigma_0} \tag{2.1}$$

Analytical solutions of the reference yield stress for uniaxial and biaxial tension loading in a plate are given in [1.21]. However, because of the complexity of the component and the consideration of the constraint effect, the FE simulations have been chosen to determine the reference yield stresses. It is defined as the stress at which the condition

$$f(L_r = 1) = \sqrt{\frac{J_e}{J}} \tag{2.2}$$

is satisfied. The function $f(L_r)$ is based on Eq. (1.16) with $L_r = 1$, $\sigma_{ref} = \sigma_Y$, see Eq. (2.1), and ε_{ref} taking the corresponding value on the stress-strain curve of the material, whereas the crack driving forces J and J_e are obtained by FE simulations, assuming elastic-plastic and elastic material behaviour, respectively.

The reference yield stress σ_0 of the critical location along the crack-front decreases for increasing crack size on the component. Consequently, the limit load for failure mode plastic collapse also decreases with growing crack size on the component. As a result, A diagram has been developed illustrating the limit load for plastic collapse as a curve with respect to difference crack sizes (Figure 2.1). This has been an extension of the CDF diagram in Figure 1.6b. Plotted together with the load versus stable crack extension curve in the same diagram (Figure 2.1), the failure assessment of the component is performed following the path of the load versus stable crack extension curve starting from a_0. If the limit load for failure mode plastic collapse curve has not crossed the load versus stable crack extension curve before its highest point, the critical load for the component is the instability load in form of ductile tearing (Figure 2.1a). On the other hand, if the limit load for failure mode plastic collapse curve crosses the load versus stable crack extension curve before its highest point, which means plastic collapse occurs first before the crack reaches instability. The critical load for the component is then determined as the limit load for plastic collapse at this crossing-point (Figure 2.1b).

The other advantage of the established two-criteria failure assessment method is that the critical crack size a_c can be determined for both failure mechanisms.

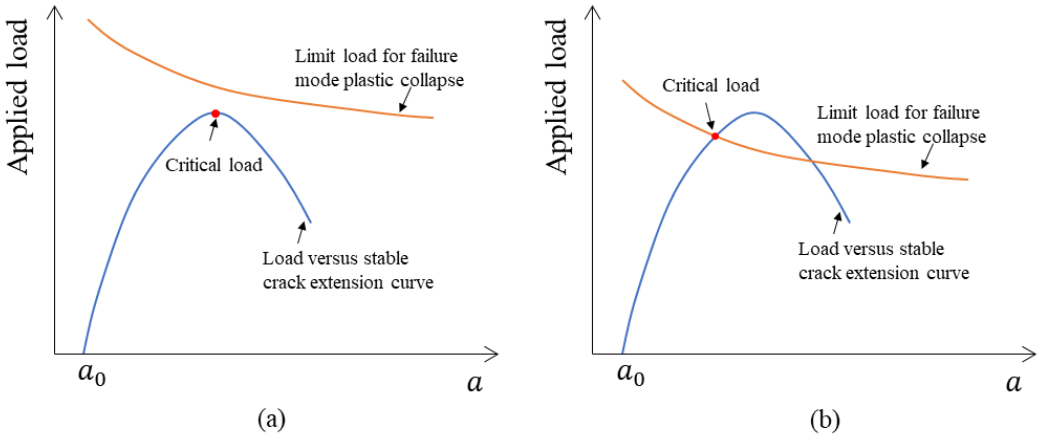

Figure 2.1 Two-criteria failure assessment method to take into consideration of the stable crack extension, failure mode of ductile tearing and failure mode of plastic collapse under increasing applied load: (a) Failure of component in form of ductile tearing; (b) Failure of component in form of plastic collapse.

2.2.2. Determination of constraint parameters

It is well known that the fracture resistance is not a pure material parameter but may also depend on the size and geometry of the component, on the loading type (tension/bending) and load magnitude, on the crack size and the location of the crack with respect to external boundaries and internal interfaces [1.4]. This phenomenon is known as the constraint effect. As discussed in the previous chapter, there are analytical solutions in the current component assessment procedures [1.9, 1.11] to modify the fracture toughness of the material for the assessed flaw based on the constraint parameters, namely T-stress and Q parameter. But there are important limitations for these parameters. Firstly, the T-stress is derived as the second term of the series expansion of the linear elastic K field solution (cf. Eq. (1.4)). Due to its nature, the T-stress cannot accurately describe the constraint effect with large ligament-yielding in elastic-plastic fracture mechanics. More importantly, both parameters are only able to characterise the level of in-plane constraint, but they do not give any indication about the out-of-plane state of stress [1.5].

The component assessment concept developed in the present work requires an accurate characterisation of the real three-dimensional crack-front loading situation for the design of the representative specimen. Consequently, the following two constraint parameters are considered.

Stress triaxiality factor h

The stress triaxiality factor h represents a physically significant definition of the triaxiality of the stress state resulting from crack-tip constraint [1.5]. Detailed information was presented by Brocks and Schmitt [2.1, 2.2] and Yuan and Brocks [2.3]. Essentially, it is defined as the ratio of the hydrostatic stress σ_{h} over the von Mises equivalent stress σ_{vM}. Both stress values can be easily obtained from FE analysis, which has been chosen for the component assessment.

$$h = \frac{\sigma_{\mathrm{h}}}{\sigma_{\mathrm{vM}}} \tag{2.3}$$

For strain hardening materials, h increases approaching the crack-tip, reaching a maximum value at some distance from this, followed by a rather linear decrease. Examples are given in Figure 2.2 for two steel materials, namely the German standard steel St E460 and the American A710.

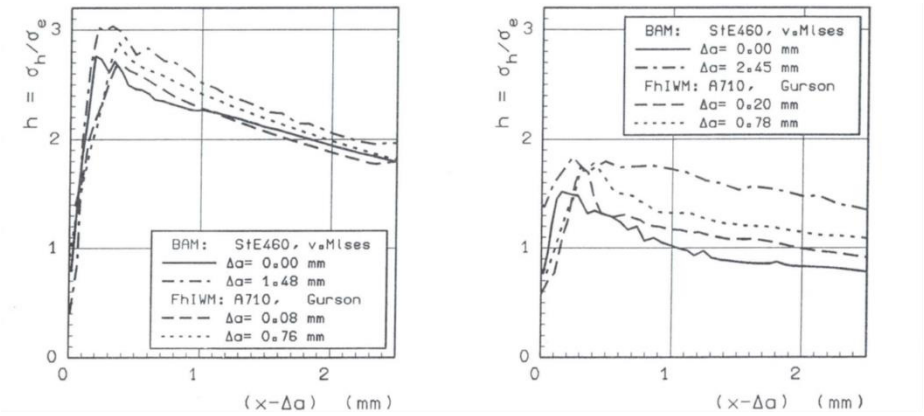

Figure 2.2 Local stress triaxiality factor h ahead of the crack-tip (σ_e: von Mises equivalent stress) [2.1].

The gradient in h requires a separate definition of the value for the analysis. Potential options are either to use the maximum value or the value extrapolated to the crack-tip. As suggested by Brocks and Schmitt [2.1], the latter is determined as linear extrapolation of the values lying within a certain distance from the crack-tip (typically 2 to 4 times $r \cdot \sigma_Y/J$), which has been shown in Figure 2.3 for the steel materials.

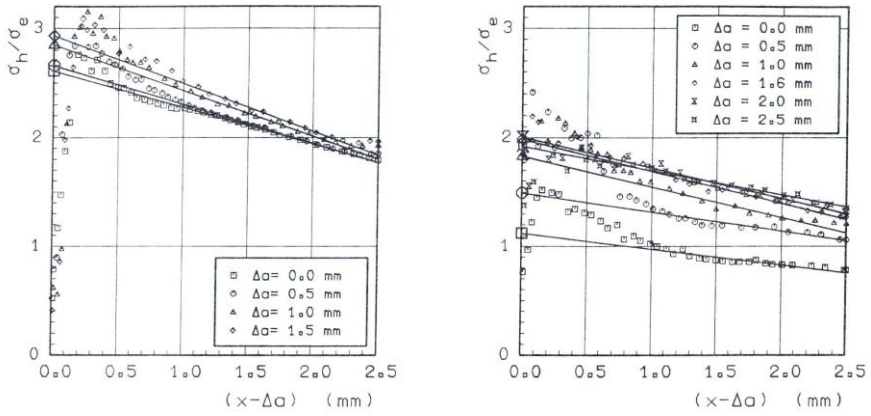

Figure 2.3 Linear extrapolation of local triaxiality h to the crack-tip (σ_e: von Mises equivalent stress) [2.1].

The latter option was also suitable to avoid the dependence of the triaxiality estimations on the finite element mesh, since the maximum value of h is affected by the detail of the mesh at the crack-tip. Therefore, this option provided a reliable and reproducible measure of the triaxiality and has been chosen in the present work.

Local constraint parameter α_l

A second constraint parameter introduced in this work is the local constraint parameter α_l (l stands for local). It is a modification of the global constraint parameter α_g proposed by Newman et al. [2.4], which has been widely used in the FE-based assessment of the fatigue-crack growth in metallic materials. The global constraint parameter is defined as:

$$\alpha_g = \frac{1}{A_T} \sum_{m=1}^{M} \left(\frac{\sigma_{yy}}{\sigma_Y}\right)_m A_m \tag{2.4}$$

with

$$A_T = \sum_{m=1}^{M} A_m \tag{2.5}$$

being A_m the projected area on the uncracked ligament of a yielded element m, $\frac{\sigma_{yy}}{\sigma_Y}$ the normalised crack opening stress for element m and A_T the total projected area for all yielded elements M. The global constraint parameter was an appropriate value to characterise the constraint as a structural feature that inhibits plastic flow and causes a higher triaxiality of stresses.

In order to characterise the local constraint effect in the ligament, a local constraint parameter α_l has been introduced in the present work. Note that there has been similar constraint parameter proposed for local constraint effect description, e.g., the hyper-local constraint factor suggested by Leach et al. [2.5]. However, due to its nature of one-dimensional characterisation, it is considered insufficient to transfer the crack-tip loading scenario with accurate geometry similarity between the real component and the specimen. Consequently, the local constraint parameter α_l is defined as:

$$\alpha_l = \left(\frac{1}{\sum_{n=1}^{N} A_n}\right) \sum_{n=1}^{N} \left(\frac{\sigma_{yy}}{\sigma_Y}\right)_n A_n \tag{2.6}$$

where for each node in the FE mesh in the uncracked ligament, a normalised crack opening stress is area-weighted for all the neighbouring elements N with stress values acquired at the element centroid. A_n stands for the projected areas of the neighbouring elements for the considered node. An illustration of an α_l calculation is shown in Figure 2.4.

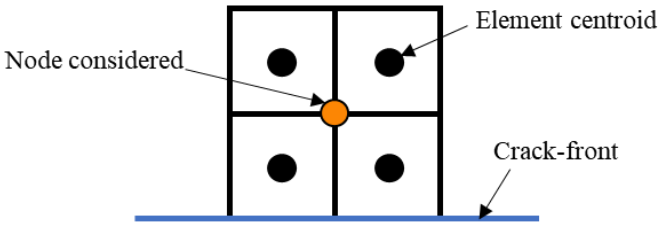

Figure 2.4 Calculation of the local constraint parameter α_l for the considered node in the FE mesh on the plane of the uncracked ligament.

The evaluation results of α_1 have shown similar tendencies with respect to the factor h ahead of the crack-front (cf. Figure 2.2). Consequently, the same extrapolation method has been used to determine the α_1 values for each position along the crack-front of the surface crack.

2.2.3. Global stability criterion

The Hill's global stability criterion [2.6, 2.7, 2.8, 2.9] has been chosen as a second independent criterion to justify the global unstable collapse of the component. In particular, the Hill's global stability criterion has been formulated by Mazière et al in [2.10] for the case of rotating disks. The essential parameter is the Modified Second Order Work (MSOW) as a measure of the mechanical work associated with a perturbation of the initial state. This approach has been validated by experiments conducted with rotating disks made of Udimet 720 in [2.11]. In the present work, a modified formulation of the global stability criterion in [2.10] has been implemented into the FE software ABAQUS [2.12] by means of a User-Material subroutine (UMAT). In contrast to [2.10], the parameter MSOW has been calculated including the traction forces induced by the turbine blades as a function of the load (rotational speed) of the turbine disk.

Hill's global stability criterion is derived from the principle of virtual power [2.6]. Referring to Figure 2.5, it is written as

$$\int_{\Omega_0} \boldsymbol{S}: \dot{\boldsymbol{F}}^* \, dv_0 = \int_{\Omega_0} \rho_0 \boldsymbol{f_i} \cdot \boldsymbol{V}^* \, dv_0 + \int_{\partial\Omega_0^2} \boldsymbol{T_i} \cdot \boldsymbol{V}^* \, ds_0 \tag{2.7}$$

$\forall \boldsymbol{V}^*$such that $\boldsymbol{V}^* = 0$ on $\partial\Omega_0^1$ with $\dot{\boldsymbol{F}}^* = \frac{\partial \boldsymbol{V}^*}{\partial \boldsymbol{X}}$, where a solid Ω (initially Ω_0) is submitted to kinematic constraints on the portion $\partial\Omega^1$ (initially $\partial\Omega_0^1$) of its boundary, to surface traction loads $\boldsymbol{T_i}$ (expressed as $\boldsymbol{T_{i0}}$ on $\partial\Omega_0^2$) on the portion $\partial\Omega^2$ (initially $\partial\Omega_0^2$), and body force $\boldsymbol{f_i}$ (expressed as $\boldsymbol{f_{i0}}$ on Ω_0) as shown in Figure 2.5 [2.10]. $\boldsymbol{S}$ denotes the first Piola-Kirchhoff stress tensor and $\boldsymbol{F}$ is the deformation gradient.

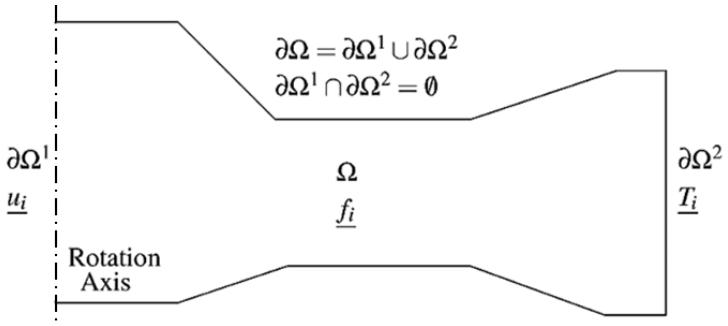

Figure 2.5 General definition of the mechanical problem for a rotating disk (modified from [2.10]).

The equilibrium in Eq. (2.7) is said to be stable if any infinitesimal perturbation in the direction of the admissible velocity $\boldsymbol{V}$ requires an additional work from external forces. Following [2.10], this condition can be written in case of a rotating disk as

$$MSOW = \int_{\Omega_0} \left(\dot{\boldsymbol{S}} : \dot{\boldsymbol{F}} - \rho_0 \|\boldsymbol{V} \times \boldsymbol{\omega}\|^2 \right) dv_0 > 0 \tag{2.8}$$

for $\forall \boldsymbol{V}$ kinematically admissible. In accordance with [2.10], the global stability of the disk is lost when the MSOW becomes negative for the velocity field $\boldsymbol{V}_{\mathrm{FEM}}$ resulting from the FE simulation. The first term in Eq. (2.8) denotes the Second Order Work (SOW), which can be understood as the power of the internal forces of the rotating disk, whereas the second term in Eq. (2.8) refers to the power of the centrifugal forces. It should be noticed that the centrifugal forces at any material points of a rotating disk depend not only on the angular velocity ω, but also on the current radius r of the material point. Since this radius increases with the speed due to the radial deformation of the disk even if the angular velocity remains constant, the so-called spin-softening effect takes place. The second term in Eq. (2.8) will therefore be non-zero and promotes instability [2.10].

In contrast to [2.10], the blades have been also included in the present method. The material of the blades is relatively stiff as compared with the disk and the blades can thus be regarded as being rigid. To take into account the surface tractions exerted by the blades, the MSOW has been reformulated as

$$MSOW = \int_{\Omega_{\mathrm{d0}}} \left(\dot{\boldsymbol{S}} : \dot{\boldsymbol{F}} - \rho_0 \|\boldsymbol{V} \times \boldsymbol{\omega}\|^2 \right) dv_0 - n_{\mathrm{blade}} \cdot m_{\mathrm{blade}} \cdot \|\boldsymbol{V}_{\mathrm{CoG}} \times \boldsymbol{\omega}\|^2 \tag{2.9}$$

where Ω_{d0} represents the initial turbine disk domain, n_{blade} denotes the number of the turbine blades on the disk, m_{blade} the mass of each turbine blade and $\boldsymbol{V}_{\mathrm{CoG}}$ the velocity field at the centre of gravity of each turbine blade. The formulation of the Hill's global stability criterion for turbine disk with blades (Eq. (2.9)) has been implemented in the FE software ABAQUS. It should be noticed that because the method is based on the global stability criterion, the FE simulations as well as post-processing on the investigated turbine disk geometry with an inserted crack can easily be conducted with no need for extra modification. The velocity fields $\boldsymbol{V}$ and $\boldsymbol{V}_{\mathrm{CoG}}$ here correspond to the rate of displacement for each integration point and for the centre of gravity of the blade. Consequently, when a velocity field and its corresponding angular velocity can be found that make the MSOW in Eq. (2.9) negative, it means that the work of the centrifugal forces becomes greater than the internal work and the stability of the rotating disk is lost. This angular velocity is considered to be the critical rotational speed of the turbine disk.

The user-subroutine UMAT has been utilised to implement the Hill's global stability criterion for the investigated turbine disk (Eq. (2.9)). The UMAT is based on the UMAT subroutine for isotropic hardening plasticity presented in [2.13], which adequately describes the plasticity behaviour of the turbine disk material Udimet 720Li. The work has been published by the author et al. in [2.14]. Note that there is a temperature gradient on the turbine disk during operating condition. The material properties vary because of this temperature gradient and therefore the following temperature-dependent material properties are included in the UMAT: thermal expansion, Young-modulus, Poisson's ratio, yield stress and the corresponding plastic strain. The layout of the assessment procedure, including the UMAT, is shown in Figure 2.6.

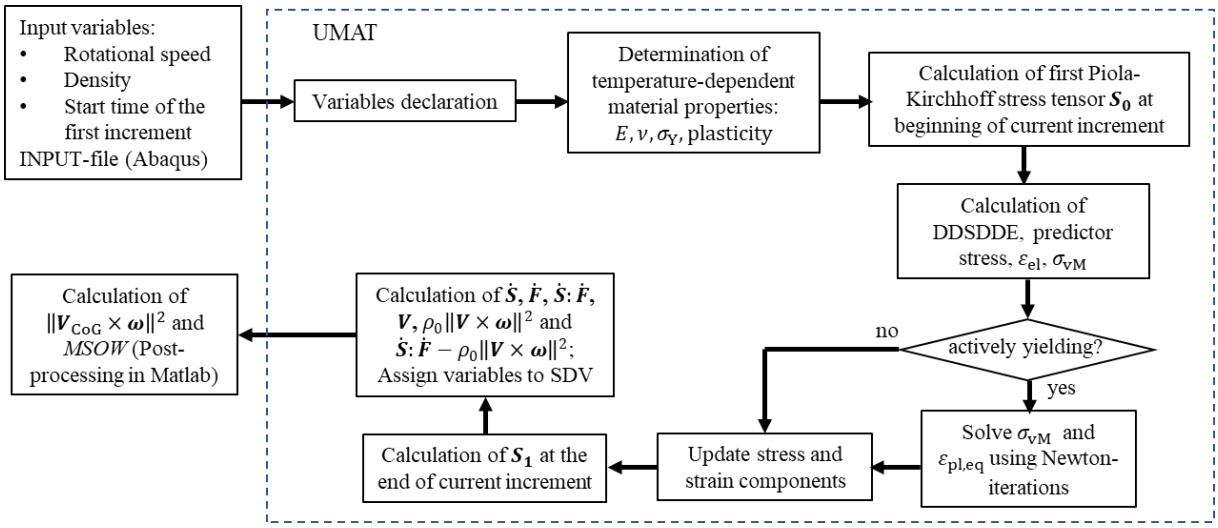

Figure 2.6 Layout of the assessment procedure in ABAQUS (post-processing in Matlab) based on Hill's global stability criterion including the UMAT for the investigated turbine disk model [2.14].

The rate of first Piola-Kirchhoff stress tensor $\dot{\boldsymbol{S}}$ can be calculated as:

$$\dot{\boldsymbol{S}} = \frac{\boldsymbol{S_1} - \boldsymbol{S_0}}{\Delta t} \tag{2.10}$$

where $\boldsymbol{S_1}$ and $\boldsymbol{S_0}$ denote the first Piola-Kirchhoff stress tensors at the end and the beginning of the current time increment Δt, respectively, which have been determined using Eq. (2.11), in which $\boldsymbol{F}$ denotes the deformation gradient and σ the Cauchy stress tensor.

$$\boldsymbol{S} = \det \boldsymbol{F} \cdot \boldsymbol{\sigma} \cdot \boldsymbol{F^{-T}} \tag{2.11}$$

The rate of deformation gradient $\dot{\boldsymbol{F}}$ has been calculated in a similar manner as $\dot{\boldsymbol{S}}$:

$$\dot{\boldsymbol{F}} = \frac{\boldsymbol{F_1} - \boldsymbol{F_0}}{\Delta t} \tag{2.12}$$

As stated in [2.10], the search for instability is not performed for all kinematically admissible velocity fields, but only for the finite element solution at the current time increment. As soon as the parameter MSOW becomes negative, the system (turbine disk and blades) is considered unstable. The velocity field $\boldsymbol{V}$ can be calculated as the displacement rate for all nodes of the turbine disk at current time increment:

$$\boldsymbol{V} = \frac{\boldsymbol{U_1} - \boldsymbol{U_0}}{\Delta t} \tag{2.13}$$

where $\boldsymbol{U}$ denotes the coordinates vector of each node in the global coordinate system. The velocity field for the centre of gravity of each turbine blade $\boldsymbol{V}_{\mathrm{CoG}}$ has been also calculated in a similar manner as $\boldsymbol{V}$ (Eq. (2.14)):

$$\boldsymbol{V}_{\mathrm{CoG}} = \frac{\boldsymbol{XC_1} - \boldsymbol{XC_0}}{\Delta t} \tag{2.14}$$

where $\boldsymbol{XC}$ denotes the centre of gravity coordinates for the turbine blade in the global coordinate system, which is a direct output variable in History Output. The angular velocity ω at the end of current time increment has also been calculated using ramp function. The magnitude of the cross product $\|\boldsymbol{V} \times \boldsymbol{\omega}\|$ has been calculated. The assumption is made here that the deformation of the turbine disk is symmetric with respect to its rotation axis so that the angular velocity vector ω is always in the direction of the rotation axis.

The term $\dot{\boldsymbol{S}}: \dot{\boldsymbol{F}} - \rho_0 \|\boldsymbol{V} \times \boldsymbol{\omega}\|^2$ in Eq. (2.9) has been calculated for each integration point in the turbine disk model as the final output of the UMAT, which is then stored in the vector SDV of the internal variables for post-processing. Then, the volume integration of this term according to Eq. (2.9) has been accomplished in post-processing, where the integration point volume v_0 is directly acquired for each integration point from the ODB-file. It should be noticed that C3D4 elements (first order tetrahedral element) have only one integration point, whereas the C3D20R elements (second order hexahedral element with reduced integration) have 8 integration points, which has been considered in the post-processing. The MSOW contribution $n_{\text{blade}} \cdot m_{\text{blade}} \cdot \|\boldsymbol{V}_{\text{CoG}} \times \boldsymbol{\omega}\|^2$ from the blades has also been calculated in post-processing. Eventually, all the contributions have been summed up according to Eq. (2.9) to calculate the parameter MSOW.

2.3. Material properties

The material used in this study for the investigated turbine disk is the Ni base superalloy Udimet 720Li ("Li" stands for "low interstitial"). The chemical composition of the alloy is related to that of Udimet 720 from which it is derived, but differs from it, see Table 2.1 [2.15] [2.16].

Table 2.1 Chemical composition of the superalloy Udimet 720 and Udimet 720Li [2.15] [2.16]

	B	C	Co	Cr	Mo	Si	Ti	W	N	Al	Zr	Ni
Udimet 720*	2.50	0.035	0.025	14.75	18.00	3.00	0.1	5.00	1.25	-	-	Bal.
Udimet 720Li*	2.51	0.014	0.011	14.66	16.14	2.98	0.05	5.08	1.23	-	-	Bal.
Udimet 720Li**	0.015	0.015	14.75	16.00	3.00	-	5.00	1.25	-	2.50	0.035	Bal.

* Material data from [2.15]
** Material data from [2.16] (the material specification for the component used in the present work)

Lower carbon and boron contents facilitate the use of secondary melting techniques for ingot conversion prior to forging, so that the need for powder processing is avoided. Udimet 720Li is applied in the hot section of aero-engines as turbine disks materials commonly between 650 °C and 750 °C for long-term and 900 °C for short term [2.17, 2.18]. Note that the material properties of the turbine disk investigated in the present study [2.16] slightly deviate from literature data from [2.15] due to chemical composition.

According to the material specification sheet provided by the engine manufacturer [2.16], the heat treatment of the investigated turbine disk material consists firstly a solution treatment at a temperature between 1080 °C and 1110 °C for 4 hours, after which the material is oil-quenched to ambient temperature. Higher solution temperatures lead to improved creep properties at the expense of reduced tensile and fatigue strength [2.19]. It is claimed an increase in cooling rate of the oil

quenching improves the tensile strength, while on the other hand the possibility of quench cracking and the development of excessive residual stresses limit the severity of the cooling rate that can be applied [2.15]. Finally, a precipitation treatment is carried out at 760 °C for 16 hours prior to air cooling.

The characteristic temperature dependency of the mechanical properties of Udimet 720Li is provided in Figure 2.7 based on the test data from [2.15] and [2.18]. Note that the ageing temperature and time of the tested material were not identical from both literature references, which may lead to slight differences in material properties. But the general tendencies of the tensile properties are comparable. It has been observed that for the temperatures between room temperature and approximately 500 °C the yield strength decreased with rising temperature for all solution temperatures and a lower solution temperature could improve the yield strength property.

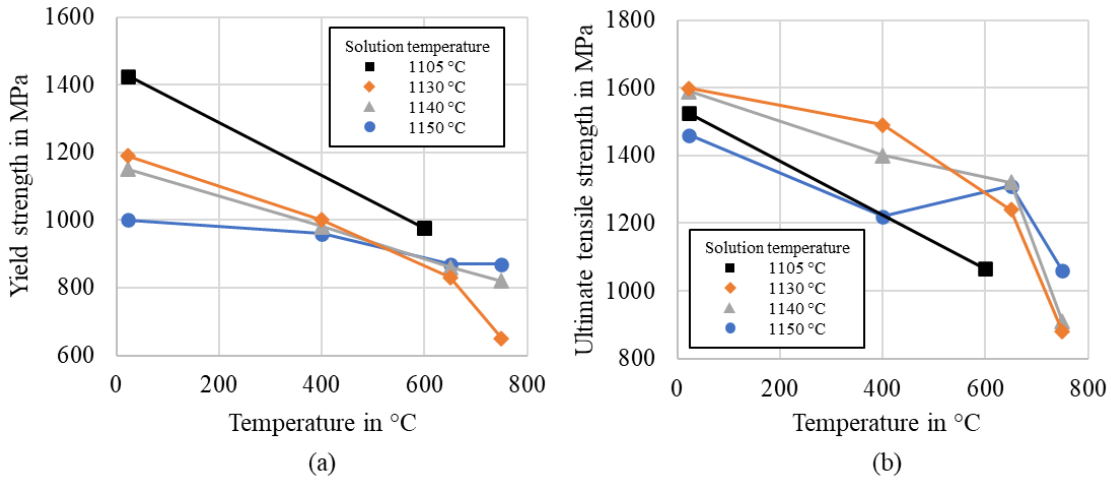

Figure 2.7 Temperature-dependent material properties of Udimet 720Li at different heat treatment conditions: (a) yield strength (0.2% offset); (b) ultimate tensile strength [2.15] [2.18].

3. Numerical simulation

3.1. Introduction

In this chapter, the numerical simulations of the turbine disk investigated as well as the constraint-designed specimen have been discussed. Firstly, the material models used in the FE simulations have been introduced. For the numerical simulations, the commercial finite element software ABAQUS has been chosen due to its capability in performing non-linear analyses of large strain events. The finite element analyses have been carried out for solid turbine disk, cracked turbine disk as well as constraint-designed fracture mechanics specimens.

3.2. Material models

For the material model used to describe the elastic-plastic response of the turbine disk investigated, the following Ramberg-Osgood relationship has been chosen:

$$\varepsilon_{\text{total}} = \varepsilon_{\text{el}} + \varepsilon_{\text{pl}} = \frac{\sigma}{E} + \left(\frac{\sigma}{K}\right)^{\frac{1}{N}} \tag{3.1}$$

where the parameters Young's modulus E, hardening coefficient K and hardening exponent N are provided by the engine manufacturer. The monotonic stress-strain curves of the material are shown in Figure 3.1 for 350 °C and 425 °C with stresses normalised by the yield stresses of the material at each temperature, with $K = 1430.92\,\text{MPa}$, $N = 0.04326$ for 350 °C and $K = 1427.36\,\text{MPa}$, $N = 0.04307$ for 425 °C. The difference in material properties at these temperatures in terms of elastic-plastic behaviour is small so that the two curves apparently coincide.

Firstly, these temperature-dependent material properties in terms of Ramberg-Osgood formulation, have been provided in ABAQUS through the function *deformation plasticity*, where the stress is defined by the total strain without history dependence. This model has been considered valid since there is no unloading process in the simulation to allow the recovery of the initial elastic strain. This has been verified by running the same simulation using the function *elastic* and *classic metal plasticity* for the corresponding material properties. Besides, the thermal expansion has also been included in the material models. As discussed in section 2.2.3, the elastic-plastic behaviour of the turbine disk material has also been modelled using UMAT. The tabular temperature-dependent values of plastic strains and corresponding yield stresses according to the Ramberg-Osgood formulation have been provided in

ABAQUS through functions *dependent variable* and *user material constant* and has also been verified against the models mentioned above.

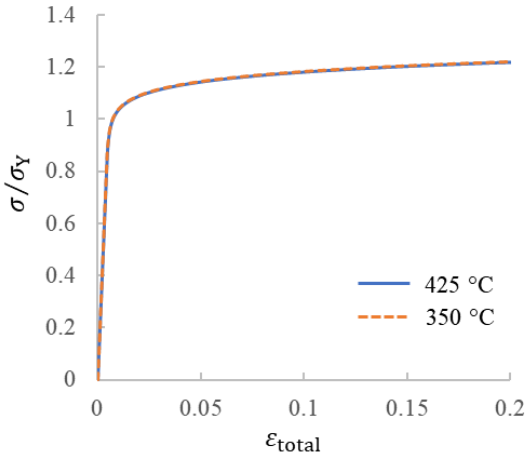

Figure 3.1 Elastic-plastic behaviour of the Udimet 720Li in Ramberg-Osgood formulation at different temperatures.

The material for the turbine blades paired with the turbine disk investigated is the Ni base single crystal superalloy CMSX-4. Since the modelling of the turbine blade has the sole purpose of considering the extra centrifugal loads to the turbine disk brought by the weight of the blade and the elastic-plastic behaviour of the turbine blade is therefore not the focus of the present work. Consequently, only elastic and orthotropic thermal expansion properties have been modelled.

3.3. FE simulations for the turbine disk

The geometry of the turbine disk has been provided by the engine manufacturer and is shown in Figure 3.2 for a single section along with the turbine blade. Using the worst-case-scenario engine flight-cycle data provided by the engine manufacturer, the finite element analyses have been firstly conducted to calculate the reference overspeed according to the analytical method from the engine manufacturer. Then, critical locations on the turbine disk have been identified by conducting simulations based on the reference overspeed with elastic-plastic material model. Semi-circular surface cracks have been integrated into the turbine disk model at these critical locations and further simulations have been carried out to calculate the crack driving force in terms of J-integral and constraint parameters.

3.3.1. Reference overspeed calculation

The reference overspeed has been calculated for hoop burst and rim peel failure modes based on the analytical solutions (cf. Eq. (1.27), Eq. (1.28)) provided by the engine manufacturer. The mechanical and thermal stresses haven been determined by FE simulations, which will be discussed in the following sections.

Hoop burst

To calculate the $\mathrm{AWMHS}_{\mathrm{limit}}$ in Eq. (1.27), the AWMT has been determined in order to obtain the material properties. The temperature gradient of the turbine disk in form of an ABAQUS ODB-file was

provided by the engine manufacturer for the whole flight cycle. The worst-case-scenario has been considered in which the highest temperature in bore area (350 °C) takes place in the flight cycle. Note that due to the thermal lag in the secondary air system, the rotational speed is not at its peak value in the flight cycle at this moment.

The temperature profile considered for hoop burst is shown in Figure 3.3 for hoop carrying section. The AWMT has been calculated as

$$AWMT = \left(\frac{1}{\sum_{n=1}^{N} A_n}\right) \sum_{n=1}^{N} T_n A_n \tag{3.2}$$

being N the number of elements in the hoop carrying section, T_n the temperature at the centroid of the element and A_n the area of the element on the symmetric surface. Note that in this two-dimensional consideration only the elements on the symmetric surface are considered. The AWMT for the hoop carrying section has been determined as 432 °C. The material properties in Eq. (1.27) have therefore been acquired for $T = 432\,°\mathrm{C}$. As a result, the $\mathrm{AWMHS}_{\mathrm{limit}}$ has been determined as 1223 MPa.

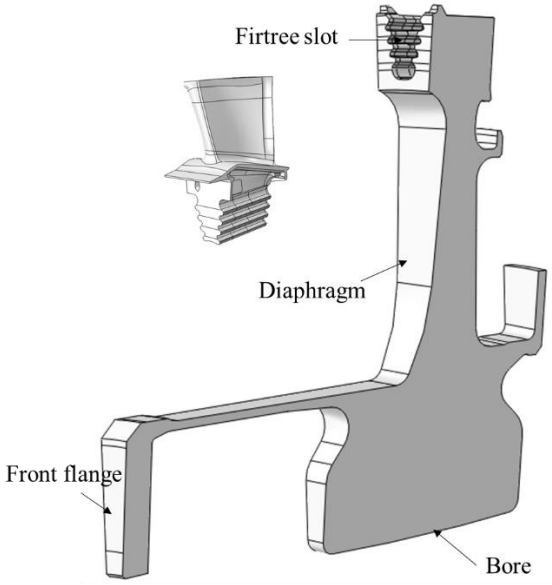

Figure 3.2 Geometry of the investigated turbine disk and blade.

In the next step, FE simulations of the turbine disk have been conducted with elastic material properties to determine the AWMHS. The symmetry of the disk even under cyclic loading conditions allowed the limitation of the mesh to a single section of the disk with one turbine blade in the firtree slot (Figure 3.4a). The contact between the blade and the firtree slot in the disk has been modelled by the “Node to Surface” contact type to avoid numerical singularity. ABAQUS C3D4 elements have been used to mesh both parts. These have been chosen due to the need to adapt the mesh to the precise shape of details such as pressure flanks in the firtree. They also allowed for a reduction of the number of degrees of freedom and therefore of the simulation time. Because of applying the contact type

"Node to Surface", only linear elements could be used. The most critical temperature profile for bore area has been used for both components. A local mesh refinement has been done for the bore area due to high stress gradient (cf. Figure 3.4b). Additionally, the interaction between the disk and other engine components e.g., retaining ring, seal, etc. has been modelled as pressure load onto the corresponding surfaces of the disk. Further boundary conditions included a displacement constraint in axial direction for the front flange surface and a displacement constraint in circumferential direction for a single node of the front flange.

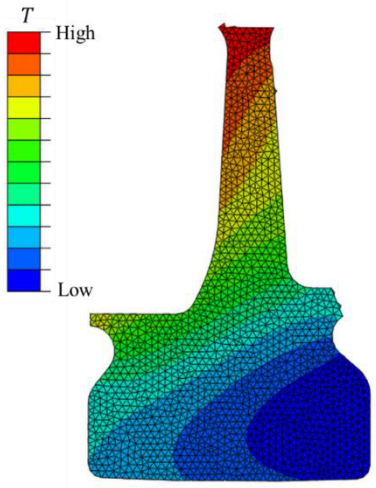

Figure 3.3 Temperature profile in hoop carrying section at worst-case-scenario.

The model has been run for various rotational speeds in terms of rotational body force in the load application in the model. For each rotational speed, the AWMHS has been calculated for the hoop carrying section (Figure 3.4b) as

$$AWMHS = \left(\frac{1}{\sum_{n=1}^{N} A_n}\right) \sum_{n=1}^{N} {\sigma_{\mathrm{hoop,el}}}_n A_n \tag{3.3}$$

similar to AWMT, where ${\sigma_{\mathrm{hoop,el}}}_n$ stands for elastic hoop stress at the centroid of each element. Finally, the reference critical rotational speed for hoop burst N_{hb} has been determined at condition $\mathrm{AWMHS} = \mathrm{AWMHS}_{\mathrm{limit}}$.

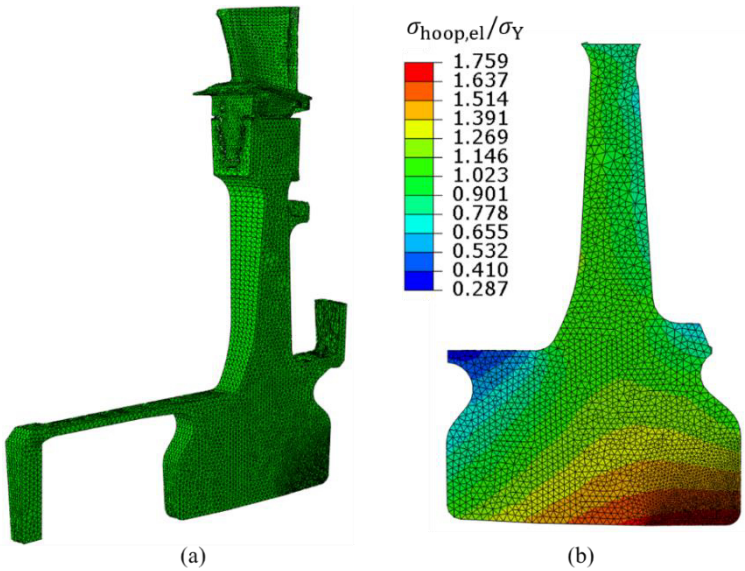

Figure 3.4 FE model of the turbine disk: (a) Meshing strategy for the turbine disk and the turbine blade investigated to determine the AWMHS; (b) Elastic hoop stress distribution of the hoop carrying section.

Rim peel

The determination of the reference critical rotational speed for rim peel has been conducted in a similar manner as for hoop burst. Firstly, the most critical temperature profile during the flight cycle for diaphragm has been used, by which the highest temperature for diaphragm is 425 °C. The MST for the diaphragm area has been determined in a similar manner as for AWMT with a result of $\mathrm{MST} = 422\ °\mathrm{C}$. This value has been used to obtain the material properties to calculate $\mathrm{MRS}_{\mathrm{limit}}$ (cf. Eq. (1.28)), which stands at $\mathrm{MRS}_{\mathrm{limit}} = 1221\ \mathrm{MPa}$.

The FE model used for hoop burst has been modified to determine the elastic MRS. The modification included refined mesh at diaphragm area (cf. Figure 3.5) due to high stress gradient and using the temperature profile discussed above. The model has been run for several increasing rotational speeds, by which the MRS has been calculated for strip domains of 2 mm height across diaphragm (cf. Figure 1.16) to obtain the maximum value for each rotational speed. The MRS for each strip domain has been calculated in a similar area-weighted manner as in Eq. (3.3). Finally, the reference critical rotational speed for rim peel N_{rp} has been determined at condition $\mathrm{MRS} = \mathrm{MRS}_{\mathrm{limit}}$ with $N_{\mathrm{rp}} = 0.88 N_{\mathrm{hb}}$. As a result, both reference rotational speeds ($N_{\mathrm{rp}}$and N_{hb}) have been compared against each other to obtain the minimum value, which has been determined as the reference overspeed N_{a} with $N_{\mathrm{a}} = N_{\mathrm{rp}}$ and $N_{\mathrm{hb}} = 114\% N_{\mathrm{a}}$. This value N_{a} will be used as a datum unit for reporting critical speeds obtained throughout this work, without disclosing actual component capabilities. Also, the yield stress σ_{Y} at a temperature of 425 °C (the corresponding material property at 350 °C only differs 0.09%) will be used as a reference unit for stress values on the component.

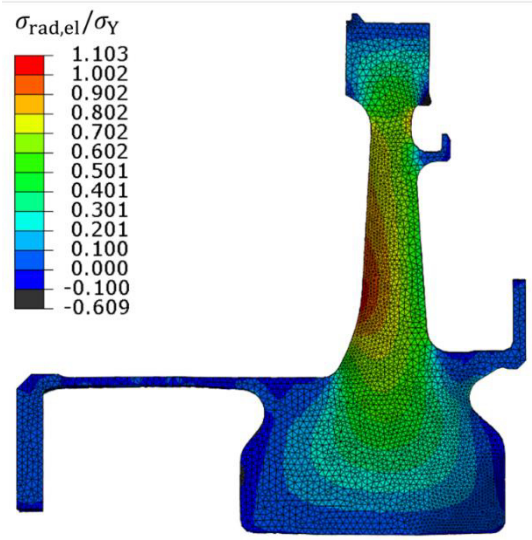

Figure 3.5 Elastic radial stress distribution on the turbine disk with refined mesh at diaphragm area.

3.3.2. Determination of critical locations on the turbine disk

To determine the critical locations on the turbine disk, the solid disk model described above (along with the blade) has been simulated for the rotational speed N_a with elastic-plastic material properties discussed in section 3.2. The rotational body force corresponding to the reference rotational speed N_a has been set as linear ramp after the introduction of temperature profile. Based on the experience from previous simulations, the mesh has been refined for diaphragm and bore area, as shown in Figure 3.6a. The von Mises equivalent stress distribution is shown in Figure 3.6b. As expected, there are two local stress peaks: the first one at the diaphragm (location 1 Figure 3.6b) under biaxial loading conditions (radial and hoop stress) corresponds to the rim peel failure mode. The second stress peak under uniaxial loading condition (hoop stress) is located at the bore (location 2 Figure 3.6b). It corresponds to the hoop-burst failure mode.

The principal stress distributions on the turbine disk are illustrated in Figure 3.7, with the highest radial stress located at the front side of the diaphragm (Figure 3.7a) and the highest hoop stress located at the rear side of the bore (Figure 3.7b). Compared with the corresponding elastic stress distributions (Figure 3.5 and Figure 3.4b), clear differences of the peak values and stress profile particularly in hoop stress distribution (although the rotational speeds in both simulations haven been slightly different) can be observed due to strain hardening of the material.

As a result, the two locations in Figure 3.6b have been determined as critical locations on the turbine disk and this has been confirmed by the past experience of the engine manufacturer.

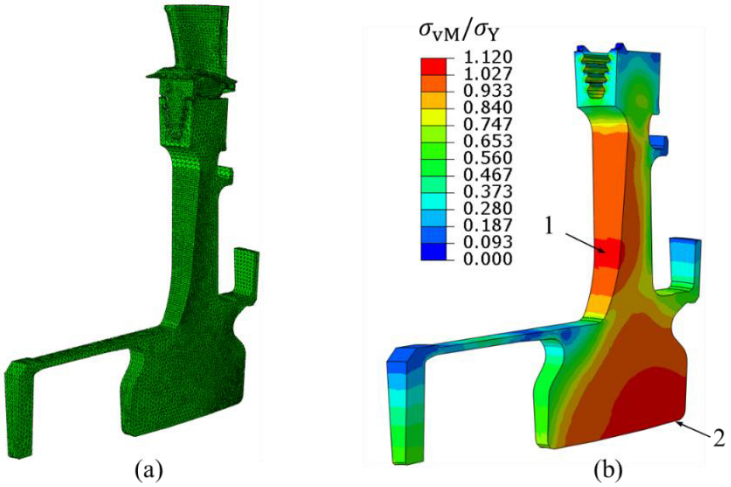

Figure 3.6 FE model of the turbine disk: (a) Meshing strategy for the turbine disk and the turbine blade investigated to identify the critical locations; (b) Von Mises stress distribution under mechanical and thermal stress at reference overspeed condition N_a (with elastic-plastic material properties). The two local high-stressed locations are marked with 1 (diaphragm) corresponding to rim-peeling failure mode and 2 (bore) corresponding to hoop-burst failure mode.

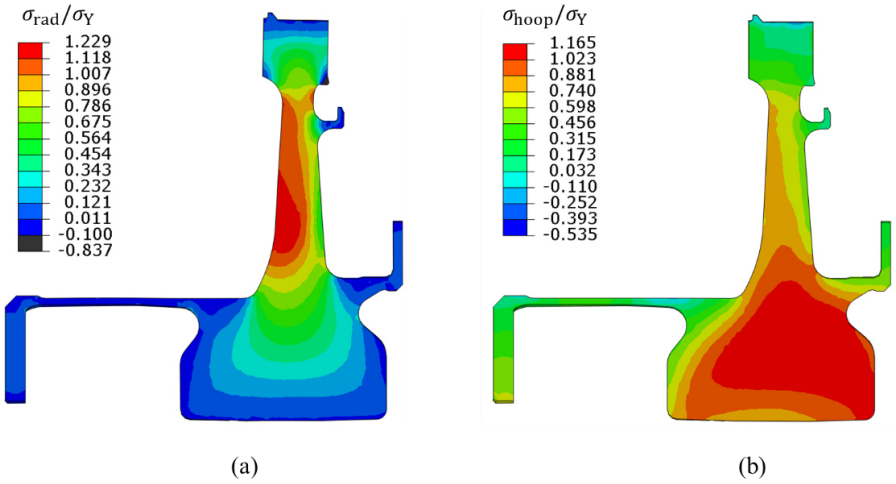

Figure 3.7 Principal stress distributions on the turbine disk under reference overspeed condition N_a (simulations with elastic-plastic material properties): (a) Radial stress distribution; (b) Hoop stress distribution.

3.3.3. Determination of fracture mechanics parameters for cracked turbine disk – crack at diaphragm

After the critical locations on the turbine disk have been determined, FE simulations have been carried out to obtain the fracture mechanics parameters according to the flaw assessment concept introduced in the present work. The critical position along the crack-front has been determined based on the crack driving force in terms of J-integral as well as the constraint parameters.

The first step is to decide the crack geometry to be analysed. According to the EASA regulations for engine certification [3.1], a semi-circular surface crack of depth 0.381 mm has to be considered for damage tolerance analyses for the end-of-life component simulation. This crack has been modelled separately at each critical location on the turbine disk determined, which are considered as potential crack initiation location. For the diaphragm, the crack has been integrated into the turbine disk model (single sector with one blade) at location 1 (Figure 3.6b) in the middle of the sector width, with the crack plane perpendicular to the maximum principal stress direction (radial direction).

Figure 3.8 illustrates the meshing strategy of the surface crack-fronts including local mesh refinement at the diaphragm, with the crack plane being modelled perpendicular to the radial direction of the disk, or the radial stress vector (Figure 3.8a). The refined mesh area around the crack-front had a tubular shape with a diameter of 0.6 mm chosen large enough to include the plastic zones ahead of the crack-front. Within the refined mesh area, ABAQUS C3D20R elements have been used to form a structured mesh with 37 nodes along the crack-front and 21 along the radius of the tube. Note that for a more precise calculation of the crack driving force and constraint parameter, and for avoiding excessive distortion of the crack-front elements, the element size along the radius of the tube was set to be increasing with an initial value of 0.008 mm. Also, mesh-morphing has been conducted to refine the mesh at the positions of the peak values of the crack driving force. The meshing strategy for the other area of the disk as well as for the blade had no change from the model used to determine the critical locations.

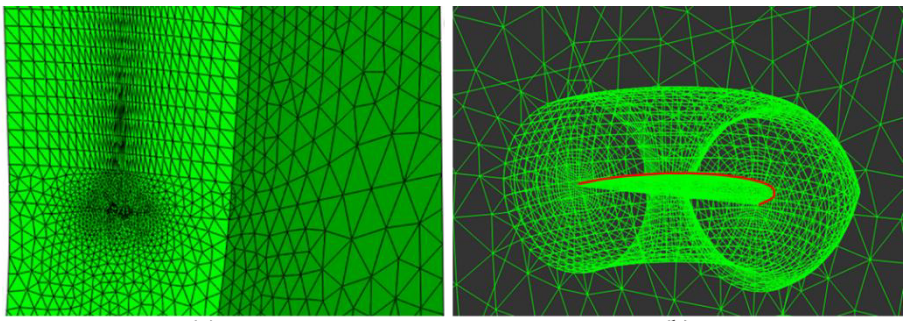

Figure 3.8 Meshing strategy for the semi-circular crack of size $a = c = 0.381$ mm at diaphragm (location 1 in Figure 3.6b) and local mesh refinement at the crack-front for fracture mechanics analysis (single sector model): (a) global view; (b) local magnification [2.14].

The boundary conditions, loads and other simulation parameters remained unchanged as in the simulation for critical locations determination, i.e., the model has been simulated for a rotational speed of N_a. Scripts have been developed for post-processing of the fracture mechanics parameters, namely the crack driving force in terms of J-integral, the stress triaxiality factor h and the local constraint parameter α_1.

As discussed in section 2.3.3, the stress triaxiality factor h and the local constraint parameter α_1 have been numerically determined for the crack at diaphragm, the distribution of which are shown in Figure 3.9 with the definition of φ. The distributions showed good agreement for both parameters, with the

maximum values taking place between $\varphi = 22°$ and $\varphi = 26°$ on the ligament, due to the biaxial loading condition at diaphragm.

The evaluation of both parameters is shown in Figure 3.10. As expected, the h factor increases approaching the crack-tip, reaching a maximum value at approximately $2r \cdot \sigma_Y/J$ (Figure 3.10a), as also stated by Brocks and Schmidt [2.1], and decreases continuously away from the crack-tip. To determine the characterising value of h for each position φ, the extrapolation method has been used (Figure 3.10a) as discussed in section 2.3.3. In Figure 3.10b the stress triaxiality factor h (extrapolated value) has been plotted for different positions along the crack-front at various rotational speeds. At the overspeed condition ($100\%N_a$), the maximum value of h takes place between $\varphi = 22°$ and $\varphi = 26°$.

For the local constraint parameter α_1, the same extrapolation method has been used to acquire the characterising value as done for h factor, due to the similar trend ahead of the crack-tip (Figure 3.10c). Also, the extrapolated value of α_1 has been plotted for different positions along the crack-front at rising rotational speeds, with the maximum value also lied between $\varphi = 22°$ and $\varphi = 26°$ for reference overspeed N_a. This trend has been considered comparable with the trend of h along the crack-front, according to which in the overspeed regime (rotational speed $96\%N_a$and $100\%N_a$), the maximum values of both constraint parameters always take place between $\varphi = 22°$ and $\varphi = 26°$. Consequently, this position has been considered as the lowest fracture resistance position along the crack-front.

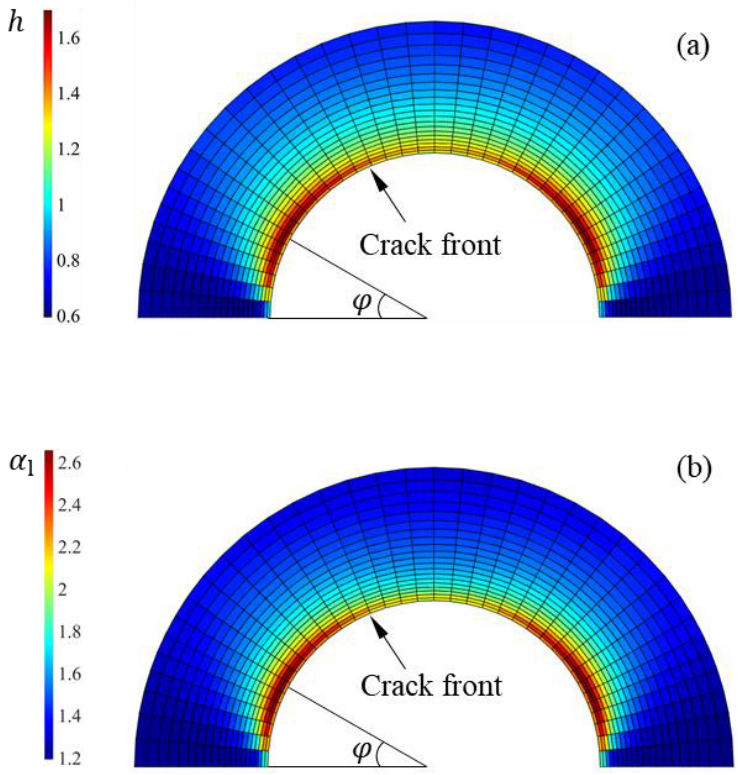

Figure 3.9 Constraint parameter distributions on the ligament of crack plane, crack at diaphragm under rotational speed of N_a: (a) Stress triaxiality factor h; (b) Local constraint parameter α_1.

Together with the values of the crack driving force in terms of J-integral, the fracture mechanics parameters for the diaphragm crack under reference overspeed N_a have been shown in Figure 3.11. The peak value of the J-integral takes place at $\varphi = 22.5°$ with a value of 14.54 N/mm. Based on this information, along with the position for the maximum values of both constraint parameters, the most critical point at the crack-front (diaphragm crack) has been identified as between $\varphi = 22°$ and $\varphi = 26°$. In other words, the crack experiences both the highest loading and the lowest fracture resistance at this position. Note that the differences in the three parameters between $\varphi = 22°$ and $\varphi = 26°$ were only small. Finally, the position $\varphi = 22.5°$ has been chosen as the critical position, with the following characterising fracture mechanics parameter values: $J = 14.54\ \mathrm{N/mm}$; $\alpha_1 = 2.925$ and $h = 1.837$.

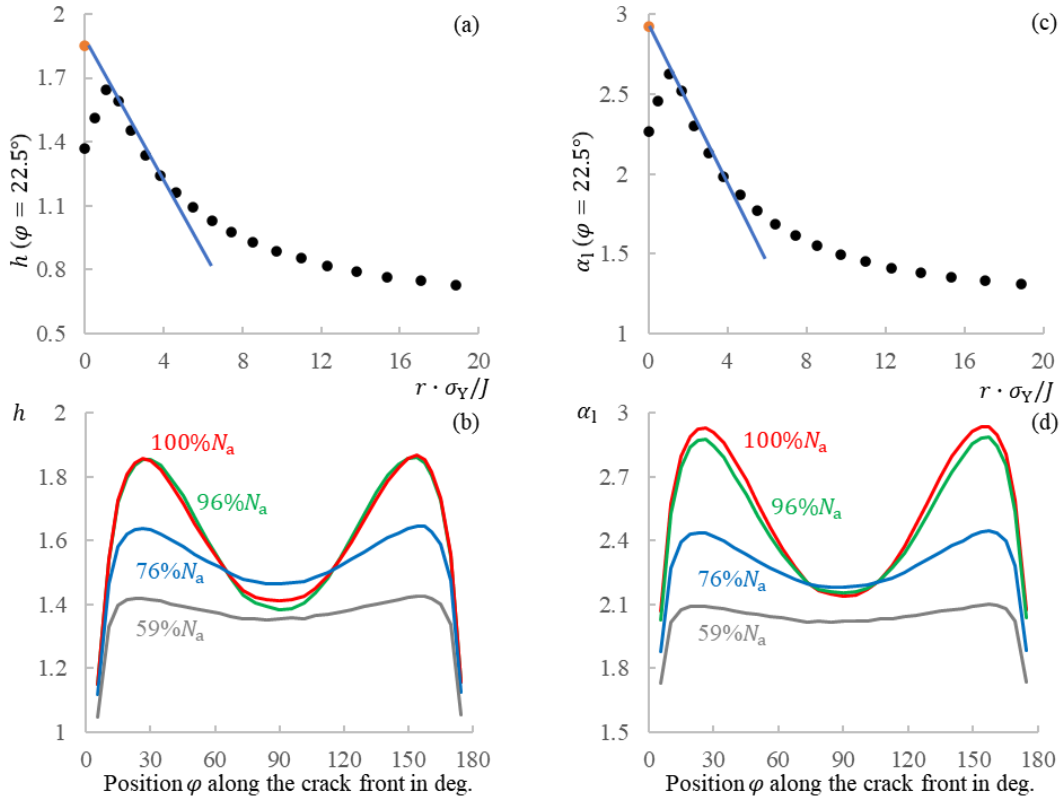

Figure 3.10 Evaluation of the stress triaxiality factor h and the local constraint parameter α_1 of the surface crack at diaphragm: (a) trend of the h ahead of the crack-tip at an angle of 22.5° under 100%N_a; (b) variation of h along the crack-front with various rotational speeds; (c) trend of the α_1 ahead of the crack-tip at an angle of 22.5° under 100%N_a; (d) variation of α_1 along the crack-front with various rotational speeds.

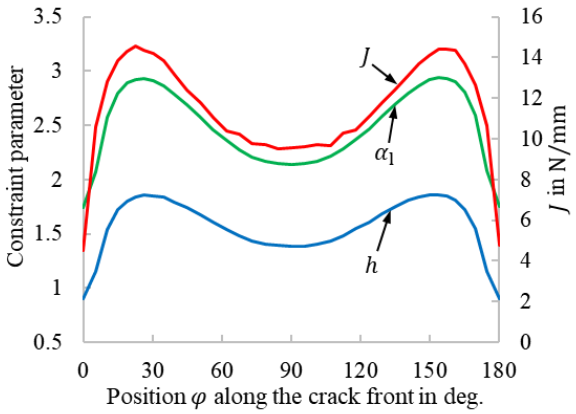

Figure 3.11 Profile of the parameters J, h and α_1 along the crack-front of the surface crack at diaphragm under overspeed condition N_a.

In order to exclude the influence of cyclic symmetric of the model to the results, a second FE model comprising a turbine disk sector with two blades has been utilised for verification. Similar to the model with one turbine blade, the same crack has been integrated at diaphragm location in the middle of the sector width (Figure 3.12). The simulation setting remained identical to the model with a single sector. The results in terms of stress distributions as well as all three fracture mechanics parameters showed good agreement with the simulation using single sector turbine disk model. Consequently, the single sector turbine disk model has been considered adequate for simulation.

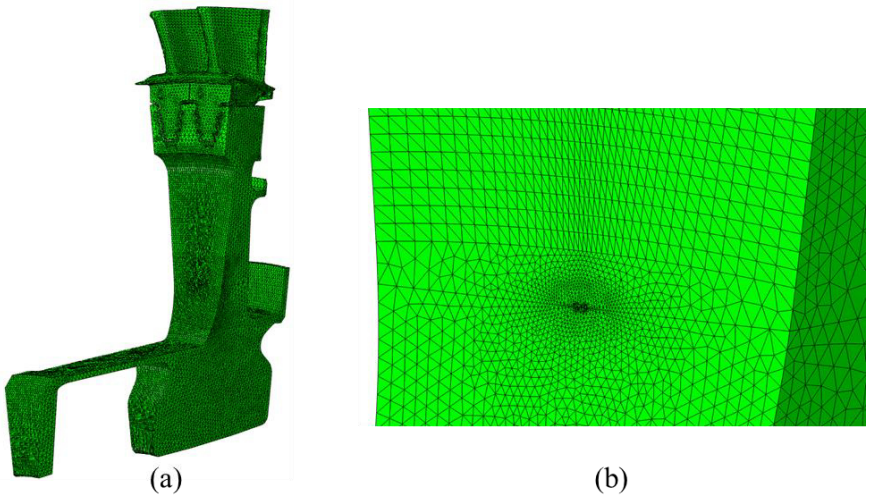

Figure 3.12 Meshing strategy for the FE model comprising a turbine disk sector with two turbine blades: (a) Model overview; (b) Magnification of crack location.

3.3.4. Determination of fracture mechanics parameters for cracked turbine disk – crack at bore

The other critical location on the turbine disk has been identified as bore (location 2 in Figure 3.6b). The same procedure has been conducted as for the diaphragm location to determine the fracture mechanics parameters, based on which the critical position along the crack-front was decided. Similarly, a semi-circular surface crack of dimension $a = c = 0.381$ mm has been integrated into the turbine disk model (single sector with one blade) at the bore (Figure 3.13a) in the middle of the sector width, with the crack plane perpendicular to the maximum principal stress direction (hoop direction). Figure 3.13 illustrated the meshing strategy of the surface crack-fronts including local mesh refinement at the bore. Like the model of diaphragm crack, the refined mesh area around the crack-front had a tubular shape with a diameter of 0.6 mm. Within the refined mesh area, ABAQUS C3D20R elements have been used with 37 nodes along the crack-front and 21 along the radius of the tube. After mesh sensitivity analysis, the element size along the radius of the tube was set to be increasing with an initial value of 0.012 mm.

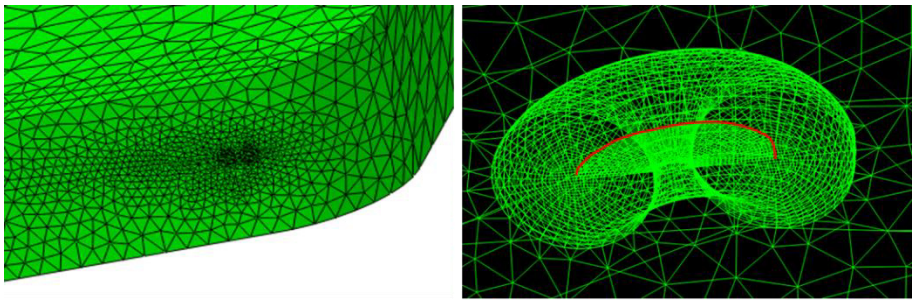

Figure 3.13 Meshing strategy for the semi-circular crack of size $a = c = 0.381$ mm at bore (location 2 in Figure 3.6b) and local mesh refinement at the crack-front for fracture mechanics analysis (single sector model): (a) global view; (b) local magnification [2.14].

With the simulation settings unchanged, the turbine disk model with bore crack has been simulated for the reference overspeed N_{a}. The fracture mechanics parameters, namely the crack driving force in terms of J-integral, the stress triaxiality factor h and the local constraint parameter α_{l} have been analysed. The distribution of both constraint parameters is shown in Figure 3.14. Similar behaviour of both constraint parameter has been observed: the maximum value takes place at the deepest position along the crack-front ($\varphi = 90°$); on each radial direction of the ligament $\varphi = const.$ both constraint parameters increase approaching the crack-tip, reaching a maximum value and decrease continuously away from the crack-tip.

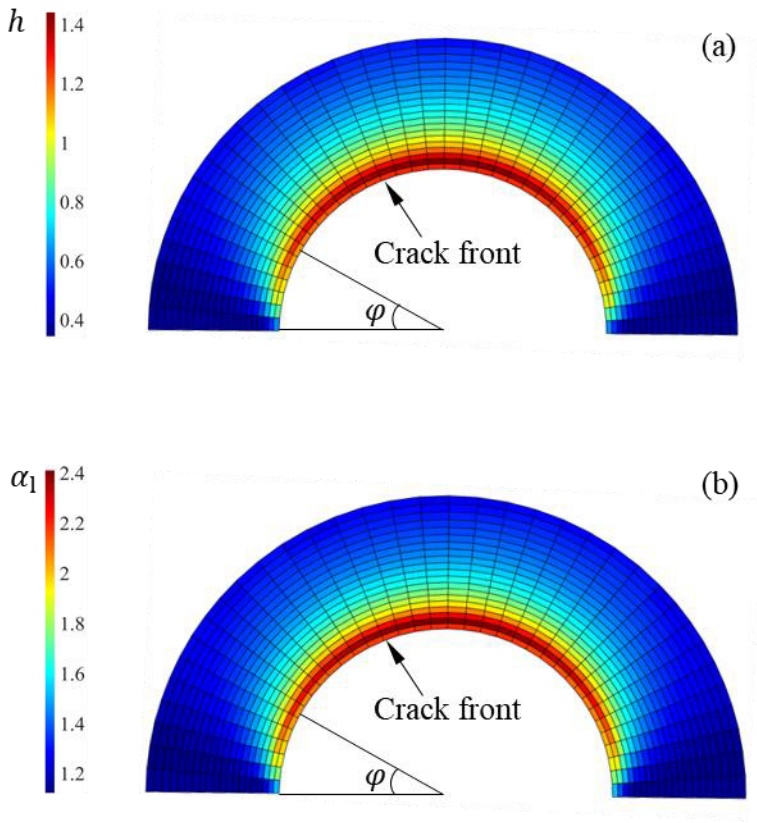

Figure 3.14 Constraint parameter distributions on the ligament of crack plane, crack at bore under rotational speed of N_a: (a) Stress triaxiality factor h; (b) Local constraint parameter α_1.

The evaluation of both constraint parameters is shown in Figure 3.15. The same extrapolation method has been used to acquire the characterising constraint parameters along the crack-front (Figure 3.15a, Figure 3.15c). Despite difference in absolute values, both constraint parameters have shown a same trend along the radial direction on the ligament with $\varphi = 90°$. The extrapolated values of both parameters have been plotted for each position φ along the crack-front for two different rotational speeds as illustrated in Figure 3.15b and Figure 3.15d ($N_{hb} = 114\% N_a$ as discussed in section 3.3.1). The peak values of both parameters at both rotational speeds are located at $\varphi = 90°$ due to the uniaxial loading condition at bore.

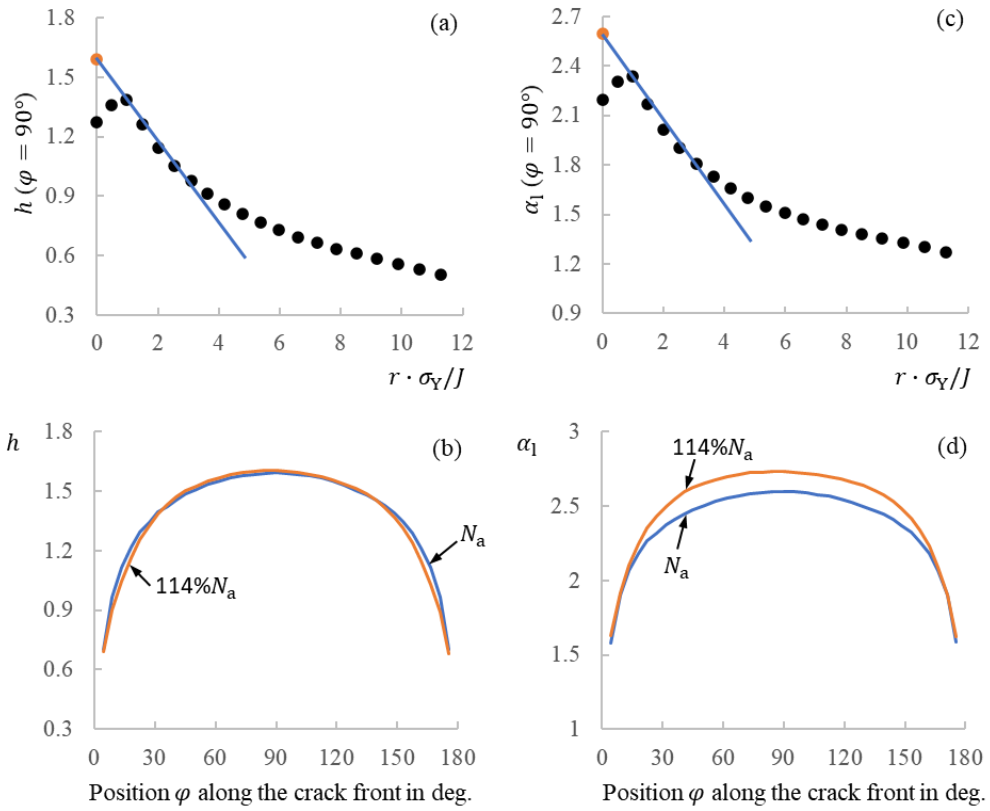

Figure 3.15 Evaluation of the stress triaxiality factor h and the local constraint parameter α_1 of the surface crack at bore: (a) trend of the h ahead of the crack-tip at an angle of 90° under N_a; (b) variation of h along the crack-front with various rotational speeds; (c) trend of the α_1 ahead of the crack-tip at an angle of 90° under N_a; (d) variation of α_1 along the crack-front with various rotational speeds.

The result of the fracture mechanics parameters including crack driving force in terms of J-integral, stress triaxiality factor h and local constraint parameter α_1 for the bore crack under reference overspeed N_a is shown in Figure 3.16. Beside the two constraint parameters, the peak value of the crack driving force in term of J-integral takes place between $\varphi = 60°$ and $\varphi = 120°$. Consequently, the position $\varphi = 90°$ has been determined as the critical position along the crack-front of bore crack, with the following characterising fracture mechanics parameter values: $J = 27.75\ \mathrm{N/mm}$; $\alpha_1 = 2.597$ and $h = 1.593$.

The single sector turbine disk model with bore crack has also been checked by running FE simulations of a turbine sector comprising two blades, which showed good agreement in terms of the fracture mechanics parameters. As a result, the size of the model has been considered to have no influence on the results.

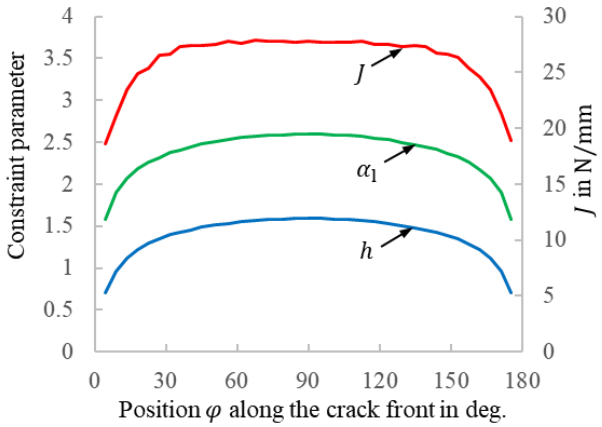

Figure 3.16 Profile of the parameters J, h and α_1 along the crack-front of the surface crack at bore under overspeed condition N_a.

3.4. Fracture mechanics specimen design

Following the component assessment concept introduced in the present work, the fracture mechanics specimens have been designed to adequately represent the loading conditions at the critical locations on the turbine disk, including mechanical loads, thermal loads and geometry similarities (constraint parameters).

3.4.1. Biaxial fracture mechanics specimen for diaphragm crack

Since the mechanical loading condition at diaphragm is biaxial, i.e., in form of radial stress and hoop stress, this has been represented by using biaxial fracture mechanics specimen.

The design criteria for the biaxial fracture mechanics specimen are as following:

(1) Comparable stress ratio λ and remote stresses in both loading directions as at diaphragm
(2) Comparable J as at the critical position of the diaphragm crack on the turbine disk
(3) Comparable h and α_1 as at the critical position of the diaphragm crack on turbine disk
(4) Tension loads within machine limits

FE simulations have been conducted for the design. The baseline biaxial specimen geometry (Figure 3.17) [4.1] has been provided by Materialprüfungsanstalt Darmstadt (MPA), where the testing of the designed biaxial specimen took place using a planar biaxial testing system [3.3]. The baseline biaxial specimen had a measurement of 110 mm*110 mm*5 mm, four wings for friction fixture on the biaxial testing machine. It has been used for several biaxial fatigue tests of the Ni based superalloy and is considered suitable to be a baseline for the quasi-static tensile tests in the present work.

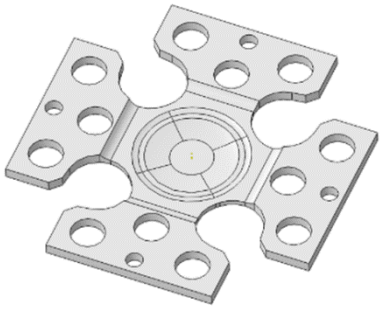

Figure 3.17 Baseline biaxial fracture mechanics specimen provided by MPA Darmstadt [4.1].

The first step was to determine the temperature profile on the biaxial specimen, due to the heating method of induction coil and cooled fixture wings used at the testing facility. A simplified quarter heat transfer model without fixture wings (Figure 3.18) has been used. The temperature in the centre of the specimen (testing area) has been set to 425°C as boundary condition to match the temperature at diaphragm of the turbine disk. The other boundary condition was the temperature (288°C) at the two outer boundary surfaces of the quarter model connecting to the fixture wings provided by MPA Darmstadt. DC3D20 elements (second order hexahedral element for heat transfer analysis) of ABAQUS have been used for meshing with refined mesh at the testing area in the centre. The temperature profile of the biaxial specimen is shown in Figure 3.18.

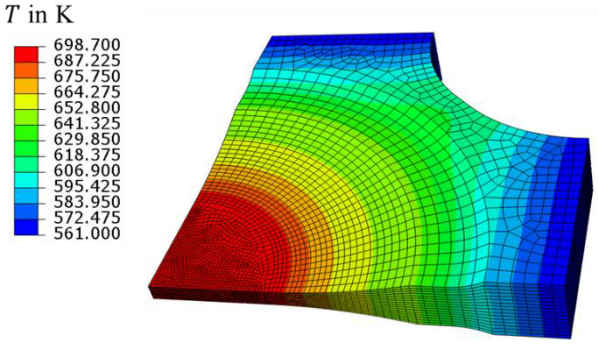

Figure 3.18 Heat transfer model of the baseline biaxial specimen, simplified quarter model without fixture wings.

The second step has been modifying the biaxial specimen geometry in order to fulfil the design criteria (1) and (4), for it has been determined that the tensile forces would be outside of the machine limits (maximum tensile force $F_{\max} = 90$ kN in each axis) when using the baseline geometry. The stress ratio λ is calculated as

$$\lambda = \frac{\sigma_{\text{hoop}}}{\sigma_{\text{rad}}} \tag{3.4}$$

where for the diaphragm location the radial stress takes the value $\sigma_{\text{rad}} = 1.200\sigma_{\text{Y}}$ and the hoop stress $\sigma_{\text{hoop}} = 0.721\sigma_{\text{Y}}$. As a result, the stress ratio for diaphragm location is $\lambda = 0.601$. For the biaxial specimen, the stress ratio is defined in a similar manner:

$$\lambda = \frac{\sigma_A}{\sigma_B} \tag{3.5}$$

being σ_A and σ_B the remote stresses at the centre of the biaxial specimen in the direction of the two tensile forces applied through both fixture wings. Note that the remote stress is defined as the stress acting at the considered location without any flaws or cracks. To match the stress ratio and both remote stresses of the turbine disk, the biaxial specimen has been modelled in FE simulations with variations of the dimensional parameters as shown in Figure 3.19. Note that an additional boundary condition of the geometry modification is the overall dimension of the biaxial specimen, which must maintain 110 mm *110 mm*5 mm due to the fixture to the testing machine.

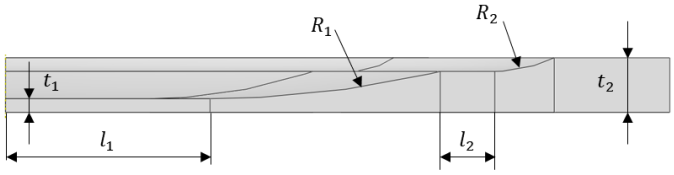

Figure 3.19 Dimensional parameters for geometry modification of the biaxial specimen (side view of eighth model).

The FE simulations of the modified biaxial specimen have made use of an eighth model without the fixture wings (Figure 3.20). C3D20R elements have been used to mesh the part with refined mesh at the specimen centre. Symmetry boundary conditions were set at the three symmetric surfaces. Two reference points have been created to simulate the load gripping points, from which the resulting tensile loads are acting on the fixture wings. Accordingly, the two reference points have been restrained in all three rotational and the two translational degrees of freedom except for the tensile force acting direction. A kinematic constraint coupling has been established between each reference point and the corresponding slave surface (cross section surface between model and fixture wing). Eventually, the tensile loads in two axes were given in form of concentrated force at the two reference points. The simulations have been conducted in a way that the temperature gradient of the specimen was firstly introduced rising from 15°C to the values determined previously. The tensile loads were then brought to the target values in ramp. The elastic-plastic material model of Udimet 720Li has been used.

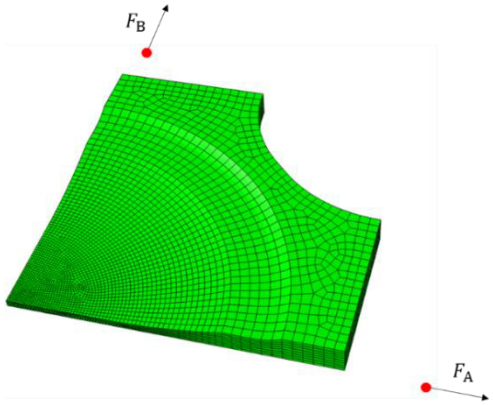

Figure 3.20 FE model of the biaxial specimen with modified geometry for determination of remote stresses at specimen centre.

After various combination and variation of the six dimensional parameters as well as the two tensile loads, a final configuration has been found that fulfils the design criteria (1) and (4). The parameters of the final configuration are listed in Table 3.1. Note that these values are the values used in the FE simulation, the corresponding values for the real component must be obtained considering the symmetric conditions of the model. The distribution of the two remote stress on the modified specimen is shown in Figure 3.21. The values at the centre of the specimen have been: $\sigma_{\mathrm{B}} = 1.202\sigma_{\mathrm{Y}}$, $\sigma_{\mathrm{A}} = 0.722\sigma_{\mathrm{Y}}$, based on which the stress ratio λ takes the value $\lambda = 0.601$. All values are within 0.2% relative difference with respect of the turbine disk diaphragm values.

Table 3.1 Dimensional and tensile force parameters of the uncracked biaxial specimen in final configuration.

Parameters	value
F_{A}	17 kN
F_B	21.8 kN
t_1	0.5 mm
t_2	2 mm
l_1	7.5 mm
l_2	2 mm
R_1	36.12 mm
R_2	5 mm

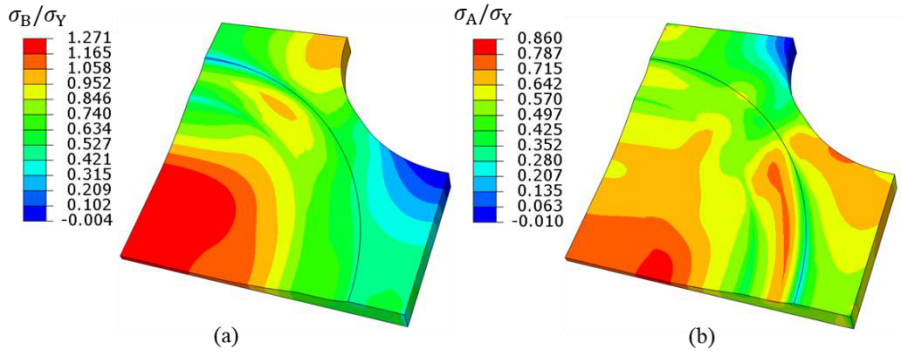

Figure 3.21 Remote stress distribution on the modified biaxial specimen.

The third step has been to design and integrate a crack into the modified biaxial specimen model and to rebuild the loading situation at the critical position of the diaphragm crack, i.e., to meet the design criteria (2), (3) and (4). There have been two different crack geometries considered: through crack and surface crack.

Biaxial specimen with through crack

The first crack geometry considered to represent the loading situation at the critical position of the diaphragm crack has been the through crack. The crack plane is supposed to be positioned perpendicular to the B-axis of the biaxial specimen (Figure 3.22). The crack opening stress vector is therefore in the direction of B-axis, representing the radial stress for the diaphragm crack. The stress vector in the direction of A-axis represents the hoop stress for the diaphragm crack.

The advantages of a through crack are firstly the homogeneous crack driving force along the crack-tip, which facilitates the mapping of the target value in terms of J-integral. Additionally, the measurement of the through crack is less difficult in the process of pre-cracking as well as the quasi-static tensile test. The alternating current potential drop (ACPD) method for the crack propagation as well as the optical crack length measurement could be used. In order to initiate the crack, a through-thickness hole in the centre of the specimen must be bored. The design of the through crack geometry has been the determination of this through-thickness hole diameter as well as the initial crack depth (Figure 3.22).

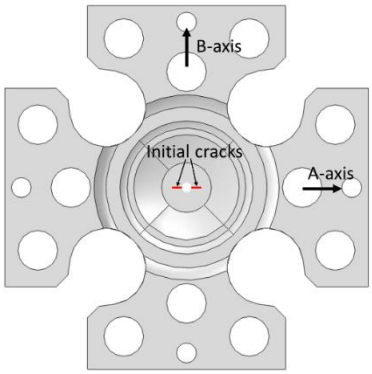

Figure 3.22 Modified biaxial specimen with through-thickness hole in the centre and initial through cracks (hole and cracks not in original scale).

Various combinations of through-thickness hole diameter D_t and initial crack depth a_0 have been modelled using the eighth model. An example is shown for $D_\mathrm{t} = 0.3\ \mathrm{mm}$ and $a_0 = 0.15\ \mathrm{mm}$ (Figure 3.23). At the specimen centre perpendicular to the B-axis, a through crack with depth a_0 has been integrated into the model starting from the through-thickness hole. The refined mesh area around the crack-front had a tubular shape with a diameter of 0.28 mm. Within the tubular shaped area, ABAQUS C3D20R elements have been used with 61 nodes along the crack-front and 21 along the radius of the tube with increasing element size. The rest of the part has been meshed using ABAQUS C3D10 elements (second order tetrahedral element).

FE simulations of the cracked specimen model with the elastic-plastic material properties have been conducted using the same simulation setting as in the uncracked specimen model. Because the size of the hole and the crack was very small compared with the biaxial specimen, the temperature field for the cracked model has been considered identical as in the uncracked model. The force ratio has been kept constant as $F_\mathrm{A}/F_\mathrm{B} = 0.7798$ (Table 3.1) for all the simulations so that the stress ratio λ can maintain the target value of 0.601. The forces in both axes have been increased in ramp using fixed time increment, the crack driving force in terms of J-integral and both constraint parameters have

been evaluated for each time increment. Additional simulations with the uncracked biaxial specimen model have been carried out using the same load settings and time increment, in order to determine the two remote stresses at the specimen centre for each time increment.

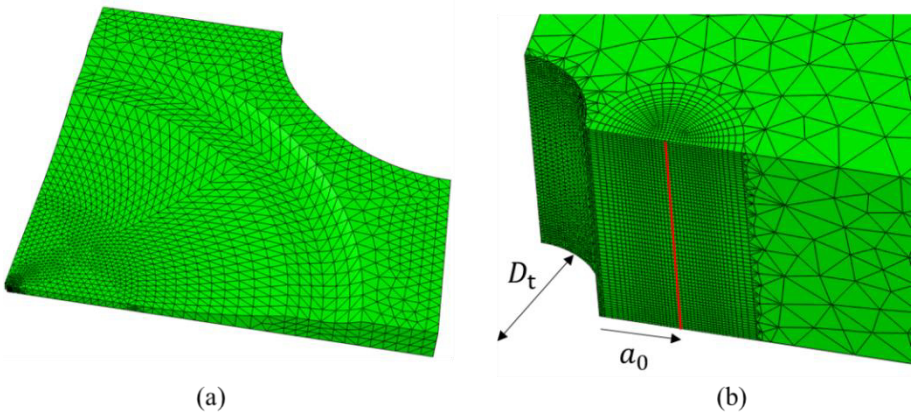

Figure 3.23 FE model for biaxial specimen with through-thickness hole in the centre and initial through crack: (a) Mesh strategy for the eighth model in global view; (b) Mesh refinement in specimen centre.

A total number of seven different through-crack geometry configurations have been simulated (Table 3.2). Among all the FE simulation results, the time increment has been located in which a J-integral value of 14.54 N/mm has been obtained for the middle point along the crack-front (on the symmetric plane of the eighth model). This point has been considered as the critical position along the crack-front of the through-crack. The two constraint parameters have been evaluated at this time increment for the critical position along the crack-front of all crack geometry configurations (Figure 3.24a). Additionally, the loads corresponding to this time increment in each simulation have been given in an uncracked biaxial specimen model to determine the corresponding remote stresses for each configuration (Figure 3.24b).

Note that design target of a J-integral value of 14.54 N/mm is based on the reference overspeed condition of the turbine disk, the real failure load could be higher than this value. As a result, the margin between the design tensile loads and the machine limits must be considered. Besides, considering the constraint parameters and the remote stresses compared to the diaphragm crack values, the through-crack configuration E has been chosen as a result. The design tensile loads for configuration E are $F_{\mathrm{B}} = 78.48\ \mathrm{kN}$ and $F_{\mathrm{A}} = 61.20\ \mathrm{kN}$. Consequently, all design criteria have been fulfilled for the biaxial specimen with through-crack configuration E, with following parameters: $\alpha_{\mathrm{I}} = 3.001$, $h = 1.966$, $\sigma_{\mathrm{B}} = 1.093\sigma_{\mathrm{Y}}$ and $\sigma_{\mathrm{A}} = 0.637\sigma_{\mathrm{Y}}$.

Table 3.2 Through-crack geometry parameters for FE simulation of cracked biaxial specimens

Designation	A	B	C	D	E	F	G
D_t in mm	0.25	0.25	0.25	0.25	0.30	0.50	0.50
a_0 in mm	0.15	0.20	0.25	0.50	0.15	0.25	0.30

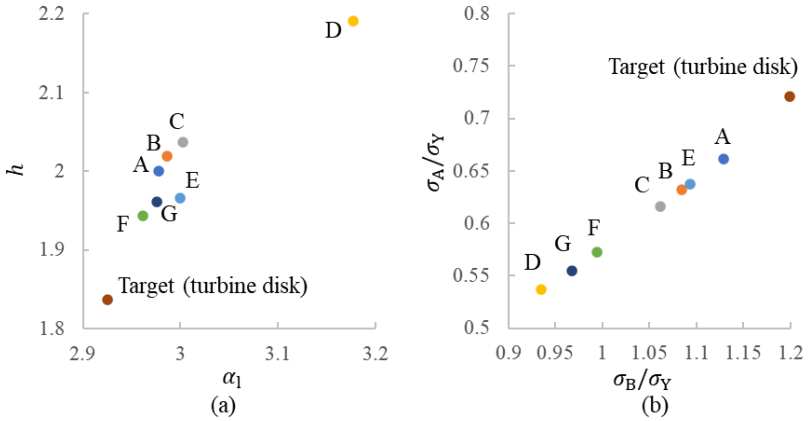

Figure 3.24 Comparison of parameters between diaphragm crack and through-crack: (a) Constraint parameters at the critical position along the crack-front for different through-crack geometry configurations and diaphragm crack on turbine disk, with J-integral values of 14.54 N/mm; (b) remote stresses for uncracked biaxial specimen with corresponding tensile loads.

Biaxial specimen with surface crack

A second biaxial specimen has been designed with surface crack to represent the loading situation of the diaphragm crack on the turbine disk. The surface crack on the biaxial specimen has been designed with the same geometry as on the turbine disk, i.e., semi-circular shape with $a = c = 0.381$ mm. The crack plane has been positioned perpendicular to the B-axis of the biaxial specimen (Figure 3.25). The crack opening stress vector is therefore in the direction of B-axis, representing the radial stress for the diaphragm crack. The stress vector in the direction of A-axis represents the hoop stress for the diaphragm crack. In order to initiate the surface crack, a notch has to be present at the centre of the specimen. The advantage of the surface crack is that not only the critical position along the crack-front of the diaphragm crack on the turbine disk can be represented but also the whole crack-front can be considered using the biaxial specimen.

Focused on the same design criteria, FE simulations have been conducted based on the modified biaxial specimen geometry. Because of the surface crack, the cracked specimen is not symmetric in thickness direction. Therefore, a quarter model has been used for FE simulations (Figure 3.26a). Two different notch geometries have been analysed: both are semi-circular shape with a height of 0.1 mm between the two semi-circular surfaces with a rounding radius of 0.05 mm. The depths of the notches are 0.20 mm and 0.25 mm, respectively. The notch variant with a depth of 0.25 mm is shown in Figure 3.26b. The crack depth, measured from the centre of the specimen, has been maintained the same as

on the turbine disk ($a = 0.381$ mm). The meshing strategy is illustrated in Figure 3.26. At the specimen centre perpendicular to the B-axis, a semi-circular surface crack has been integrated into the model along with the notch. The refined mesh area around the crack-front had a tubular shape with a radius of 0.305 mm. Within the tubular shaped area, ABAQUS C3D20R elements have been used with 21 nodes along the crack-front and 26 along the radius of the tube. Because of the presence of the notch, the tubular area around the crack-front has been partitioned again to regulate the structured mesh. The rest of the part has been meshed using ABAQUS C3D10 elements.

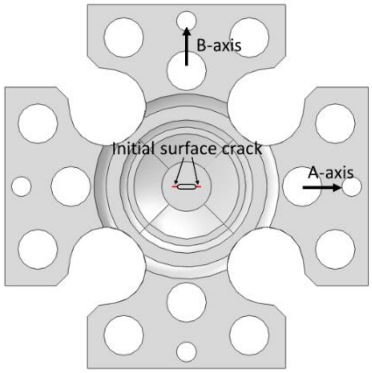

Figure 3.25 Modified biaxial specimen with notch in the centre and initial surface crack (notch and crack not in original scale).

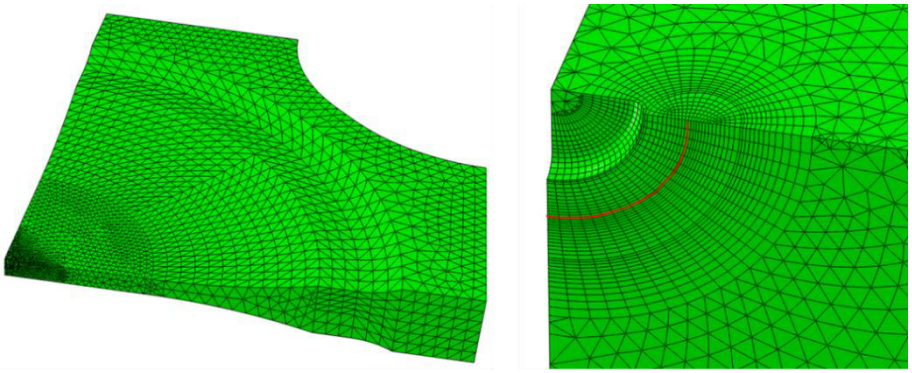

Figure 3.26 FE model for biaxial specimen with notch in the centre and initial surface crack: (a) Mesh strategy for the quarter model in global view; (b) Mesh refinement in specimen centre.

The same FE simulation settings have been used as in the uncracked model, including material properties, the temperature field, boundary conditions (except for the symmetry on thickness direction) and load type. The tensile loads on both axes have been set per ramp, after the introduction of the temperature field. The both constraint parameters have been evaluated at the time increment when the crack driving force in terms of J-integral at position $\varphi = 22.5°$ matched the diaphragm crack value at the same position. The result of all fracture mechanics parameters and their comparison with diaphragm crack values are shown in Figure 3.27. Because of the symmetric boundary condition of the biaxial specimen model, the values from $\varphi = 0°$ to $\varphi = 90°$ are shown. The results of both notch

variants have shown good agreement with turbine disk values in terms of J-integral and both constraint parameters along the crack-front. Particularly, the variant with 0.20 mm notch depth showed better compliance with turbine disk values in terms of both constraint parameters with a maximum 3.9% relative difference, whereas for the 0.25 mm notch depth variant the maximum relative difference stood at 6.3%. The tensile loads require for both variants are $F_{\mathrm{B}} = 83.5\ \mathrm{kN}$; $F_{\mathrm{A}} = 65.1\ \mathrm{kN}$ for 0.25mm notch depth variant and $F_{\mathrm{B}} = 83.6\ \mathrm{kN}$; $F_{\mathrm{A}} = 65.2\ \mathrm{kN}$ for 0.20mm notch depth variant. The relative difference in remote stresses between the two variants is within 1.1% and 5.8% between the cracked biaxial specimen and turbine disk values. Considering the differences in the parameters discussed above, the variant with 0.20 mm notch of the biaxial specimen with surface crack has been deemed adequate for representing the loading situation of the diaphragm crack on turbine disk, with following parameter: $J = 14.67\ \mathrm{N/mm}$, $\alpha_1 = 2.860$ and $h = 1.776$.

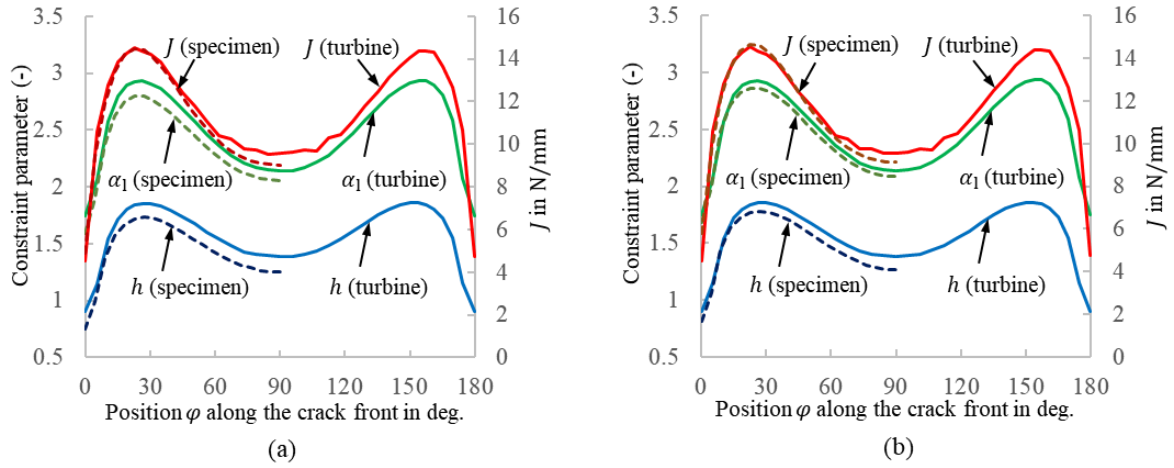

Figure 3.27 Comparison of constraint parameters and J-integral along the crack-front of the semi-circular surface cracks of size $a = c = 0.381\ \mathrm{mm}$ on turbine disk diaphragm under N_{a} (solid) and on biaxial specimen (dashed): (a) Biaxial specimen with 0.25 mm notch depth; (b) Biaxial specimen with 0.20 mm notch depth.

3.4.2. Uniaxial fracture mechanics specimen for bore crack

The loading condition for the bore crack on turbine disk is uniaxial in form of hoop stress perpendicular to the crack plane. This loading condition has therefore been represented by uniaxial fracture mechanics specimen.

The design criteria for the uniaxial fracture mechanics specimen are similar to the biaxial case discussed in section 3.4.1:

(1) Comparable remote stress on the specimen in the loading direction as at bore
(2) Comparable J as at the critical position of the bore crack on the turbine disk
(3) Comparable h and α_1 as at the critical position of the bore crack on turbine disk
(4) Tension load within machine limits

Since the uniaxial fracture mechanics specimen required relatively simple specimen geometry and the stress distribution could be analytically predicted in comparison with the biaxial specimen, two different types of uniaxial specimen (flat specimen and round specimen) have been designed based on analytical and numerical calculations. A semi-circular surface crack of the same dimension as on the turbine disk has been considered present for each uniaxial specimen at the specimen centre. The fracture mechanics parameters are supposed to be matched for the crack-front and especially at the critical position, between the crack on the designed specimen and on the turbine disk.

Flat uniaxial fracture mechanics specimen

The first type of specimen designed was the flat uniaxial fracture mechanics specimen. The advantages of flat specimen are the good producibility and standardisation e.g., DIN EN ISO 6892-2 [3.2]. The uniaxial testing machine with high temperature capability at Bundesanstalt für Materialforschung und -prüfung (BAM) has a maximum tensile capability of 60 kN. The cross-section testing area has been designed to be 40 mm^2, which is sufficient for a comparable remote stress as in the turbine disk. The rest of the specimen geometry has been designed according to DIN EN ISO 6892-2. The geometry of the flat specimen is shown in Figure 3.28.

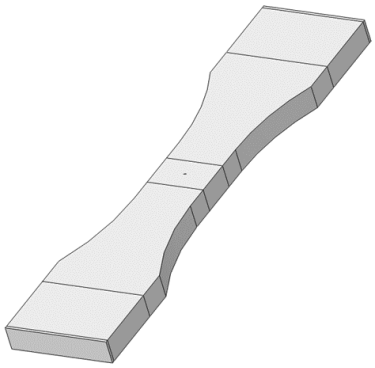

Figure 3.28 Flat uniaxial fracture mechanics specimen geometry with 40 mm^2 cross-section testing area

Three design variants with different dimensions, U-A, U-B and U-C (Table 3.3), have been simulated using FE simulations to explore the influence of overall length and aspect ratio (ratio of width and thickness of testing area) to the fracture mechanics parameters. Like the biaxial specimen variant with surface crack, a semi-circular notch has been integrated at the centre of the specimen for crack initiation. The notch had a width of 0.50 mm on surface and a rounding radius of 0.005 mm. Taken advantage of the two symmetric planes, a quarter model has been utilised in the FE simulation (Figure 3.29a). The same crack geometry has been used as on the turbine disk ($a = c = 0.381\ \mathrm{mm}$). The meshing strategy is illustrated in Figure 3.29 for specimen variant U-A. At the specimen centre perpendicular to the loading direction, a semi-circular surface crack has been integrated into the model along with the notch. The refined mesh area around the crack-front had a tubular shape with a radius of 0.305 mm. Within the tubular shaped area, ABAQUS C3D20R elements have been used with 21 nodes along the crack-front and 26 along the radius of the tube. Because of the presence of the notch, the tubular area around the crack-front has been partitioned again to regulate the structured mesh.

The rest of the part has been meshed using ABAQUS C3D10 elements. Because the testing of the uniaxial specimen would be carried out in an oven at 350 °C isothermally, the temperature field of the specimen has been set isotherm for the whole model. Beside the two symmetric boundary conditions, a single node at the upper edge of the model has been constrained in z-direction (Figure 3.29a). Compressive loads of estimated 370 MPa in form of pressure have been set at the contact surfaces between specimen and clamping jaws (dotted area in Figure 3.29a). The tensile load has been modelled as shear surface traction on the same surfaces. The simulations have been conducted so that the temperature was increased from room temperature (15 °C) to 350 °C in the first step, before the loads were applied in ramps. Fixed time increments have been used to match the crack driving force in terms of J-integral with the bore crack values. The constraint parameters as well as remote stress have been evaluated at the time increment with the comparable J values as for the bore crack.

Table 3.3 Dimensions of the designed flat uniaxial fracture mechanics specimens

Designation	U-A	U-B	U-C
Overall length in mm	100	80	80
Testing area cross-section in mm	8*5	8*5	10*4

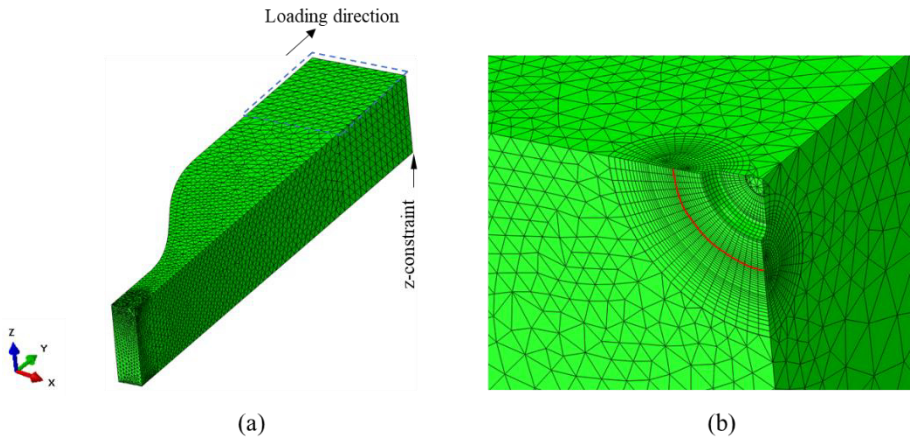

Figure 3.29 FE model for flat uniaxial specimen (U-A) with notch in the centre and initial surface crack, contact surfaces between specimen and clamping jaws in dotted area: (a) Mesh strategy for the quarter model in global view; (b) Mesh refinement in specimen centre.

The evaluation results of J-integral and constraint parameters are shown in Figure 3.30 for all three variants of flat specimen. Little differences were notice between the three variants. The critical position along the crack-front has been determined as $\varphi = 90°$ for all flat specimens based on the crack driving force in terms of J-integral. At this position, the J-integral and both constraint parameters have shown comparable results with the values of the bore crack with relative differences below 3% across all variants and turbine disk. Additionally, the J values between the flat specimens and turbine disk have shown good agreement in terms of trends and values along the crack-front. The constraint parameters of the flat specimens have all shown slightly larger values between $\varphi = 20°$ and $\varphi = 50°$

than the turbine disk. However, this has been considered acceptable because the crack driving force did not reach its maximum value in this area and higher constraint parameters have been conservative in comparison to the turbine disk. The remote stresses at the centre of the flat specimens U-A, U-B and U-C have been 96.7%, 96.6% and 96.7% of the turbine disk bore value, respectively. Eventually, all three flat specimen variants have been considered acceptable for representation of the crack-front loading situation of the bore crack on the turbine disk.

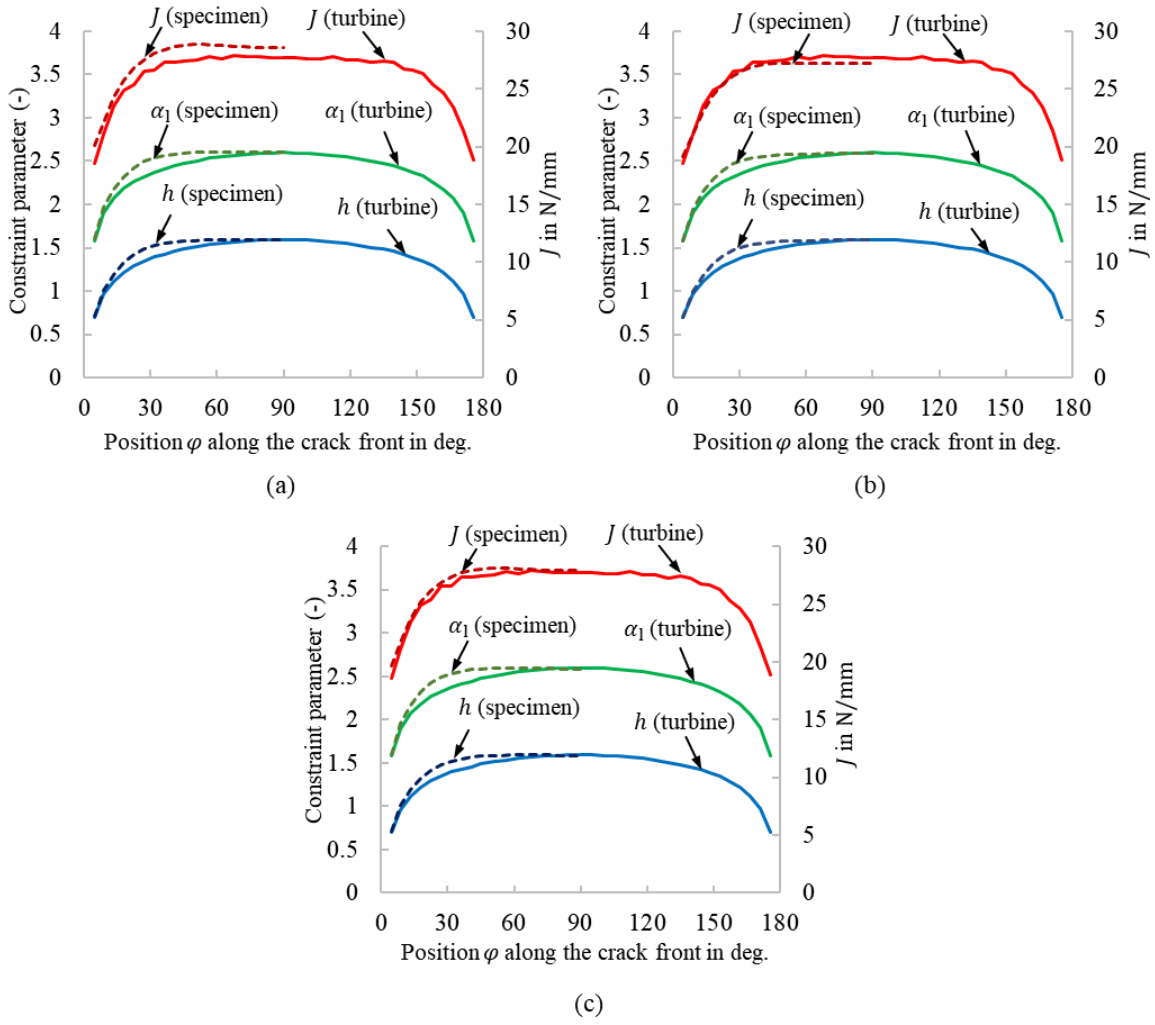

Figure 3.30 Comparison of constraint parameters and J-integral along the crack-front of the semi-circular surface cracks of size $a = c = 0.381$ mm on turbine disk bore under N_a (solid) and on flat uniaxial specimen (dashed) with 0.25 mm notch depth: (a) Flat uniaxial specimen variant U-A; (b) Flat uniaxial specimen variant U-B; (c) Flat uniaxial specimen variant U-C.

Round uniaxial fracture mechanics specimen

Beside the flat uniaxial specimen, a second type of uniaxial specimen has been designed with round shape. The advantage of the round specimen is the less requirement on amount of material for production in comparison with flat specimen. However, because of the special requirement in the present work, the round specimen differed from the general shape and standardisation in DIN EN ISO 6892-2 and there has been no further guideline for such design. As a result, the design was based on DIN EN ISO 6892-2 with several changes including testing area geometry. The geometry of the designed round specimen is shown in Figure 3.31.

The overall geometry of the round specimen has been designed according to DIN EN ISO 6892-2, which had a length of 75 mm, threads of M16 at both ends. Due to the need of a notch as well as a semi-circular surface crack, the middle of the specimen has been shaped to have two flat surfaces of width 8 mm. Like the flat specimens, the cross-section area of the round specimen has been designed close to 40 mm^2 in order to match the remote stress of the bore on the turbine disk. The testing area cross-section has been designed to have an area of 40.48 mm^2 due to the rounding surfaces. Based on the experience of flat specimen, the thickness of the testing area was determined to be 4.6 mm. A semi-circular notch of same geometry as in the flat specimen has been considered for crack initiation, which has been located in the centre of the specimen. The same semi-circular surface crack of dimension $a = c = 0.381\ \mathrm{mm}$ was also considered for the round specimen.

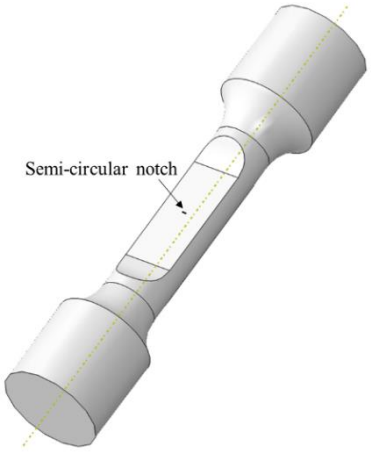

Figure 3.31 Round uniaxial fracture mechanics specimen geometry with 40.48 mm^2 cross-section testing area.

The FE simulations have been carried out to determine the fracture mechanics parameters as well as remote stress for the round specimen. The geometry of the FE model (quarter model with two symmetric planes) with mesh is shown in Figure 3.32. Basically, the meshing strategy of the round specimen remained the same as in the flat specimen model, including element types, crack-front mesh structure and refinement. The temperature field has also been isotherm. Since the tensile load was supposed to be transferred via threads, the surface compression pressure has been omitted. The tensile load has been modelled as shear surface traction on the surface with thread (thread not modelled). Other boundary conditions and simulation settings remained unchanged from the flat specimen simulation.

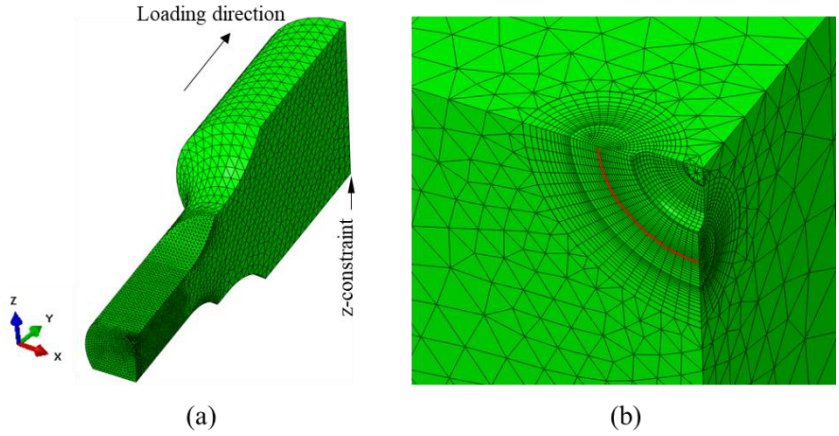

Figure 3.32 FE model for round uniaxial specimen with notch in the centre and initial surface crack: (a) Mesh strategy for the quarter model in global view; (b) Mesh refinement in specimen centre.

The crack driving force in terms of J-integral has been matched with the bore crack value at position $\varphi = 90°$ using small time increments in the simulation. The constraint parameters and the remote stress have been determined for this time increment. The comparison of the J-integral and both constraint parameters between the round specimen and turbine disk is shown in Figure 3.33. The critical position along the crack-front of the round specimen has been determined as $\varphi = 90°$, although the J-integral showed slightly higher values near $\varphi = 30°$. The trend and values of the three fracture mechanics parameters of the round specimen have been considered comparable with respect to turbine disk. The remote stress at the centre of the round specimen was 97.1% of the target turbine disk bore value. Eventually, the round uniaxial specimen design has been considered adequate to represent the crack-front loading situation of the bore crack on the turbine disk with following parameters: $J = 27.90$ N/mm, $\alpha_1 = 2.583$, $h = 1.592$ and $F_{\text{axial}} = 48.45$ kN.

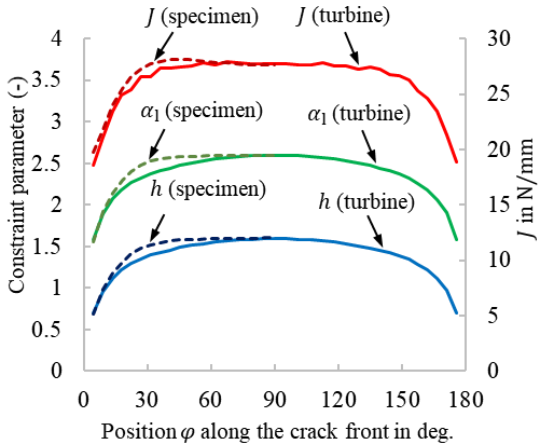

Figure 3.33 Comparison of constraint parameters and J-integral along the crack-front of the semi-circular surface cracks of size $a = c = 0.381$ mm on turbine disk bore under N_a (solid) and on round uniaxial specimen (dashed) with 0.25 mm notch depth.

4. Experiments and analyses

4.1. Introduction

For acquisition of material property parameters and validation of the proposed method, two types of experiments have been conducted: biaxial fracture mechanics experiment, uniaxial fracture mechanics experiment. Additional spin-tests of turbine disks were conducted previously by the engine manufacturer for investigation and the test results have been used for validation in this work. In this chapter, both types of experiments as well as the spin-tests have been discussed, including specimen extraction and finishing, design, conduction and analysis of the biaxial as well as uniaxial experiments and the spin-test of turbine disk for method validation. The information and calibration regarding both testing machines utilised in the experiments could be found in the appendix.

4.2. Specimen extraction and finishing

In order to manufacture the designed biaxial and uniaxial specimens, a high-pressure turbine disk made of Udimet 720Li of the investigated model (Figure 4.1) was sourced from the engine manufacturer. The status of the disk was after end-finishing, heat-treated and not shot-peened. A Computer-Aided Design (CAD) model (Figure 4.2) was used to create the specimen extraction plan. Note that the turbine disk features like flanges and seals were not included in the CAD model for simplification.

The target of the specimen extraction was to extract the specimens at their corresponding locations on the turbine disk, i.e., biaxial specimen from diaphragm and uniaxial specimen from bore, while keeping the loading directions aligned between specimens and turbine disk. The extraction plan is shown in Figure 4.2. There were totally five groups of (designated A - E) specimens distributed evenly along the circumferential direction of the turbine disk, each group contained two biaxial specimens and three uniaxial specimens. The B-axis of the biaxial specimens has been aligned with the radial direction of the turbine disk, while the loading direction of the uniaxial specimens stood perpendicular to the radial direction of the disk. The round type of uniaxial specimen has been chosen due to limited amount of material at bore. Eventually, ten biaxial specimens and fifteen uniaxial specimens have been extracted from the turbine disk, with the biaxial specimens in form of double-pack quad blank and uniaxial specimens in round blank. The blanks were then finished according to the design specifications discussed previously. The finished specimens are shown in Figure 4.3.

Figure 4.1 High pressure turbine disk made of Udimet 720Li used for specimen extraction [4.1]: (a) Top view; (b) Bottom view.

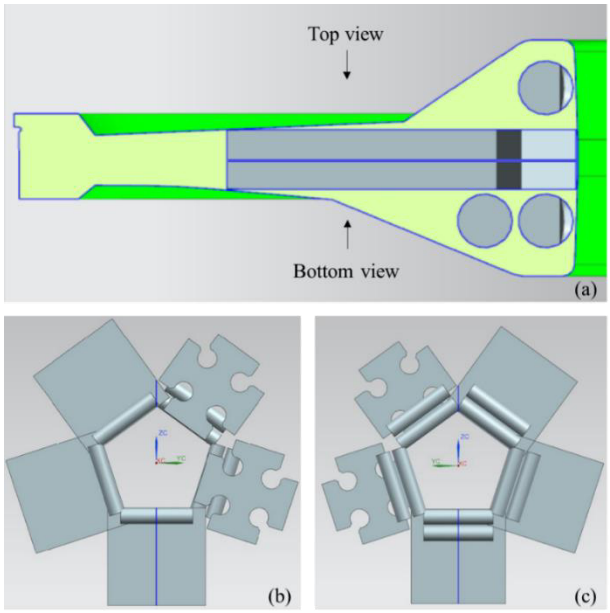

Figure 4.2 Specimen extraction plan [4.1]: (a) Specimen extraction location on the turbine disk, biaxial specimen (two specimens per group) from diaphragm, uniaxial specimen (three specimens per group) from bore; (b) Top view; (c) Bottom view.

Figure 4.3 Extracted specimen after finishing process: (a) Biaxial specimen [4.1]; (b) Uniaxial specimen.

4.3. Biaxial fracture mechanics experiments

Biaxial fracture mechanics experiments were carried out in order to determine the critical load and failure mode for the cracked biaxial specimen. Of the ten extracted biaxial specimens, seven were configured for through-crack variant (six successfully tested) and three for surface crack variant (two successfully tested). In this section, results of the biaxial experiments with both crack variants have been presented.

4.3.1. Biaxial experiments with through-crack variant

As discussed in section 3.4.1, a through-thickness hole with a diameter of 0.3 mm has been placed in the centre of the biaxial specimen for crack initiation. This was realised by means of Electrical Discharge Machining (EDM). Two different coatings have been applied on the surface within the testing area of the specimen in an alternating quarter pattern for temperature field and strain field monitoring. The set-up of the biaxial experiment is shown in Figure 4.4.

The biaxial experiments have been conducted in the following steps:

1) Adjustment of the induction coil power rating
2) Uniaxial tensile pre-cracking
3) Establishment of temperature field
4) Quasi-static biaxial tensile test

The first step of the experiment was to adjust the induction coil power rating. The reason of this step was because the induction coil had to be dismantled every time before the dismantling of the biaxial specimen. As a result, the relative position between the induction coil and the specimen surface differed among experiments. In order to guarantee the target temperature at the specimen centre, the induction coil power rating had to be adjusted to compensate the position difference. A target of 425 °C was to be regulated at the centre of the specimen. This has been accomplished by means of thermal element (4 in Figure 4.4c), infrared camera (1 in Figure 4.4a) and induction coil (5 in Figure 4.4d). The specimen was heated up through the induction coil placed at the back side of the specimen. The black-coloured coating on two quarters of testing area surface (Figure 4.4c) was provided by the engine manufacturer with a known emission coefficient. Its thermal radiation was picked up by the infrared camera to establish the temperature field on the specimen surface. The temperature value readings from the thermal element were used to calibrate the infrared camera. After establishment of the required temperature field, the target value of the thermal element reading has been noted.

The second step has been pre-cracking of the biaxial specimen in room temperature under cyclic tensile loads. The loads have been applied on B-axis of the specimen in sinusoidal form with $R = 0.1$ and $F_{\max} = 33\ \mathrm{kN}$. The target of the pre-cracking has been to initiate a pair of through-cracks with a depth of 0.30 mm (measured from the centre of the specimen) on both sides of the centre hole with crack planes perpendicular to B-axis. The specimen centre surface including the through-thickness hole has been monitored using a Digital Image Correlation (DIC) system developed by MPA Darmstadt and Fraunhofer Institute [4.2] (2 in Figure 4.4b). The initial through-crack depth has been monitored live using the DIC camera. Besides, ACPD probes (3 in Figure 4.4c) have also been welded in the upper and

lower vicinity of the through-thickness hole to detect crack initiation and growth. Examples of the initial crack picked up by the DIC camera is shown in Figure 4.5 for specimen surface with metallic spray pattern (white surface in Figure 4.4c) and specimen surface without treatment.

With the pre-cracking completed, the specimen is heated up to establish 425 °C in the centre. The noted target value for thermal element has been provided to the control system. The final step of the experiment has been the quasi-static tensile test of the pre-cracked biaxial specimen under target temperature. The infrared camera has been replaced by the DIC system for crack growth and strain field monitoring. An additional feature of the DIC system was the optical extensometer (Figure 4.6). The displacement of the selected reference pixels, which sit in 10 mm distance pairs on both loading axes, has been calculated by the DIC system and the strain results have been therefore in terms of engineering strain. At the meantime, the crack growth has also been monitored by the ACPD method. The quasi-static tensile test has been force-controlled with a constant force ratio $F_A/F_B = 0.7798$ through the test. The loading rate has been determined according to ASTM E399-19 [1.7]. The test ended right after the moment when the fracture of the specimen took place.

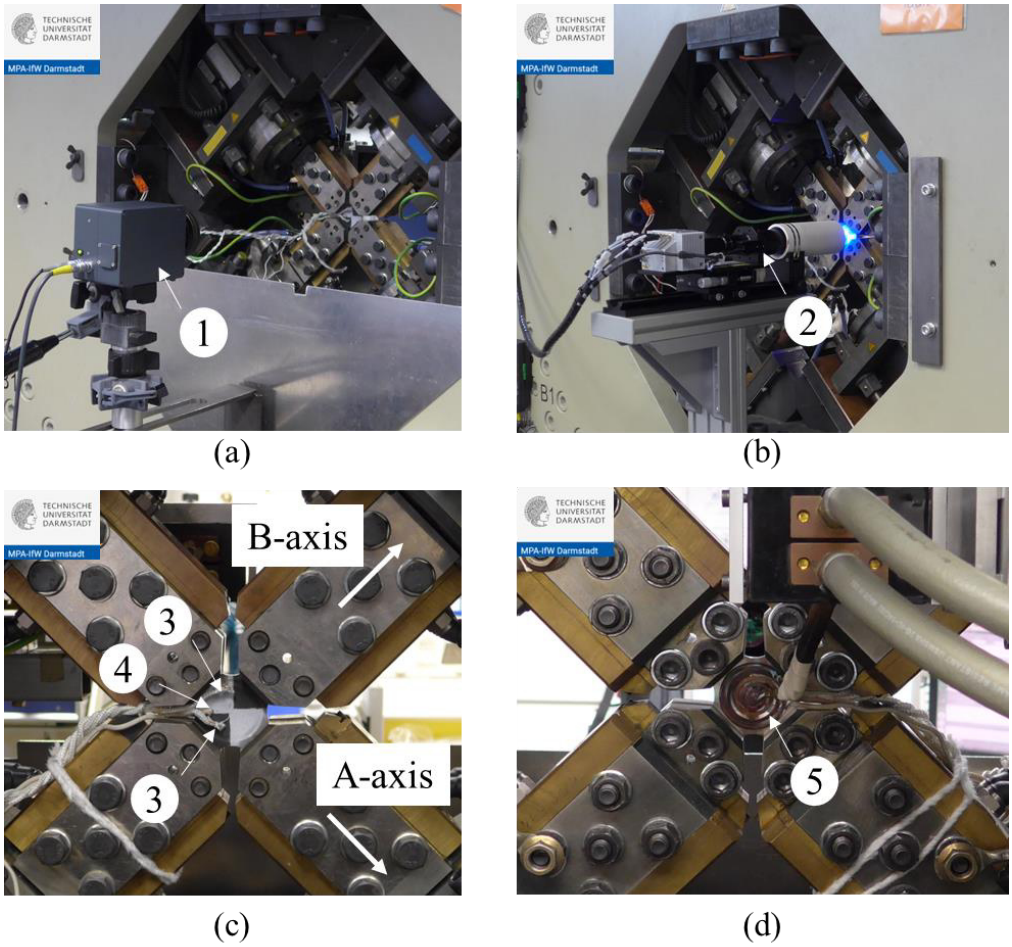

(a) (b) (c) (d)

Figure 4.4 Set-up of the biaxial experiment [4.1]: (a) Regulation and establishment of temperature field for biaxial specimen; (b) Crack and strain field monitoring; (c) Front view of biaxial specimen and clamping jaws; (d) Back view of biaxial specimen and clamping jaws.

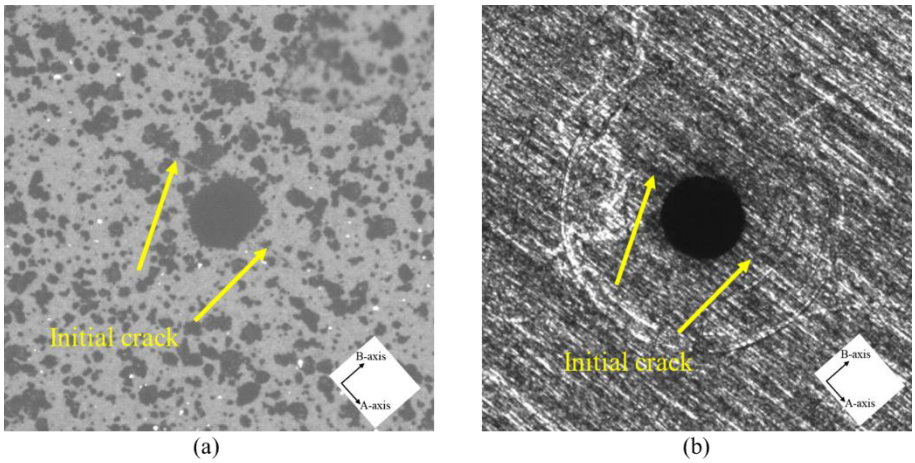

Figure 4.5 Initial crack picked up by the DIC camera during pre-cracking [4.1]: (a) Specimen surface with metallic spray pattern; (b) Specimen surface without treatment.

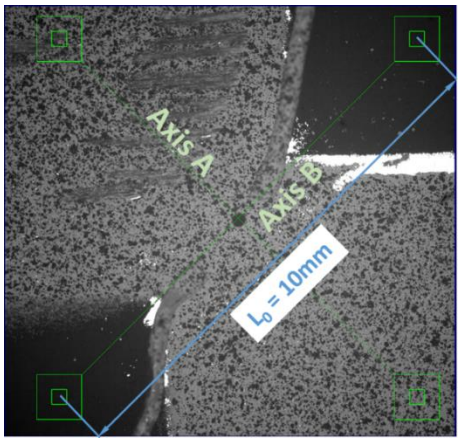

Figure 4.6 Crack extension measurement and optical extensometer feature of the DIC system for through-crack variant, reference pixels in green squares [4.1].

Test of biaxial specimen C2

A total number of six biaxial specimens with through-crack have been tested. The test of biaxial specimen C2 has been discussed in detail, whereas the data for the rest of the tests are located in appendix.

After establishing the temperature field and adjusting the induction coil power rating (Figure 4.7), the biaxial specimen C2 was cooled down to room temperature and was then subject to the uniaxial tensile pre-cracking. As discussed, the tensile cyclic loads for the pre-cracking applied on B-axis of the specimen have been in sinus form with $R = 0.1$ and $F_{\max} = 33\ \mathrm{kN}$ at $f = 10\ \mathrm{Hz}$. A total number of 57 000 cycles has accumulated during the pre-cracking process. Because of the uncertainties in the crack growth measurement using DIC camera and ACPD method for such a short length, the exact initial crack length can only be measured after the experiment when the fracture surface is available.

The initial crack length of the specimen C2 was 0.56 mm determined using DIC camera, with the specimen mounted in the biaxial testing machine (see Figure 4.8).

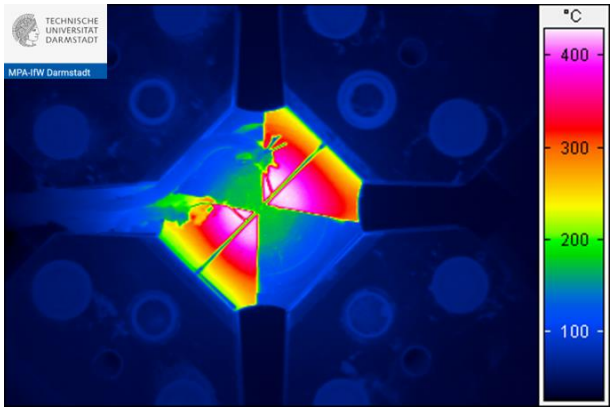

Figure 4.7 Thermal graphic (temperature field) of the biaxial specimen (C2) surface during adjustment of induction coil power rating with a target temperature of 425 °C at specimen centre [4.1].

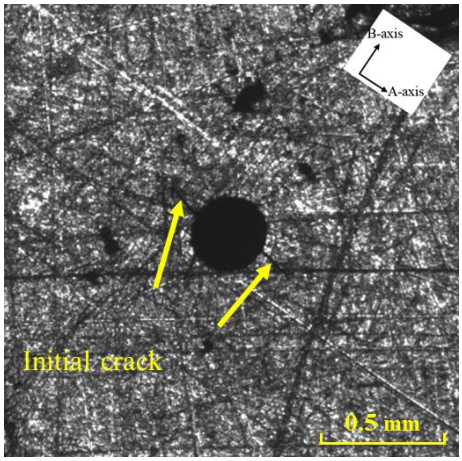

Figure 4.8 Initial crack of size $2a_0 = 0.56$ mm determined by DIC camera for biaxial specimen C2 [4.1].

With completed pre-cracking, the specimen has been heated up so that the centre of the specimen remained at 425°C for 30 min. Then the final step, quasi-static biaxial tensile test, took place. Because the constant force ratio between the two axes has to be maintained, the test has been conducted using force-controlled method. Specific for the specimen C2, in order to detect any possible crack growth during the loading process, a series of five stress relaxations has been conducted during the test, in which 30% of the reached current peak forces in both axes have been relaxed (Figure 4.9). The loading rate on the B-axis has been selected as $\dot{F}_{\mathrm{B}} = 1\ \mathrm{kN/s}$ from the beginning until F_{B} reached 70 kN, after which the loading rate maintained $\dot{F}_{\mathrm{B}} = 0.5\ \mathrm{kN/s}$ ($\dot{F}_{\mathrm{B}} = -0.5\ \mathrm{kN/s}$ at relaxation). During the whole test, the loading rate on the A-axis remained proportional with respect to the loading rate on the B-axis through the pre-determined force ratio of $F_{\mathrm{A}}/F_B = 0.7798$. The specimen was biaxially loaded reaching $F_{\mathrm{B}} = 72\ \mathrm{kN}$ when the first relaxation took place. After each relaxation, the specimen was then biaxially loaded until 2 kN higher than the previous peak force on the B-axis. After the five relaxations, the specimen was then biaxially loaded until the fracture occurred.

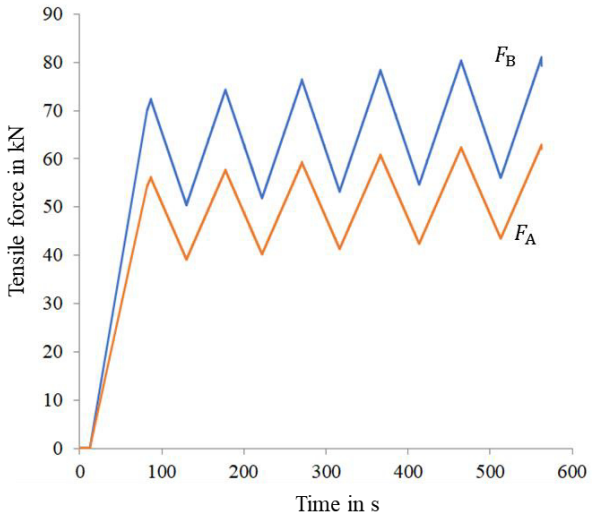

Figure 4.9 Loading history for the quasi-static biaxial tensile test of specimen C2.

The force-strain curve of the quasi-static tensile test has been measured by the force sensors and the DIC, shown in Figure 4.10. The yielding started when the tensile force on the B-axis reached about 55 kN. While the plastic material behaviour could be clearly observed on the B-axis, the force and strain measured by the DIC optical extensometer on the A-axis remained predominantly linear through the whole test. With the accumulated plastic strain, the five stress relaxations could be clearly observed on the B-axis, marked with 1 to 5 at the end of each reloading sequence (the first two overlapped). The fracture of the specimen is marked with 6 in Figure 4.10 on the B-axis, with a force of 81.13 kN.

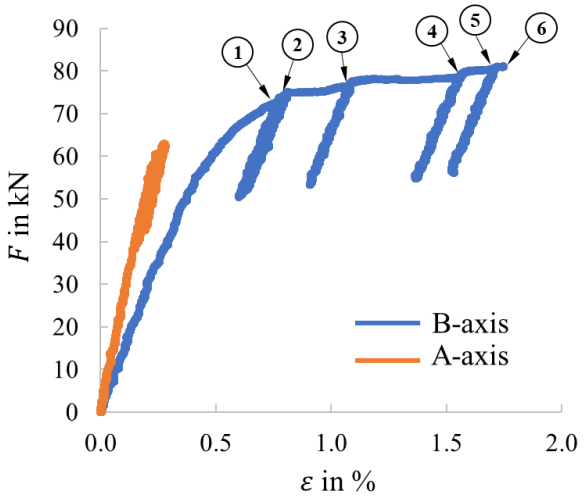

Figure 4.10 Force-strain curve for the quasi-static biaxial tensile test of specimen C2.

Fractographic analysis of the fracture surface under optical microscope was performed (Figure 4.11). The dark surfaces extending from the through-thickness hole in the middle are the initial crack after pre-cracking. The crack-fronts have been straight. Stable crack extension could be observed on the fracture surface through flat smooth surfaces beyond initial crack, the crack-fronts of the final crack

extension before fracture have been marked with solid red splines in Figure 4.11. The fracture surfaces beyond these crack-fronts were rough and not within the same surface as the initial crack surface, which showed the sign of the final fracture of the biaxial specimen. The surface view of the fractured biaxial specimen C2 was shown in Figure 4.12. Flat surfaces for stable crack extension could be observed. The kink at the end of each stable crack extension surface represented the starting point of the final fracture.

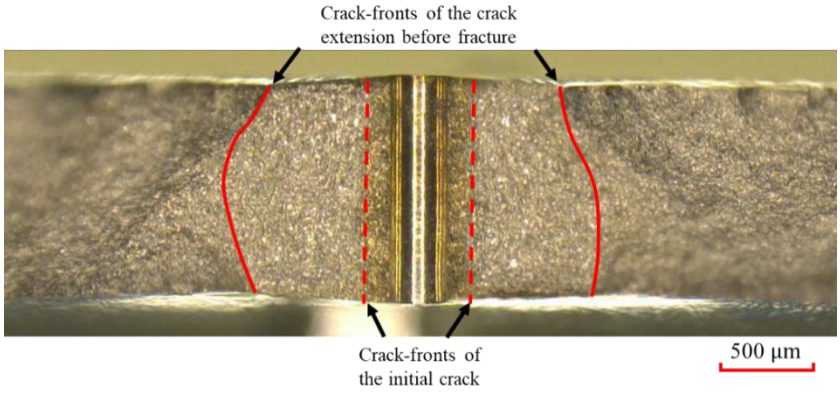

Figure 4.11 Fractographic analysis with optical microscope of the fracture surface at crack plane of the biaxial specimen C2 (lower part).

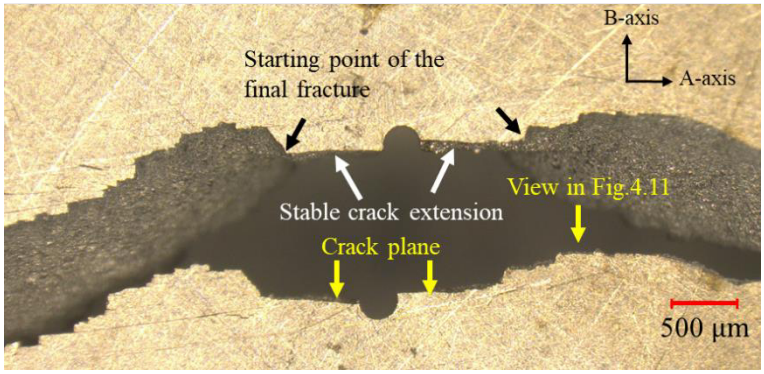

Figure 4.12 View of the specimen surface of the fractured biaxial specimen C2.

The fracture surface has then been examined under scanning electron microscope (SEM) and was shown in Figure 4.13. The fracture surface on the right side of the through-thickness hole was considered (compare Figure 4.11). The initial crack surface as well as the stable crack extension were shown in Figure 4.13a, with the crack-front of the initial crack highlighted in yellow. A number of dimples (1 in Figure 4.13a) have been observed on the stable crack extension surface, which is the evidence of considerable plastic deformation of the material in this area. Transcrystalline fracture facettes (2 in Figure 4.13a) surrounded by the dimples were also to be seen in this area. Noted that on the stable crack extension surface, the transcrystalline fracture facettes are generally perpendicular to the crack opening stress direction, or B-axis. On the final fracture surface (Figure 4.13b), transcrystalline fracture facettes (2 in Figure 4.13b) could also be observed with surrounding dimples (1 in Figure 4.13b). However, the transcrystalline fracture facettes were generally larger on the final

fracture surface than on the stable crack extension surface and their facing directions have been more of a random pattern. Consequently, it has been determined that the ligament of the biaxial specimen went through considerable plastic deformation during stable crack extension and final fracture. The crack-fronts of initial crack as well as stable crack extension before fracture shown in Figure 4.11 have been confirmed.

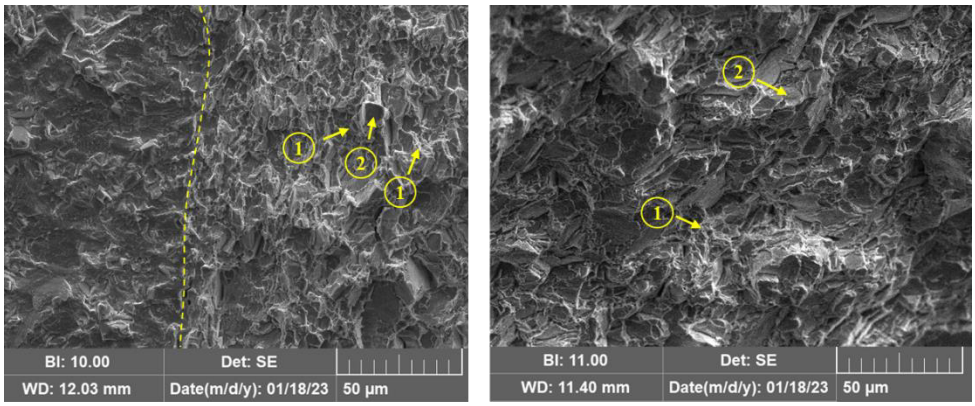

Figure 4.13 Fractographic analysis with scanning electron microscope (SEM) of the fracture surface of the biaxial specimen C2: (a) Initial crack surface and stable crack extension surface; (b) Final fracture surface.

Determination of stable crack extension length

To determine the stable crack extension length, three methods have been considered, namely stress relaxation slopes, ACPD values and DIC images. However, since the biaxial specimens were specially designed to rebuild the constraint and local loading conditions of the turbine disk, the standard stress relaxation slope method, e.g., according to [1.7], was not applicable. Besides, the noise of the ACPD values was high (Figure 4.14), it has been decided that its accuracy was not as good as the DIC images in terms of crack extension measurement. Consequently, the crack extension has been determined through DIC images.

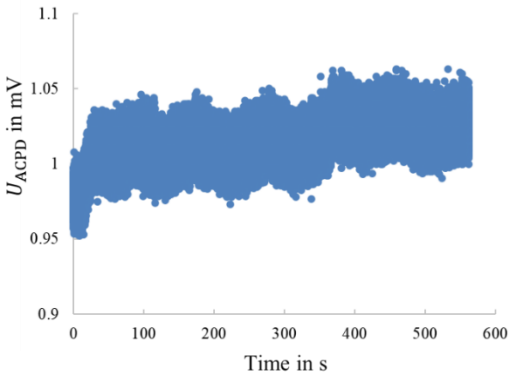

Figure 4.14 ACPD values for the quasi-static biaxial tensile test of specimen C2.

It could be observed in Figure 4.11 that the final stable crack extension length on the specimen surface is shorter than it at the middle of the specimen thickness, which formed a curve-like crack-front on both sides. This is due to the fact that the constraint at the middle of the specimen has been slightly larger than it at the surface and consequently a lower material resistance in the specimen middle. As a result, the crack extension measured by the DIC camera on the specimen surface was supposed to be shorter than it at the specimen middle, therefore, in order to establish a characteristic crack depth for calculation and simulation, an equivalent crack depth a_{eq} has been introduced. A simplified crack surface model has been shown in Figure 4.15. The crack-fronts have been modelled as arrow-form, with the location of surface points and the deepest point along the crack-front on each side measured from the fractographic analyse. The equivalent crack depth a_{eq} has been calculated as

$$2a_{\mathrm{eq}} = \frac{A_{\mathrm{crack}}}{B} \tag{4.1}$$

where A_{crack} stands for the crack area and B stands for the specimen thickness. In essence, the equivalent crack depth referred to the symmetric crack with straight crack-fronts which had the same crack area as in the simplified crack surface model. As a result, the equivalent crack depth was larger than the crack depth measured on the surface and lower than the deepest point of the stable crack extension length.

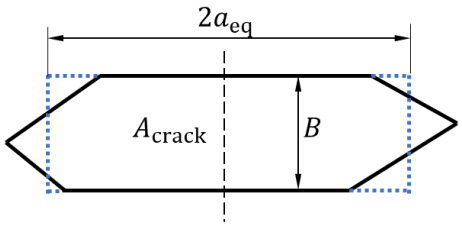

Figure 4.15 Simplified crack surface model for determination of equivalent crack depth a_{eq}.

The stable crack extension length of the biaxial specimen C2 has been determined. First, the stable crack extensions on the specimen surface were determined based on DIC images. Six images during the quasi-static test (Figure 4.16) have been chosen, namely at the end of each reloading sequence before the further increase of the plastic strain and the last moment before the final fracture (point 1 to point 6 in Figure 4.10). It has been assumed that during the stable crack extension, the ratio between the crack depth referring to the deepest point along the crack-front and the crack depth on the specimen surface would remain constant, such that the ratio between the equivalent crack depth and crack depth measured by the DIC camera would remain constant:

$$\frac{a_{\mathrm{eq}}}{a_{\mathrm{DIC}}} = const. \tag{4.2}$$

This constant has been calculated based on the fractographic analysis measurements on the fracture surface, e.g., Figure 4.11 for the final length of stable crack extension before fracture. For the test of biaxial specimen C2, this constant has been determined as $a_{\mathrm{eq}}/a_{\mathrm{DIC}} = 1.294$. The equivalent crack

depths during the test have been calculated based on this constant. The results of the stable crack extension length have been summarised in Table 4.1.

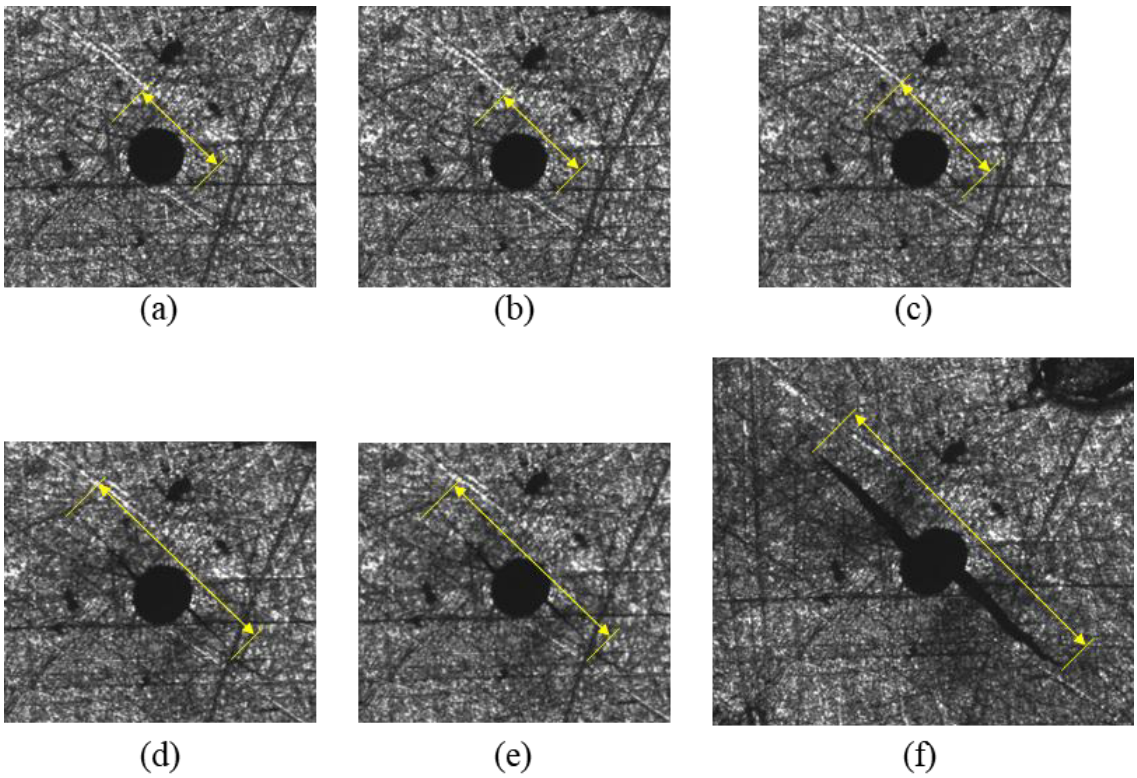

Figure 4.16 Stable crack extension measurement ($2a_{\mathrm{DIC}}$) on specimen (C2) surface based on DIC images: (a) Point 1 in Figure 4.10; (b) Point 2 in Figure 4.10; (c) Point 3 in Figure 4.10; (d) Point 4 in Figure 4.10; (e) Point 5 in Figure 4.10; (f) Point 6 in Figure 4.10.

Table 4.1 Stable crack extension on biaxial specimen C2

Point Nr. in Figure 4.10	F_{B} in kN	$2a_{\mathrm{eq}}$ in µm	$2a_{\mathrm{DIC}}$ in µm (measured)
1	72	728*	563
2	74	728*	563
3	76	768*	593
4	78	1428*	1104
5	80	1428*	1104
6	81.13	1927**	1489

*re-calculated; **measured by fractography

Determination of crack growth resistance curve (R-curve)

Among all the experiments of biaxial specimen with through-crack variant, the experiment of specimen C2 has yielded the best result in terms of following aspects:

- The initial crack-fronts have been straight
- The stable crack extension surface remained in the same surface as the initial crack
- The initial crack as well as stable crack extension have been generally symmetric with respect to the specimen centre

Consequently, it has been decided to generate the crack growth resistance curve (R-curve) based on the stable crack extension data collected from quasi-static test of the biaxial specimen C2, while the R-curves determined based on the rest of the tested specimens are to be found in appendix. Since the biaxial specimen was of non-standard form, the analytical approaches to calculate the crack-tip loadings were not applicable. As a result, FE simulations have been carried out to determine the crack-tip loadings in terms of J-integral. Six FE simulations have been carried out in order to determine the J-integral value for the middle point along the crack-front. The FE model of the biaxial specimen (1/8 model) used in section 3.4.1 has been utilised. Through-cracks with straight crack-fronts and crack depths of a_{eq} have been modelled (Figure 4.17) with the load settings on B-axis according to Table 4.1. The loads on A-axis have been set with the constant force ratio with respect to the loads on B-axis as discussed in section 3.4.1. Other boundary conditions and settings remained unchanged as in the simulations discussed in section 3.4.1. The simulation results including J values have been summarised in Table 4.2. The initial crack depth $2a_0$ has been determined according to Eq. (4.1) using measurements from the fracture surface (Figure 4.11). As a result, the initial crack depth was calculated as $2a_0 = 0.65\ \mathrm{mm}$. The crack growth has been defined as

$$\Delta a = a_{\mathrm{eq}} - a_0 \tag{4.3}$$

which described the crack extension at each crack-front. The J values were then illustrated against the corresponding crack growth values in Figure 4.18. Based on these data, a fit-curve has been generated as the R-curve, which had an analytical expression of

$$J = 94.6 \cdot \Delta a^{0.67} \tag{4.4}$$

with J in N/mm and Δa in mm.

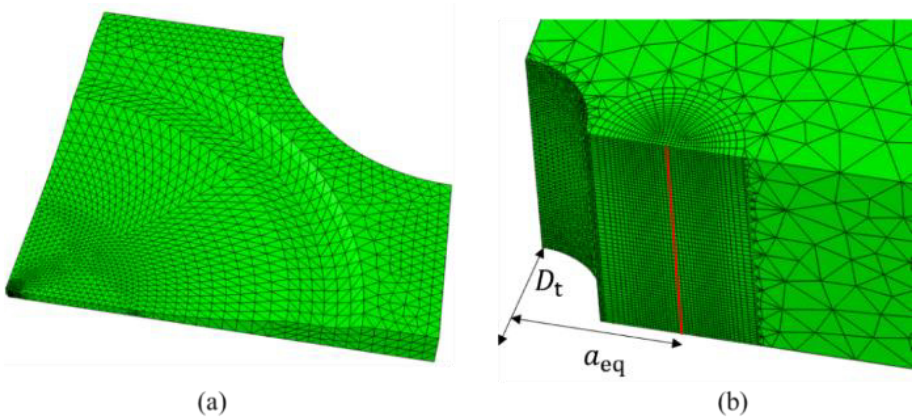

Figure 4.17 FE model for determination of R-curve based on stable crack extension data from quasi-static test of biaxial specimen C2.

Table 4.2 Results from FE simulations for determination of R-curve

Point Nr. in Figure 4.10	a_{eq} in mm	Δa in mm	J in N/mm
1	0.364	0.039	10.04
2	0.364	0.039	11.86
3	0.384	0.059	15.40
4	0.714	0.389	39.88
5	0.714	0.389	50.53
6	0.964	0.639	79.56

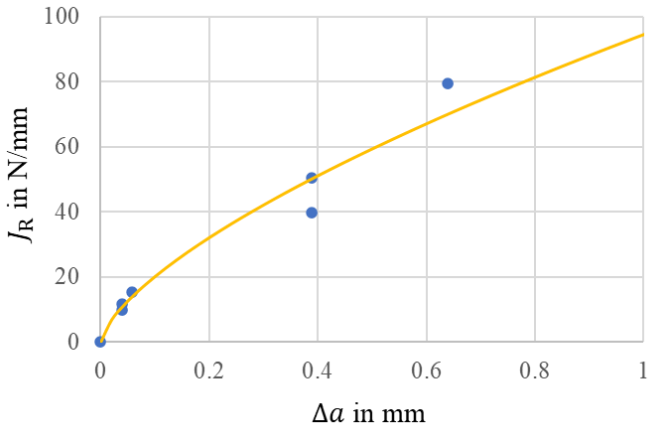

Figure 4.18 Crack growth resistance curve (R-curve) based on stable crack extension data from quasi-static test of biaxial specimen C2 (BV5).

4.3.2. Biaxial experiments with surface crack variant

As discussed in section 3.4.1, a semi-circular surface crack of size $a = c = 0.381$ mm was supposed to be placed in the centre of the biaxial specimen. For crack initiation, a semi-circular notch has been manufactured by means of EDM in the centre of the specimen with the notch symmetric plane perpendicular to the B-axis (Figure 4.19). The set-up and the procedures of the experiment have been identical to the experiments with through-thickness crack variant. Two biaxial quasi-static tension experiments have been conducted for specimen with surface cracks (specimen E1 and D2). The experiment using biaxial specimen E1 has been discussed in detail, while the data of the other test could be found in appendix.

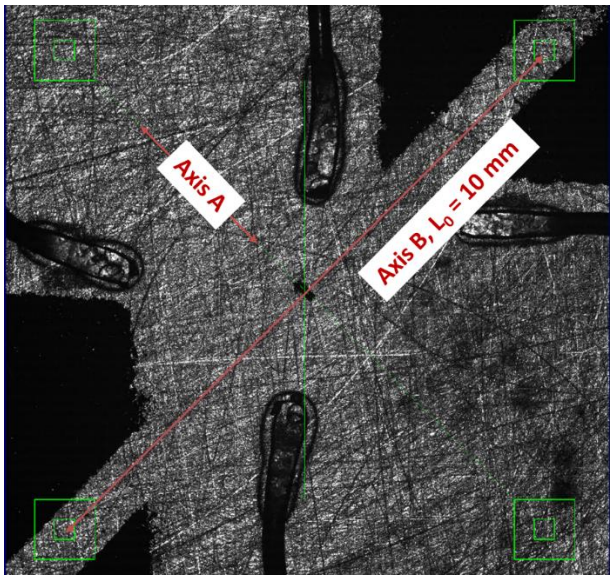

Figure 4.19 Crack extension measurement and optical extensometer feature of the DIC system for surface crack variant, reference pixels in green squares [4.1].

Test of biaxial specimen E1

After establishing the temperature field and adjusting the induction coil power rating, the biaxial specimen E1 was cooled down to room temperature and was then subject to the uniaxial tensile pre-cracking. The tensile cyclic loads for the pre-cracking applied on B-axis of the specimen have been in sinus form with $R = 0.1$ and $F_{\max} = 30$ kN at $f = 10$ Hz in the first stage. 40 000 cycles have been accumulated. In a second stage, the tensile cyclic loads have been increased to $R = 0.1$ and $F_{\max} = 32$ kN at $f = 10$ Hz with 45 000 cycles accumulated, until the initial crack has been detected.

Because of the uncertainties in the crack growth measurement using DIC camera and ACPD method for such a short length, the exact initial crack length can only be measured after the experiment when the fracture surface is available. The initial crack length of the specimen E1 was $2c_0 = 0.71$ mm determined using DIC camera, with the specimen mounted in the biaxial testing machine (Figure 4.20).

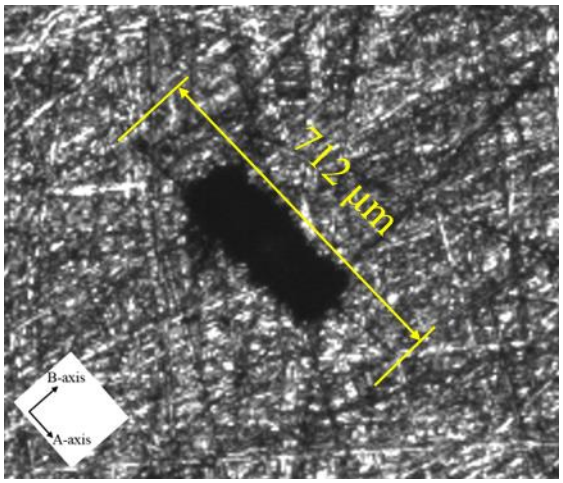

Figure 4.20 Initial crack of size $2c_0 = 0.71$ mm determined by DIC camera for biaxial specimen E1.

With completed pre-cracking, the specimen has been heated up so that the centre of the specimen remained at 425 °C for 30 min. Then the final step, quasi-static biaxial tensile test, took place. Like the tests with through-cracked biaxial specimens, the test has been conducted using force-controlled method. The loadings for the biaxial specimen E1 have been monotonic in both axes with the pre-determined force ratio $F_A/F_B = 0.7798$. The loading rate on the B-axis has been selected as $\dot{F}_B = 1$ kN/s from the beginning until F_B reached 70 kN, after which the loading rate maintained $\dot{F}_B = 0.5$ kN/s until fracture. The loading history of the test has been shown in Figure 4.21.

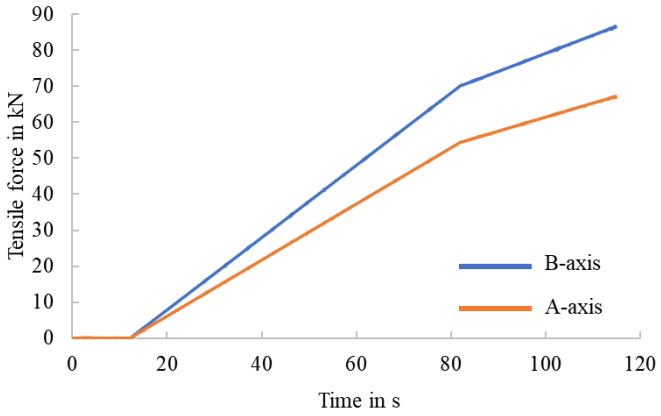

Figure 4.21 Loading history for the quasi-static biaxial tensile test of specimen E1.

The force-strain curve of the quasi-static tensile test is shown in Figure 4.22. The yielding measured on the B-axis started when the tensile force on the B-axis reached about 55 kN. Unlike the biaxial tests of specimen with through-crack variants, in the test of specimen E1, plastic strain could be observed on the A-axis when the force on the A-axis reached about 60 kN. Five points (marked with 1 to 5 in Figure 4.22) have been chosen along the force-strain curve of the B-axis in order to determine the crack extension using DIC images. The fracture of the specimen is marked with 6 in Figure 4.22 on the B-axis, with a force of 86.63 kN.

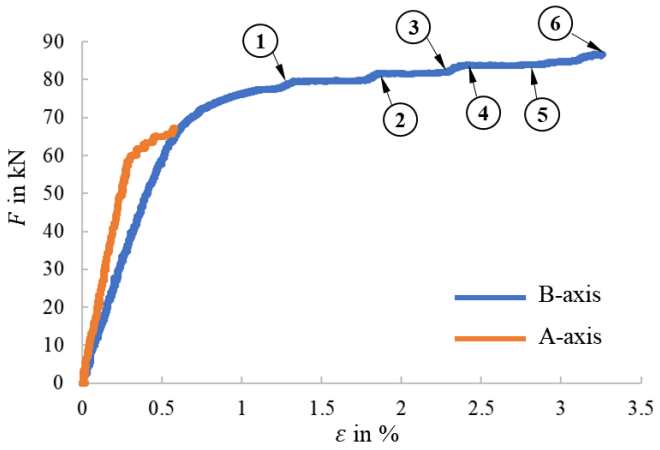

Figure 4.22 Force-strain curve for the quasi-static biaxial tensile test of specimen E1.

The DIC images corresponding to the six points marked in Figure 4.22 have been shown in Figure 4.23. Stable crack extensions during the test could be observed. However, due to the different crack-tip loading condition in comparison to the through-crack variant, huge plastic deformation took place around the surface points of the crack in the early stage of the monotonic tensile loading process. This has caused some reflections of the DIC camera light-source ahead of the surface point crack-tip (black areas particularly on the left side in Figure 4.23), which made the stable crack extension measurement inaccurate in this case.

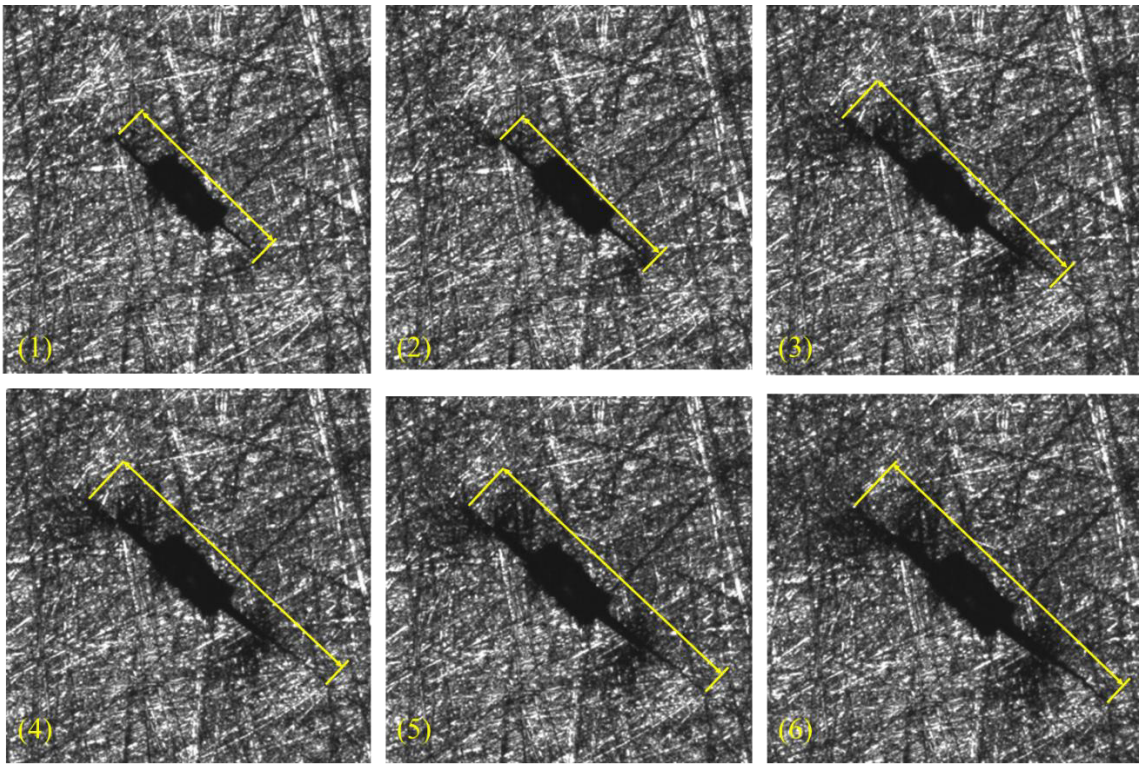

Figure 4.23 Stable crack extension measurement ($2c_{\mathrm{DIC}}$) on specimen (E1) surface based on DIC images, figure numbering corresponding to marks in Figure 4.22 [4.1].

Fractographic analysis of the fracture surface at crack plane under optical microscope was performed (Figure 4.24). The dark semi-circular surface extending from the semi-circular notch in the middle was the initial crack after pre-cracking. Stable crack extension could be observed on the fracture surface through flat smooth surface beyond initial crack, the crack-front of the final crack extension before fracture has been marked with solid red splines in Figure 4.24. Compared with the DIC image (6) in Figure 4.23 (the moment right before final fracture), the stable crack extension on the surface to the left side was longer than the measurement based on DIC image. The surface view of the fractured biaxial specimen E1 was showed in Figure 4.25 with crack plane indicated. Flat surfaces for stable crack extension could be observed. The kink at the end of each stable crack extension surface represented the starting point of the final fracture.

The fracture surface has then been examined under scanning electron microscope (SEM) and was shown in Figure 4.26. The fracture surfaces in the direction of the maximum stable crack extension were considered (compare Figure 4.24). The stable crack extension surface was shown in Figure 4.26a, with the crack-fronts highlighted in yellow. Transcrystalline fracture facettes surrounded by the dimples were also to be seen in this area. Noted that on the stable crack extension surface, the transcrystalline fracture facettes are generally in the crack plane perpendicular to the crack opening stress direction, or B-axis. The final fracture surface (Figure 4.26b) was not in the crack plane. As a result, the specimen has been tilted under the SEM in order to get good focus. Transcrystalline fracture facettes could also be observed with surrounding chains of dimples (highlighted with arrows). The number of these dimples has been larger than in Figure 4.26a, which indicated larger plastic deformation at final fracture surface. Consequently, it has been determined that the ligament of the biaxial specimen went through considerable plastic deformation during stable crack extension and final fracture.

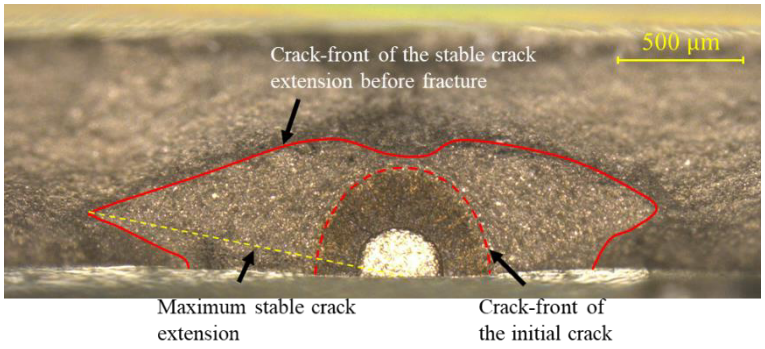

Figure 4.24 Fractographic analysis with optical microscope of the fracture surface at crack plane of the biaxial specimen E1 (lower part).

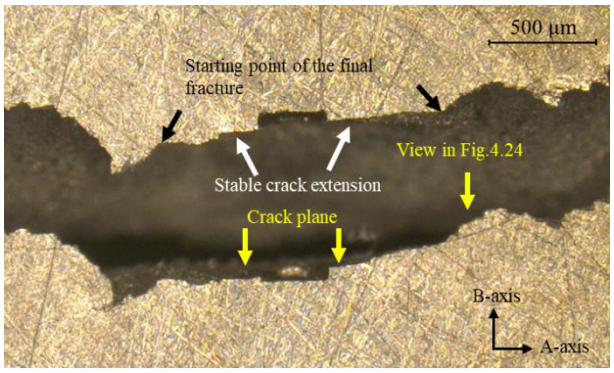

Figure 4.25 View of the specimen surface of the fractured biaxial specimen E1.

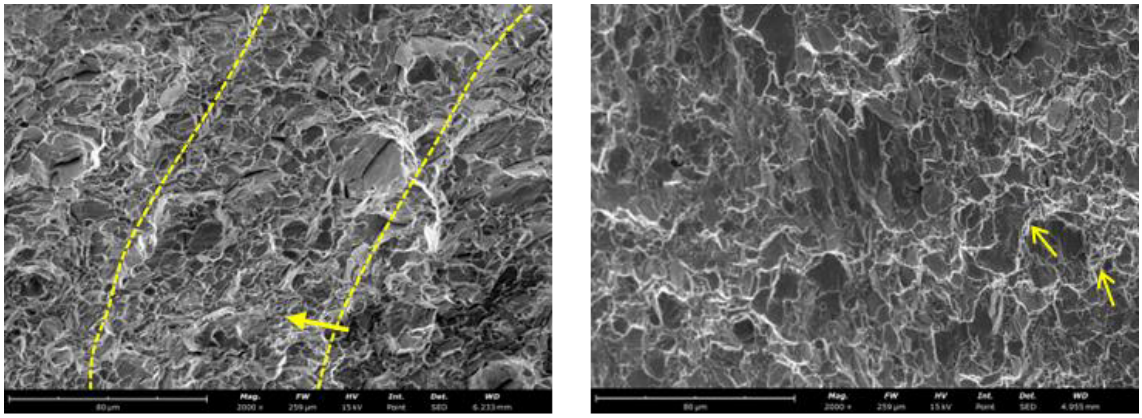

Figure 4.26 Fractographic analysis with scanning electron microscope (SEM) of the fracture surface of the biaxial specimen E1: (a) Stable crack extension surface; (b) Final fracture surface.

4.3.3. Digital Image Correlation (DIC) analysis

All biaxial quasi-static experiments have been conducted using DIC camera for crack extension measurement and optical extensometer. During the experiments, the DIC camera has been recording high-resolution images of the specimen surface with 25 Hz frequency. The advantage was that the series of images recorded could be used for digital image correlation analysis to calculate the strain field on the specimen surface. The failure mode could then be determined based on the variation of this strain field. The DIC analyse of the strain field for the test of biaxial specimen C2 with through-crack variant and for the test of biaxial specimen E1 with surface crack have been discussed in this section.

The software GOM Correlate has been used to post-process the DIC images and to calculate the strain field on the specimen surface. The von Mises equivalent strain (true) has been calculated as

$$\varepsilon'_{\mathrm{eq}} = \sqrt{\frac{2}{3}\varepsilon'^{\mathrm{dev}}_{ij}\varepsilon'^{\mathrm{dev}}_{ij}} \tag{4.5}$$

for strain field characterisation. For each biaxial specimen, the original condition image (reference state) has been used for calibration, which was the biaxial specimen on the testing machine after establishing the temperature field with no forces on both axes. The sequenced DIC images have then been loaded for strain field calculation. The facets have been defined over the testing area of the specimen excluding the ACPD probes. Global coordinates transformation was done to align the primary axes to the tensile force axes of the specimen.

DIC strain field analysis for biaxial test with through-crack variant

The von Mises equivalent strain on the surface of biaxial specimen C2 has been calculated based on the DIC images (Figure 4.27). Their corresponding positions were illustrated in a F-ε-diagram (Figure 4.28). The F-ε curve in Figure 4.28 has been identical to Figure 4.10, the only difference has been the points chosen along the curve. Points before and at the beginning of ligament yielding have been considered here for strain field analysis. The plastic deformation begins at a von Mises equivalent strain of 0.73% (marked in the legend of Figure 4.27) at 425 °C according to the material data provided by the engine manufacturer. In Figure 4.27a, the force on B-axis has been 60 kN. The von Mises equivalent strain on the ligament ahead of both crack-fronts has been around 0.6%. There was generally only elastic deformation on the ligament. In Figure 4.27b when the force on B-axis reached 70 kN, the von Mises equivalent strain on the ligament reached 0.78% with high local above 2% directly near crack-tips. With increasing loads on both axes, the von Mises equivalent strain on the ligament increased with high plastic deformation took place from the crack-tip in the crack growing directions. In Figure 4.27f, the last frame recorded before fracture, the whole ligament went through high plastic deformation with von Mises equivalent strain values beyond 2%. Based on these facts, the failure mode of the biaxial specimen C2 has been determined as plastic collapse.

DIC strain field analysis for biaxial test with surface crack variant

The von Mises equivalent strain on the surface of biaxial specimen E1 has been calculated based on the DIC images (Figure 4.29). Their corresponding positions were illustrated in a F-ε-diagram (Figure 4.30). Like in the analysis for the through-crack variant, the corresponding von Mises equivalent strain of 0.73% has been marked in the legend of Figure 4.29 to represent the beginning of plastic deformation. Figure 4.29a showed the strain field which was elastic on the ligament. The force on the B-axis has been 38 kN and the von Mises equivalent strain has been around 0.4% on the ligament. Figure 4.29b illustrated the beginning of the plastic yielding of the ligament with $F_B = 50\ \mathrm{kN}$. In Figure 4.29c the whole ligament has been plastically deformed with a von Mises equivalent strain of around 1%. High local plastic deformation could be observed ahead of the crack-tips. Figure 4.29d and Figure 4.29e illustrated the further hardening of the ligament. The plastic deformation of the ligament on the crack plane has been profound. Figure 4.29f showed the last frame DIC image before fracture. The von Mises equivalent strain on the whole ligament was generally above 3%, which indicated the failure mode of plastic collapse for the biaxial specimen E1.

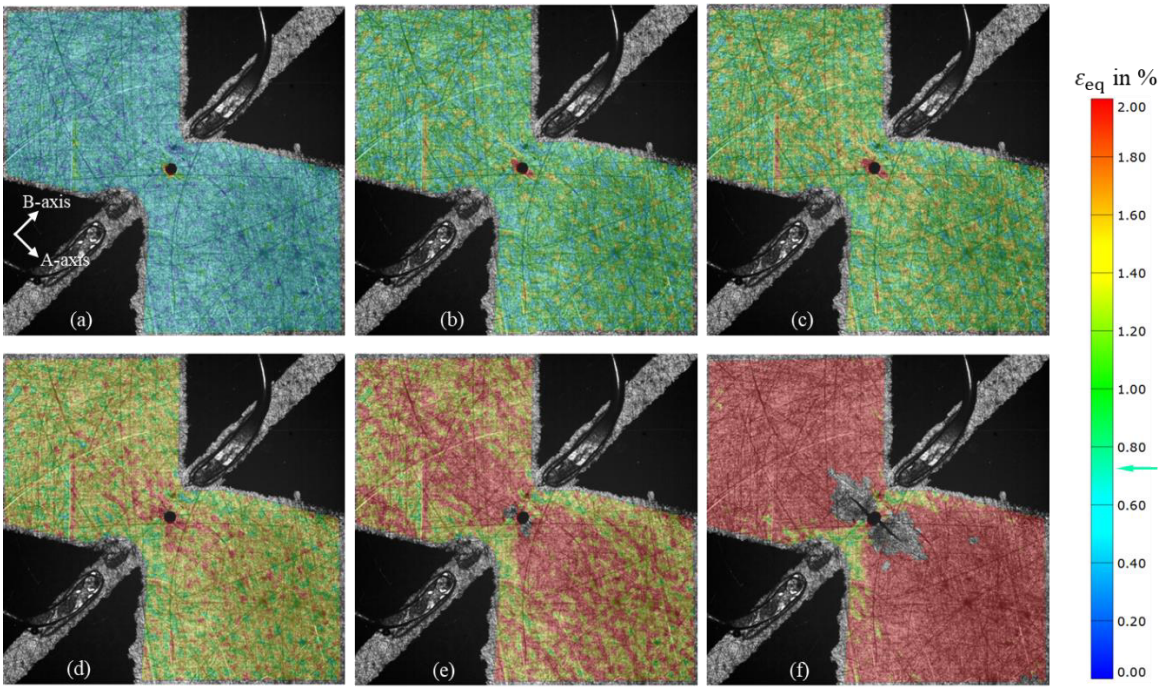

Figure 4.27 DIC analysis: von Mises equivalent strain on the surface of the biaxial specimen C2 with through-crack.

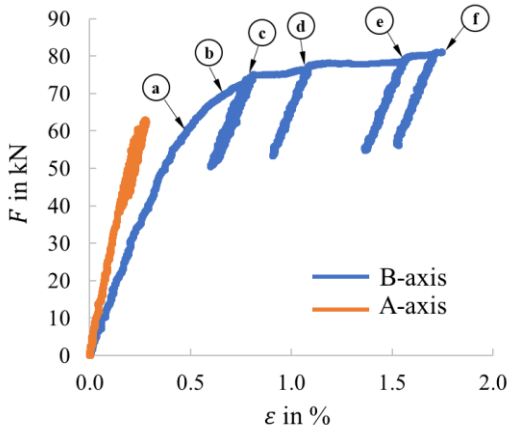

Figure 4.28 Corresponding positions of the DIC images (Figure 4.27) in F-ε-diagram.

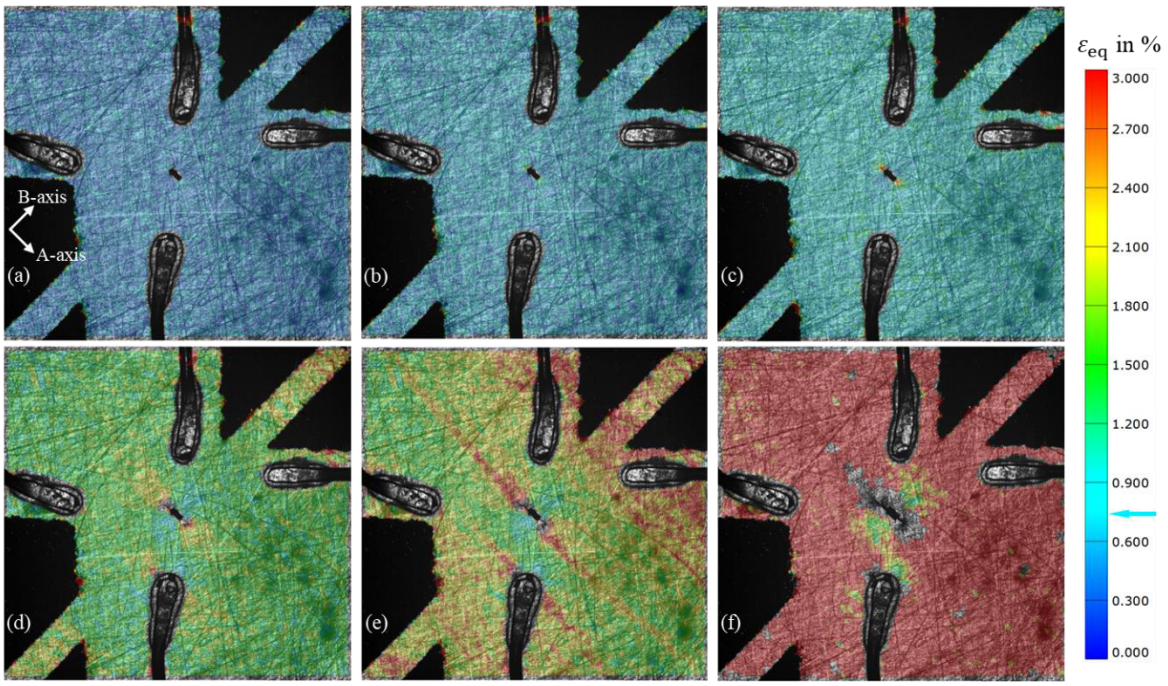

Figure 4.29 DIC analysis: von Mises equivalent strain on the surface of the biaxial specimen E1 with surface crack.

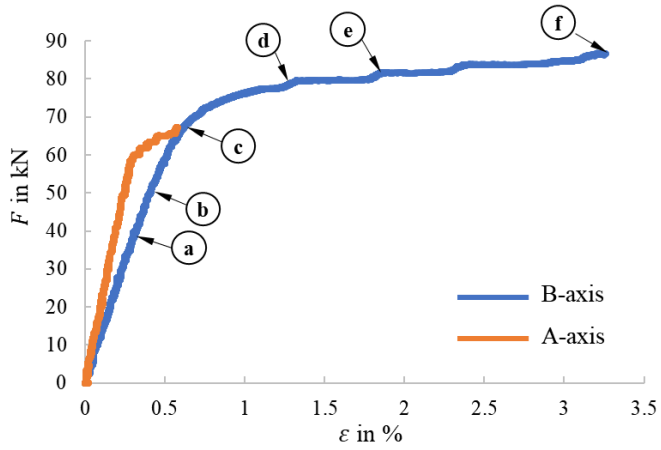

Figure 4.30 Corresponding positions of the DIC images (Figure 4.29) in F-ε-diagram.

4.4. Uniaxial fracture mechanics experiments

Uniaxial fracture mechanics experiments were carried out in order to determine the critical load and failure mode for the cracked uniaxial specimen. As discussed in section 3.4.2, the round specimen with semi-circular notch has been chosen. The semi-circular notch has been realised by means of EDM. The experiment set-up is shown in Figure 4.31. Basically, the uniaxial experiments have been conducted in a similar manner as the biaxial experiments, including following steps:

1) Uniaxial tensile pre-cracking
2) Establishment of temperature field
3) Quasi-static uniaxial tensile test

The first step of the experiment has been pre-cracking. The pre-cracking process has been conducted in room temperature under cyclic loads. The target of the pre-cracking has been to initiate a semi-circular surface crack of dimension $a_0 = c_0 = 0.381\ \mathrm{mm}$ with the crack plane in the centre of the specimen perpendicular to the loading direction. The compressive pre-cracking was carried out first. However, buckling of the specimen has been observed before crack initiation. Consequently, the pre-cracking was carried out under cyclic tensile loads with $R = 0.1$ and $F_{\max} = 28\ \mathrm{kN}$. The crack initiation was monitored using a microscope (1 in Figure 4.31a). In order to achieve better detection of crack initiation and more accurate crack length measurement, the specimen surface around the notch has been tinted with blue paint. The cyclic loading was halted after certain cyclic numbers to check the crack initiation as well as crack length on the surface. An example of the completed pre-cracking has been shown in Figure 4.32 with the initial crack seen on specimen surface.

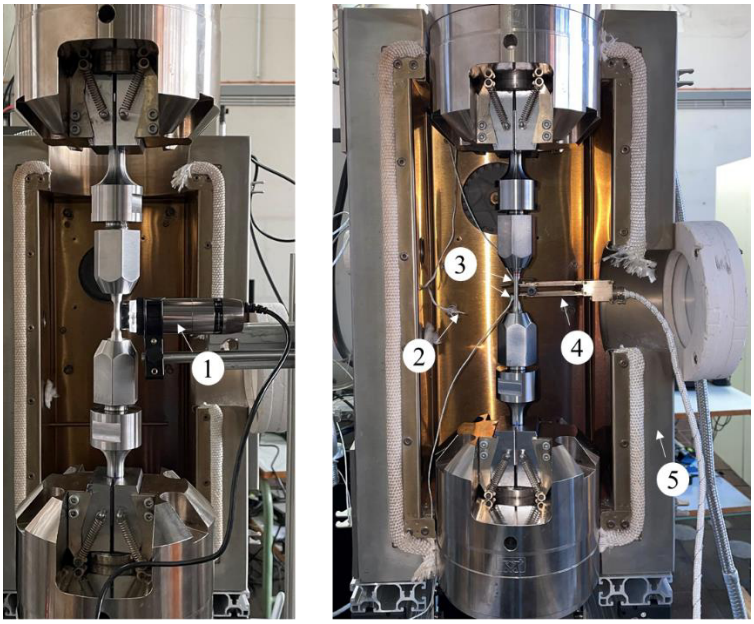

Figure 4.31 Set-up of the uniaxial experiment: (a) Crack initiation and growth monitoring during pre-cracking; (b) Target temperature establishment and quasi-static uniaxial tensile test.

After pre-cracking, the crack monitoring microscope was removed. An extensometer (4 in Figure 4.31b) and three thermal elements have been set up. For strain measurement, the extensometer was clamped onto the flat surfaces of the specimen with the notch and the crack plane in the middle of the contact points. One of the three thermal elements (2 in Figure 4.31b) has been positioned into the inner cavity of the oven (5 in Figure 4.31b) without any contact to measure the air temperature. The rest thermal elements were clamped onto the rear surface of the specimen (3 in Figure 4.31b) by the extensometer to measure the temperature on the specimen surface. The closed oven was heated up

until the surface temperature of the specimen reached 350 °C. The holding time of 40 min was carried out to ensure a homogeneous temperature of the specimen.

Subsequently, the quasi-static uniaxial tensile test was conducted with strain-controlled loads. The global strain rate has been determined according to [1.7] to be equivalent to a stress intensity factor rate of $\dot{K_{\mathrm{Ic}}} = 0.55\ \mathrm{MPa}\sqrt{\mathrm{m}}/\mathrm{s}$, which turned out to be $\dot{\varepsilon_{\mathrm{g}}} = 0.00011668/s$. The local strain in the loading direction was measured by the extensometer, with the measuring points at 5 mm above and beneath the crack plane, respectively. The test ended right after the moment when the fracture of the specimen took place.

4.4.1. Test of uniaxial specimen A1

Apart from the first uniaxial specimen which was damaged by buckling during pre-cracking, a total number of ten uniaxial specimens with semi-circular surface crack have been successfully tested. The test of biaxial specimen A1 has been discussed in detail, whereas the data for the rest of the tests are located in appendix.

The uniaxial specimen A1 was firstly subjected to uniaxial tensile pre-cracking in room temperature. As discussed, the tensile cyclic loads for the pre-cracking applied on axial direction of the specimen have been in sinus form with $R = 0.1$ and $F_{\mathrm{max}} = 28\ \mathrm{kN}$ at $f = 15\ \mathrm{Hz}$. The pre-cracking process was paused after 30 000, 50 000, 52 000 and 54 000 cycles to check crack initiation and extension. Eventually, a total number of 56 000 cycles has accumulated during the pre-cracking process and the initial crack length at specimen surface was 0.78 mm as determined by the microscope mounted on the testing machine (Figure 4.32). Because of the uncertainties in the crack growth measurement on-site using the microscope, the exact initial crack length can only be measured after the experiment when the fracture surface is available.

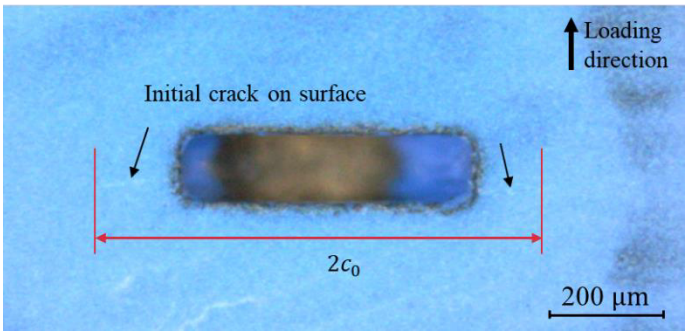

Figure 4.32 Initial crack of size $2c_0 = 0.78\ \mathrm{mm}$ for uniaxial specimen A1 after 56 000 cycles.

After the pre-cracking, the microscope has been removed and the extensometer has been clamped onto the uniaxial specimen. The electric oven was mounted to the testing machine with the thermal elements set in place. The specimen has been heated up to the pre-determined 350 °C and held with this temperature for 40 min (Figure 4.33). Subsequently, the quasi-static uniaxial tensile test began. The test has been conducted in a global strain-controlled manner with $\dot{\varepsilon_{\mathrm{g}}} = 0.00011668/s$. The global strain was determined as the displacement of the cylinder divided by the length of the testing area of the specimen. The loading history in terms of global strain of the test A1 has been illustrated in Figure

4.34. Serrated yielding effect has been observed as the global strain went beyond 6.47%, which were shown in Figure 4.34 in form of a series of seven spikes in the loading history. Each time at the occurrence of the serrated yielding where the global strain erratically increased, the testing machine controller has regulated down the tensile force so that the global strain would get back to the pre-determined slope and then further increased the load. The test was ended when the fracture of the specimen took place with a global strain of 15.73% and a tensile force of 52.51 kN.

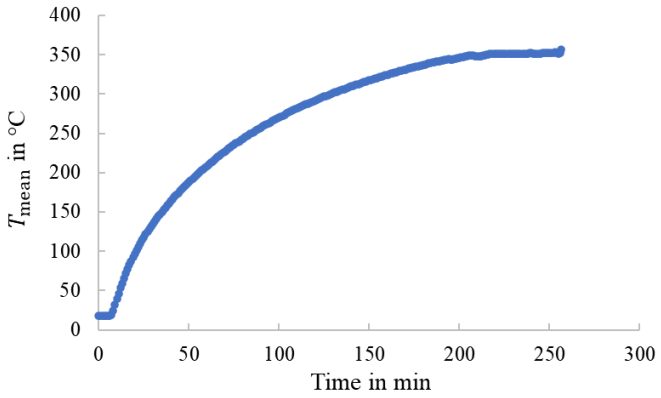

Figure 4.33 Mean temperature on the uniaxial specimen A1 surface during temperature establishment process.

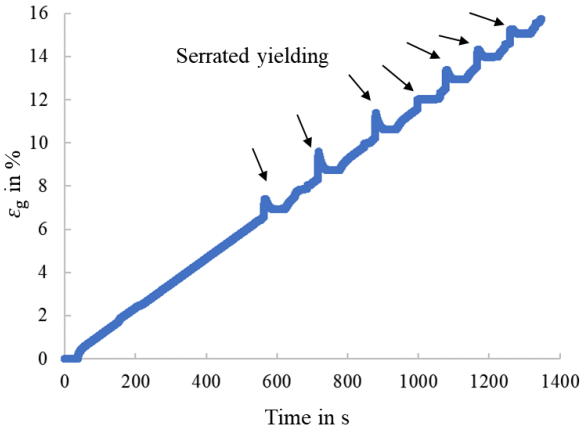

Figure 4.34 Loading history (global strain) for the quasi-static uniaxial tensile test of specimen A1.

The force-strain curve of the quasi-static tensile test is shown in Figure 4.35 with the local strain measured by the extensometer. The yielding started when the tensile force reached about 39 kN. The first serrated yielding took place when the local strain reached 1.074%. This was in alignment with the critical strain (1.187%) to reach first serration for nickel-base superalloy reported by Huron [4.3]. The test reported in [4.3] has been conducted with superalloy Rene'88DT at 399 °C with a strain rate of 0.0001/s. As explained before, the testing machine controller (for test of specimen A1) has regulated down the tensile force immediately after the serrated yielding took place, which caused the elastic

strain to be relaxed. The reloading process hereafter could be used to determine if stable crack extension had occurred based on the slope of the elastic reloading process in the force-local strain curve and therefore the stiffness of the specimen (Figure 4.36). The initial elastic loading and the seven reloading processes have been identified in Figure 4.35. Due to the limited duration of the reloading process Reload_4, it has been excluded from the slope calculation. The elastic part of the initial loading and each reloading process has been considered and a linear fit-curve has been generated based on the points from the selected force-local strain curve. Then from both ends of the selected points, the number of the points has been reduced until the slope of the linear fit-curve did not change. This linear fit-curve along with its slope has been noted for each reloading process (Figure 4.36).

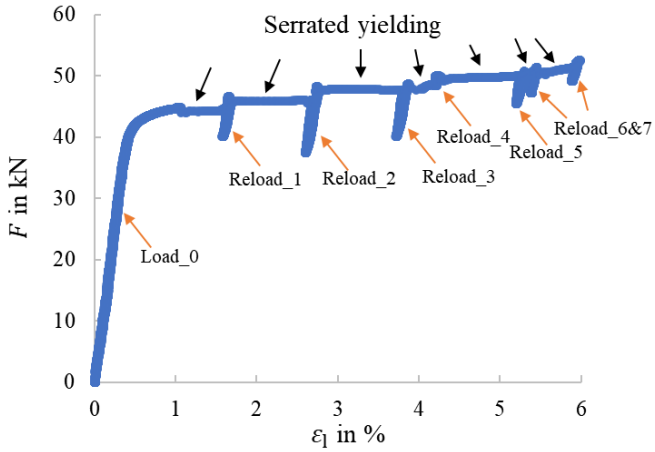

Figure 4.35 Force-local strain curve for the quasi-static uniaxial tensile test of specimen A1.

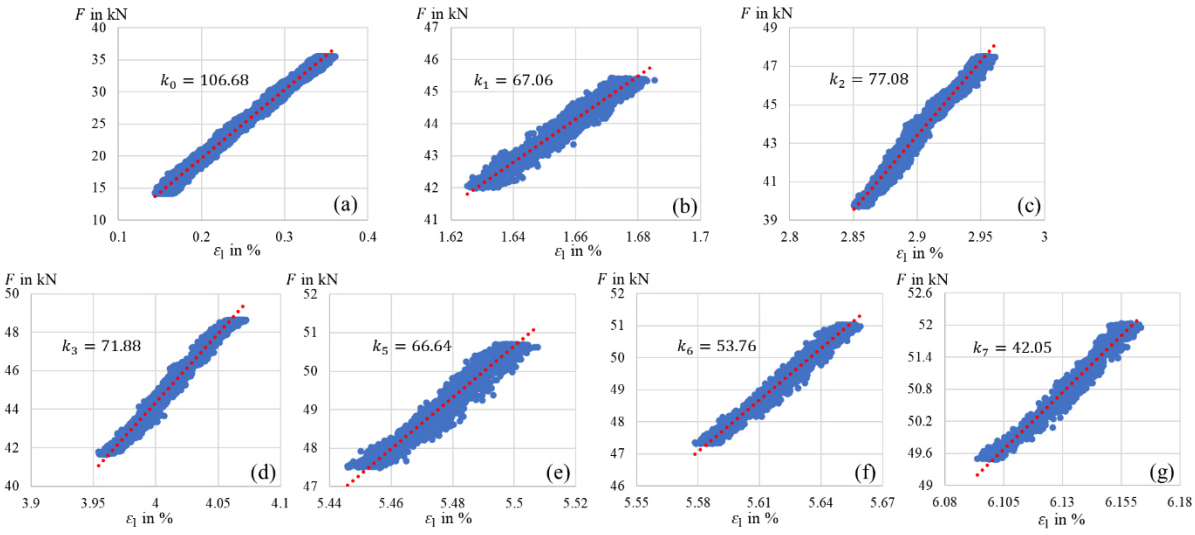

Figure 4.36 Determination of slopes of the elastic loading and reloading process in the quasi-static uniaxial tensile test of specimen A1: (a) Load_0; (b) Reload_1; (c) Reload_2; (d) Reload_3; (e) Reload_5; (f) Reload_6; (g) Reload_7.

The result of the reloading slope has shown that all slopes of the reloading processes were lower than the initial elastic loading process. Starting from Reload_2, the reloading slope decreased constantly through the test. Therefore, the stiffness of the specimen was decreasing through the test, which

confirmed the occurrence of the stable crack extension. As a result, combined phenomena of serrated yielding and stable crack extension were confirmed through the test.

Fractographic analyses were carried out for the fractured specimen after the test. The fracture surface has been shown in Figure 4.37. The initial crack was in semi-circular shape with $2c_0 = 0.774\,\mathrm{mm}$. Unlike the biaxial specimen, the stable crack extension was not entirely in the crack-plane. The stable crack extension has been primarily in the crack-plane in trapeze shape, whereas from both surface points of the initial crack, the crack extended in two secondary planes (Figure 4.38) but only to a limited extent. The correlation between the test data discussed above and the information gained from the fracture surface was difficult since the crack depth and shape during each reloading process could not be determined. It has been attempted to generate a R-curve based on the reloading slopes and the estimated crack depth. However, since the specimen has been non-standard shape and due to the irregular shape of the stable crack extension, the results were unrealistic and therefore not considered.

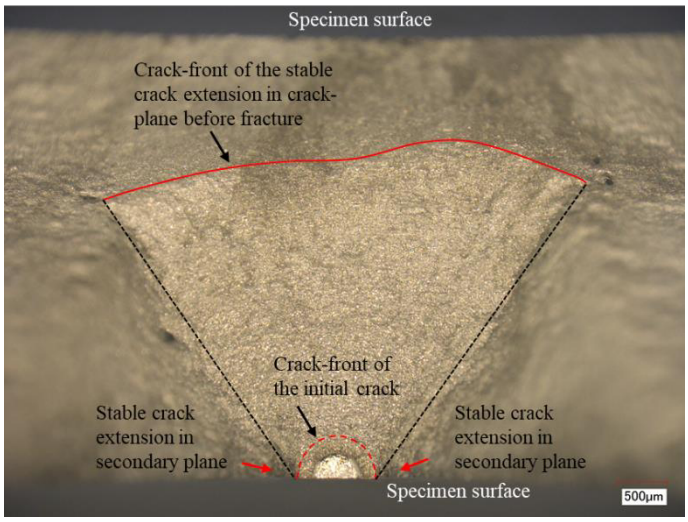

Figure 4.37 Fractographic analysis with optical microscope of the fracture surface at crack plane of the uniaxial specimen A1 (lower part).

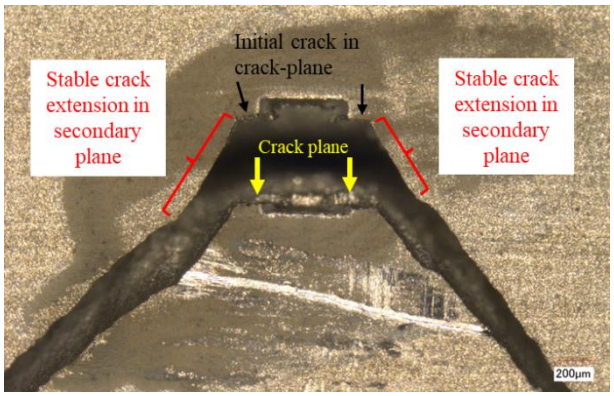

Figure 4.38 View of the specimen surface of the fractured uniaxial specimen A1.

The fracture surface has then been examined under scanning electron microscope (SEM) and was shown in Figure 4.39. Three locations on the fracture surface were chosen for comparison, namely

location a (Figure 4.39a) on the stable crack extension surface, location b (Figure 4.39b) on the final fracture surface behind the stable crack extension surface and location c (Figure 4.39c) on the final fracture surface at secondary plane. At location a, transcrystalline fracture facettes were generally facing at the same direction, namely perpendicular to the crack extension direction. The crack-fronts of the stable crack extension as well as the extension direction were marked in yellow dotted lines and arrow in Figure 4.39a. At location b, the fracture facettes were oriented randomly surrounded by a great number of dimples which was in accordance with final fracture. The specimen has been tilted under the SEM in order to get good focus at location c, where the fracture surface looked similar to the fracture surface at location b. It was therefore determined that the most area on the secondary plane has been the final fracture surface.

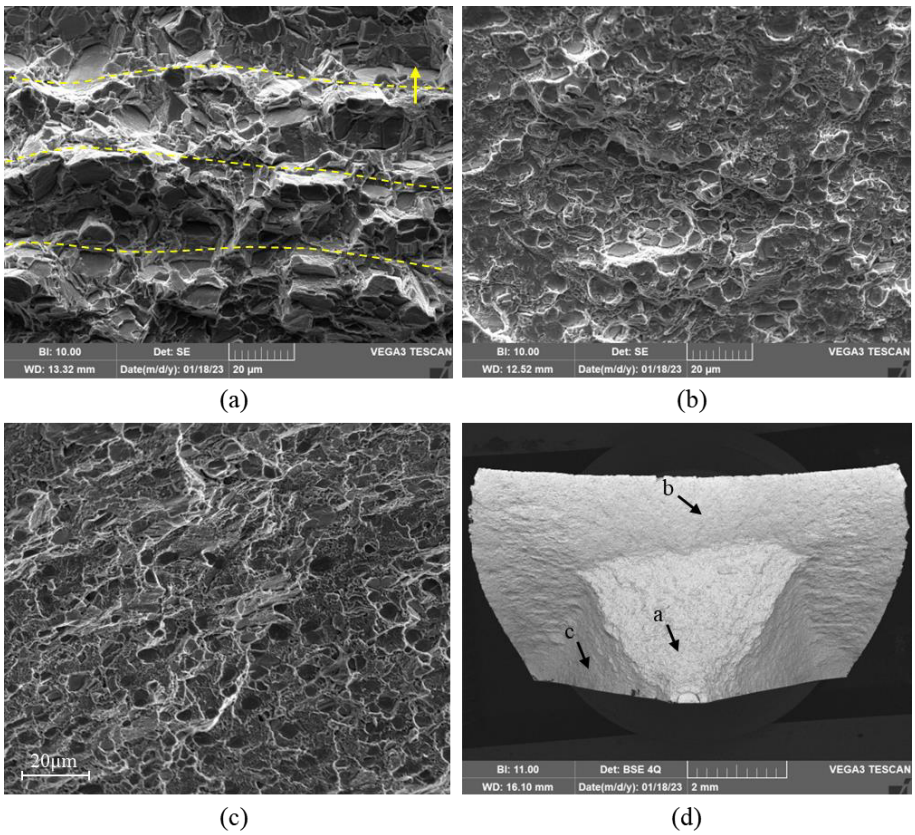

Figure 4.39 Fractographic analysis with scanning electron microscope (SEM) of the fracture surface of the uniaxial specimen A1: (a) Stable crack extension surface; (b) Final fracture surface; (c) Final fracture surface on secondary plane; (d) Global view of the fracture surface.

There were two types of specimen geometries after the fracture that were shown in Figure 4.40. The first type was a symmetric specimen geometry with respect to the notch (Figure 4.40a, Figure 4.40b), while the other was asymmetric (Figure 4.40c, Figure 4.40d). Of the twelve specimens tested (including two specimens for R-curve determination), five were of symmetric fracture type and seven were of asymmetric fracture type. The crack extension direction on the specimen surface has been around 60° with respect to the crack plane (horizontal plane) for all tested specimens, while in some cases symmetric secondary cracks were observed (Figure 4.41a). This has been in accordance with the

maximum crack opening stress direction, or in this case the axial stress direction. FE simulation of the specimen B2 (half model) with initial crack and secondary crack under the maximum load recorded in the test has shown the maximum axial stress originated from the initial crack had a direction of +/- 57° to the horizontal plane (Figure 4.41b), which has been in agreement with the test results. Also as observed in Figure 4.37, the crack extended within the crack plane in the thickness direction of the specimen. This has also been in agreement with the highest axial stress direction ahead of the crack-front at the deepest point along the crack-front in the plane perpendicular to the crack plane (Figure 4.41c).

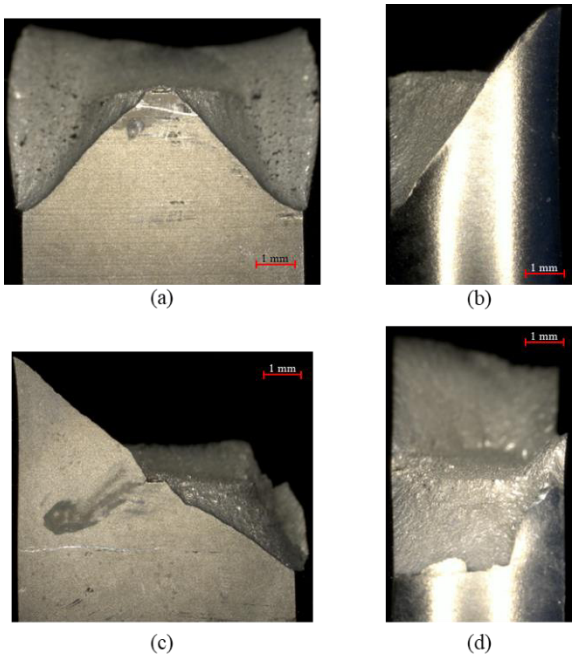

Figure 4.40 Geometries of the uniaxial specimen after fracture: (a) symmetric fracture form viewed from the surface with notch; (b) view from the right of (a); (c) asymmetric fracture form viewed from the surface with notch; (d) view from the right of (c).

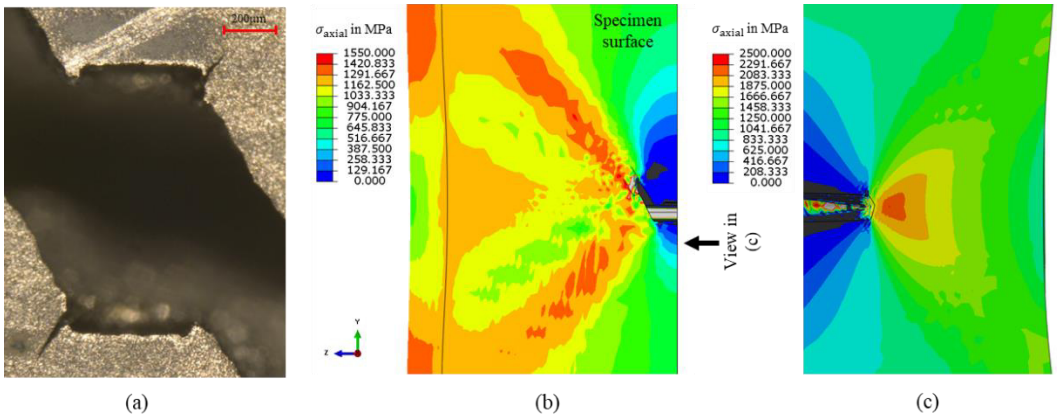

Figure 4.41 Crack extension direction on specimen surface: (a) fractured specimen surface with notch and secondary cracks of uniaxial specimen B2; (b) axial stress distribution on the cracked specimen (B2) surface; (c) axial stress distribution ahead of the crack-front at the deepest position along the crack-front, perpendicular to the crack plane.

4.4.2. Determination of R-curve for uniaxial specimen

Since the R-curve could not be determined based on the reloading slopes, two uniaxial specimens (C2 and C3) have been specifically tested to acquire the R-curve for the considered surface crack on the uniaxial specimen. In contrast to the uniaxial tensile test discussed before, the R-curve determination tests have been conducted in the following steps:

1) Uniaxial tensile pre-cracking
2) Establishment of temperature field
3) Quasi-static uniaxial tension (global strain-controlled) until F_0
4) Cyclic loading
5) Quasi-static uniaxial tension (global strain-controlled) until $F_0 + \Delta F$

The step 3) to step 5) were conducted repeatedly until the fracture of the specimen took place. The idea was to load the specimen to different tensile force level and the make use of cyclic loading to mark the crack-front at the last load level.

The pre-cracking has been conducted for both specimens using the cyclic loading parameters discussed in section 4.4.1, with totally 50 000 cycles for specimen C2 and 53 000 cycles for specimen C3. The initial crack sizes were comparable to the design value, with $a_0 = 0.373\ \mathrm{mm}$ and $c_0 = 0.378\ \mathrm{mm}$ (average) for specimen C2 as well as $a_0 = 0.354\ \mathrm{mm}$ and $c_0 = 0.340\ \mathrm{mm}$ (average) for specimen C3. For the test with uniaxial specimen C2, the load levels reached have been 49.2 kN, 50 kN, 51 kN and 52 kN. The fracture took place at the next increment with a tensile force of 52.93 kN. Between each load level, cyclic loading with $R = 0.1$ and $F_{\max} = 25\ \mathrm{kN}$ has been applied for 10 000 cycles. For the test with specimen C3, the load levels have been from 49 kN until 52.5 kN with 0.5 kN load increase between each level. The cyclic loading has remained the same with the previous test but only 5000 cycles after each load level. The fracture of the specimen C3 took place at a tensile force of 52.91 kN.

The fracture surfaces of both specimens have been shown in Figure 4.42. Although a series of load levels with cyclic loadings in between have been conducted, only two fatigue crack growth “rings” could be clearly identified. As a result, only the first two load levels in both tests have been analysed for R-curve determination. For specimen C2, the crack depths (measured at the deepest point along the crack-front as shown in Figure 4.42a) after stable crack extension with their corresponding loads were 0.505 mm at 49.2 kN and 0.923 at 50 kN, while for specimen C3 the results were 0.442 mm at 49 kN and 0.594 mm at 49.5 kN.

As done for the biaxial specimen R-curve, the FE simulations were carried out to determine the crack driving force in terms of J-integral for each crack depth. The simplified FE model (quarter-model) has been used. The crack has been modelled in the initial crack plane without the secondary plane (shear lips from specimen surface). The modelled crack has the parameters a as the measured crack depth and c as the crack length measured on the surface in the secondary plane (Figure 4.42c). As a result, the crack modelled has more area than the projected crack area measured from the real fracture surface on the crack plane, which has been conservative.

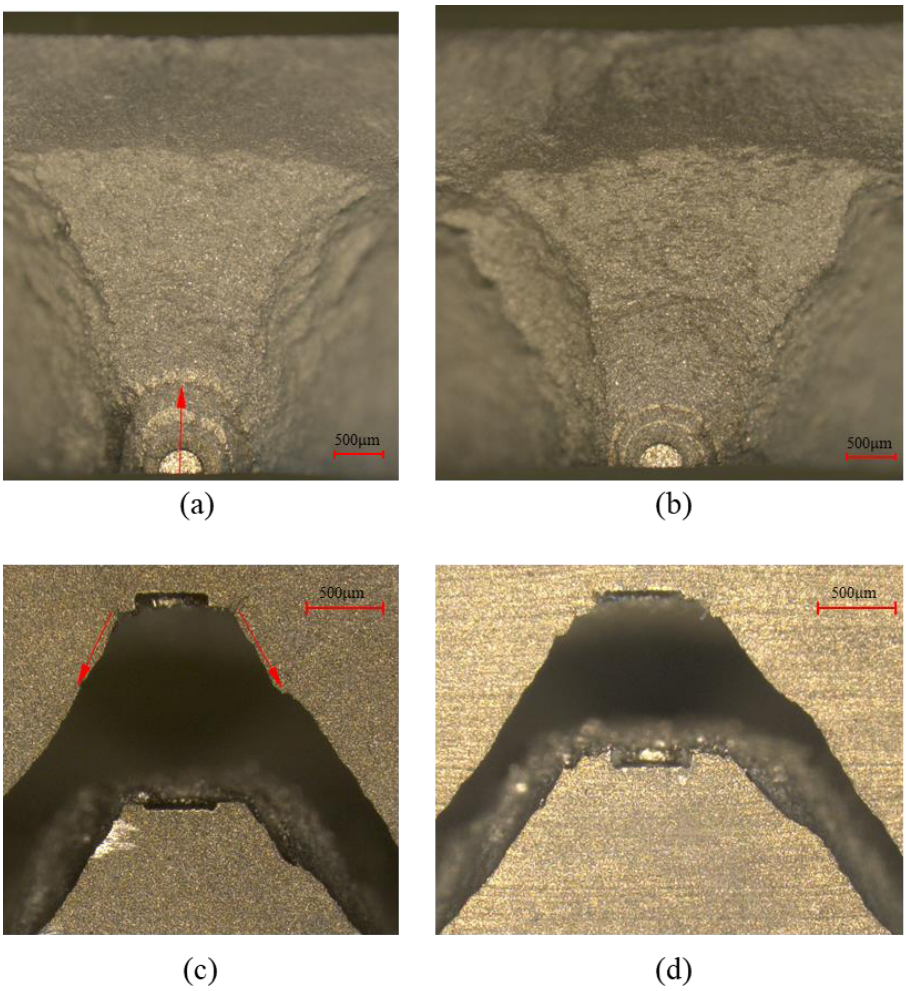

Figure 4.42 Fracture surface of uniaxial specimen C2 and C3 with marked crack-fronts: (a) Specimen C2 with crack-fronts marked after 49.2 kN and 50 kN; (b) Specimen C3 with crack-fronts marked after 49 kN and 49.5 kN; (c) Crack on specimen surface C2; (d) Crack on crack on specimen surface C3.

The J-integral values have been determined at the deepest point along the crack-front from FE simulation results for the four crack geometries measured from the fracture surfaces. The results were presented in Figure 4.43 with the comparison of the biaxial R-curve discussed in section 4.3.1. Analogue to the biaxial R-curve, a fit-curve has been generated as the uniaxial R-curve, which had an analytical expression of

$$J = 121.2 \cdot \Delta a^{0.64} \tag{4.6}$$

with J in N/mm and Δa in mm. Note that the uniaxial R-curve lies above the biaxial R-curve, this was because the constraint ahead of the critical location along the crack-front of the uniaxial specimen has been lower than that of the biaxial specimen (compare Figure 3.27, Figure 3.33), which effectively increased the fracture toughness with the same material.

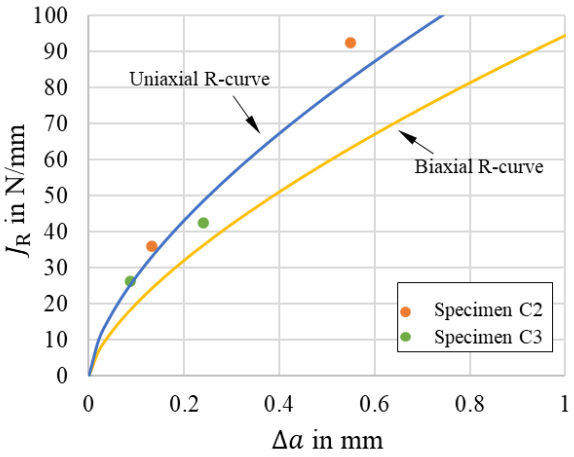

Figure 4.43 Determination of R-curve for uniaxial specimen with surface crack, biaxial R-curve shown for comparison.

4.5. Spin-tests of turbine disk

For certification and design validation purpose, spin-tests of production-similar turbine disks have been conducted by the engine manufacturer. The experimental proof against the hoop burst failure mode (bore) as well as the rim peel failure mode (diaphragm) has been conducted using production-similar disks of older engine models, by which the loading conditions were considered similar to the turbine disk investigated in this work. Both disks used in the spin-tests were of the same material (Udimet 720 Li) and production process as the turbine disk investigated in this work.

4.5.1. Rim peel test

This rig test has been set up for the rim peel proof of the investigated turbine disk (Figure 4.44), which has made use of a high-pressure turbine disk of a similar engine model produced by the engine manufacturer. The test disk (Figure 4.44) was designed with a thin diaphragm thickness so that it was primarily prone to rim peel failure mode. The test disk has been bolted to a backing disk, which was connected to an electric motor that drove the whole assembly. The test has been conducted with temperature gradient which compensated for the thermal stress at diaphragm at worst overspeed condition. The temperature at the critical position at diaphragm (Pos. 1 in Figure 4.44) was 650 °C through the test. A total of three increments with increasing rotational speeds have been conducted, with the third increment reaching a rotational speed of $0.703N_a$ [4.4]. Inspections were conducted between each increment in order to detect potential cracks. The inspections after the first two increments revealed no crack on the test disk, while the inspection after the third increment confirmed multiple fine cracks visible along the circumference of the test disc at Pos.1 in Figure 4.44 [4.5]. However, the test disk has not failed or fractured after the third increment.

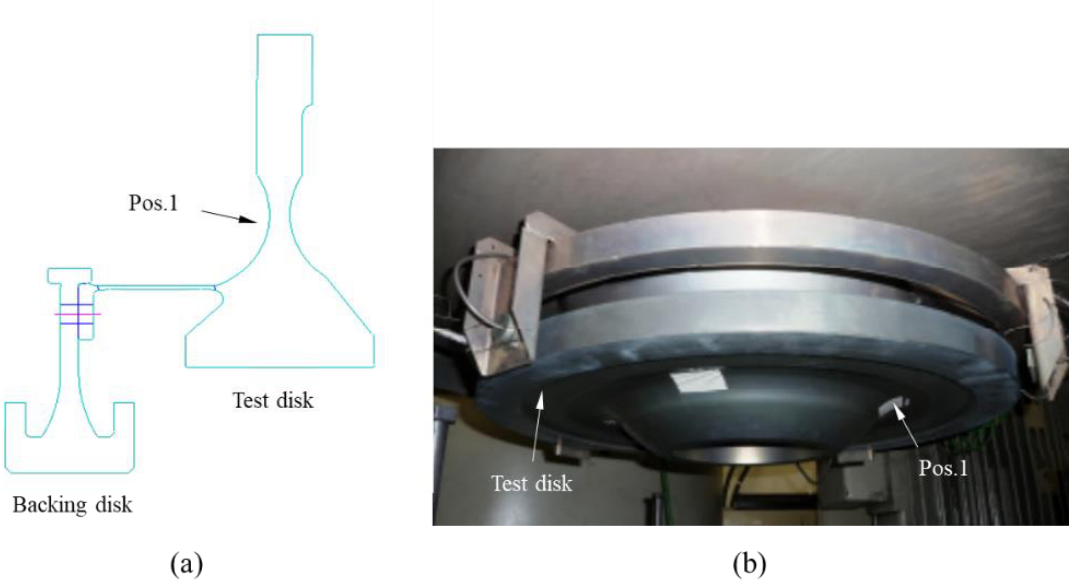

Figure 4.44 Test-rig setup of the rim peel test, test disk analysed for rim peel proof of the investigated turbine disk in this work: (a) schematic view of the test rig; (b) test assembly mounted in the Test Facility (modified from [4.4]).

Stress analyses have been conducted for the test disk after the rim peel test. The FE model of the test disk has been run with elastic-plastic material properties and the radial stress distribution on the test disk has been shown in Figure 4.45. The highest radial stress took place at the thinnest diaphragm thickness position as expected in Pos. 1 in Figure 4.44. Since the thinnest diaphragm thickness position was designed to recreate the worst loading conditions for failure mode rim peel and the radial stress has been inhomogeneous through thickness, the mean radial stress through thickness (shown as black strip in Figure 4.45) has been calculated as the determining value. The time plot of the mean radial stress and stress ratio $\lambda = \sigma_{\mathrm{hoop}}/\sigma_{\mathrm{rad}}$ has been illustrated in Figure 4.46. The stress ratio has maintained the value around 0.6 throughout the test and took the value of 0.587 at the beginning of the third increment with the maximum rotational speed. This has been considered comparable with the stress ratio at overspeed condition ($\lambda = 0.601$) at investigated disk diaphragm. Stress relaxation due to creep strain during the five-minute dwell period has been observed. As a result, the highest mean radial stress value corresponding to the maximum rotational speed at the beginning of the increment, $1.293\sigma_{\mathrm{Y}}$, has been considered as the “safe” plastic collapse limit, though the test disk formally not failed.

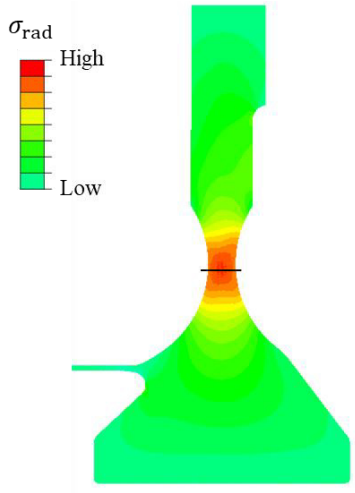

Figure 4.45 Radial stress distribution on the test disk in the rim peel test at the maximum rotational speed tested ($0.703N_a$ in the third increment) [4.5].

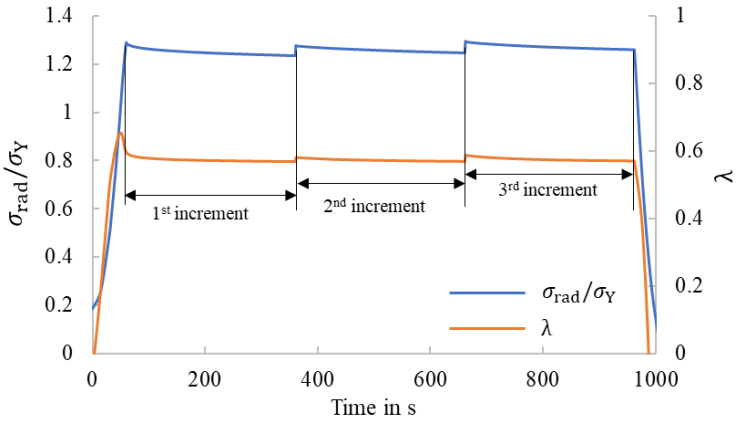

Figure 4.46 Time plot of mean radial stress (elastic-plastic) and stress ratio at diaphragm critical location through the rim peel test [4.5].

4.5.2. Hoop burst test

This rig test has been set up for the hoop burst proof of the investigated turbine disk (Figure 4.47). However, it re-used hardware already tested about 20 years ago for the development of the high-pressure turbine disks of an older engine model [4.6] based on the fact that the stage 1 bore geometry and loading conditions were similar to the turbine disk considered in this work. The test-rig comprised two turbine disks (stage 1 and stage 2), an adaptor disk and a drive-arm. The drive-arm was connected to an electric motor that drove the whole assembly. For a conservative transferability and value read-across for the investigated turbine disk, an additional increment with higher loads has been conducted on the test-rig.

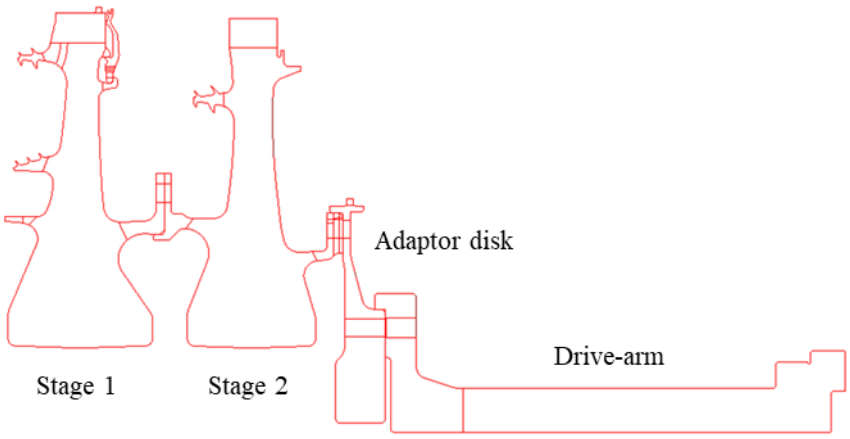

Figure 4.47 Test-rig setup of the hoop burst test, stage 1 disk analysed for hoop burst proof of the investigated turbine disk in this work (modified from [4.6]).

The rig-test was run isothermally at 590 °C. The last load increment was conducted at a rotational speed of $0.971N_{\mathrm{a}}$. The test-rig failed because of imbalance as the next load increment started. However, the stage 1 disk remained intact and showed no sign of hoop burst damage.

The maximum rotational speed $0.971N_{\mathrm{a}}$ recorded in the spin-test could not be directly used as the critical or limit rotational speed for the investigated turbine disk in the component level. Consequently, the stress values of the stage 1 disk corresponding to the maximum rotational speed tested have been calculated using FE simulations and have been considered as the critical load for the investigated disk. The critical rotational speed for hoop burst mode of the investigated turbine disk was determined based on these stress values. In the FE model, all parasitic masses (blades etc.) with the exception of a rear cover plate have been modelled as external forces and are therefore not shown as physical domains (Figure 4.47). The Area Weighted Mean Hoop Stress (elastic) has been calculated in the red marked areas of stage 1 disk (Figure 4.48). The hoop stress distributions of the stage 1 disk have been shown in Figure 4.49, with elastic and elastic-plastic simulations (same analysis only with different material properties), respectively. The hoop stress versus rotational speed curves of the stage 1 disk have been shown in Figure 4.50. The elastic AWMHS could be considered as a good representation of primary stresses in a disc under high speed. This has been demonstrated by doing the same analysis considering elastic-plastic material behaviour (Figure 4.49b). The elastic-plastic AWMHS obtained was $1.063\sigma_{\mathrm{Y}}$. The difference between elastic and elastic-plastic values has been in the order of stress prediction precision. This coincidence showed that the plastic deformation redistributed the originally non-uniform stresses towards a more uniform stress. The reason was the flat stress-strain curve. The strain compatibility was not a big obstacle, the mean stress behaved nearly statically independent and has been in equilibrium with the external centrifugal loads. As there was no thermal gradient on the rig-test, there has been negligible thermal strain. The elastic stress nonuniformity was mainly based on the different amount of centrifugal force carried (this has been noticeable in the outer diaphragm only) and based on the shape of the disc with different stiffness distribution.

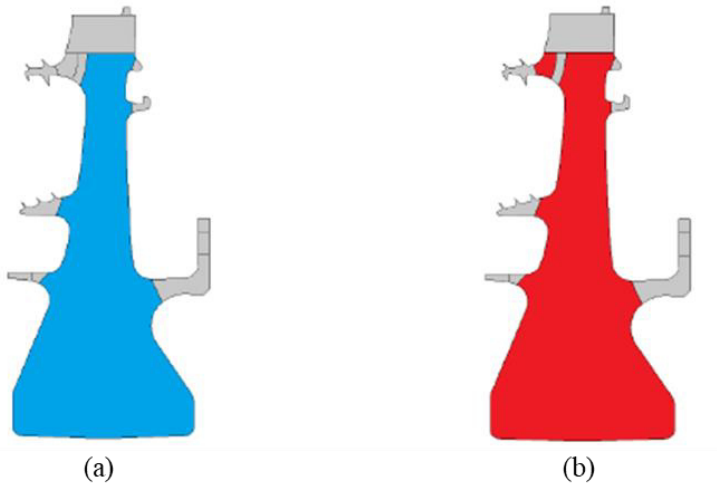

Figure 4.48 Domains on stage 1 of hoop burst rig-test disk FE model (hoop carrying section): (a) domains only considering disk body below airhole, $\mathrm{AWMHS} = 1.074\sigma_{\mathrm{Y}}$; (b) domains considering disk body above airhole, $\mathrm{AWMHS} = 1.070\sigma_{\mathrm{Y}}$ [4.7].

Plastic collapse occurred in a simplified view, when by further speed increase the whole cross section deformed more and more plastically, until instability, e.g., by spin softening effect. The last point was, however, not properly modelled in this simulation.

The total hoop strain has been accordingly quite nonuniform in the elastic-plastic simulation (Figure 4.49c), the high stressed area would first reach a stage where a crack might be extended, or a new crack has been initiated by ductile damage (not modelled in this simulation). Consequently, the highest value $1.070\sigma_{\mathrm{Y}}$, though formally not failed, could be used as the “safe” plastic collapse limit.

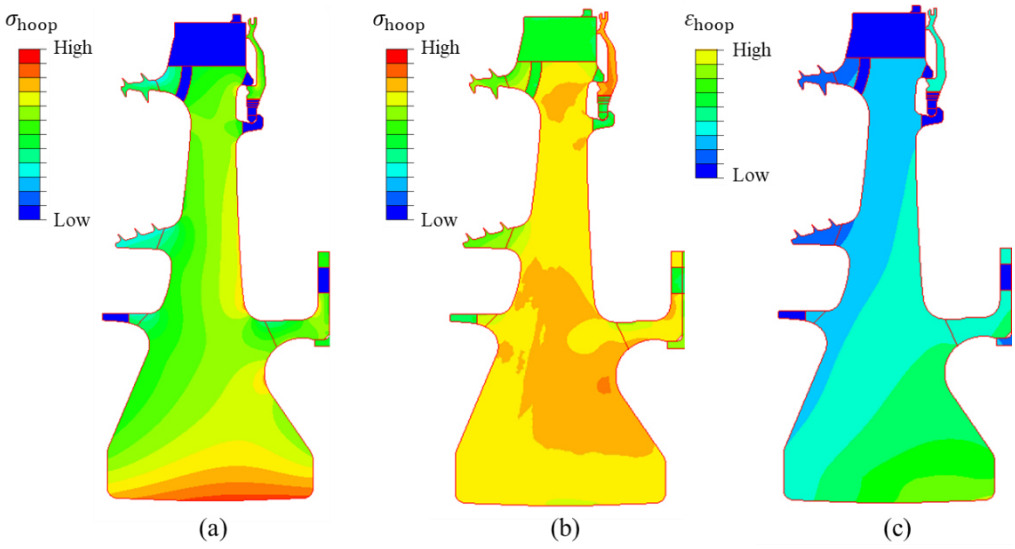

Figure 4.49 Hoop stress and total hoop strain (elastic-plastic) distribution on stage 1 disk of the hoop burst rig-test at maximum rotational speed $0.971N_{\mathrm{a}}$ (same legend scale for both stress distributions): (a) FE simulation using elastic material properties, $\mathrm{AWMHS} = 1.070\sigma_{\mathrm{Y}}$; (b) FE simulation using elastic-plastic material properties, $\mathrm{AWMHS} = 1.063\sigma_{\mathrm{Y}}$; (c) FE simulation using elastic-plastic material properties [4.7].

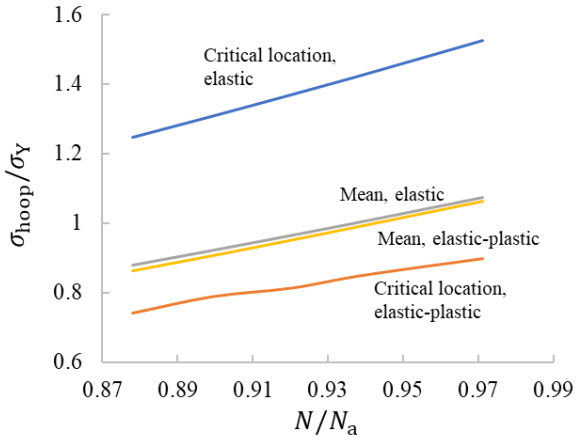

Figure 4.50 Hoop stress values versus rotational speed of stage 1 disk of the hoop burst rig-test [4.7].

5. Analysis of the representative specimens

5.1. Introduction

The structural integrity analysis of the biaxial and the uniaxial specimens have been established and discussed in this chapter.

Considering the stable crack extension in all tests (excluding the two pre-test of the biaxial specimens), the analytical failure assessment procedure has been established as following: the first step has been to determine the crack geometric parameters based on the test results for representative FE simulations. Then, FE simulations have been carried out to determine the crack-tip loading parameters in terms of J-integral as well as stress values. Based on these results, the two-criteria failure assessment method has been conducted. Critical loads for the failure mode plastic collapse were determined for various crack length. Besides, the load versus stable crack extension curves were determined to identify the limit loads for stable crack extension. The critical load with its corresponding failure mode has been determined according to the two-criteria failure assessment method.

The predicted results in terms of failure mode and load for the specimens have been compared with the test results. The maximum ligament yielding parameter $L_{\mathrm{r}}^{\max}$ has been obtained based on the test results ($L_{\mathrm{r}}^{\max}{}_{\mathrm{test}}$).

5.2. Analytical failure assessment for the biaxial specimens with through-crack

The analytical failure assessment based on the established assessment procedure has been conducted for the biaxial specimens with through-crack and has been discussed in this section. The test results for the biaxial specimens with through-crack has been given in Table 5.1 with the failure load as the force on B-axis recorded at final fracture, the failure mode determined based on DIC strain field analysis, the initial crack length a_0 and the maximum stable crack extension length a_{fin}. Both a_0 and a_{fin} have been determined according to Eq. (4.1).

Table 5.1 Test results for biaxial specimens with through-crack

	Test-Nr.	Specimen designation	Failure load (test) in kN	a_0 in µm	a_{fin} in µm	Failure mode (Test)
Pre-test (biaxial) with through-crack	BV1	A1	76.5	480	480	Plastic collapse
	BV2	A2	76.8	552	552	Plastic collapse
Test (biaxial) with through-crack	BV3	D1	84.8	268	1036	Plastic collapse
	BV4	B1	81.1	350	566	Plastic collapse
	BV5	C2	81.1	325	964	Plastic collapse
	BV6	C1	83.2	303	450	Plastic collapse

As described, the FE models have been prepared to determine the crack-tip loading parameters and stress values. The simplified FE model for the biaxial specimen for R-curve determination (Figure 4.17) has been used. It has been assumed that the crack-front is of straight-line form. Different equivalent crack depths a_{eq} have been chosen and modelled.

5.2.1. Determination of limit load for failure mode plastic collapse

According to the definition of the ligament yielding parameter (Eq. (2.1)), the applied load could be written as

$$\sigma_{\mathrm{app}} = L_{\mathrm{r}} \cdot \sigma_0 \tag{5.1}$$

where σ_0 denotes the reference yield stress. While the failure mode plastic collapse has been characterised as the failure scenario at which $L_{\mathrm{r}} = L_{\mathrm{r}}^{\max}$, the limit load for plastic collapse could be calculated as

$$\sigma_{\mathrm{plc}} = L_{\mathrm{r}}^{\max} \cdot \sigma_0. \tag{5.2}$$

In order to determine the limit loads for plastic collapse, it is necessary to generate a solution for the reference yield stress σ_0 for each equivalent crack depths a_{eq}. As introduced in section 1.4.3, taking into account the critical points along the crack-fronts, there are two ways to calculate the reference yield stress using an R6-like method: analytical solutions or FE simulations [1.3]. Due to the complex geometry of the component and loading conditions, these have been obtained by FE simulations.

Firstly, the relationship between reference stress and applied load in terms of tensile force (in this case the force on B-axis) has to be determined. The FE simulation set-ups have been basically the same with exception of the time increment and load settings. In comparison with the simulations discussed before, smaller time increments have been used for accurate load resolution. Based on the previous simulation results, the loads on both axes have been set so that the deformation in the specimen centre started in elastic region and ended in plastic region. Note that the applied stress σ_{app} as well as

the reference stress σ_{ref} in Eq. (2.1) are the remote elastic stress normal to the crack plane [1.3]. It has been determined by running FE simulation of the uncracked simplified biaxial specimen model with elastic material properties (Mesh and settings illustrated in Figure 3.20). As explained in section 3.4.1, the applied stress σ_{app} as well as the reference stress σ_{ref} in this case were the σ_{B} values. The stress versus force result has been generated for the specimen centre with the stress values read from the centroid of the specimen centre element (Figure 5.1).

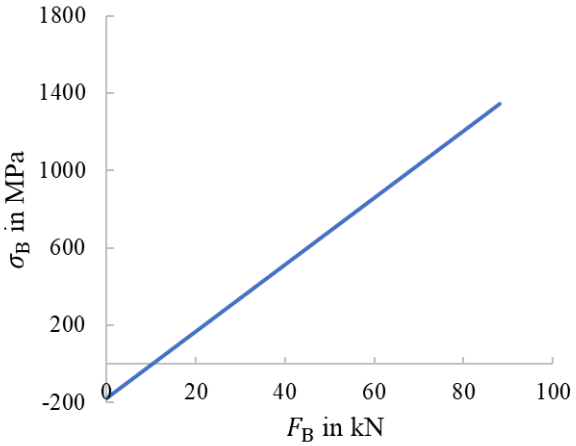

Figure 5.1 Stress versus force in specimen centre of the FE simulation for uncracked biaxial specimen with elastic material properties.

The thermal stresses as a result of temperature gradient on the biaxial specimen have also been considered in reference stress determination. Like the simulation discussed before, a step has been created to increase the specimen temperature from room temperature to the pre-determined temperature field. The compressive thermal stress in the specimen centre has been illustrated in Figure 5.1 at $F_{\mathrm{B}} = 0$.

The next step has been to determine the crack driving force in terms of J-integral for different crack sizes. Both J and elastic J-integral J_{e} have been determined. For that purpose, the FE model for R-curve determination with through-thickness hole and crack has been used. Based on this model, a series of models with different crack depth a_{eq} has been created with the same boundary conditions, loads and time increment settings as in the simulation to determine reference stresses in the previous step. For each equivalent crack depth a_{eq}, two simulations have been carries out with elastic and elastic-plastic material properties, respectively. The J_{e} and J have been determined from the two simulations for the critical location along the crack-front, which in this case has been the middle point along the crack-front. These J_{e} and J values were subsequently assigned to the corresponding reference stress values for different applied loads.

The reference yield stress σ_0 for each equivalent crack depth a_{eq} has been determined based on these FE simulation results. According to section 1.4.3, the target J/J_{e} value has been calculated based on the true stress-strain curve of the material at 425 °C with $L_{\mathrm{r}} = 1$ or in other words, at $\sigma_{\mathrm{ref}} = \sigma_{\mathrm{Y}}$. The plastic correction function $f(L_{\mathrm{r}})$ was given in Eq. (1.16). As a result, the target J/J_{e} value, or

$f(L_r = 1)^{-2}$ has been determined as $\frac{J}{J_e} = f(L_r = 1)^{-2} = 1.7220$. An example of reference yield stress determination has been shown in Figure 5.2 for the biaxial specimen with an equivalent crack depth $a_{eq} = 0.3\ \text{mm}$. In this case, the reference yield stress σ_0 took the value of 1103 MPa. The complete results of reference yield stress for different crack depths determined at the critical point along the crack-front of the through-crack were shown in Figure 5.3. The reference yield stress decreased as the crack depth increased.

Finally, the limit load for failure mode plastic collapse in terms of stress has been calculated using Eq. (5.2) for the biaxial specimen with through-crack (Figure 5.3). For the analytical analyses, the factor L_r^{max} has been determined based on the empirical assumption using Eq. (1.17) as

$L_r^{max} = \frac{1}{2} \cdot \frac{\sigma_Y + R_m}{\sigma_Y} = 1.1369$, with the material properties taken at temperature 425 °C. This empirical L_r^{max} value would be compared later with experimental results. These critical load stress values were then converted to force values for better comparability against test results using the relationship established in Figure 5.1. Logically, this force has been the tensile force in B-axis, which is normal to the crack plane. Since these critical loads were calculated based on the reference yield stresses, they also decreased as the crack depth increased.

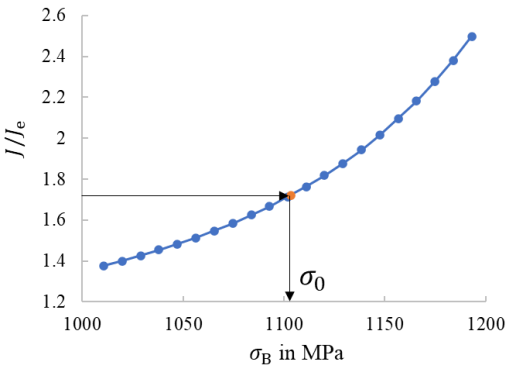

Figure 5.2 Determination of reference yield stress based on FE simulations for the critical location along the through-crack on the biaxial specimen with $a_{eq} = 0.3\ \text{mm}$.

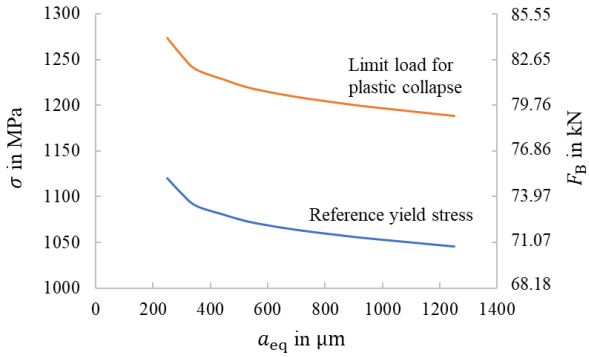

Figure 5.3 Reference yield stress $\sigma_0$and limit load for failure mode plastic collapse in terms of stress and force for biaxial specimen with through-crack, determined for various crack depths at the critical location along crack-front.

5.2.2. Determination of load versus stable crack extension curve

Due to the stable crack extension observed in the biaxial tests with through-crack, the critical load for failure mode ductile tearing has been determined using the CDF philosophy. The load versus stable crack extension curve has been determined following the flow chart Figure 5.4. In contrast to the flow chart Figure 1.7, the assessment has been conducted with help of FE simulations instead of SINTAP/FITNET equations for component with complex geometries and loading conditions. An assessment example of biaxial specimen C2 (Test BV5) has been discussed in detail, while the results for the rest of the biaxial specimens to be found in appendix.

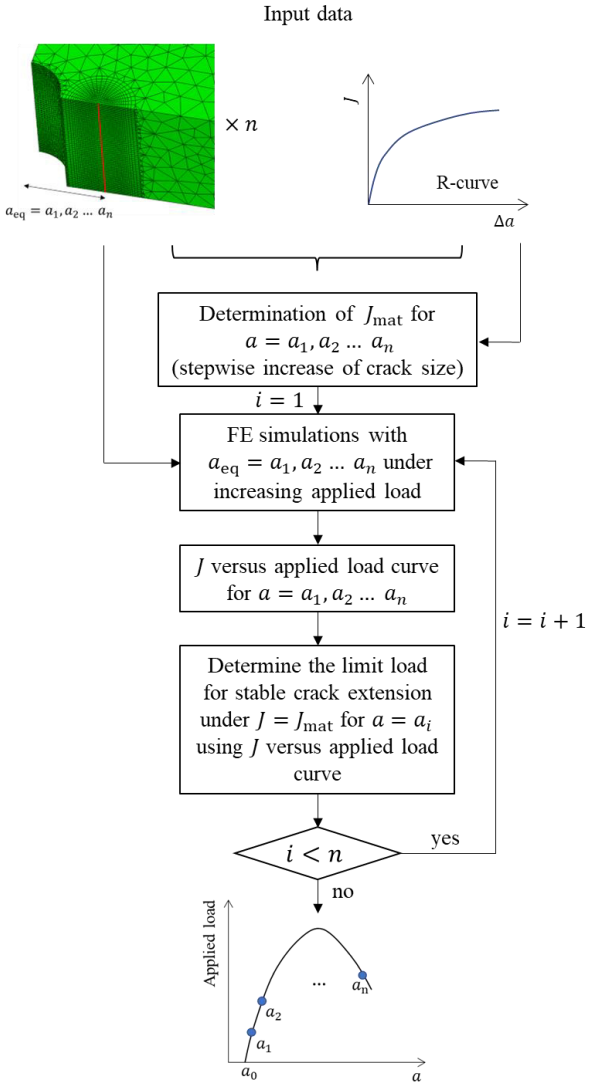

Figure 5.4 Flow chart for determining the applied load versus stable crack extension curve based on FE simulations.

Firstly, the R-curve determined in section 4.3.1 has been used. Based on this, the crack growth resistance versus crack depth curve has been generated for biaxial specimen C2 with an initial crack depth of $a_0 = 0.325$ mm (Figure 5.5). The fracture toughness J_{mat} was then determined based on this

crack growth resistance versus crack depth curve for stepwise increasing crack depths $a = a_1, a_2 \dots a_n$. In Figure 5.5, the fracture toughness J_{mat} has been determined for the crack depth $a = 0.35$ mm (stable crack extension of $\Delta a = 0.025$ mm) with a value of 7.989 N/mm.

In the next step, FE simulations have been carried out following the flow chart Figure 5.4. A series of FE simulations were conducted with stepwise increasing equivalent crack depths $a_{\mathrm{eq}} = a_1, a_2 \dots a_n$ with elastic-plastic material properties using the same model as in 5.2.1. J-integral has been determined at the critical location along the crack-front for each crack depth a_{eq} with growing applied load. In Figure 5.6, the J versus applied load curve has been shown for $a_{\mathrm{eq}} = 0.35$ mm.

Subsequently, under the condition $J = J_{\mathrm{mat}}$, the limit load for stable crack extension has been determined based on the J versus applied load curve for $a = a_{\mathrm{eq}}$. For the considered component with the crack depth $a = a_{\mathrm{eq}}$, if the applied load has been increased beyond this limit load, stable crack extension would take place. In Figure 5.6, the limit load for stable crack extension has been determined for $a_{\mathrm{eq}} = 0.35$ mm and $\Delta a = 0.025$ mm with a value of $F_{\mathrm{B}} = 68.20$ kN.

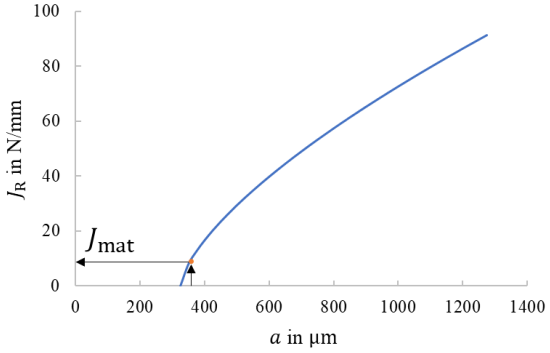

Figure 5.5 Determination of J_{mat} for biaxial specimen C2 ($a_0 = 0.325$ mm) with a crack growth $\Delta a = 0.025$ mm ($a = 0.35$ mm) based on crack growth resistance versus crack depth curve.

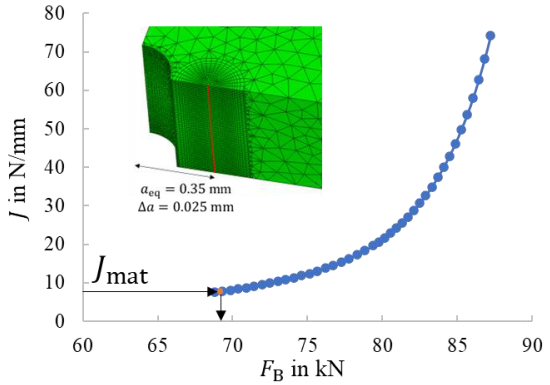

Figure 5.6 Determination of limit load for stable crack extension for the biaxial specimen (through-crack) with $a_{\mathrm{eq}} = 0.35$ mm and $\Delta a = 0.025$ mm based on the J versus applied load curve.

This procedure has been carried out for a series of stepwise increasing crack depths in order to generate the complete load versus stable crack extension curve (Figure 5.4). Starting from the initial

crack depth a_0, the curve illustrated the applied load needed for stable crack extension. From the point with highest value of applied load, in order to continue the stable crack extension following the path, the applied load has to be reduced. Otherwise, the instable crack extension takes place at this point. Consequently, this point determines the critical load for failure mode ductile tearing (instability load).

In the case of the biaxial specimen with through-crack, FE simulations have been carried out for equivalent crack depths a_{eq} of 0.35 mm, 0.40 mm, 0.45 mm, 0.50 mm, 0.55 mm, 0.65 mm, 0.75 mm, 0.94 mm, 1.10 mm and 2.50 mm. The load versus stable crack extension curve for the biaxial specimen C2 has been illustrated in Figure 5.7 with the critical load and crack size for failure mode ductile tearing as $F_{\mathrm{dt}} = 81.24\ \mathrm{kN}$ and $a_{\mathrm{dt}} = 1.80\ \mathrm{mm}$.

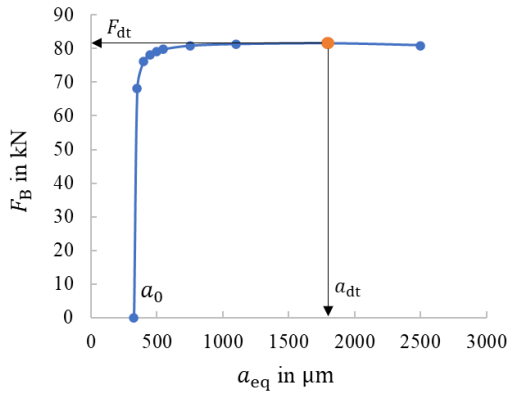

Figure 5.7 Load versus stable crack extension curve for the biaxial specimen C2 with initial crack $a_0 = 0.325\ \mathrm{mm}$, critical load for failure mode ductile tearing F_{dt} determined as the point with the highest F_{B} value along the curve.

5.2.3. Two-criteria failure assessment

As introduced in section 2.2.1, the two-criteria failure assessment method has been used to predict the failure load as well as the failure load of the biaxial specimen with through-crack. The limit load curve for failure mode plastic collapse (Figure 5.3) has been illustrated together with the load versus stable crack extension curve (Figure 5.7) with respect to the crack size. An example of the two-criteria failure assessment for biaxial specimen C2 has been shown in Figure 5.8. It could be observed that the load versus stable crack extension curve crossed the limit load curve for plastic collapse before reaching its maximum. As a result, plastic collapse has been identified as the failure mode for biaxial specimen C2 with a failure load of $F_{\mathrm{plc}} = 81.0\ \mathrm{kN}$. Also, the critical crack depth for biaxial specimen C2 has been determined as $a_{\mathrm{plc}} = 0.95\ \mathrm{mm}$ according to Figure 5.8.

The critical loads for both failure modes, i.e., F_{plc} and F_{dt}, have been close to each other. The reason has been that for the analysed cracked specimen both limit curves have been shallow. Compared with the actual test results in Table 5.1, the experimental results (DIC strain field) have shown plastic collapse as the failure mode for specimen C2. This confirmed the analysis result $F_{\mathrm{plc}} < F_{\mathrm{dt}}$. However, the predicted failure load and critical crack size deviated by a relative difference of 0.12% as well as 1.5% in comparison to the experimental results for specimen C2.

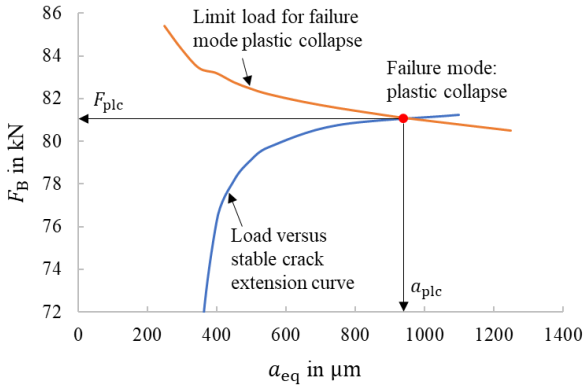

Figure 5.8 Failure assessment of the biaxial specimen C2 with through-crack based on two-criteria failure assessment method, failure mode determined as plastic collapse.

Likewise, the failure analyses have been carried out for the rest of the biaxial specimens with through-crack based on the two-criteria failure assessment method (Figure 5.9). The failure loads and modes have been determined for each specimen und were summarised in Table 5.2. The predicted failure mode of all analyses has been plastic collapse as illustrated in Figure 5.9. This has been in agreement with the DIC strain field analyses of the biaxial tests.

Except for the specimen A1 and A2, all predicted failure loads have been lower than the failure loads recorded in tests. Note that the first two tests with specimen A1 and A2 were pre-tests in order to explore the crack initiation and growth behaviours under uniaxial cyclic loads in order to finalise the settings for pre-cracking. Both specimens went through high number of cycles with different mean loads and amplitudes. As a result, the initial crack size on both specimens (Table 5.1) were larger than designed (designed value $a_0 = 0.30\,\mathrm{mm}$) and a degradation of material properties was also suspected. Besides, for the failure analyses of specimen A1 and A2 (Figure 5.9a and Figure 5.9b), the R-curve acquired based on the biaxial test of specimen C2 has been used. Since the initial crack sizes of specimen A1 and A2 were noticeably larger (47.6% and 69.8%) than the initial crack size of specimen C2, the constraint along the crack-front of specimen A1 and A2 were therefore higher than the constraint along the crack-front of specimen C2. Consequently, the fracture toughness (R-curve) for specimen A1 and A2 were theoretically lower than the values used in analyses. As a result, the analyses of both pre-test specimens have shown higher predicted failure loads (up to 4.8%) than recorded in the tests.

On the other hand, the analyses of the rest of the biaxial specimen tests with through-crack have shown conservative results. The predicted failure loads remained within 4% relative difference in comparison to the test results. The ligament yielding parameter ${L_r^{max}}_{test}$ corresponding to the failure load recorded in test have been calculated according to Eq. (2.1) as the ratio between the failure load in terms of remote stress and the reference yield stress of the critical crack size. Except for the pre-test specimens, all biaxial specimens have shown a maximum ligament yielding parameter ${L_r^{max}}_{test}$ larger than the value from the empirical calculation from Eq. (1.17) ($L_r^{max} = 1.1369$).

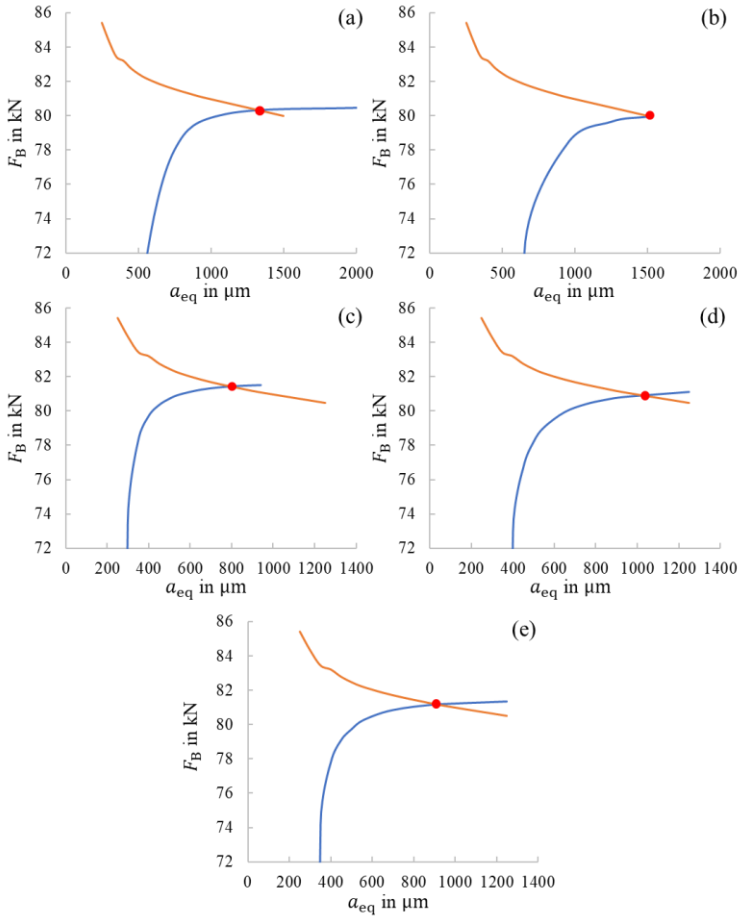

Figure 5.9 Determination of the failure load and failure mode based on the two-criteria failure assessment method for biaxial specimens with through-crack: (a) Specimen A1, pre-test; (b) Specimen A2, pre-test; (c) Specimen D1; (d) Specimen B1; (e) Specimen C1.

In order to verify the FE model with the equivalent crack depths a_{eq} for through-crack, the FE simulation with the real crack geometry has been carried out for comparison. The real crack geometry of the specimen D1 has been modelled due to its highest relative difference of the predicted failure load to the test value. The mesh of the FE model with the local structured mesh refinement has been shown in Figure 5.10. The crack has been modelled as a spline that follows the real crack-front point on both surfaces and the deepest point. The fracture surface of biaxial specimen D1 was illustrated in Figure 5.10c with the crack-front considered marked. Note that only one crack-front (marked in in Figure 5.10c) has been modelled with symmetric boundary condition applied. The crack-front with the largest stable crack extension has been chosen. The equivalent crack depths a_{eq} for the specimen D1 has been determined as $a_{eq} = 1.190$ mm as discussed in section 4.3.1. The model with this equivalent crack depths a_{eq} has been prepared. Both models were simulated at the same conditions as in the test with a $F_B = 83.1$ kN, which is the average value of the predicted failure load and test value.

Table 5.2 Failure assessment results for biaxial specimens with through-crack

	Specimen designation	Failure load (predicted) in kN	Failure load (test) in kN	Relative difference to test	Failure mode (predicted)	$L_r^{max}{}_{test}$
Biaxial specimen with through-crack (from Pre-test)	A1	80.2	76.5	+4.8%	Plastic collapse	1.0618
	A2	79.9	76.8	+4.0%	Plastic collapse	1.0724
Biaxial specimen with through-crack	D1	81.4	84.8	-4.0%	Plastic collapse	1.2115
	B1	80.9	81.1	-0.25%	Plastic collapse	1.1577
	C2	81.0	81.1	-0.12%	Plastic collapse	1.1560
	C1	81.2	83.2	-2.4%	Plastic collapse	1.1894

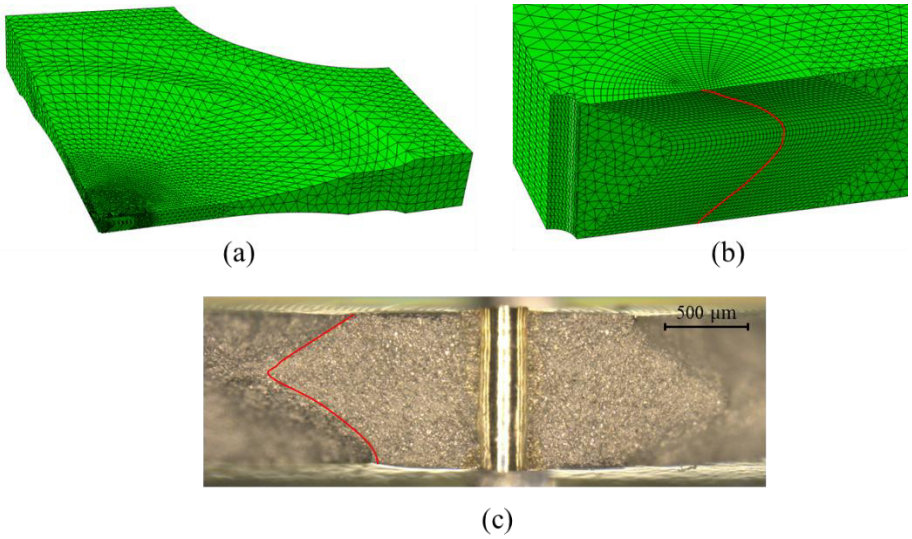

Figure 5.10 FE models with real crack geometry of biaxial specimen D1: (a) Mesh of the quarter model; (b) Local structured mesh refinement along the crack-front; (c) Fracture surface of the specimen D1 with crack-front marked.

At the deepest point along the crack-front based on real crack geometry, the crack-tip loading in terms of J-integral has been 98.4 N/mm. In comparison, at the centre of the crack-front with the equivalent crack depths a_{eq} the J value has been 118.7 N/mm. As a result, the crack-tip loading of the simplified model with equivalent crack depths a_{eq} has been higher than the value from the real crack geometry, which showed conservatism of the assessment results.

5.3. Analytical failure assessment for biaxial specimen with surface crack

The analytical failure assessment based on the established assessment procedure has been conducted for the biaxial specimens with surface crack and has been discussed in this section. The test results for the biaxial specimens with surface crack has been given in Table 5.3 with the failure load as the force on B-axis recorded at final fracture, the failure mode determined by DIC strain field analysis, the mean initial crack length a_0, the maximum stable crack extension on specimen surface c_{fin} as well as in the specimen thickness direction a_{fin}. Both a_{fin} and c_{fin} have been determined as follows: since the stable crack extension surface on the biaxial specimen with surface crack has semi-ellipse shape except for the crack extension on specimen surface (see Figure 4.24 and Figure 5.11), a fit-ellipse has been generated for the stable crack extension surface contour (Figure 5.12). a_{fin} has been determined as the semi-minor axis of this fit-ellipse, while c_{fin} being the semi-major axis. The mean initial crack length a_0 has been determined as

$$a_0 = \frac{1}{3}\left(c_{0,\mathrm{l}} + a_{0,\mathrm{c}} + c_{0,\mathrm{r}}\right) \tag{5.3}$$

being $c_{0,\mathrm{l}}$ and $c_{0,\mathrm{r}}$ the initial crack lengths on specimen surface and $a_{0,\mathrm{c}}$ the initial crack depth in specimen thickness direction (Figure 5.12). The maximum stable crack extension direction on the crack plane has been marked with s.

Table 5.3 Test results for biaxial specimens with surface crack

	Test-Nr.	Specimen designation	Failure load (test) in kN	a_0 in µm	a_{fin} in µm	c_{fin} in µm	Failure mode (Test)
Test (biaxial) with surface crack	BV8	E1	86.6	399	573	1220	Plastic collapse
	BV10	D2	85.3	358	476	1549	Plastic collapse

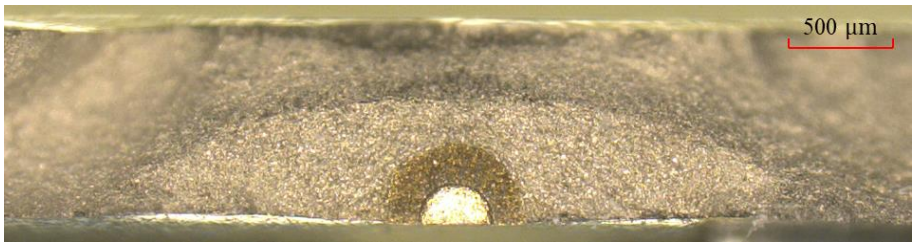

Figure 5.11 Fracture surface on the biaxial specimen D2 with surface crack (lower part).

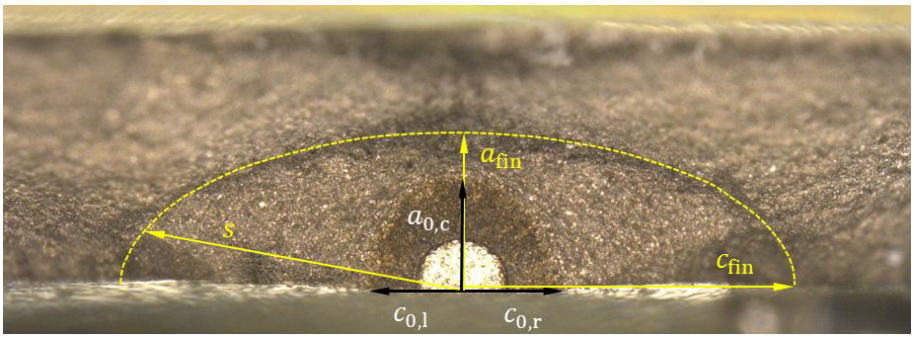

Figure 5.12 Parameterisation of the crack surface geometry on the biaxial specimen with surface crack for analysis.

5.3.1. Determination of limit load for failure mode plastic collapse

Following the procedure described in section 5.2.1, the limit load for failure mode plastic collapse has been determined for the biaxial specimen with surface crack. The FE simulations have been conducted to determine the crack-tip loadings in terms of J-integral. Since the reference stress (remote stress) does not depend on the crack geometry, the reference stress curve for the biaxial specimen acquired in section 5.2.1 has been used. For the FE simulations, the FE model shown in Figure 3.26 has been used. Since the initial crack has been in semi-circular shape and the contour of the maximum stable crack extension has been in form of ellipse, the surface crack in the FE simulation has been modelled in the following manner:

- Phase 1: quarter-circular shape with a radius of a until $a = a_{\mathrm{fin}}$;
- Phase 2: quarter-ellipse shape with semi-minor axis a_{fin} and stepwise increasing semi-major axis until $c = c_{\mathrm{fin}}$;
- Phase 3: quarter-ellipse shape with $\frac{a}{c} = \frac{a_{\mathrm{fin}}}{c_{\mathrm{fin}}}$.

For conservatism the a_{fin} and c_{fin} values have been chosen as the maximum values from both test results ($a_{\mathrm{fin}} = 0.573$ mm, $c_{\mathrm{fin}} = 1.549$ mm). For characterisation of the crack size the crack extension along the maximum stable crack extension direction has been used and notes as s. The angle between the maximum stable crack extension direction and the specimen surface has been determined as the average value from the two tests and was 10°. As a result, the crack size s has following relationship with crack length c and crack depth a (Phase 2 and 3 through analytical formula for ellipse):

- Phase 1: $s = a = c$ for $s \leq 0.573$ mm
- Phase 2 and 3: $s = \frac{a}{\sqrt{1-0.97\cdot\frac{c^2-a^2}{c^2}}}$ for $s > 0.573$ mm

The reference yield stress σ_0 for each crack size s has been determined at the critical location along the crack-front of the modelled surface crack based on these FE simulation results. Note that this critical location varied as the crack changed its shape to quarter-ellipse in phase 2: the angle between the direction of the most critical location and specimen surface changed from 22.5° to 10°.

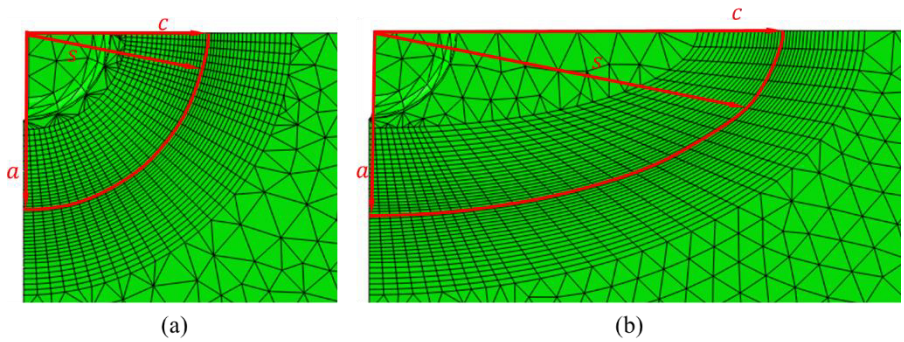

Figure 5.13 Structured Mesh around the crack-front and crack geometric parameters in the FE model of biaxial specimen with surface crack: (a) Model in phase 1; (b) Model in phase 2.

Since the boundary conditions have not changed from the analysis of biaxial specimen with through-crack, the target J/J_e value, or $f(L_r = 1)^{-2}$ has remained with the value of 1.7220. An example of reference yield stress determination has been shown in Figure 5.14 for the biaxial specimen with a surface crack size $s = 0.4$ mm. In this case, the reference yield stress σ_0 took the value of 1134 MPa. The complete results of reference yield stress for different crack sizes determined at the critical point along the crack-front of the surface crack were shown in Figure 5.15. The reference yield stress decreased as the crack size increased. The "S" shape of both curves resulted from the stress gradient along the A-axis of the specimen from the specimen centre. Since there was no stress gradient in the thickness direction of the specimen, the through-crack was not affected. However, as the surface crack size (in ellipse shape) increased above about 0.8 mm, the stress ratio (remote stress) along the crack-front varied with higher values at the critical location, which caused the reference yield stress and the limit load for plastic collapse to decrease more sharply.

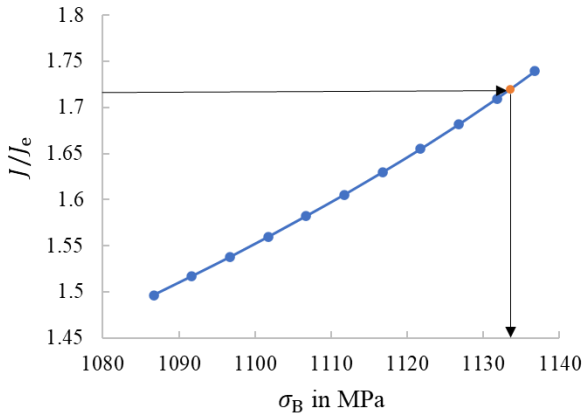

Figure 5.14 Determination of reference yield stress based on FE simulations for the critical location along the surface crack on the biaxial specimen with $s = 0.4$ mm.

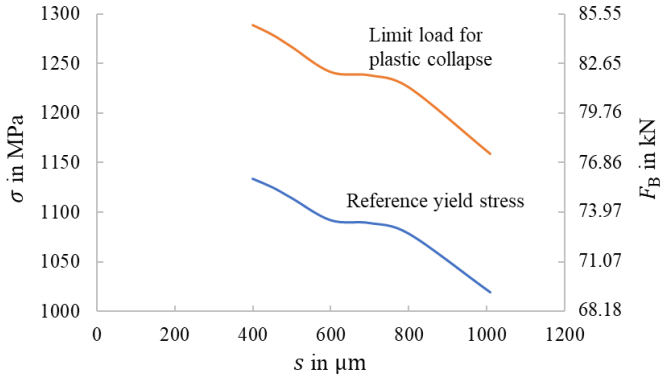

Figure 5.15 Reference yield stress σ_0 and limit load for failure mode plastic collapse in terms of stress and force for biaxial specimen with surface crack, determined for various crack sizes at the critical location along crack-front.

5.3.2. Determination of load versus stable crack extension curve

Due to the stable crack extension observed in the biaxial tests with surface crack, the critical load for failure mode ductile tearing has been determined using the CDF philosophy. The load versus stable crack extension curve has been determined following the flow chart Figure 5.4. The FE simulations were carried out using the models described in section 5.3.1. An assessment example of biaxial specimen E1 (Test BV8) has been discussed in detail, while the results for the rest of the biaxial specimens to be found in appendix.

Since it was not able to determine the R-curve based on the biaxial specimen tests with surface crack with satisfying accuracy (see section 4.3.2), the R-curve determined based on test results of biaxial specimen with through-crack has been used. This was due to the fact that the constraint ahead of the critical location along the crack-front has been identical for both crack variants as per designed. Besides, the other boundary conditions for both specimens were also the same. Based on the R-curve, the crack growth resistance versus crack depth curve has been generated for biaxial specimen E1 with an initial crack depth of $a_0 = 0.399\,\mathrm{mm}$ (Figure 5.16). The fracture toughness J_{mat} was then determined based on this crack growth resistance versus crack depth curve for stepwise increasing crack sizes $s = s_1, s_2 \ldots s_n$. In Figure 5.16, the fracture toughness J_{mat} has been determined for the crack depth $s = 0.500\,\mathrm{mm}$ (stable crack extension of $\Delta a = 0.101\,\mathrm{mm}$) with a value of 20.360 N/mm.

FE simulations have been carried out for stepwise increasing crack sizes $s = s_1, s_2 \ldots s_n$ to determine the crack-tip loading parameter in terms of J-integral at the critical location along the crack-front with growing applied load. In Figure 5.17, the J versus applied load curve has been shown for $s = 0.500\,\mathrm{mm}$. Subsequently, under the condition $J = J_{\mathrm{mat}}$, the limit load for stable crack extension has been determined for $s = 0.500\,\mathrm{mm}$ and $\Delta a = 0.101\,\mathrm{mm}$ with a value of $F_{\mathrm{B}} = 84.32\,\mathrm{kN}$.

In the case of the biaxial specimen with surface crack, FE simulations have been carried out for crack sizes s of 0.40 mm, 0.45 mm, 0.50 mm, 0.60 mm, 0.70 mm and 1.01 mm. The load versus stable crack extension curve for the biaxial specimen E1 has been illustrated in Figure 5.18. The decreasing part of

the curve has been omitted due to the additional numerical expense. It has been shown later that the critical load for failure mode ductile tearing has never been reached for these specimens.

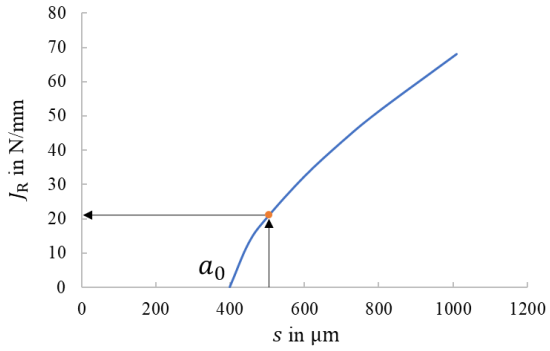

Figure 5.16 Determination of J_{mat} for biaxial specimen E1 ($a_0 = 0.399$ mm) with a crack growth $\Delta a = 0.101$ mm ($s = 0.500$ mm) based on crack growth resistance versus crack depth curve.

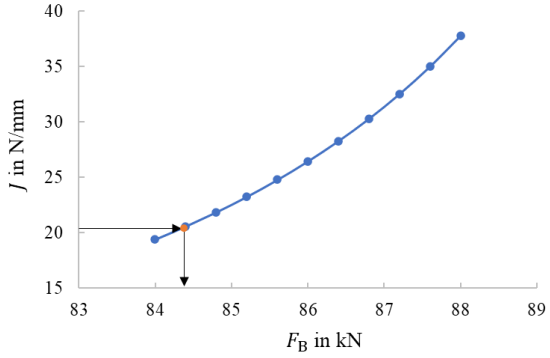

Figure 5.17 Determination of limit load for stable crack extension for the biaxial specimen (surface crack) with $s = 0.500$ mm and $\Delta a = 0.101$ mm based on the J versus applied load curve.

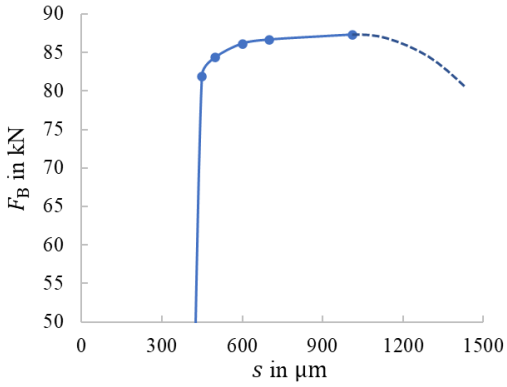

Figure 5.18 Load versus stable crack extension curve for the biaxial specimen E1 with initial crack $a_0 = 0.399$ mm, decreasing part (dashed) of the curve omitted due to numerical expense.

5.3.3. Two-criteria failure assessment

The two-criteria failure assessment method has been used to predict the failure mode as well as the failure load of the biaxial specimen with surface crack. The limit load curve for failure mode plastic collapse has been illustrated together with the load versus stable crack extension curve with respect to the crack size. The two-criteria failure assessment for biaxial specimen E1 and D2 has been shown in Figure 5.19. As a result, plastic collapse has been identified as the failure mode for both biaxial specimen E1 and D2 with failure loads of 83.8 kN and 84.4 kN, respectively. Also, the failure mode for both specimens have been determined as plastic collapse according to Figure 5.19, which has shown good agreement with the DIC strain field analysis.

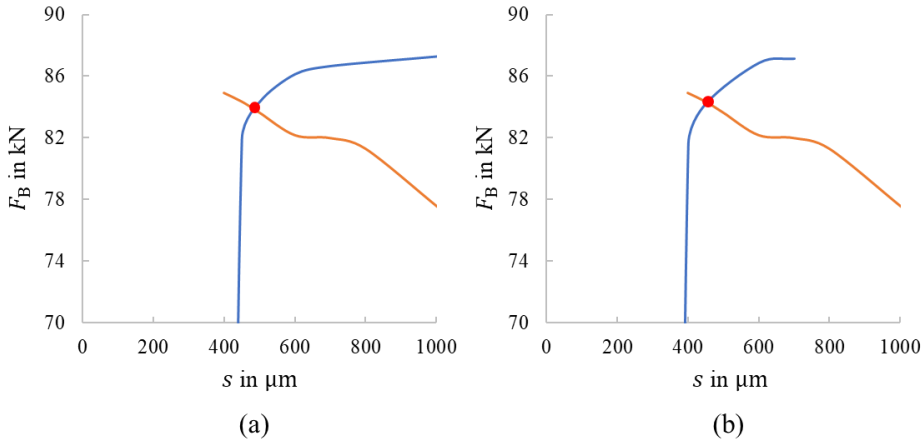

Figure 5.19 Failure assessment of the biaxial specimen with surface crack based on two-criteria failure assessment method: (a) Biaxial specimen E1, failure mode determined as plastic collapse; (b) Biaxial specimen D2, failure mode determined as plastic collapse.

The predicted failure loads and modes for each specimen were summarised in Table 5.4. All predicted failure loads have been lower than the failure loads recorded in tests, which were conservative. The predicted failure loads remained within 3.2% relative difference in comparison to the test results. Also, the maximum ligament yielding parameters ${L_r^{max}}_{test}$ determined based on test results were higher than the analytically calculated values L_r^{max}.

A summary of predicted failure load and failure load recorded in test comparison has been shown in Figure 5.20. Except for both pre-tests (specimen A1 and A2), all failure loads predicted using the established failure assessment procedure have been lower than their corresponding test values, i.e., the points were located beneath the 45° orange dotted line in Figure 5.20, which showed conservatism of the assessment procedure. Besides, all predicted values stayed within the 4% relative difference corridor with respect to the test values.

Table 5.4 Failure assessment results for biaxial specimens with surface crack

	Specimen designation	Failure load (predicted) in kN	Failure load (test) in kN	Relative difference to test	Failure mode (predicted)	$L_r^{max}{}_{test}$
Biaxial specimen with surface crack	E1	83.8	86.6	-3.2%	Plastic collapse	1.2106
	D2	84.4	85.3	-1.1%	Plastic collapse	1.1900

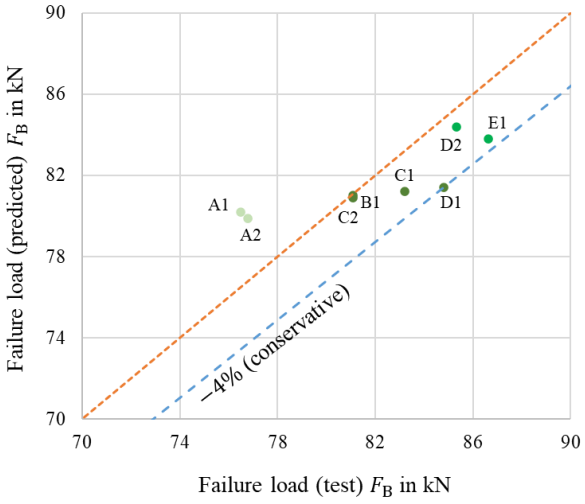

Figure 5.20 Summary of predicted failure load versus failure load recorded in test for all biaxial specimens.

5.4. Analytical failure assessment for uniaxial specimen

The analytical failure assessment based on the established assessment procedure has been conducted for the uniaxial specimens with surface crack and has been discussed in this section. The test results for the uniaxial specimens with surface crack has been given in Table 5.5 with the failure load as the force on the tensile axis recorded at final fracture, the mean initial crack length a_0, the maximum stable crack extension in the specimen thickness direction a_{fin}. The crack geometry parameters have been shown in Figure 5.21. Similar to the surface crack on the biaxial specimen, the initial crack length a_0 has been determined according to Eq. (5.3). Since the crack-front of the maximum stable crack extension was in form of an arc. A fit-arc has been generated to represent the crack-front of the maximum stable crack extension. The radius of this fit-arc has been defined as a_{fin}.

Table 5.5 Test results for uniaxial specimens with surface crack

	Test-Nr.	Specimen designation	Failure load (test) in kN	a_0 in µm	a_{fin} in µm
Pre-test (uniaxial) with surface crack	UV1	E1	47.7	789	3842
Test (uniaxial) with surface crack	UV2	E2	54.8	308	3617
	UV3	E3	54.7	329	3380
	UV4	D1	52.1	476	3346
	UV5	D3	51.6	405	3004
	UV6	B1	54.7	372	3329
	UV7	B2	54.5	313	3383
	UV8	A1	52.5	387	3013
	UV9	A2	52.5	380	3067
	UV10	A3	53.6	370	3217

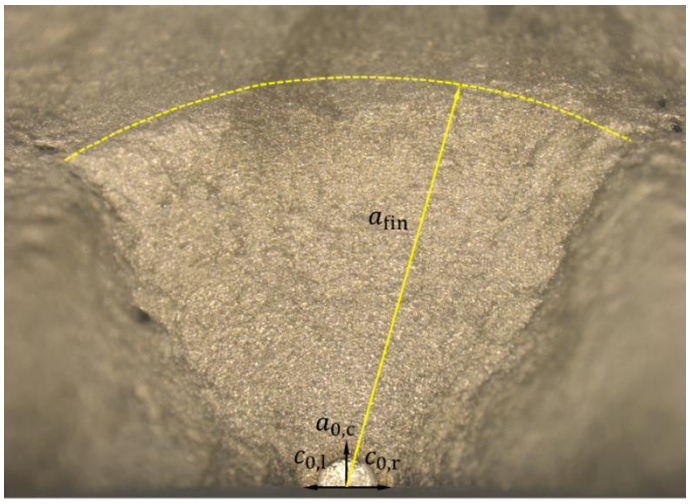

Figure 5.21 Parameterisation of the crack surface geometry on the uniaxial specimen with surface crack for analysis.

5.4.1. Determination of limit load for failure mode plastic collapse

Following the procedure described in section 5.2.1, the limit load for failure mode plastic collapse has been determined for the uniaxial specimen with surface crack. The FE simulations have been conducted to determine the remote reference stress and crack-tip loadings in terms of J-integral. The FE model (quarter model for uniaxial specimen without crack) used for the remote reference stress determination has been shown in Figure 5.22. The simulation has been conducted with elastic material

properties. The stress versus force results were generated for the specimen surface centre (Figure 5.23) with the stress values read from the centroid of the specimen surface centre element.

Unlike the test conditions for biaxial specimen, there was no temperature gradient present for the uniaxial specimen. As a result, thermal stress has not been considered in the following assessment. To determine the crack-tip loadings in terms of J-integral for different crack sizes, the FE model for uniaxial specimen design (Figure 3.32) has been used as a baseline. Based on this model, a series of models with semi-circular crack of different crack depth a has been created with the same boundary conditions, loads and time increment settings as in the simulation to determine reference stresses in the previous step. For each crack depth a two simulations have been carries out with elastic and elastic-plastic material properties, respectively. The J_{e} and J have been determined from the two simulations for the critical location along the crack-front, which in this case has been the deepest point along the crack-front. These J_{e} and J values were subsequently assigned to the corresponding reference stress values for different applied loads.

The reference yield stress σ_0 for each crack depth a has been determined based on these FE simulation results. The target J/J_{e} value has been calculated based on the true stress-strain curve of the material at 350 °C with $L_{\mathrm{r}} = 1$. The plastic correction function $f(L_{\mathrm{r}})$ was given in Eq. (1.16). As a result, the target J/J_{e} value, or $f(L_{\mathrm{r}} = 1)^{-2}$ has been determined as 1.7002. The slight difference between this value and the corresponding value for biaxial specimen is due to the difference in the local temperatures at both specimens, which slightly affected material properties, as well as due to different constraints (compare Figure 3.27, Figure 3.33). An example of reference yield stress determination has been shown in Figure 5.24 for the uniaxial specimen with a crack depth $a = 0.45$ mm. In this case, the reference yield stress σ_0 took the value of 1056 MPa. The complete results of reference yield stress for different crack depths determined at the critical point along the crack-front were shown in Figure 5.25, which decreased as the crack depth increased. The factor $L_{\mathrm{r}}^{\max}$ has been determined using Eq. (1.17) with the material properties taken at temperature 350 °C. The factor $L_{\mathrm{r}}^{\max}$ has been calculated as 1.1359. The limit load for failure mode plastic collapse has been determined in the same way as for the biaxial specimen, the result of which has been illustrated in Figure 5.25.

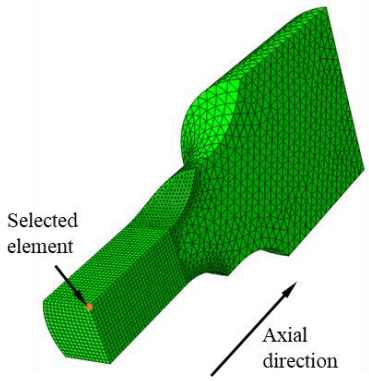

Figure 5.22 Mesh of the FE model to determine the remote reference stress for uniaxial specimen.

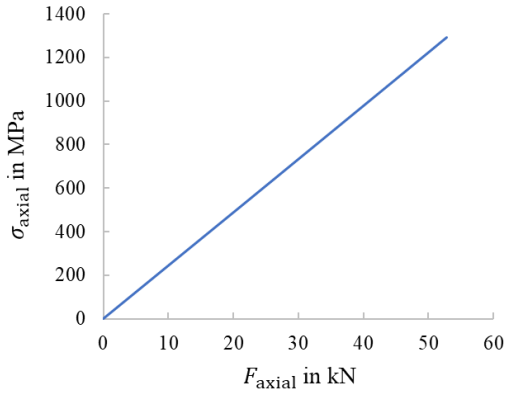

Figure 5.23 Stress versus force in specimen centre of the FE simulation for uncracked uniaxial specimen with elastic material properties.

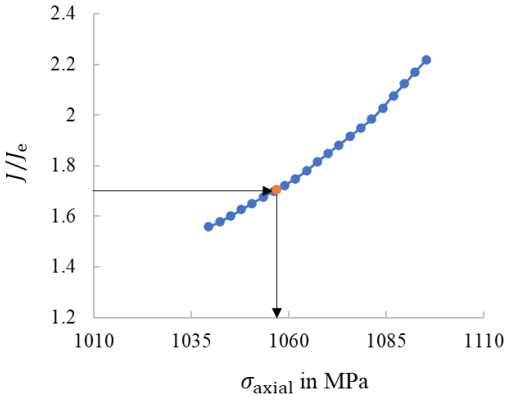

Figure 5.24 Determination of reference yield stress based on FE simulations for the deepest location along the surface crack on the uniaxial specimen with $a = 0.45$ mm.

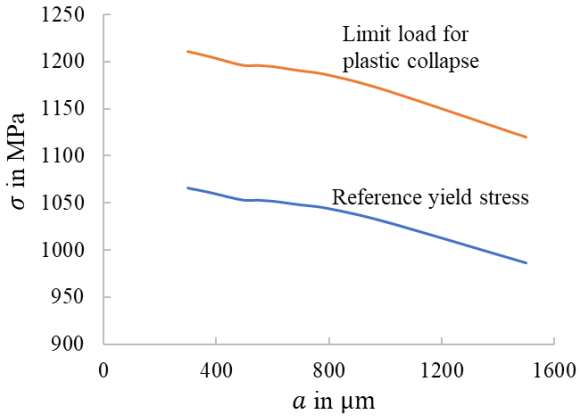

Figure 5.25 Reference yield stress σ_0 and limit load for failure mode plastic collapse in terms of stress and force for uniaxial specimen with surface crack, determined for various crack depths at the critical location along crack-front.

5.4.2. Determination of load versus stable crack extension curve

Due to the stable crack extension observed in the uniaxial tests with surface crack, the critical load for failure mode ductile tearing has been determined using the CDF philosophy. The load versus stable crack extension curve has been determined following the flow chart Figure 5.4. The FE simulations were carried out using the models described in section 5.4.1. An assessment example of uniaxial specimen A1 (Test UV8) has been discussed in detail, while the results for the rest of the biaxial specimens to be found in appendix.

The uniaxial R-curve determined in section 4.4.2 has been used. Based on the R-curve, the crack growth resistance versus crack depth curve has been generated for uniaxial specimen A1 with an initial crack depth of $a_0 = 0.387$ mm. The fracture toughness J_{mat} was then determined based on this crack growth resistance versus crack depth curve for stepwise increasing crack sizes $a = a_1, a_2 \ldots a_n$. Then, FE simulations have been carried out for these stepwise increasing crack sizes $a = a_1, a_2 \ldots a_n$ to determine the crack-tip loading parameter in terms of J-integral at the critical location along the crack-front with growing applied load. In, the J versus applied load curve has been shown for $s = 0.800$ mm. Subsequently, under the condition $J = J_{\mathrm{mat}} = 68.78$ N/mm, the limit load for stable crack extension has been determined for $s = 0.800$ mm and $\Delta a = 0.413$ mm with a value of $\sigma_{\mathrm{axial}} = 1197$ MPa.

In the case of the uniaxial specimen with surface crack, FE simulations have been carried out for crack sizes a of 0.45 mm, 0.50 mm, 0.55 mm, 0.60 mm, 0.65 mm, 0.70 mm, 0.80 mm, 1.00 mm, 1.20 mm and 1.50 mm. The load versus stable crack extension curve for the uniaxial specimen A1 has been illustrated in Figure 5.27 with the critical load and crack size for failure mode ductile tearing $\sigma_{\mathrm{dt}} = 1199$ MPa and $a_{\mathrm{dt}} = 0.7$ mm.

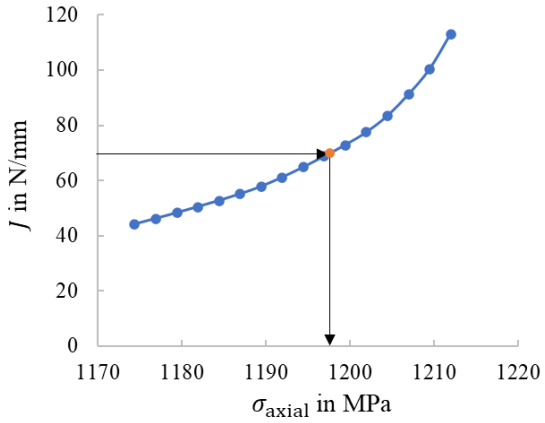

Figure 5.26 Determination of limit load for stable crack extension for the uniaxial specimen (surface crack) with $a = 0.800$ mm and $\Delta a = 0.413$ mm based on the J versus applied load curve.

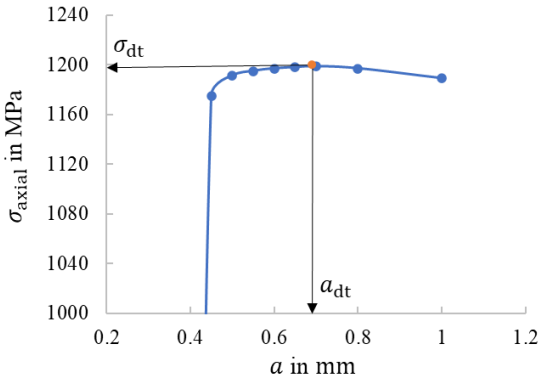

Figure 5.27 Load versus stable crack extension curve for the uniaxial specimen A1 with initial crack $a_0 = 0.387$ mm.

5.4.3. Two-criteria failure assessment

The two-criteria failure assessment method has been used to predict the failure mode as well as the failure load of the uniaxial specimen with surface crack. The limit load curve for failure mode plastic collapse has been illustrated together with the load versus stable crack extension curve with respect to the crack size. The two-criteria failure assessment for uniaxial specimen A1 and E1 has been shown in Figure 5.28, while the rest of the results could be found in appendix. Of the ten uniaxial specimens analysed, nine have been determined to have failure mode of plastic collapse with the rest one to fail in form of ductile tearing (E1).

In Figure 5.28a, the failure mode for specimen A1 was determined as plastic collapse, as the limit load curve for plastic collapse crossed the load versus stable crack extension curve before its maximum value. The failure load for specimen A1 has been determined as 1196 MPa, or 48.90 kN. In Figure 5.28b, the failure mode for specimen E1 was determined as ductile tearing, as the load versus stable crack extension curve reached its maximum value before crossing the limit load for plastic collapse. For the uniaxial specimen with a relatively large initial crack size (for specimen E1: $a_0 = 0.789$ mm), the load versus stable crack extension curve showed a clear peak value. The failure load for specimen E1 has been determined as 1151 MPa, or 47.05 kN.

The predicted failure loads and modes for each specimen were summarised in Table 5.6. The failure loads in terms of stress σ_{axial} were converted to force value F_{axial} according to Figure 5.23. All predicted failure loads have been lower than the failure loads recorded in tests, which were considered conservative. The predicted failure loads remained within 10.6% relative difference in comparison to the test results. On the other hand, the maximum ligament yielding parameters ${L_r^{max}}_{test}$ determined based on test results were also higher than the analytically calculated values L_r^{max}. Note that these ${L_r^{max}}_{test}$ values from the uniaxial tests (except for the pre-test specimen E1) have been even higher than those from the biaxial tests, which supported the failure mode of plastic collapse for the uniaxial specimens.

A summary of predicted failure load and failure load recorded in test comparison for uniaxial specimens has been shown in Figure 5.29. All failure loads predicted using the established failure assessment procedure have been lower than their corresponding test values, which showed conservatism of the assessment procedure.

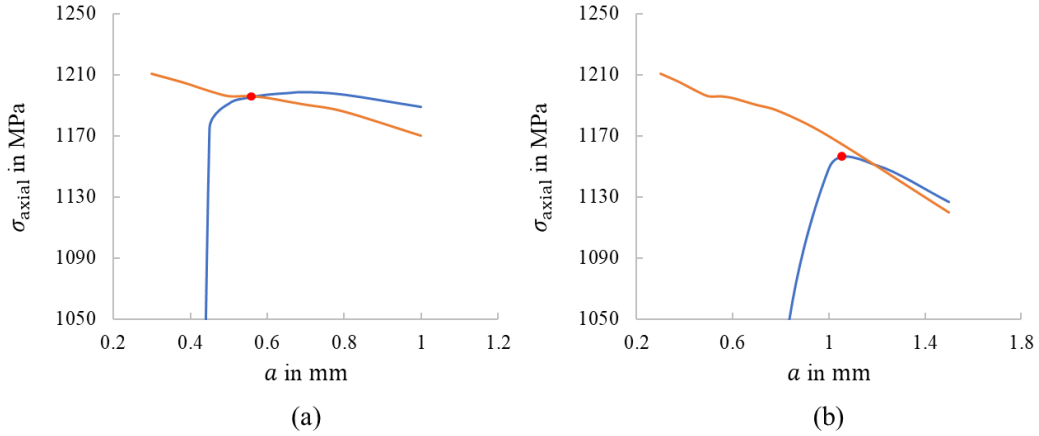

Figure 5.28 Failure assessment of the uniaxial specimen with surface crack based on two-criteria failure assessment method: (a) Uniaxial specimen A1 with initial crack $a_0 = 0.387$ mm, failure mode determined as plastic collapse; (b) Uniaxial specimen E1 with initial crack $a_0 = 0.789$ mm, failure mode determined as ductile tearing.

Table 5.6 Failure assessment results for uniaxial specimens with surface crack

	Specimen designation	Failure load (predicted) F_{axial} in kN	Failure load (test) F_{axial} in kN	Relative difference to test	Failure mode (predicted)	$L_{\mathrm{r}}^{\mathrm{max}}{}_{\mathrm{test}}$
Pre-test (uniaxial) with surface crack	E1	47.05	47.7	-1.4%	Ductile tearing	1.1798
Test (uniaxial) with surface crack	E2	49.14	54.8	-10.3%	Plastic collapse	1.3506
	E3	49.02	54.7	-10.4%	Plastic collapse	1.3487
	D1	48.61	52.1	-6.7%	Plastic collapse	1.2712
	D3	48.86	51.6	-5.3%	Plastic collapse	1.2613
	B1	48.90	54.7	-10.6%	Plastic collapse	1.3525
	B2	49.06	54.5	-10.0%	Plastic collapse	1.3398
	A1	48.90	52.5	-6.9%	Plastic collapse	1.2839
	A2	48.90	52.5	-6.8%	Plastic collapse	1.2838
	A3	48.90	53.6	-8.8%	Plastic collapse	1.3176

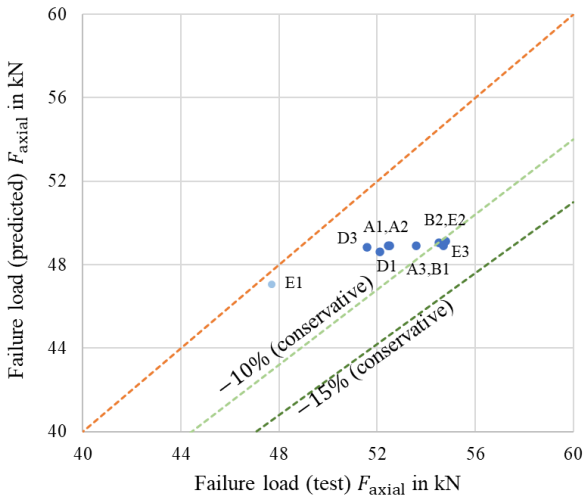

Figure 5.29 Summary of predicted failure load versus failure load recorded in test for all uniaxial specimens.

6. Implementation of the methodology for structural integrity assessment of metallic component

6.1. Introduction

The established assessment methodology has been implemented on the investigated turbined disk with the inputs from the specimen test results. The critical loads have been determined for both critical locations on the turbine disk based on two-criteria failure assessment method with the critical ligament yielding parameters determined from specimen tests. Additionally, an independent numerical burst speed assessment method based on Hill's global stability criterion has been established for the turbine disk. Critical loads were also determined for the component based on this method. These critical loads have been compared against the values determined from the spin-tests, which have shown good agreement. Eventually, a structural integrity assessment procedure for the turbine disk has been established for the engineering use.

6.2. Determination of critical load for the turbine disk

The critical load in terms of rotational speed for the turbine disk has been determined based on the established two-criteria failure assessment method. The maximum ligament yielding parameter ${L_{\mathrm{r}}^{\max}}_{\mathrm{test}}$ acquired from specimen tests have been used to replace $L_{\mathrm{r}}^{\max}$ for the plastic collapse limit load determination.

6.2.1. Critical load for diaphragm (rim peel)

The structural integrity assessment for the diaphragm on the investigated turbine disk has been carried out based on the two-criteria failure assessment method as introduced in section 2.2.1. Firstly, in order to determine the limit load for failure mode plastic collapse, FE simulations have been conducted for stepwise increasing crack size. As discussed in section 3.3, semi-circular surface crack has been modelled at the critical location at diaphragm. The FE model described in section 3.3.3 (Figure 3.8) has been used as a baseline. The crack-tip loadings in terms of J-integral were determined for different crack size at the critical location along the crack-front.

To determine the remote reference stress, FE simulations with the turbine disk FE model without crack (Figure 3.6) using the elastic material properties has been conducted. As is shown in Figure 6.1, the

radial stresses (normalised with yield stress) acquired from the element centroid at the diaphragm critical location have been plotted against rotational speed (normalised with reference overspeed N_a as introduced in section 3.3.1). Thermal stress as a result of temperature gradient has also been considered in the assessment, shown at $N = 0$ in Figure 6.1.

The reference yield stress σ_0 for each crack depth a has been determined based on the FE simulation results with the target J/J_e of 1.7220, which has been determined for a temperature of 425 °C. An example of reference yield stress determination has been shown in Figure 6.2a for the semi-circular surface crack of size $a = 0.50$ mm at diaphragm, which turned out to be $1.370\sigma_Y$. The complete results of reference yield stress for different crack sizes determined at the critical point along the crack-front were shown in Figure 6.2b, which decreased as the crack size increased.

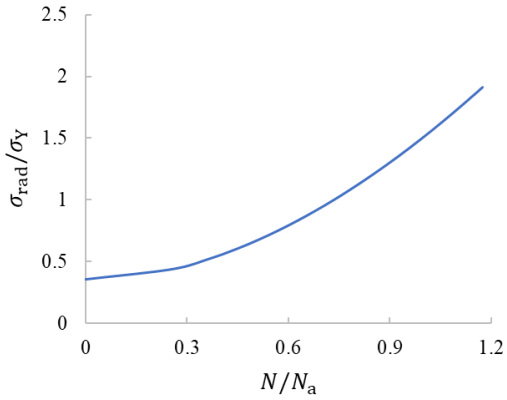

Figure 6.1 Radial stress versus rotational speed curve for critical location at diaphragm of the FE simulation for uncracked turbine disk with elastic material properties, N_a is the reference overspeed.

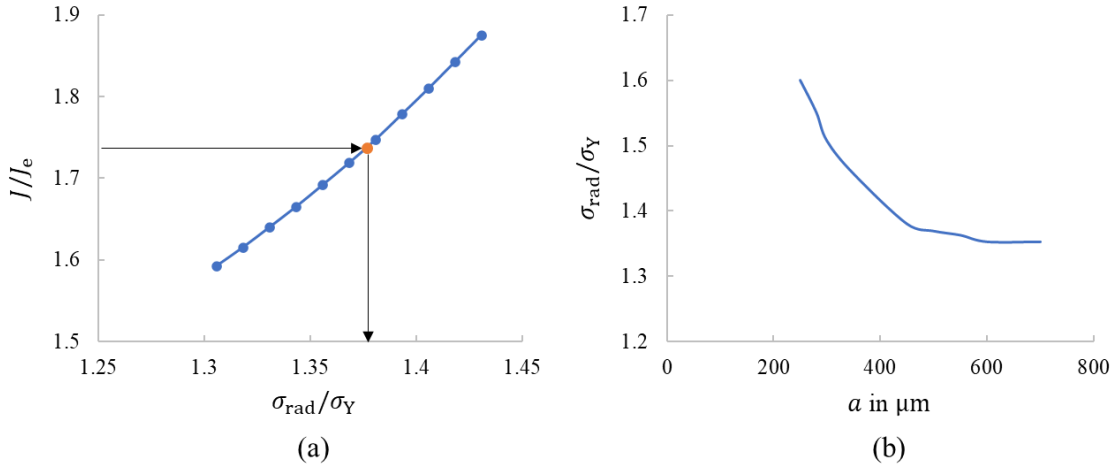

Figure 6.2 Determination of the reference yield stress for different crack sizes (semi-circular surface crack) at turbine disk diaphragm: (a) Determination of the reference yield stress for a crack of size $a = 0.50$ mm; (b) Reference yield stress for different crack sizes at diaphragm.

Since all the biaxial specimen designed to represent the crack-tip loading conditions of the turbine disk diaphragm have been determined to have failure mode plastic collapse, the critical ligament yielding

parameter $L_{\mathrm{r}}^{\max}{}_{\mathrm{test}}$ at failure of each biaxial specimen has been chosen to replace $L_{\mathrm{r}}^{\max}$ in the analytical calculation of limit load for plastic collapse at diaphragm. Since the initial pre-cracks of all six biaxial tests (the two pre-tests excluded) were considered valid with respect to the design value (within +/- 10% relative deviation), the $L_{\mathrm{r}}^{\max}{}_{\mathrm{test}}$ values from these tests were used. The limit load curves for plastic collapse at diaphragm were illustrated in Figure 6.3 with the notation on which specimen the $L_{\mathrm{r}}^{\max}{}_{\mathrm{test}}$ has been based. Since the $L_{\mathrm{r}}^{\max}{}_{\mathrm{test}}$ values were similar between biaxial specimen D1 and E1, C1 and D2, B1 and C2, the limit load curves in Figure 6.3 have fallen into three groups.

Similar to the assessment of fracture mechanics specimen, the load versus stable crack extension curve was also generated for the surface crack at turbine disk diaphragm following the workflow illustrated in Figure 5.4. For the assessment of an initial semi-circular surface crack of size $a_0 = 0.381$ mm, the FE simulations of the turbine disk with surface crack at diaphragm have been carried out for crack sizes a of 0.40 mm, 0.45 mm, 0.50 mm, 0.55 mm, 0.60 mm and 0.70 mm to determine the crack-tip loading in terms of J-integral. The R-curve from the biaxial specimen test has been used to determine the fracture toughness J_{mat} for each crack size.

Eventually, based on the two-criteria failure assessment method, the load versus stable crack extension curve for the turbine disk with an initial surface crack of size $a_0 = 0.381$ mm at diaphragm was illustrated together with limit load curves for plastic collapse based on biaxial test results in Figure 6.3. Since the load versus stable crack extension curve crossed all the limit load curves for plastic collapse before reaching its maximum value, the failure mode of plastic collapse could be determined. The failure loads in terms of radial stress were $1.585\sigma_{\mathrm{Y}}$ for specimen B1 and C2 based values, $1.626\sigma_{\mathrm{Y}}$ for specimen C1 and D2 based values as well as $1.645\sigma_{\mathrm{Y}}$ for specimen D1 and E1 based values. These values have been converted to rotational speeds based on the curve from Figure 6.1, which have been $1.034N_{\mathrm{a}}$, $1.053N_{\mathrm{a}}$ and $1.062N_{\mathrm{a}}$, respectively.

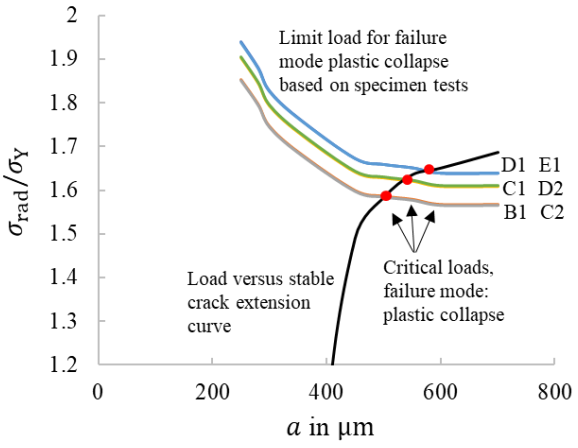

Figure 6.3 Two-criteria failure assessment of the turbine disk diaphragm with semi-circular surface crack of size $a_0 = 0.381$ mm, limit load curves for plastic collapse determined based on $L_{\mathrm{r}}^{\max}{}_{\mathrm{test}}$ values from biaxial specimen tests, failure mode determined as plastic collapse for diaphragm.

6.2.2. Critical load for bore (hoop burst)

Following the same procedure, the structural integrity assessment for the bore on the investigated turbine disk has been carried out based on the two-criteria failure assessment method.

The results of elastic hoop stress have been acquired from the critical location at bore (element centroid) of the turbine disk, using the FE model discussed in the last section but with the most adverse temperature field for bore. The hoop stress has been plotted against rotational speed in Figure 6.4. Thermal stress as a result of temperature gradient has also been considered in the assessment, shown at $N = 0$ in Figure 6.4. The reference yield stress σ_0 for each crack depth a has been determined based on the FE simulation results with the target J/J_e of 1.7002 under a temperature of 350 °C. An example of reference yield stress determination has been shown in Figure 6.5a for the semi-circular surface crack of size $a = 0.50$ mm at bore, which turned out to be $1.285\sigma_Y$. The complete results of reference yield stress for different crack sizes determined at the critical point along the crack-front were shown in Figure 6.5b, which decreased as the crack size increased.

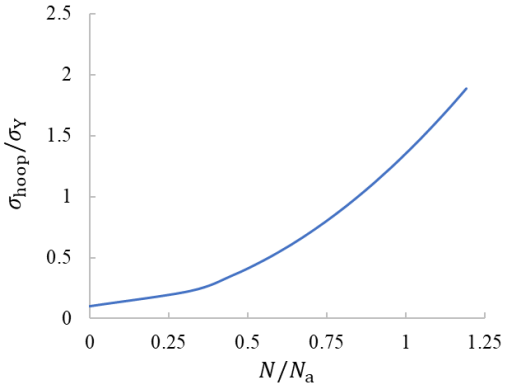

Figure 6.4 Hoop stress versus rotational speed curve for critical location at bore of the FE simulation for uncracked turbine disk with elastic material properties, N_a is the reference overspeed.

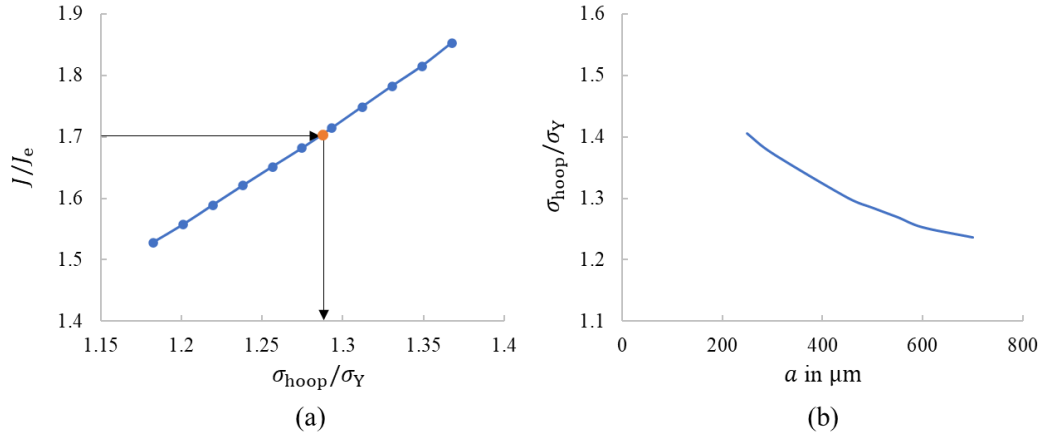

Figure 6.5 Determination of the reference yield stress for different crack sizes (semi-circular surface crack) at turbine disk bore: (a) Determination of the reference yield stress for a crack of size $a = 0.50$ mm; (b) Reference yield stress for different crack sizes at bore.

The initial pre-crack size a_0 of the uniaxial specimens have been compared to the designed value of 0.381 mm. As a result, five of the uniaxial specimens (A1, A2, A3, B1 and D3) remained with the +/- 10% relative deviation with respect to the designed value and were considered valid for the critical ligament yielding parameter ${L_{\mathrm{r}}^{\max}}_{\mathrm{test}}$ determination.

As discussed in section 5.4.3, the assessment of uniaxial tests suggested that the failure mode of the selected five uniaxial specimens was plastic collapse. Therefore, the limit load curves for plastic collapse at bore were determined based on the critical ligament yielding parameter ${L_{\mathrm{r}}^{\max}}_{\mathrm{test}}$ acquired from the five selected uniaxial tests. These curves have been shown in Figure 6.6 with uniaxial specimen designations. The uniaxial R-curve has been used to determine the load versus stable crack extension curve for the bore crack. Following the same procedure as done for the diaphragm crack, the load versus stable crack extension curve for an initial semi-circular surface crack of size $a_0 = 0.381\ \mathrm{mm}$ has been determined based on the FE simulations, in which the same series of semi-circular surface crack geometries have been modelled at the bore on the turbine disk.

Based on the two-criteria failure assessment method, the load versus stable crack extension curve for the turbine disk with an initial surface crack of size $a_0 = 0.381\ \mathrm{mm}$ at bore was shown together with limit load curves for plastic collapse based on uniaxial test results in Figure 6.6. The failure mode of plastic collapse could be determined. The failure loads in terms of hoop stress were $1.628\sigma_{\mathrm{Y}}$ for specimen D3 based values, $1.651\sigma_{\mathrm{Y}}$ for specimen A1 and A2 based values, $1.688\sigma_{\mathrm{Y}}$ for specimen A3 based values as well as $1.721\sigma_{\mathrm{Y}}$ for specimen B1 based values. These values have been converted to rotational speeds based on the curve from Figure 6.4, which have been $1.103N_{\mathrm{a}}$, $1.111N_{\mathrm{a}}$, $1.124N_{\mathrm{a}}$, and $1.136N_{\mathrm{a}}$, respectively.

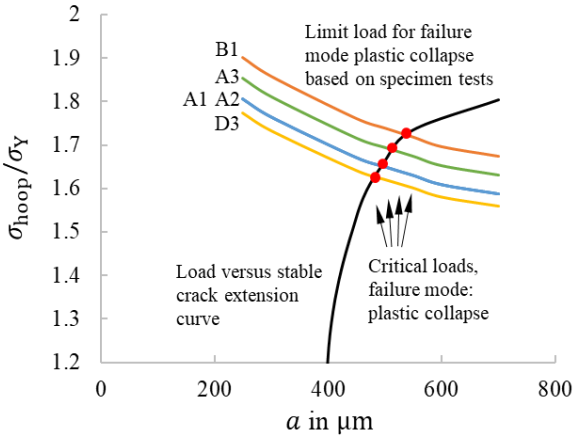

Figure 6.6 Two-criteria failure assessment of the turbine disk bore with semi-circular surface crack of size $a_0 = 0.381\ \mathrm{mm}$, limit load curves for plastic collapse determined based on ${L_{\mathrm{r}}^{\max}}_{\mathrm{test}}$ values from uniaxial specimen tests, failure mode determined as plastic collapse for bore.

6.3. Methodology validation with spin-test results

The structural integrity assessment methodology presented in this work has been validated by comparing the critical loads determined by the methodology for both turbine disk critical locations, or in other words for both failure mode rim peel and hoop burst to the values acquired from the two spin-tests.

For the critical load at diaphragm (investigated turbine disk) for failure mode rim peel, the critical load acquired from rim peel spin test in terms of radial stress has been converted to the rotational speed of the investigated turbine disk by conducting FE simulation using elastic-plastic material properties. Since the rim peel spin test has been designed with a thin diaphragm thickness that recreated the worst loading conditions of the investigated disk diaphragm, the radial stress (elastic-plastic) at the critical diaphragm location has been plotted against rotational speed in Figure 6.7. Based on the critical load acquired from rim peel spin test $\sigma_{\mathrm{rad}} = 1.293\sigma_{\mathrm{Y}}$, the critical rotational speed for diaphragm has been determined as $1.099N_{\mathrm{a}}$.

Compared against the critical rotational speeds (for diaphragm) determined using the assessment procedures proposed in this work, the predicted values have been 4.5% lower than the spin test value in average. This has been considered reasonable since there has been a stress gradient (see Figure 3.21) in the maximum crack extension direction (ca. 10° from specimen surface) in the biaxial specimen. Especially the stress in the A-axis direction increased ahead of the crack-front with increasing crack size. Consequently, the stress ratio at the plastic collapse of the biaxial specimen ($\lambda = 0.68$) has been higher than it in the spin-test disk ($\lambda = 0.587$), which meant the critical plastic collapse load predicted by the biaxial specimen would be lower than by the spin-test.

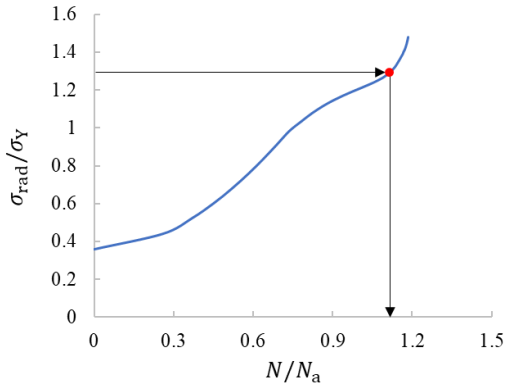

Figure 6.7 Radial stress (elastic-plastic) versus rotational speed at critical diaphragm location of investigated turbine disk.

For the critical position bore (failure mode hoop burst), the critical load in terms of AWMHS determined from the hoop burst spin-test $\sigma_{\mathrm{hoop}} = 1.070\sigma_{\mathrm{Y}}$ has been converted to the critical rotational speed for the investigated turbine disk using the AWMHS results discussed in section 3.3.1, which took the value of $1.071N_{\mathrm{a}}$. The usage of the AWMHS for stress correlation has been discussed in 4.5.2. Additionally, the secondary stress in bore area due to plastic deformation has been high enough so that only after the redistribution the remaining primary stress could represent the real plastic collapse limit. Note that the test disk used in the spin-test has not failed at the maximum

rotational speed tested. As a result, this critical speed of $1.071N_{\mathrm{a}}$ was considered a "safe" plastic collapse limit. Compared against the critical rotational speeds (for bore) determined using the assessment procedures proposed in this work, the predicted values have been 4.4% higher than the spin test value in average, which effectively increased the safety margin for hoop burst proof.

Despite the fact that both spin-test disks have not formally failed during the test, the predicted critical rotational speeds by the proposed assessment procedure have shown good agreement with the spin-test results. Moreover, in comparison to the failure assessment of the investigated turbine disk based on BS7910 option 3 FAD standard approach reported in [2.14] by the author et al, an increase of up to 5.6% in the predicted rotational speed could be observed for the proposed procedure, which showed the benefits of the representative specimen-based assessment procedure. It has been also planned to conduct additional spin-tests for further methodology validation, in which mini-disks with initial cracks at both critical locations would be tested.

6.4. Critical load assessment based on global stability criterion

As introduced in section 2.2.3, a second independent approach based on Hill's global stability criterion has been considered to calculate the critical load for the investigated turbine disk for comparison. In contrast to the fracture mechanics-based methodology, this global stability criterion-based approach used a single energy-based parameter MSOW to judge the stability of the whole turbine disk domain. As a result, different failure modes cannot be determined, instead, a global failure load could be calculated. The following results have been published in [2.14].

The calculation of parameter MSOW according to Eq. (2.9) has been implemented into FE program ABAQUS using UMAT as discussed in section 2.2.3. The UMAT has been verified with respect to the original built-in material model in ABAQUS using a single hexahedral element model under tension, leading thereby to agreeing results (0.04% average difference for σ_{vM}). Also, the calculation of the deformation gradient $\boldsymbol{F}$ has been verified with an analytical solution. A third verification of the UMAT has been conducted on the investigated turbine disk with regard to the built-in material model in ABAQUS (Figure 6.8). The average difference in σ_{vM} between the two models has been found to be 0.06%.

To avoid numerical instability, the time-independent simulations made use of small time increments. After each increment, the MSOW has been calculated for the whole turbine disk domain. To make the MSOW comparable between different time increments, it has been normalised with respect to the spin softening term $\int_{\Omega_{\mathrm{d0}}}(\rho_0\|\boldsymbol{V}\times\boldsymbol{\omega}\|^2)\,dv_0$ (see Eq. (2.9)). When the rotational speed reached the overspeed condition, the time increment has been refined for better precision. The simulations have been carried out for the cracked disk as well as for the turbine disk models without crack (solid disk) (Figure 6.9). Note that the worst-case-scenario temperature profiles of the turbine disk are different for both cases. The results in Figure 6.9 showed that the critical rotational speed based on the global stability criterion has been $1.176N_{\mathrm{a}}$ for all four simulations, with relative differences within 0.09%. The trends of the normalised MSOW with an increasing rotational speed for turbine disks with and without

crack were shown to be almost identical (with an average relative difference within 3%). In other words, the cracks have a negligible influence on the stability behaviour for both locations. However, comparing the results of the disk without crack (solid disk) between (a) and (b) in Figure 6.9, it could be concluded that the difference in thermal stresses due to different temperature profiles, had a noteworthy influence on the normalised MSOW value at the beginning of the overspeed regime until approximately $1.1N_{\mathrm{a}}$. However, this influence has been compensated by the higher deformation of the disk with higher rotational speed such that critical rotational speed was not affected.

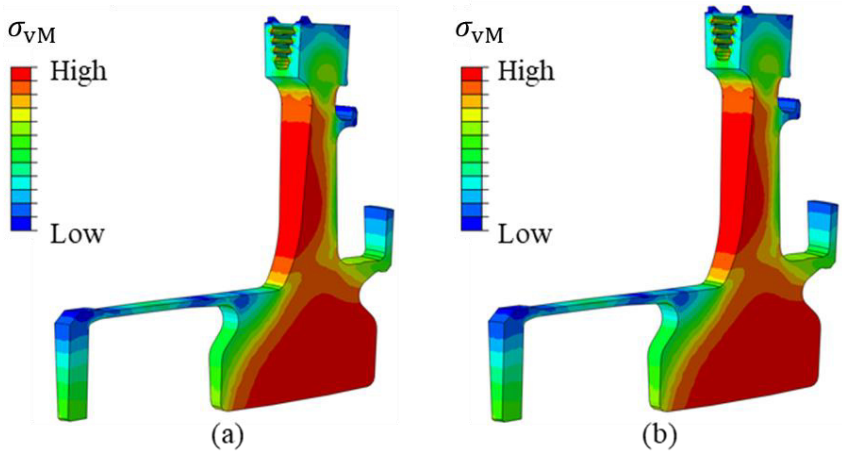

Figure 6.8 Verification of the UMAT on the investigated turbine disk against original built-in material model in ABAQUS in form of von Mises stress distribution: (a) UMAT; (b) original built-in material model in ABAQUS [2.14].

Additional RIKS-analyses (arc length method [6.1, 6.2]) have been carried out for comparison with the previous analyses. The Load Proportional Factor, or LPF and the corresponding rotational speed of the RIKS-analysis were shown in Figure 6.10. The LPF is defined as the current load (in this simulation the rotational body force) divided by the final load given in the INPUT-file. This approach provided solutions regardless of whether the response is stable or unstable [6.1]. For the diaphragm case, the maximum LPF was 0.966 at an arc length of 25.85, which corresponds to a rotational speed of $1.177N_{\mathrm{a}}$ (Figure 6.9a), whereas the peak LPF was 0.958 with an arc length of 25.85 for the bore case. The latter corresponds to a rotational speed of $1.176N_{\mathrm{a}}$ (Figure 6.9b). It could be concluded that the RIKS-analyses were in good agreement with the results of the global stability criterion analyses.

An overview of the predicted critical rotational speeds using the proposed two-criteria failure assessment method as well as Hill's global stability criterion has been given in Table 6.1 with comparison to the spin-test results. Despite the fact that both spin-test disks have not formally failed during the test, the predicted critical rotational speeds by the proposed assessment procedure have shown good agreement with the spin-test results with 4.5% and 4.4% average relative deviation for diaphragm and bore, respectively. The assessment based on Hill's stability criterion has yielded less conservative results for both diaphragm and bore locations with 7.0% and 9.8% relative deviation with respect to sin-test results. When compared within the same assessment method, the two-criteria failure assessment procedure as well as the spin-test have shown that the diaphragm has been more critical than the bore on the investigated turbine disk, as the critical rotational speeds for diaphragm

have been lower than for bore. However, based on the Hill's global stability criterion, there has been no noticeable difference for both turbine disk locations in terms of critical rotational speed.

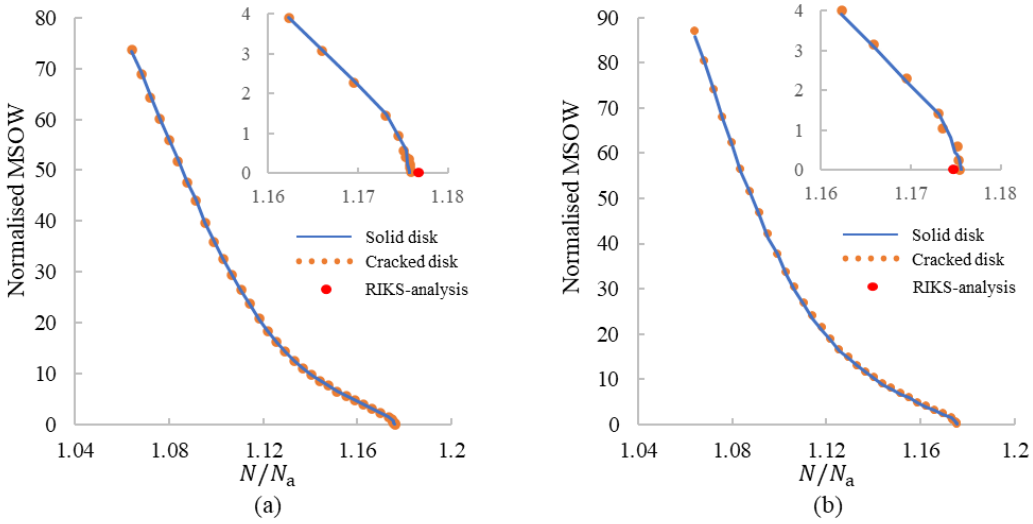

Figure 6.9 Determination of the critical rotational based on Hill's global stability criterion (RIKS-analysis shown for reference), N_a is the analytically calculated reference overspeed based on the method used by the engine manufacturer: (a) turbine disk with and without crack at the diaphragm, critical temperature profile for diaphragm; (b) turbine disk with and without crack at bore, critical temperature profile for bore [2.14].

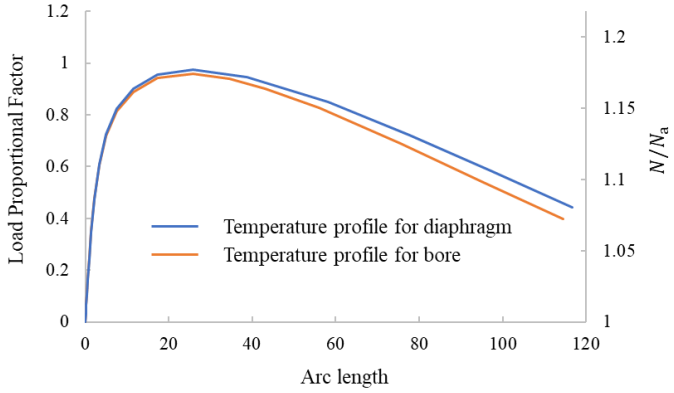

Figure 6.10 Profile of the Load Proportional Factor and the corresponding rotational speed in RIKS-analysis for the turbine disk without crack using the critical temperature profiles for both locations [2.14].

Table 6.1 Critical rotational speed (normalised with respect to N_a) determined by the presented procedure and method

	Two-criteria failure assessment procedure	Hill's global stability criterion	Spin-test
Rim peel (diaphragm)	$1.034N_a$	$1.176N_a$	$1.099N_a$
	$1.053N_a$		
	$1.062N_a$		
Hoop burst (bore)	$1.103N_a$	$1.176N_a$	$1.071N_a$
	$1.111N_a$		
	$1.124N_a$		
	$1.136N_a$		

6.5. Formulation of structural integrity assessment procedure

The structural integrity assessment procedure for metallic component based on representative specimens has been formulated as follows:

- Stress analysis of the component under worst-case operation conditions to identify critical locations or regions on the component. (numerical or analytical)
- Consideration of the component with crack at the critical locations. Crack geometry and size based on regulations, field experience or NDI limits etc. Determination of the crack driving force and constraint parameters for the critical location along the crack-front. (numerical or analytical)
- Design of representative specimens with crack. Design targets: maintain comparable loading conditions (mechanical and thermal) as in each component critical location, maintain same crack driving force and constraint parameters at the critical position along the crack-front as in each component critical location. Material of the designed specimen should be identical to the component.
- Experiments of the designed specimens to acquire R-curves for each component critical location, failure loads and modes.
- Determination of the reference yield stress and critical ligament yielding parameter for each component critical location. (numerical or analytical)
- Failure assessment of each component critical location using two-criteria failure assessment method based on the acquired R-curve and critical ligament yielding parameter. Determination of failure mode and load for each component critical location. (numerical or analytical)

Concluding remarks

The presented work addressed the development of a novel structural integrity assessment procedure for metallic component based on representative specimens.

The fracture mechanics-based assessment procedure has been developed with the application on the Ni base superalloy gas turbine disk used in aero-engines. In contrast to the failure assessment based on elaborate component test, the representative specimens have been designed to recreate the critical loading conditions of the turbine disk during an overspeed case. Firstly, the turbine disk has been analysed by means of FE simulations using the worst-case-scenario boundary conditions for the overspeed case. Under mechanical and thermal loadings, the critical locations on the turbine disk have been determined (at diaphragm and bore). Then, under consideration of damage tolerance criterion and regulations, a surface crack of size 0.381 mm has been modelled at the determined critical locations on the turbine disk. Under a reference overspeed condition, the crack driving force in terms of J-integral as well as two constraint parameters, stress triaxiality factor h and local constraint parameter α_1, have been determined along the crack-front. The critical position along the crack-front at both locations on the component has been determined as the position with the highest J-integral and constraint parameter values.

Based on these values, the representative specimens have been designed using FE simulations. For diaphragm location, where the crack has been under biaxial loading conditions, biaxial specimen with through-crack as well as surface crack has been designed. The design criteria for biaxial specimen have been to maintain the same crack driving force in terms of J-integral, the same biaxial stress ratio and comparable constraint parameters as in the turbine disk diaphragm. For the biaxial specimen with through-crack, the homogenous J-integral and constraint parameter values along its crack-front represent the critical position along the crack-front on the component, whereas in the biaxial specimen with surface crack, all parameters along its crack-front matched the turbine disk crack-front values. For the bore location, where the crack has been under uniaxial loading condition, uniaxial specimen with surface crack has been designed. With the same design criteria except for the biaxial stress ratio, the uniaxial specimen has been designed such that all three parameters along the crack-front matched the target values of the turbine disk crack.

The experiments of the designed representative specimens, which have been manufactured from a production turbine disk provided by the engine manufacturer, have been conducted. Crack growth resistance curves (R-curve) have been determined based on the test results of designed biaxial and uniaxial specimens and FE simulations, respectively. The failure loads of the representative specimens have been recorded during the quasi-static tensile tests. The failure mode of the biaxial specimens has been determined as plastic collapse by means of strain field analysis based on Digital Image Correlation (DIC) methods.

Using the proposed two-criteria failure assessment method, the tested representative specimens have been analysed to determine the failure mode and load. With help of FE simulations, the plastic collapse loads have been determined for different crack sizes based on the reference yield stress and analytical solutions. Using the R-curve determined previously, the load versus stable crack extension curve has been generated for each tested specimen by means of FE simulations. The critical failure load and mode (between ductile tearing and plastic collapse) have been determined for each tested specimen by plotting the limit curve for plastic collapse load and the load versus stable crack extension together. For the specimens with a comparable initial crack size as design value, the failure mode has been determined as plastic collapse by the assessment method. The predicted failure load results by the assessment method have been compared against the test results and have been conservative with an average 1.85% relative difference for biaxial specimens and 8.42% for uniaxial. The critical ligament yielding parameters have been determined for both turbine disk critical locations based on specimen test results.

The failure assessment for the investigated turbine disk has been conducted using the two-criteria failure assessment method based on the R-curves and critical ligament yielding parameters determined for both turbine disk critical locations. Failure mode of plastic collapse have been determined for both locations. Failure load in terms of critical rotational speeds for diaphragm (rim peel) and bore (hoop burst) have been determined. Compared with the predicted critical rotational speed by the standard BS7910 approach using option 3 FAD assessment, a benefit of up to 5.6% in critical rotational speed has been concluded. In addition, spin-tests have been carried out by the engine manufacturer, in which two production-similar test disks were tested. Despite the fact that both spin-test disks have not formally failed during the test, the predicted critical rotational speeds by the proposed assessment procedure have shown good agreement with the spin-test results with up to 4.5% relative difference. An additional independent burst speed assessment method based on Hill's global stability criterion has been implemented for the investigated bladed turbine disk. The numerical method has yielded less conservative critical rotational speed in comparison to the values discussed above. Consequently, a structural integrity assessment procedure for metallic component based on representative specimens has been formulated. In particular, for the future industrial usage of the proposed structural integrity assessment procedure, additional scale factors could be imposed onto the fracture toughness values for failure mode ductile tearing and onto the maximum ligament yielding parameter for failure mode plastic collapse based on material property values statistical distributions as e.g., suggested by the author et al. in [6.3].

List of Figures

Figure 1.1 Example of a Failure Assessment Diagram according to BS7910 [1.1]. 5

Figure 1.2 Example of a SINTAP assessment based on FAD approach including constraint effects [1.3]. 8

Figure 1.3 Failure Assessment Diagram (FAD) for a constant crack size under increasing load [1.3]..... 9

Figure 1.4 Ligament yielding ranges and corresponding failure mechanisms in a FAD [1.1]..... 9

Figure 1.5 Determination of the critical condition of a component following the CDF philosophy when the fracture toughness is given by a single value. The $L\mathrm{rmax}$ limit assigns the plastic collapse limit [1.3]. 12

Figure 1.6 Types of CDF analysis for determining the instability load of a component for failure mode ductile tearing: (a) CDF curves are determined for constant applied loads and compared with the R-curve of the material ($a0$ marks the original crack size in the component); (b) The load versus stable crack extension curve determined following the route in Figure 1.7 [1.3]. 12

Figure 1.7 Flow chart for determining the applied load versus stable crack extension characteristics in Figure 1.6b [1.3]..... 13

Figure 1.8 Comparison of $J - Qavg$ trajectories for SE(T) specimens and cracked pipes: (a) pin-loaded SE(T); (b) clamped SE(T) [1.11]. 14

Figure 1.9 Intersection of crack driving force lines with material toughness locus for cracked pipes with different crack sizes based on $J - Ap$ and $J - Ad$ approaches [1.12]..... 15

Figure 1.10 Constraint modified Option 3 FALs, k is the biaxiality ratio with k=0 being uniaxial [1.14]. 16

Figure 1.11 Failure Assessment diagram for a pipe with coplanar surface cracks under combined internal pressure and axial tension (modified from [1.16]). 17

Figure 1.12 Reference yield stress as function of crack size determined for the steering knuckle by finite element analysis: (a) reference yield stress versus crack depth curves; (b) Schematic view of the investigated component (modified from [1.22]). 18

Figure 1.13 Cutaway of an aircraft engine (modified from [1.26]). 19

Figure 1.14 Cross section of a typical bladed turbine disk. 20

Figure 1.15 Rotor integrity failure modes. 20

Figure 1.16 Hoop carrying section and strip domain on diaphragm of a typical turbine disk. 21

Figure 2.1 Two-criteria failure assessment method to take into consideration of the stable crack extension, failure mode of ductile tearing and failure mode of plastic collapse under increasing applied load: (a) Failure of component in form of ductile tearing; (b) Failure of component in form of plastic collapse. 26

Figure 2.2 Local stress triaxiality factor h ahead of the crack-tip (σe: von Mises equivalent stress) [2.1]. 27

Figure 2.3 Linear extrapolation of local triaxiality h to the crack-tip (σe: von Mises equivalent stress) [2.1]. 27

Figure 2.4 Calculation of the local constraint parameter αl for the considered node in the FE mesh on the plane of the uncracked ligament. 28

Figure 2.5 General definition of the mechanical problem for a rotating disk (modified from [2.10]). 29

Figure 2.6 Layout of the assessment procedure in ABAQUS (post-processing in Matlab) based on Hill's global stability criterion including the UMAT for the investigated turbine disk model [2.14]. 31

Figure 2.7 Temperature-dependent material properties of Udimet 720Li at different heat treatment conditions: (a) yield strength (0.2% offset); (b) ultimate tensile strength [2.15] [2.18]. 33

Figure 3.1 Elastic-plastic behaviour of the Udimet 720Li in Ramberg-Osgood formulation at different temperatures. 35

Figure 3.2 Geometry of the investigated turbine disk and blade. 36

Figure 3.3 Temperature profile in hoop carrying section at worst-case-scenario. 37

Figure 3.4 FE model of the turbine disk: (a) Meshing strategy for the turbine disk and the turbine blade investigated to determine the AWMHS; (b) Elastic hoop stress distribution of the hoop carrying section. 38

Figure 3.5 Elastic radial stress distribution on the turbine disk with refined mesh at diaphragm area. 39

Figure 3.6 FE model of the turbine disk: (a) Meshing strategy for the turbine disk and the turbine blade investigated to identify the critical locations; (b) Von Mises stress distribution under mechanical and thermal stress at reference overspeed condition $N\mathrm{a}$ (with elastic-plastic material properties). The two local high-stressed locations are marked with 1 (diaphragm) corresponding to rim-peeling failure mode and 2 (bore) corresponding to hoop-burst failure mode. 40

Figure 3.7 Principal stress distributions on the turbine disk under reference overspeed condition $N\mathrm{a}$ (simulations with elastic-plastic material properties): (a) Radial stress distribution; (b) Hoop stress distribution. 40

Figure 3.8 Meshing strategy for the semi-circular crack of size $a = c = 0.381\ \mathrm{mm}$ at diaphragm (location 1 in Figure 3.6b) and local mesh refinement at the crack-front for fracture mechanics analysis (single sector model): (a) global view; (b) local magnification [2.14]. 41

Figure 3.9 Constraint parameter distributions on the ligament of crack plane, crack at diaphragm under rotational speed of $N\mathrm{a}$: (a) Stress triaxiality factor h; (b) Local constraint parameter $\alpha\mathrm{l}$. . 42

Figure 3.10 Evaluation of the stress triaxiality factor h and the local constraint parameter $\alpha\mathrm{l}$ of the surface crack at diaphragm: (a) trend of the h ahead of the crack-tip at an angle of 22.5° under $100\%N\mathrm{a}$; (b) variation of h along the crack-front with various rotational speeds; (c) trend of the $\alpha\mathrm{l}$ ahead of the crack-tip at an angle of 22.5° under $100\%N\mathrm{a}$; (d) variation of $\alpha\mathrm{l}$ along the crack-front with various rotational speeds. 43

Figure 3.11 Profile of the parameters J, h and $\alpha\mathrm{l}$ along the crack-front of the surface crack at diaphragm under overspeed condition $N\mathrm{a}$. 44

Figure 3.12 Meshing strategy for the FE model comprising a turbine disk sector with two turbine blades: (a) Model overview; (b) Magnification of crack location. 44

Figure 3.13 Meshing strategy for the semi-circular crack of size $a = c = 0.381\ \mathrm{mm}$ at bore (location 2 in Figure 3.6b) and local mesh refinement at the crack-front for fracture mechanics analysis (single sector model): (a) global view; (b) local magnification [2.14]. 45

Figure 3.14 Constraint parameter distributions on the ligament of crack plane, crack at bore under rotational speed of $N\mathrm{a}$: (a) Stress triaxiality factor h; (b) Local constraint parameter $\alpha\mathrm{l}$. 46

Figure 3.15 Evaluation of the stress triaxiality factor h and the local constraint parameter $\alpha\mathrm{l}$ of the surface crack at bore: (a) trend of the h ahead of the crack-tip at an angle of 90° under $N\mathrm{a}$; (b) variation of h along the crack-front with various rotational speeds; (c) trend of the $\alpha\mathrm{l}$ ahead of the crack-tip at an angle of 90° under $N\mathrm{a}$; (d) variation of $\alpha\mathrm{l}$ along the crack-front with various rotational speeds. 47

Figure 3.16 Profile of the parameters J, h and $\alpha\mathrm{l}$ along the crack-front of the surface crack at bore under overspeed condition $N\mathrm{a}$. 48

Figure 3.17 Baseline biaxial fracture mechanics specimen provided by MPA Darmstadt [4.1]. 49

Figure 3.18 Heat transfer model of the baseline biaxial specimen, simplified quarter model without fixture wings. 49

Figure 3.19 Dimensional parameters for geometry modification of the biaxial specimen (side view of eighth model). 50

Figure 3.20 FE model of the biaxial specimen with modified geometry for determination of remote stresses at specimen centre. 50

Figure 3.21 Remote stress distribution on the modified biaxial specimen. 51

Figure 3.22 Modified biaxial specimen with through-thickness hole in the centre and initial through cracks (hole and cracks not in original scale). 52

Figure 3.23 FE model for biaxial specimen with through-thickness hole in the centre and initial through crack: (a) Mesh strategy for the eighth model in global view; (b) Mesh refinement in specimen centre. 53

Figure 3.24 Comparison of parameters between diaphragm crack and through-crack: (a) Constraint parameters at the critical position along the crack-front for different through-crack geometry configurations and diaphragm crack on turbine disk, with J-integral values of 14.54 N/mm; (b) remote stresses for uncracked biaxial specimen with corresponding tensile loads. 54

Figure 3.25 Modified biaxial specimen with notch in the centre and initial surface crack (notch and crack not in original scale). 55

Figure 3.26 FE model for biaxial specimen with notch in the centre and initial surface crack: (a) Mesh strategy for the quarter model in global view; (b) Mesh refinement in specimen centre. 55

Figure 3.27 Comparison of constraint parameters and J-integral along the crack-front of the semi-circular surface cracks of size $a = c = 0.381$ mm on turbine disk diaphragm under Na (solid) and on biaxial specimen (dashed): (a) Biaxial specimen with 0.25 mm notch depth; (b) Biaxial specimen with 0.20 mm notch depth. 56

Figure 3.28 Flat uniaxial fracture mechanics specimen geometry with 40 mm^2 cross-section testing area 57

Figure 3.29 FE model for flat uniaxial specimen (U-A) with notch in the centre and initial surface crack, contact surfaces between specimen and clamping jaws in dotted area: (a) Mesh strategy for the quarter model in global view; (b) Mesh refinement in specimen centre. 58

Figure 3.30 Comparison of constraint parameters and J-integral along the crack-front of the semi-circular surface cracks of size $a = c = 0.381$ mm on turbine disk bore under Na (solid) and on flat uniaxial specimen (dashed) with 0.25 mm notch depth: (a) Flat uniaxial specimen variant U-A; (b) Flat uniaxial specimen variant U-B; (c) Flat uniaxial specimen variant U-C. 59

Figure 3.31 Round uniaxial fracture mechanics specimen geometry with 40.48 mm^2 cross-section testing area. 60

Figure 3.32 FE model for round uniaxial specimen with notch in the centre and initial surface crack: (a) Mesh strategy for the quarter model in global view; (b) Mesh refinement in specimen centre. 61

Figure 3.33 Comparison of constraint parameters and J-integral along the crack-front of the semi-circular surface cracks of size $a = c = 0.381\ \mathrm{mm}$ on turbine disk bore under Na (solid) and on round uniaxial specimen (dashed) with 0.25 mm notch depth. 61

Figure 4.1 High pressure turbine disk made of Udimet 720Li used for specimen extraction [4.1]: (a) Top view; (b) Bottom view. 63

Figure 4.2 Specimen extraction plan [4.1]: (a) Specimen extraction location on the turbine disk, biaxial specimen (two specimens per group) from diaphragm, uniaxial specimen (three specimens per group) from bore; (b) Top view; (c) Bottom view. 63

Figure 4.3 Extracted specimen after finishing process: (a) Biaxial specimen [4.1]; (b) Uniaxial specimen..... 63

Figure 4.4 Set-up of the biaxial experiment [4.1]: (a) Regulation and establishment of temperature field for biaxial specimen; (b) Crack and strain field monitoring; (c) Front view of biaxial specimen and clamping jaws; (d) Back view of biaxial specimen and clamping jaws..... 65

Figure 4.5 Initial crack picked up by the DIC camera during pre-cracking [4.1]: (a) Specimen surface with metallic spray pattern; (b) Specimen surface without treatment. 66

Figure 4.6 Crack extension measurement and optical extensometer feature of the DIC system for through-crack variant, reference pixels in green squares [4.1]. 66

Figure 4.7 Thermal graphic (temperature field) of the biaxial specimen (C2) surface during adjustment of induction coil power rating with a target temperature of 425 °C at specimen centre [4.1]. 67

Figure 4.8 Initial crack of size $2a0 = 0.56\ \mathrm{mm}$ determined by DIC camera for biaxial specimen C2 [4.1]..... 67

Figure 4.9 Loading history for the quasi-static biaxial tensile test of specimen C2. 68

Figure 4.10 Force-strain curve for the quasi-static biaxial tensile test of specimen C2..... 68

Figure 4.11 Fractographic analysis with optical microscope of the fracture surface at crack plane of the biaxial specimen C2 (lower part)..... 69

Figure 4.12 View of the specimen surface of the fractured biaxial specimen C2. 69

Figure 4.13 Fractographic analysis with scanning electron microscope (SEM) of the fracture surface of the biaxial specimen C2: (a) Initial crack surface and stable crack extension surface; (b) Final fracture surface. 70

Figure 4.14 ACPD values for the quasi-static biaxial tensile test of specimen C2..... 70

Figure 4.15 Simplified crack surface model for determination of equivalent crack depth $a\mathrm{eq}$. 71

Figure 4.16 Stable crack extension measurement ($2a\mathrm{DIC}$) on specimen (C2) surface based on DIC images: (a) Point 1 in Figure 4.10; (b) Point 2 in Figure 4.10; (c) Point 3 in Figure 4.10; (d) Point 4 in Figure 4.10; (e) Point 5 in Figure 4.10; (f) Point 6 in Figure 4.10..... 72

Figure 4.17 FE model for determination of R-curve based on stable crack extension data from quasi-static test of biaxial specimen C2. 74

Figure 4.18 Crack growth resistance curve (R-curve) based on stable crack extension data from quasi-static test of biaxial specimen C2 (BV5). 74

Figure 4.19 Crack extension measurement and optical extensometer feature of the DIC system for surface crack variant, reference pixels in green squares [4.1]..... 75

Figure 4.20 Initial crack of size $2c0 = 0.71\ \mathrm{mm}$ determined by DIC camera for biaxial specimen E1. 76

Figure 4.21 Loading history for the quasi-static biaxial tensile test of specimen E1. 76

Figure 4.22 Force-strain curve for the quasi-static biaxial tensile test of specimen E1..... 77

Figure 4.23 Stable crack extension measurement ($2c\mathrm{DIC}$) on specimen (E1) surface based on DIC images, figure numbering corresponding to marks in Figure 4.22 [4.1]..... 77

Figure 4.24 Fractographic analysis with optical microscope of the fracture surface at crack plane of the biaxial specimen E1 (lower part)..... 78

Figure 4.25 View of the specimen surface of the fractured biaxial specimen E1. 79

Figure 4.26 Fractographic analysis with scanning electron microscope (SEM) of the fracture surface of the biaxial specimen E1: (a) Stable crack extension surface; (b) Final fracture surface. 79

Figure 4.27 DIC analysis: von Mises equivalent strain on the surface of the biaxial specimen C2 with through-crack. 81

Figure 4.28 Corresponding positions of the DIC images (Figure 4.27) in F-ε-diagram. 81

Figure 4.29 DIC analysis: von Mises equivalent strain on the surface of the biaxial specimen E1 with surface crack..... 82

Figure 4.30 Corresponding positions of the DIC images (Figure 4.29) in F-ε-diagram. 82

Figure 4.31 Set-up of the uniaxial experiment: (a) Crack initiation and growth monitoring during pre-cracking; (b) Target temperature establishment and quasi-static uniaxial tensile test. 83

Figure 4.32 Initial crack of size $2c0 = 0.78\ \mathrm{mm}$ for uniaxial specimen A1 after 56 000 cycles. 84

Figure 4.33 Mean temperature on the uniaxial specimen A1 surface during temperature establishment process. 85

Figure 4.34 Loading history (global strain) for the quasi-static uniaxial tensile test of specimen A1... 85

Figure 4.35 Force-local strain curve for the quasi-static uniaxial tensile test of specimen A1. 86

Figure 4.36 Determination of slopes of the elastic loading and reloading process in the quasi-static uniaxial tensile test of specimen A1: (a) Load_0; (b) Reload_1; (c) Reload_2; (d) Reload_3; (e) Reload_5; (f) Reload_6; (g) Reload_7. 86

Figure 4.37 Fractographic analysis with optical microscope of the fracture surface at crack plane of the uniaxial specimen A1 (lower part). 87

Figure 4.38 View of the specimen surface of the fractured uniaxial specimen A1. 87

Figure 4.39 Fractographic analysis with scanning electron microscope (SEM) of the fracture surface of the uniaxial specimen A1: (a) Stable crack extension surface; (b) Final fracture surface; (c) Final fracture surface on secondary plane; (d) Global view of the fracture surface. 88

Figure 4.40 Geometries of the uniaxial specimen after fracture: (a) symmetric fracture form viewed from the surface with notch; (b) view from the right of (a); (c) asymmetric fracture form viewed from the surface with notch; (d) view from the right of (c). 89

Figure 4.41 Crack extension direction on specimen surface: (a) fractured specimen surface with notch and secondary cracks of uniaxial specimen B2; (b) axial stress distribution on the cracked specimen (B2) surface; (c) axial stress distribution ahead of the crack-front at the deepest position along the crack-front, perpendicular to the crack plane..... 89

Figure 4.42 Fracture surface of uniaxial specimen C2 and C3 with marked crack-fronts: (a) Specimen C2 with crack-fronts marked after 49.2 kN and 50 kN; (b) Specimen C3 with crack-fronts marked after 49 kN and 49.5 kN; (c) Crack on specimen surface C2; (d) Crack on crack on specimen surface C3. 91

Figure 4.43 Determination of R-curve for uniaxial specimen with surface crack, biaxial R-curve shown for comparison. 92

Figure 4.44 Test-rig setup of the rim peel test, test disk analysed for rim peel proof of the investigated turbine disk in this work: (a) schematic view of the test rig; (b) test assembly mounted in the Test Facility (modified from [4.4]). 93

Figure 4.45 Radial stress distribution on the test disk in the rim peel test at the maximum rotational speed tested ($0.703N\mathrm{a}$ in the third increment) [4.5]. 94

Figure 4.46 Time plot of mean radial stress (elastic-plastic) and stress ratio at diaphragm critical location through the rim peel test [4.5]. 94

Figure 4.47 Test-rig setup of the hoop burst test, stage 1 disk analysed for hoop burst proof of the investigated turbine disk in this work (modified from [4.6]). 95

Figure 4.48 Domains on stage 1 of hoop burst rig-test disk FE model (hoop carrying section): (a) domains only considering disk body below airhole, $\mathrm{AWMHS} = 1.074\sigma\mathrm{Y}$; (b) domains considering disk body above airhole, $\mathrm{AWMHS} = 1.070\sigma\mathrm{Y}$ [4.7]. 96

Figure 4.49 Hoop stress and total hoop strain (elastic-plastic) distribution on stage 1 disk of the hoop burst rig-test at maximum rotational speed $0.971N\mathrm{a}$ (same legend scale for both stress distributions): (a) FE simulation using elastic material properties, $\mathrm{AWMHS} = 1.070\sigma\mathrm{Y}$; (b) FE simulation using elastic-plastic material properties, $\mathrm{AWMHS} = 1.063\sigma\mathrm{Y}$; (c) FE simulation using elastic-plastic material properties [4.7]. 96

Figure 4.50 Hoop stress values versus rotational speed of stage 1 disk of the hoop burst rig-test [4.7]. 97

Figure 5.1 Stress versus force in specimen centre of the FE simulation for uncracked biaxial specimen with elastic material properties. 100

Figure 5.2 Determination of reference yield stress based on FE simulations for the critical location along the through-crack on the biaxial specimen with $a\mathrm{eq} = 0.3\ \mathrm{mm}$. 101

Figure 5.3 Reference yield stress $\sigma 0$and limit load for failure mode plastic collapse in terms of stress and force for biaxial specimen with through-crack, determined for various crack depths at the critical location along crack-front. 101

Figure 5.4 Flow chart for determining the applied load versus stable crack extension curve based on FE simulations. 102

Figure 5.5 Determination of $J\mathrm{mat}$ for biaxial specimen C2 ($a0 = 0.325\ \mathrm{mm}$) with a crack growth $\Delta a = 0.025\ \mathrm{mm}$ ($a = 0.35\ \mathrm{mm}$) based on crack growth resistance versus crack depth curve. 103

Figure 5.6 Determination of limit load for stable crack extension for the biaxial specimen (through-crack) with $a\mathrm{eq} = 0.35\ \mathrm{mm}$ and $\Delta a = 0.025\ \mathrm{mm}$ based on the J versus applied load curve. 103

Figure 5.7 Load versus stable crack extension curve for the biaxial specimen C2 with initial crack $a0 = 0.325\ \mathrm{mm}$, critical load for failure mode ductile tearing $F\mathrm{dt}$ determined as the point with the highest $F\mathrm{B}$ value along the curve. 104

Figure 5.8 Failure assessment of the biaxial specimen C2 with through-crack based on two-criteria failure assessment method, failure mode determined as plastic collapse. 105

Figure 5.9 Determination of the failure load and failure mode based on the two-criteria failure assessment method for biaxial specimens with through-crack: (a) Specimen A1, pre-test; (b) Specimen A2, pre-test; (c) Specimen D1; (d) Specimen B1; (e) Specimen C1. 106

Figure 5.10 FE models with real crack geometry of biaxial specimen D1: (a) Mesh of the quarter model; (b) Local structured mesh refinement along the crack-front; (c) Fracture surface of the specimen D1 with crack-front marked. 107

Figure 5.11 Fracture surface on the biaxial specimen D2 with surface crack (lower part). 108

Figure 5.12 Parameterisation of the crack surface geometry on the biaxial specimen with surface crack for analysis. 109

Figure 5.13 Structured Mesh around the crack-front and crack geometric parameters in the FE model of biaxial specimen with surface crack: (a) Model in phase 1; (b) Model in phase 2. 110

Figure 5.14 Determination of reference yield stress based on FE simulations for the critical location along the surface crack on the biaxial specimen with $s = 0.4$ mm. 110

Figure 5.15 Reference yield stress $\sigma 0$and limit load for failure mode plastic collapse in terms of stress and force for biaxial specimen with surface crack, determined for various crack sizes at the critical location along crack-front. 111

Figure 5.16 Determination of Jmat for biaxial specimen E1 ($a0 = 0.399$ mm) with a crack growth $\Delta a = 0.101$ mm ($s = 0.500$ mm) based on crack growth resistance versus crack depth curve. 112

Figure 5.17 Determination of limit load for stable crack extension for the biaxial specimen (surface crack) with $s = 0.500$ mm and $\Delta a = 0.101$ mm based on the J versus applied load curve. 112

Figure 5.18 Load versus stable crack extension curve for the biaxial specimen E1 with initial crack $a0 = 0.399$ mm, decreasing part (dashed) of the curve omitted due to numerical expense. 112

Figure 5.19 Failure assessment of the biaxial specimen with surface crack based on two-criteria failure assessment method: (a) Biaxial specimen E1, failure mode determined as plastic collapse; (b) Biaxial specimen D2, failure mode determined as plastic collapse. 113

Figure 5.20 Summary of predicted failure load versus failure load recorded in test for all biaxial specimens. 114

Figure 5.21 Parameterisation of the crack surface geometry on the uniaxial specimen with surface crack for analysis. 115

Figure 5.22 Mesh of the FE model to determine the remote reference stress for uniaxial specimen. 116

Figure 5.23 Stress versus force in specimen centre of the FE simulation for uncracked uniaxial specimen with elastic material properties. 117

Figure 5.24 Determination of reference yield stress based on FE simulations for the deepest location along the surface crack on the uniaxial specimen with $a = 0.45$ mm. 117

Figure 5.25 Reference yield stress $\sigma 0$and limit load for failure mode plastic collapse in terms of stress and force for uniaxial specimen with surface crack, determined for various crack depths at the critical location along crack-front..... 117

Figure 5.26 Determination of limit load for stable crack extension for the uniaxial specimen (surface crack) with $a = 0.800$ mm and $\Delta a = 0.413$ mm based on the J versus applied load curve. .. 118

Figure 5.27 Load versus stable crack extension curve for the uniaxial specimen A1 with initial crack $a0 = 0.387$ mm. 119

Figure 5.28 Failure assessment of the uniaxial specimen with surface crack based on two-criteria failure assessment method: (a) Uniaxial specimen A1 with initial crack $a0 = 0.387$ mm, failure mode determined as plastic collapse; (b) Uniaxial specimen E1 with initial crack $a0 = 0.789$ mm, failure mode determined as ductile tearing. 120

Figure 5.29 Summary of predicted failure load versus failure load recorded in test for all uniaxial specimens..... 121

Figure 6.1 Radial stress versus rotational speed curve for critical location at diaphragm of the FE simulation for uncracked turbine disk with elastic material properties, Na is the reference overspeed..... 123

Figure 6.2 Determination of the reference yield stress for different crack sizes (semi-circular surface crack) at turbine disk diaphragm: (a) Determination of the reference yield stress for a crack of size $a = 0.50$ mm; (b) Reference yield stress for different crack sizes at diaphragm. 123

Figure 6.3 Two-criteria failure assessment of the turbine disk diaphragm with semi-circular surface crack of size $a0 = 0.381$ mm, limit load curves for plastic collapse determined based on Lrmaxtest values from biaxial specimen tests, failure mode determined as plastic collapse for diaphragm. 124

Figure 6.4 Hoop stress versus rotational speed curve for critical location at bore of the FE simulation for uncracked turbine disk with elastic material properties, Na is the reference overspeed.... 125

Figure 6.5 Determination of the reference yield stress for different crack sizes (semi-circular surface crack) at turbine disk bore: (a) Determination of the reference yield stress for a crack of size $a = 0.50$ mm; (b) Reference yield stress for different crack sizes at bore..... 125

Figure 6.6 Two-criteria failure assessment of the turbine disk bore with semi-circular surface crack of size $a0 = 0.381$ mm, limit load curves for plastic collapse determined based on Lrmaxtest values from uniaxial specimen tests, failure mode determined as plastic collapse for bore..... 126

Figure 6.7 Radial stress (elastic-plastic) versus rotational speed at critical diaphragm location of investigated turbine disk..... 127

Figure 6.8 Verification of the UMAT on the investigated turbine disk against original built-in material model in ABAQUS in form of von Mises stress distribution: (a) UMAT; (b) original built-in material model in ABAQUS [2.14]. 129

Figure 6.9 Determination of the critical rotational based on Hill's global stability criterion (RIKS-analysis shown for reference), $N\mathrm{a}$ is the analytically calculated reference overspeed based on the method used by the engine manufacturer: (a) turbine disk with and without crack at the diaphragm, critical temperature profile for diaphragm; (b) turbine disk with and without crack at bore, critical temperature profile for bore [2.14]. 130

Figure 6.10 Profile of the Load Proportional Factor and the corresponding rotational speed in RIKS-analysis for the turbine disk without crack using the critical temperature profiles for both locations [2.14]. 130

List of Tables

Table 1.1 Overview of the SINTAP assessment options 7

Table 2.1 Chemical composition of the superalloy Udimet 720 and Udimet 720Li [2.15] [2.16] 32

Table 3.1 Dimensional and tensile force parameters of the uncracked biaxial specimen in final configuration. 51

Table 3.2 Through-crack geometry parameters for FE simulation of cracked biaxial specimens 54

Table 3.3 Dimensions of the designed flat uniaxial fracture mechanics specimens 58

Table 4.1 Stable crack extension on biaxial specimen C2 72

Table 4.2 Results from FE simulations for determination of R-curve 74

Table 5.1 Test results for biaxial specimens with through-crack 99

Table 5.2 Failure assessment results for biaxial specimens with through-crack 107

Table 5.3 Test results for biaxial specimens with surface crack 108

Table 5.4 Failure assessment results for biaxial specimens with surface crack 114

Table 5.5 Test results for uniaxial specimens with surface crack 115

Table 5.6 Failure assessment results for uniaxial specimens with surface crack 121

Table 6.1 Critical rotational speed (normalised with respect to $N\mathrm{a}$) determined by the presented procedure and method 131

List of Symbols

A	area	J_{e}	elastic J-integral
a	crack depth	J_{mat}	fracture toughness in terms of J-integral
a_{dt}	critical crack depth for ductile tearing failure	J_{R}	crack growth resistance in terms of J-integral
a_{DIC}	crack depth measured by the DIC camera	K	stress intensity factor
a_{eq}	equivalent crack depth	K	hardening coefficient
a_{fin}	crack depth at maximum stable crack extension	$K_{\mathrm{mat}}, K_{\mathrm{mat}}^{\mathrm{c}}$	fracture toughness in terms of stress intensity factor, corrected
a_{plc}	critical crack depth for plastic collapse failure	K_{r}	fracture ratio (=K/K_{mat})
a_0	initial crack depth	L_{r}	ligament yielding parameter
Δa	stable crack extension	$L_{\mathrm{r}}^{\max}$	maximum ligament yielding parameter (analytical)
c	half crack length	$L_{\mathrm{r}}^{\max}{}_{\mathrm{test}}$	maximum ligament yielding parameter (experimental)
c_0	initial half crack length	m_{blade}	mass of the turbine blade
E	Young's modulus	N	hardening exponent
f	frequency	N	rotational speed
$\boldsymbol{F}$	deformation gradient	N_{a}	analytically calculated reference overspeed
F_{dt}	critical load for ductile tearing failure in terms of force	$N_{\mathrm{rp}}, N_{\mathrm{hb}}$	critical speed for rim peel failure, hoop burst failure
F_{plc}	plastic collapse load in terms of force	n_{blade}	number of the turbine blades
$\boldsymbol{f_i}$	body force	P, P_{L}	Load, elastic perfectly plastic limit load
$f(L_{\mathrm{r}})$	ligament yielding correction function	R	load ratio
h	stress triaxiality factor	r	radial distance from crack-tip
J	J-integral	R_{m}	ultimate tensile strength
		$R_{\mathrm{p0.2}}$	yield strength with 0.2% offset

s	crack extension in the direction of the maximum stable crack extension	ν	Poisson's ratio
$\boldsymbol{S}$	first Piola-Kirchhoff stress tensor	ρ_0	density
T	temperature	σ_0	reference yield stress
$\boldsymbol{T_i}$	surface traction load	σ_{app}	applied stress
U_{ACPD}	potential drop of the ACPD probes	σ_{dt}	ductile tearing load in terms of stress
$\boldsymbol{V}, \boldsymbol{V_{\mathrm{CoG}}}$	velocity field	σ_{h}	hydrostatic stress
v_0	integration point volume	σ_{hoop}	hoop stress
$\boldsymbol{XC}$	centre of gravity coordinates	σ_{plc}	plastic collapse load in terms of stress
α_{h}	hyper-local constraint parameter	σ_{rad}	radial stress
α_{l}	local constraint parameter	σ_{ref}	reference stress
β	structural constraint parameter	σ_{vM}	von Mises equivalent stress
δ_{ij}	Kronecker delta	σ_{plc}	plastic collapse load in terms of stress
δ_{mat}	fracture toughness in terms of CTOD	σ_{rad}	radial stress
$\varepsilon_{\mathrm{el}}$	elastic strain	σ_{ref}	reference stress
$\varepsilon'_{\mathrm{eq}}$	von Mises equivalent strain (true)	σ_{vM}	von Mises equivalent stress
$\dot{\varepsilon_{\mathrm{g}}}$	global strain rate	σ_{Y}	yield stress
ε_{l}	local strain	σ_{yy}	crack opening stress
$\varepsilon_{\mathrm{pl}}, \varepsilon_{\mathrm{pl,eq}}$	plastic strain, equivalent plastic strain	φ	circumferential position along crack-front
$\varepsilon_{\mathrm{ref}}$	reference strain	ω	angular velocity
λ, λ_F	biaxial stress ratio, biaxial force ratio		

List of Abbreviations

ACPD	Alternating Current Potential Drop	FE	Finite Element
AWMHS	Area-Weighted Mean Hoop Stress	FITNET	European Fitness for Service Network
AWMT	Area-Weighted Mean Temperature	LPF	Load Proportional Factor
BS	British Standard	MRS	Mean Radial Stress
CAD	Computer-Aided Design	MSOW	Modified Second Order Work
CDF	Crack Driving Force	MST	Mean Section Temperature
C(T)	Compact Tension	ODB	Output Database
CTOD	Crack Tip Opening Displacement	SDV	State Dependent Variable
DDSDDE	Constitutive Jacobian Matrix	SE(B)	Three-point Bending
DIC	Digital Image Correlation	SEM	Scanning Electron Microscope
EASA	European Union Aviation Safety Agency	SE(T)	Single Edge notch Tension
ECA	Engineering Critical Assessment	SINTAP	Structural Integrity Assessment Procedure
EDM	Electrical Discharge Machining	SOW	Second Order Work
FAD	Failure Assessment Diagram	UMAT	User-Material Subroutine
FAL	Failure Assessment Line		

References

[1.1] British Standard Institution, London, BS 7910:2019 - Guide to methods for assessing the acceptability of flaws in metallic structures, BSI Standards Limited 2019, ISBN 978 0 580 52086 0, 2019

[1.2] Harrison, R.P., Loosemore, K. and Milne, I., Assessment of the Integrity of Structures Containing Defects, CEGB, CEGB Report R/H/R6, 1976.

[1.3] Zerbst, U., Schödel, M., Webster, S. and Ainsworth, R.A., Fitness-for-Service Fracture Assessment of Structures Containing Cracks - A Workbook based on the European SINTAP/FITNET Procedure, 2007

[1.4] Zerbst, U., Madia, M., Review – Analytical flaw assessment, Engineering Fracture Mechanics 187 (2018) 316–367, 2018

[1.5] Madia, M., Effect of Constraint on Crack Propagation in Mechanical Components, Ph.D. Thesis, POLITECNICO DI MILANO, Department of Mechanical Engineering, 2008

[1.6] Ainsworth, R.A., Bannister, A. and Zerbst, U., An overview on the European flaw assessment procedure SINTAP and its validation, Int. J. Press. Vess. Piping, 77, pp. 869–76, 2000

[1.7] ASTM International, Standard Test Method for Linear-Elastic Plane-Strain Fracture Toughness K_{Ic} of Metallic Materials – Designation E399-19, 2019

[1.8] Barbosa, V.S., Ruggieri, C., Fracture toughness testing using non-standard bend specimens - Part I: Constraint effects and development of test procedure, Engineering Fracture Mechanics, 195 (2018) 279-296, 2018

[1.9] Barbosa, V.S., Ruggieri, C., Fracture toughness testing using non-standard bend specimens - Part II: Experiments and evaluation of T_0 reference temperature for a low alloy structural steel, 195 (2018) 297-312, 2018

[1.10] Cravero, S., Ruggieri, C., Correlation of fracture behavior in high pressure pipelines with axial flaws using constraint designed test specimens. Part I: Plane-strain analyses, Engineering Fracture Mechanics 72 (2005) 1344–1360, 2005

[1.11] Silva, L.A.L., Cravero, S., Ruggieri, C., Correlation of fracture behavior in high pressure pipelines with axial flaws using constraint designed test specimens. Part II: 3-D effects on constraint, Engineering Fracture Mechanics 73 (2006) 2123–2138, 2006

[1.12] Wang, Y.H., Wang, G.Z., Tu, S.T., Xuan, F.Z., Ductile fracture prediction based on J-integral and unified constraint parameters for cracked pipes, Engineering Fracture Mechanics 215 (2019) 1-15, 2019

[1.13] Seal, C.K., Sherry, A.H., Predicting the effect of constraint on cleavage and ductile fracture toughness using area contour toughness scaling, Engineering Fracture Mechanics 186 (2017) 347–367, 2017

[1.14] Kouzoumis, K., Hadley, I., Mostafavi, M., Effect of Biaxiality on Engineering Critical Assessments, Procedia Structural Integrity 17 (2019) 347–354, 2019

[1.15] Oh, C., Kim, Y., Budden, P., Ainsworth, R.A., Biaxial stress effects on estimating J under combined mechanical and thermal stresses, International Journal of Pressure Vessels and Piping 88 (2011) 365-374, 2011

[1.16] Seah, T.T., Qian, X., Zhang, Y., Constraint-based failure assessment for pipelines with coplanar circumferential cracks under biaxial loading, International Journal of Pressure Vessels and Piping 190 (2021) 104320, 2021

[1.17] James, P.M., Hooton, D.G., Madew, C.J., Sharples, J.K., Jackson, M., Extension of the simplified method for the interaction of primary and secondary stresses, Proc ASME PVP. ASME, PVP2009-77367, 2009

[1.18] Zerbst, U., Ainsworth, R.A., Madia, M., Reference load versus limit load in engineering flaw assessment: a proposal for a hybrid analysis option, Eng Fract Mech 2012;91:62-72, 2012

[1.19] Zerbst, U., Pempe, A., Scheider, I., Ainsworth, R.A., Schönfeld, W., Proposed extension of the SINTAP/FITNET thin wall option based on a simple method for reference load determination, Eng Fract Mech 2009;76:74-87, 2009

[1.20] Zerbst, U., Kiyak, Y., Madia, M., Burgold, A., Riedel, G., Reference loads for plates with semi-elliptical surface cracks subjected to tension and bending for application within R6 type flaw assessment, Eng Fract Mech 2013;99:132-40, 2013

[1.21] Madia, M., Arafah, D., Zerbst, U., Reference load solutions for plates with semi-elliptical surface cracks subjected to biaxial tensile loading, International Journal of Pressure Vessels and Piping 119 (2014) 19-28, 2014

[1.22] Zerbst, U., Madia, M., Kiyak, Y., Breidung, M., Baer, W., Küppers, M., Stiffness/constraint effects in analytical flaw assessment. A technical note, Engineering Fracture Mechanics 273 (2022) 108728, 2022

[1.23] Johnson, C.W., Holloway, C.M., Questioning the Role of Requirements Engineering in the Causes of Safety-Critical Software Failures, 1st IET International Conference on System Safety, 352 – 361, 2006

[1.24] Australian Transport Safety Bureau (ATSB), In-flight uncontained engine failure overhead Batam Island, Indonesia 4 November 2010 VH-OQA Airbus A380-842, AO-2010-089, 2010

[1.25] William, E. N. and Monroe, P. C., Understanding and preventing steam turbine overspeeds. In Proc. 26th Turbomachinery Symposium, 129–142, 1997

[1.26] Rolls-Royce plc., Pearl 700, available on https://www.flickr.com/photos/rolls-royceplc/48935744002/in/album-72157711434743583/, 2019

[1.27] European Union Aviation Safety Agency (EASA), Certification Specifications and Acceptable Means of Compliance for Engines CS-E Amendment 5, 2018

[1.28] Corran, R.S.J., Williams, S.J., Lifing methods and safety criteria in aero gas turbines, Engineering Failure Analysis 14 518–528, 2007

[2.1] Brocks, W., Schmitt, W., Quantitative assessment of the role of crack-tip constraint on ductile tearing, ASTM STP 1171, Philadelphia, 1993

[2.2] Brocks, W., Schmitt, W., The second parameter in J-R curves: constraint or triaxiality?, ASTM STP 1244, Philadelphia, 1995

[2.3] Yuan, H., Brocks, W., Quantification of constraint effects in elastic-plastic crack-front fields, J. Mech. Phys. Solids, 1998;46(2):219-241, 1998

[2.4] Newman, J.C., A crack opening stress equation for fatigue crack growth, Int J Fracture 24: R131–5, 1984

[2.5] Leach, A.M., Daniewicz, S.R., Newman Jr., J.C., A new constraint based fracture criterion for surface cracks. Engineering Fracture Mechanics 74:1233-1242, 2007

[2.6] Hill, R., A general theory of uniqueness and stability in elastic-plastic solids, J. Mech. Phys. Solids 6, 236–249, 1958

[2.7] Hill, R., Some basic principles in the mechanics of solids without a natural time, J. Mech. Phys. Solids 7, 209–225, 1959

[2.8] Petryk, H., Theory of bifurcation and instability in time-independent plasticity. Bifurcation and Stability of Dissipative Systems. In: CISM Courses and Lectures. Springer-Verlag, Wien, pp. 95–152, 1993

[2.9] Tvergaard, V., Tensile instabilities at large strains. Bifurcation and Stability of Dissipative Systems. In: CISM Courses and Lectures. Springer-Verlag, Wien, pp. 251–291, 1993

[2.10] Mazière, M., Besson, J., Forest, S., Tanguy, B., Chalons, H., Vogel, F., Overspeed burst of elastoviscoplastic rotating disks: Part I – Burst of a superalloy turbine disk, European Journal of Mechanics A/Solids, 28 (2009) 36–44, 2009

[2.11] Mazière, M., Besson, J., Forest, S., Tanguy, B., Chalons, H., Vogel, F., Overspeed burst of elastoviscoplastic rotating disks: Part II – Burst of a superalloy turbine disk. European Journal of Mechanics A/Solids, 28 (2009) 428-432, 2009

[2.12] ABAQUS ver.2019, Reference Manual, 2019.

[2.13] Boulbes, R.J., Troubleshooting finite-element modeling with Abaqus, © Springer Nature Switzerland AG, ISBN 978-3-030-26739-1, P151-157, 2020

[2.14] Zhu, J., Madia, M., Schurig, M., Fedelich, B., Schlums, H., Zerbst, U., Burst speed assessment of aero-engine turbine disk based on failure assessment diagram and global stability criterion. Engineering Fracture Mechanics, 277 (2023) 109005, 2023.

[2.15] Jackson, M.P., Reed, R.C., Heat treatment of UDIMET 720Li: the effect of microstructure on properties, Materials Science and Engineering A259 (1999) 85–97, 1999

[2.16] Higgins, J., Ni-16Cr-14.75Co-5Ti-3Mo-2.5Al-1.25W-0.015C-0.015B-0.035Zr VIM/EFR/VAR alloy discs and associated rotating components, Rolls-Royce plc., 2022

[2.17] Ren, W., Nicholas, T.. The effects of low cycle fatigue and plastic deformation on the subsequent high cycle fatigue limit of nickel-base superalloy Udimet 720Li. Mater Sci Eng, A332:238–48, 2002

[2.18] Wan, Z., Hu, L., Sun, Y., Wang, T., Li, Z., Zhang, Y., Effect of solution treatment on microstructure and tensile properties of a U720LI Ni-based superalloy, Vacuum 156 (2018) 248–255, 2018

[2.19] Bain, K.R., Gambone, M.L., Hyzak, J.M., Thomas, M.C. in: S. Reichman, D.N. Duhl, G. Maurer, S. Antolovich, C. Lund (Eds.), Superalloys 1988, The Metallurgical Society, Warrendale, PA, 1988, pp. 13–22

[3.1] European Union Aviation Safety Agency (EASA), Certification Memorandum EASA CM – PIFS – 007 Issue: 01: Engine Critical Parts - Damage Tolerance Assessment Manufacturing and Surface Induced Anomalies, 2013

[3.2] DIN Deutsches Institut für Normung, Metallische Werkstoffe – Zugversuch – Teil 2: Prüfverfahren bei erhöhter Temperatur (ISO 6892-2:2011); Deutsche Fassung EN ISO 6892-2, 2011

[3.3] Erbe, A., Conrad, F., Kraemer, K.M., Kontermann, C., Bianchini, M., Kulawinski, D., Oechsner, M., A systematic experimental study on the impact of multiaxiality on fatigue life of cast steels at high temperature, Procedia Structural Integrity, Vol. 38 p. 192-201, 2022

[4.1] Conrad, F., Figures and test data for Project Roboflex, MPA Darmstadt, 2022

[4.2] Conrad, F., Blug, A., Kerl, J., Fehrenbach, J., Regina, D.J., Bertz, A., Kontermann, C., Carl, D., Oechsner, M., GPU-based digital image correlation system for uniaxial and biaxial crack growth investigations, Procedia Structural Integrity 28 (2020) 2195–2205, 2020

[4.3] Huron, E.S., Serrated Yielding in a nickel-base superalloy, Engineered Materials Technology Laboratories, GE Aircraft Engines, 1992.

[4.4] Lehmann, L., MRA44654 MK 4 HPTD Rim Peel Overspeed Rig Test, GEVA mbH, 2011

[4.5] Sandala, R., MRA44654 Trent 900 HPT Disc Rim Peel Rig Test stress analysis, Rolls-Royce Deutschland, 2012

[4.6] Kuhlmey, U., Test Report for SP.406 HPT Over Speed Test, MT-14_S0019, Rolls-Royce Deutschland, 2017

[4.7] Kähler, B., BR700-710D5-21 - HP Turbine - Disc - Overspeed Test SP.406.BR7NG in Udimet 720Li – Stress Test Report, Rolls-Royce Deutschland, 2017

[6.1] Dassault Systemes, SIMULIA User Assistance 2019 / Abaqus / Unstable collapse and postbuckling analysis, Unstable collapse and postbuckling analysis - SIMULIA User Assistance 2019 (3ds.com), 2019

[6.2] Riks, E., An incremental approach to the solution of snapping and buckling problems. Int. J. Solids Structures 15, 529–551, 1979

[6.3] Zhu, J., Madia, M., Schurig, M., Schlums, H., Zerbst, U., Fracture mechanics-based structural integrity assessment of aero-engine turbine disks under overspeed conditions, Proceedings of ASME Turbo Expo 2022, GT2022-79925, 2022

[6.4] Haeuser, C., Lenz, M., Calibration certificate 22/06067J D-K-17552-01-00, MPA Kalibrierdienst, 2022

Appendix

1. Information of the biaxial testing machine [4.1].

Manufacturer	Instron
Controlling system	Instron 8800
Description	Planar biaxial testing system, 4*servo-hydraulic cylinders
Rated Force capabilities	500 kN (static) 250 kN (dynamic)
Calibration	DIN EN ISO 9513
Accuracy class	0.5

2. Information of the uniaxial testing machine [6.4].

Manufacturer	Carl Schenck AG
Controlling system	MTS Flex Test 200
Description	Uniaxial testing system, 1*servo-hydraulic cylinder
Rated Force capabilities	60 kN (static)
Calibration	DIN EN ISO 9513
Accuracy class	1.0

3. Test results of the biaxial specimen quasi-static tensile test.

Note: Displacement measurement error during test BV2.

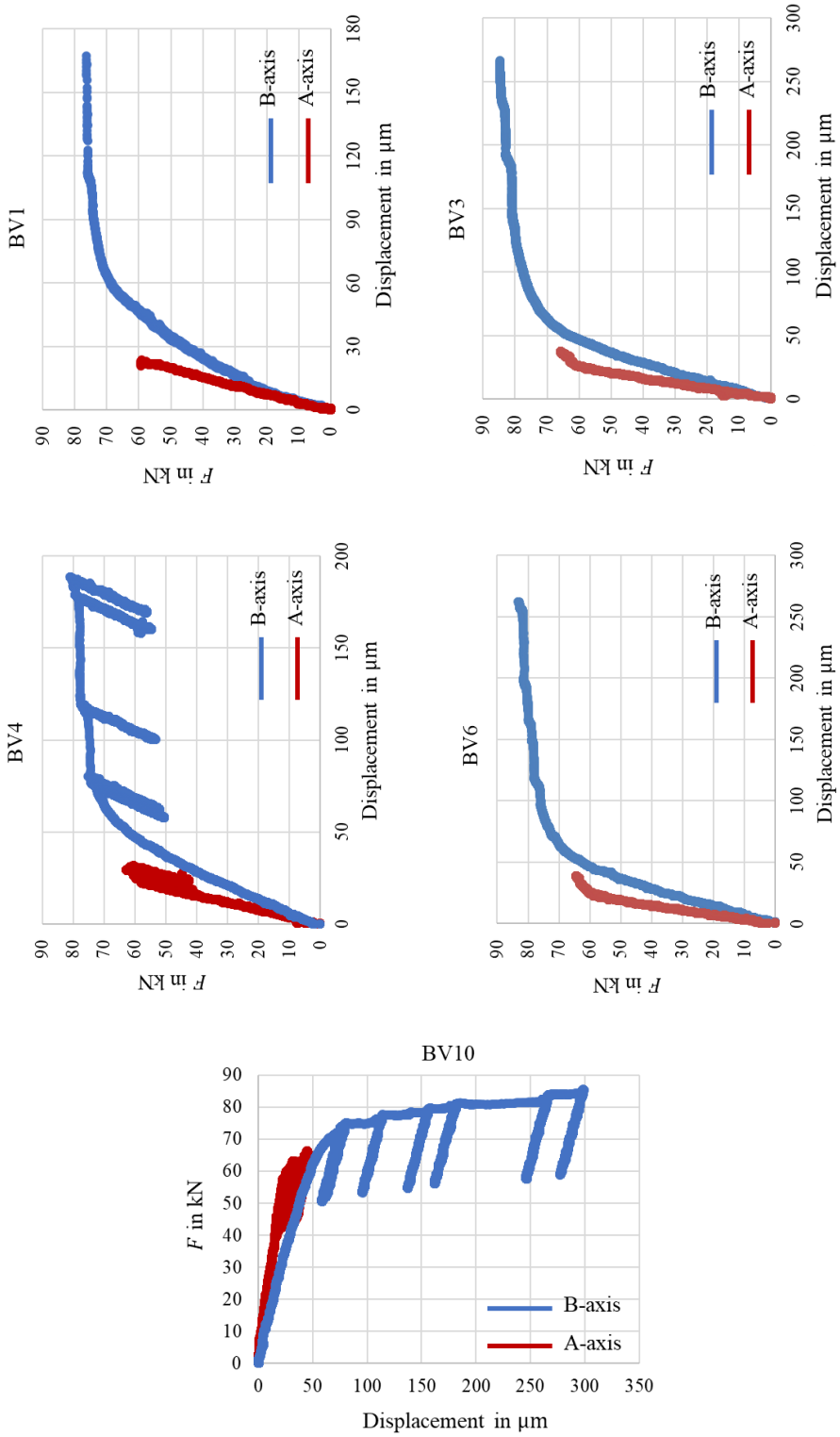

4. Fractographic analysis of the tested biaxial specimens

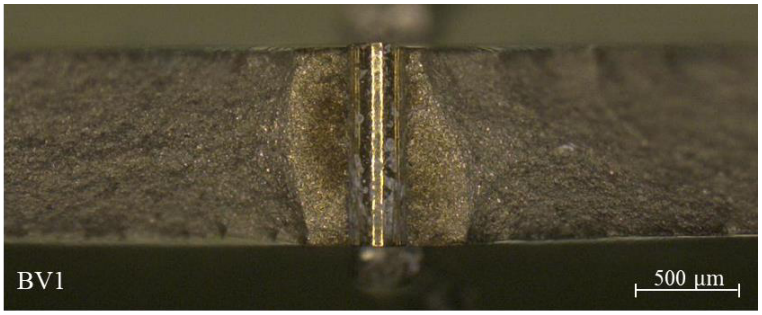

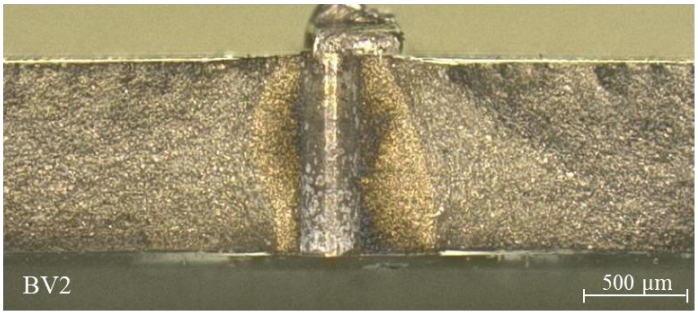

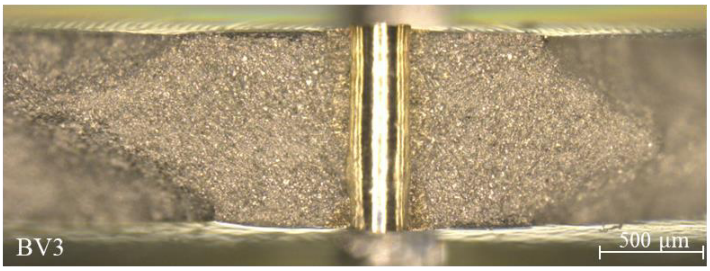

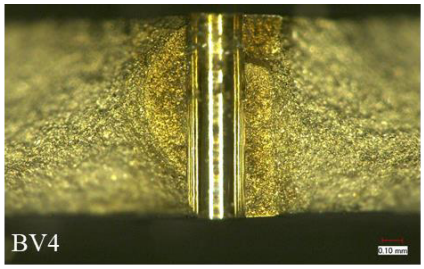

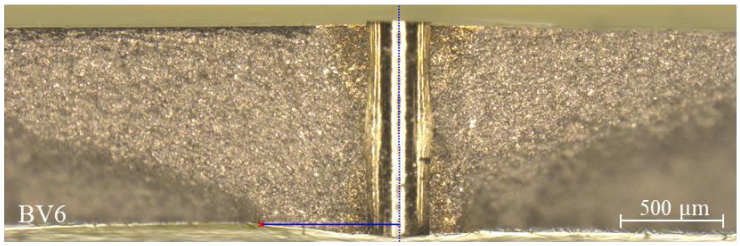

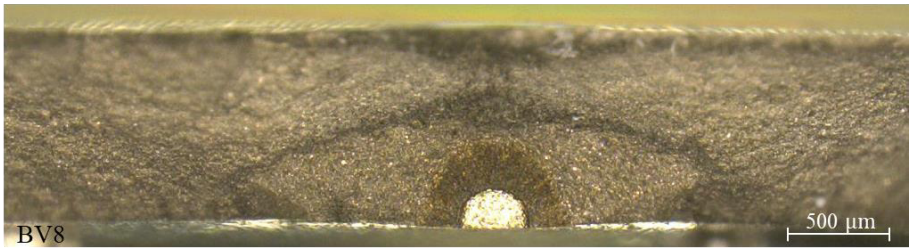

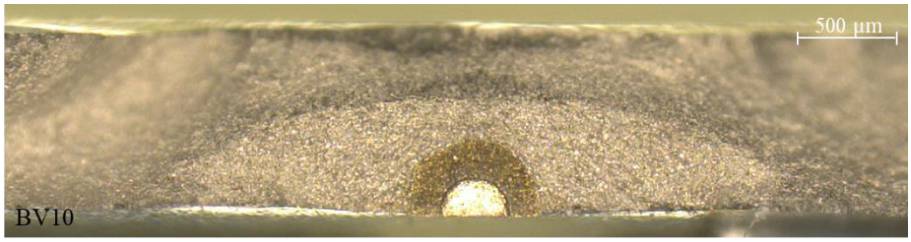

5. R-curves determined based on biaxial specimen tests.
    - Biaxial test BV3:

Crack growth and crack driving force for biaxial test BV3 ($a_0 = 0.268$ mm)

a_{eq} in mm	Δa in mm	J in N/mm
0.317	0.049	11.61
0.382	0.114	25.40
0.420	0.152	38.15
0.440	0.172	44.91
0.647	0.379	72.30
1.007	0.739	111.5
1.036	0.768	111.7

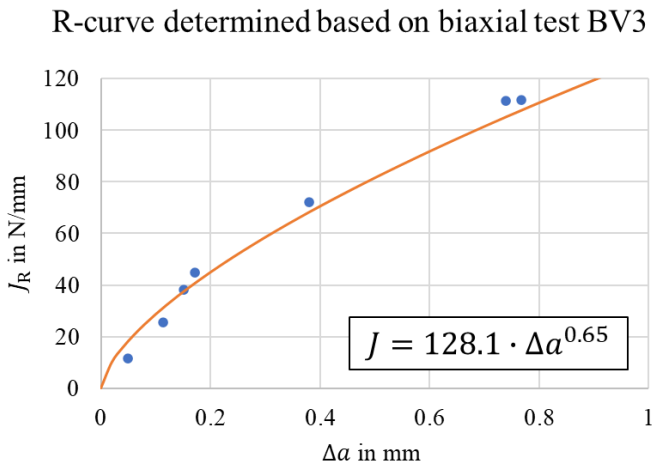

- Biaxial test BV4:

Crack growth and crack driving force for biaxial test BV4 ($a_0 = 0.350$ mm)

a_{eq} in mm	Δa in mm	J in N/mm
0.351	0.001	11.48
0.380	0.030	15.49
0.549	0.199	30.73
0.560	0.210	39.48
0.566	0.216	45.62

- Biaxial test BV6:

Crack growth and crack driving force for biaxial test BV6 ($a_0 = 0.303$ mm)

a_{eq} in mm	Δa in mm	J in N/mm
0.310	0.007	11.29
0.331	0.028	19.44
0.360	0.057	22.56
0.402	0.099	33.33
0.450	0.147	48.26

- Summary

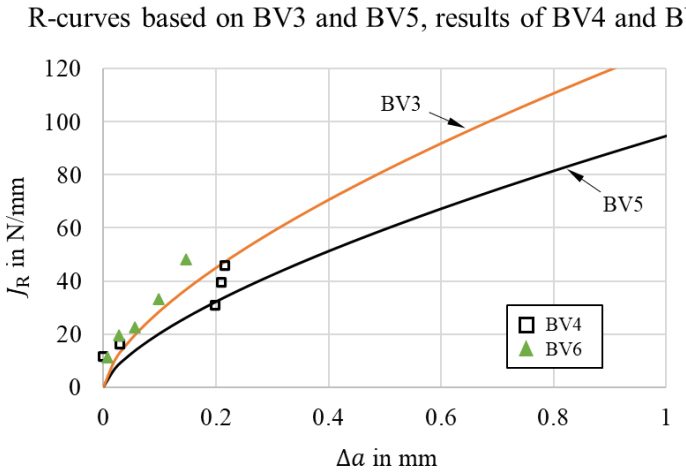

Note:

- The biaxial pre-tests BV1 and BV2 have been excluded from R-curve analysis, since there has been no stable crack extension observed in these tests.
- The biaxial tests with surface cracks BV8 and BV10 have been excluded from R-curve analysis, since the stable crack extension along the crack front has been inhomogeneous and no correlation between the crack extension on specimen surface and the maximum crack extension direction possible.
- For BV4: the initial crack fronts have been asymmetric, stable crack extension not entirely in the initial crack plane. Based on the DIC images, the equivalent crack depths determined based on the area-weighted model were limited to approximately 0.2 mm.
- For BV6: the initial crack fronts have not been in straight-line across the thickness, more stable crack extension took place at the aft side of the specimen (DIC camera on the front side). Based on the DIC images, the equivalent crack depths determined based on the area-weighted model were limited to approximately 0.15 mm.
- Despite the irregularities of the initial crack fronts and the stable crack extensions in BV4 and BV6, the hybrid method showed its robustness in R-curve determination where the $J - \Delta a$ results of the both specimens showed good agreement with R-curves determined based on BV3 and BV5.

6. Test results of the uniaxial specimen quasi-static tensile test.

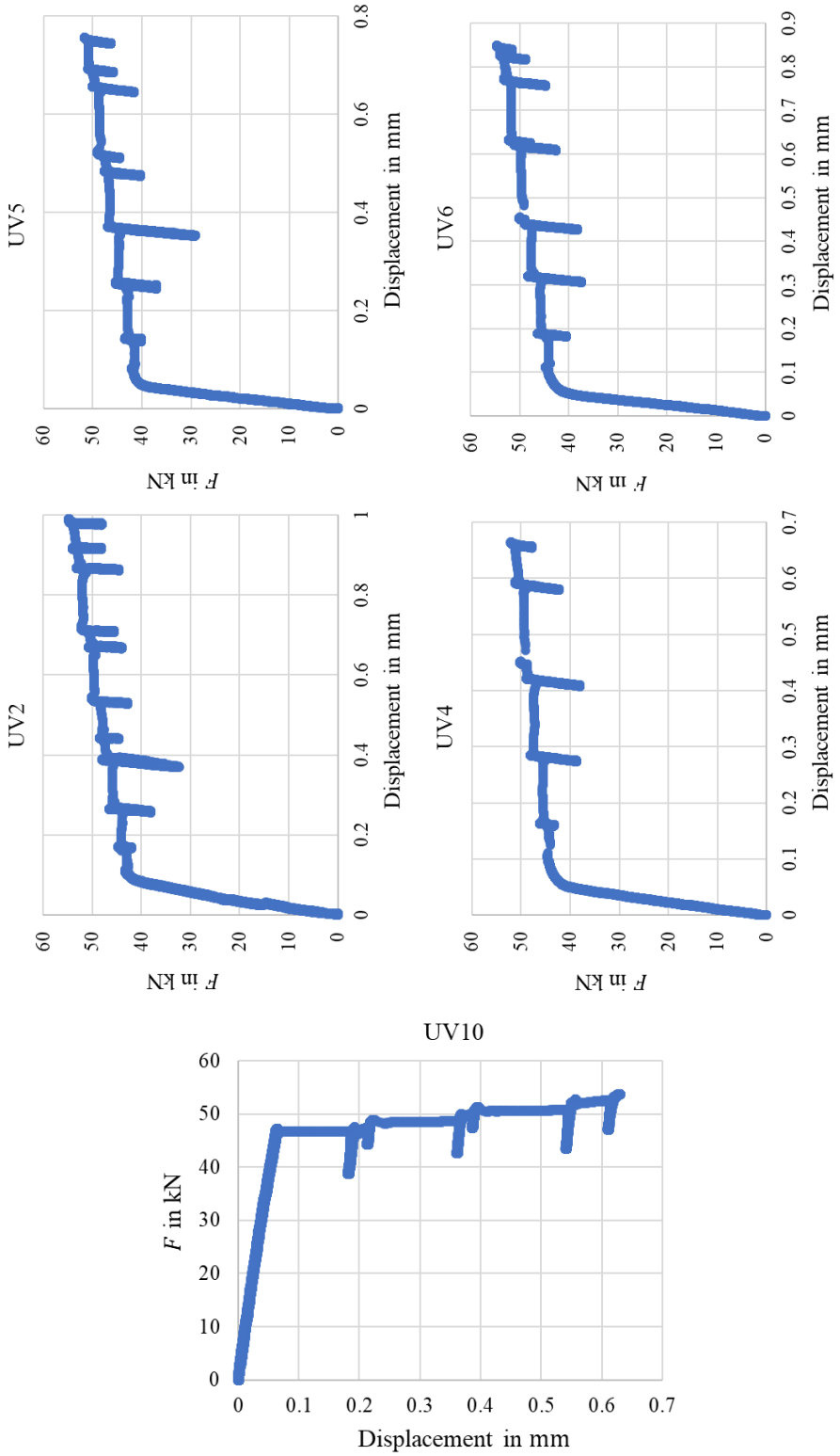

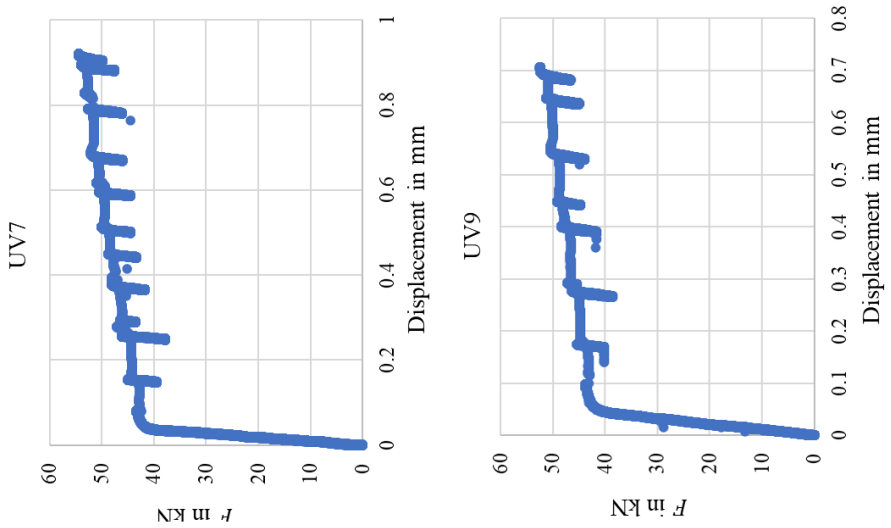

Note: Displacement measurement error during test UV1 and UV3.

7. Fractographic analysis of the tested uniaxial specimens

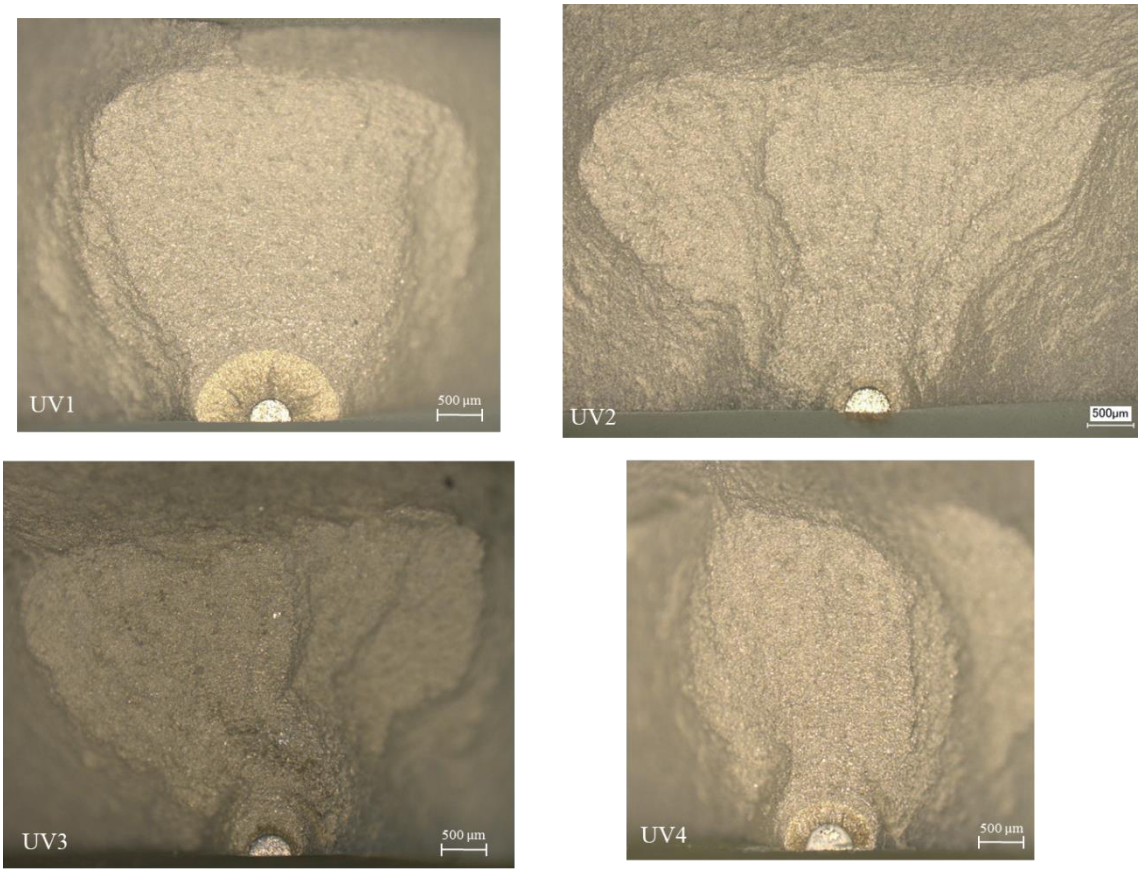

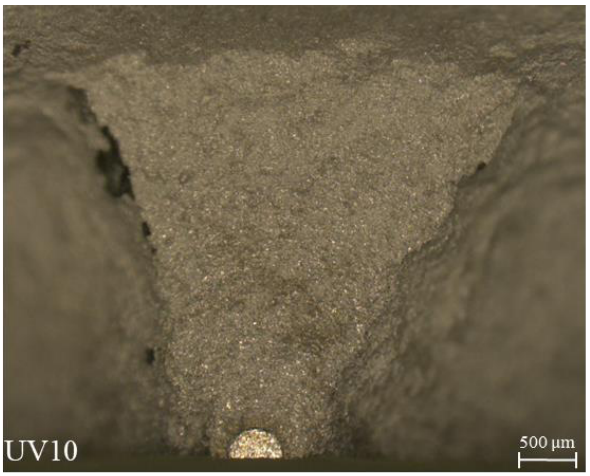
UV10
500 µm

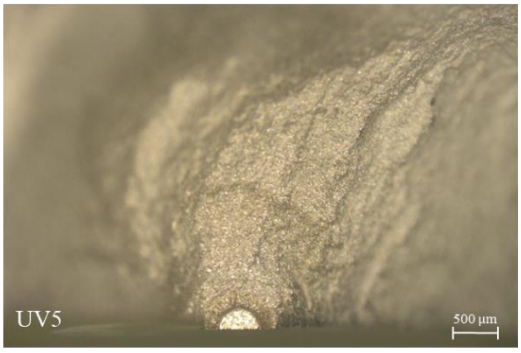
UV5
500 µm

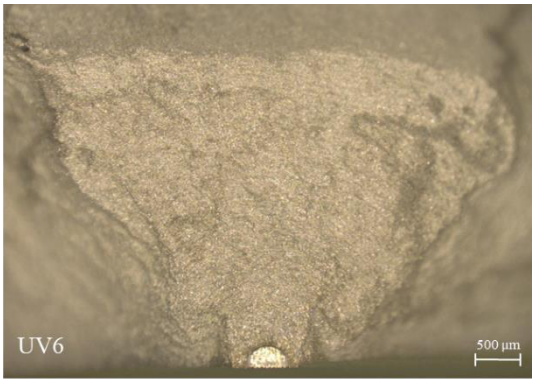
UV6
500 µm

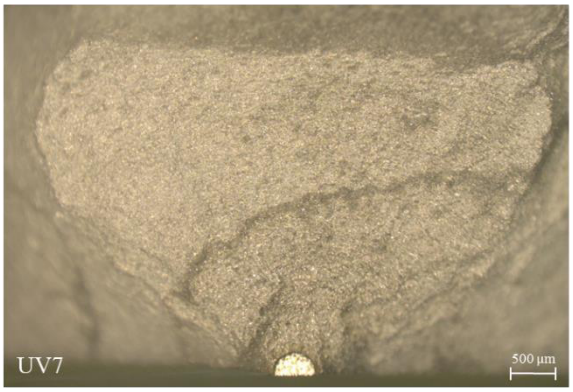
UV7
500 µm

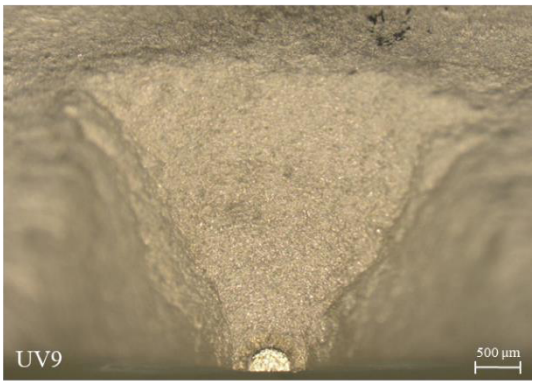
UV9
500 µm

8. Two-criteria failure assessment for uniaxial specimens

Note: A single assessment has been conducted for uniaxial test UV6 and UV10 due to the initial crack sizes of the two specimens only differ 0.002 mm.

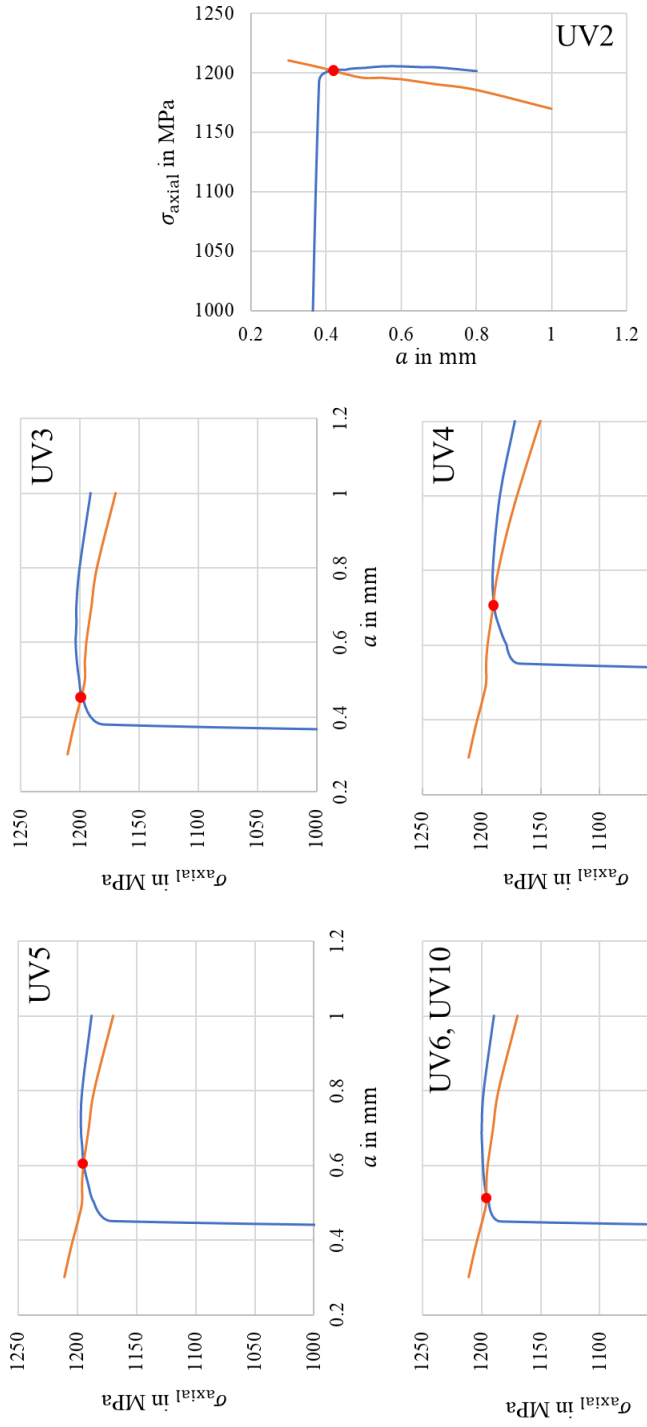

UV7
UV9
σ_{axial} in MPa
a in mm
1250
1200
1150
1100
1050
1000
0.2
0.4
0.6
0.8
1
1.2